

**The Incandescent Remains of Stellar Death:  
High Energy Emission from Supernova Remnants and Pulsar  
Wind Nebulae**

by

**Katie Amanda Auchettl, B.Sc. (Hons), M.Sc.**



**Thesis**

Submitted by Katie Amanda Auchettl  
for fulfillment of the Requirements for the Degree of  
**Doctor of Philosophy (0057)**

Supervisors: Dr. Patrick Slane (SAO), A/Prof. Csaba Balázs (Monash),  
and Dr. Jasmina Lazendic-Galloway (Monash)

**School of Physics and Astronomy  
Monash University**

June, 2015

## **Copyright Notices**

### **Notice 1**

Under the Copyright Act 1968, this thesis must be used only under the normal conditions of scholarly fair dealing. In particular no results or conclusions should be extracted from it, nor should it be copied or closely paraphrased in whole or in part without the written consent of the author. Proper written acknowledgement should be made for any assistance obtained from this thesis.

### **Notice 2**

I certify that I have made all reasonable efforts to secure copyright permissions for third-party content included in this thesis and have not knowingly added copyright content to my work without the owner's permission.

---

# Contents

<b>Contents</b>	<b>i</b>
<b>Abstract</b>	<b>iii</b>
<b>List of research outputs</b>	<b>v</b>
<b>General Declaration</b>	<b>vii</b>
<b>Acknowledgements</b>	<b>ix</b>
<b>1 Introduction</b>	<b>1</b>
1.1 Supernovae	1
1.2 Supernova remnants	2
1.2.1 Dynamical evolution	3
1.2.2 Morphologies of supernova remnants	6
1.2.3 Heating collisionless plasmas to X-ray emitting temperatures	10
1.2.4 Ionisation equilibrium of the X-ray emitting plasma in a SNR	12
1.2.5 Thermal emission from an X-ray emitting plasma	13
1.3 Pulsars and their Pulsar Wind Nebulae	17
1.3.1 The properties of the central pulsar	18
1.3.2 Evolution of a pulsar wind nebula	19
1.3.3 The morphology of pulsar wind nebulae	19
1.3.4 Emission from a pulsar and its nebula	21
1.4 Cosmic rays and their non thermal emission	22
1.4.1 Diffusive shock acceleration	26
1.4.2 Cosmic-ray propagation	27
1.4.3 Non-thermal emission from accelerated particles	30
1.5 Observational signatures of SNRs interacting with their surroundings	35
1.5.1 Maser emission	36
1.5.2 Line and molecular emission	37
1.6 Thesis outline	37
<b>2 Extracting the size of the cosmic electron-positron anomaly</b>	<b>39</b>
2.1 Introductory remarks	41
2.2 Declaration for thesis chapter 2	42
2.3 Published material: Paper I	44

<b>3</b>	<b><i>Fermi</i>-LAT observations of supernova remnant Kesteven 79</b>	<b>59</b>
3.1	Introductory remarks	60
3.2	Declaration for thesis chapter 3	62
3.3	Published material: Paper II	64
<b>4</b>	<b>Multi-wavelength analysis of Galactic supernova remnant MSH 11–61A</b>	<b>79</b>
4.1	Introductory remarks	80
4.2	Declaration for thesis chapter 4	82
4.3	Published material: Paper III	84
<b>5</b>	<b>X-ray analysis of the proper motion and pulsar wind nebula for PSR J1741-2054</b>	<b>97</b>
5.1	Introductory remarks	98
5.2	Declaration for thesis chapter 5	100
5.3	Published material: Paper IV	103
<b>6</b>	<b>Conclusions and Future Work</b>	<b>111</b>
6.1	Summary	112
6.2	Future Work	115
	<b>Appendices</b>	<b>119</b>
<b>A</b>	<b>Bayesian Inference and Model Selection</b>	<b>119</b>
A.1	Definitions of Probability	119
A.2	Bayes' Theorem	120
A.2.1	Prior $P(H_i(\Theta) I)$	121
A.2.2	Nuisance Parameters	121
A.2.3	Calculation of the likelihood and the Bayesian evidence	122
A.2.4	Model/Hypothesis testing using the evidence function.	122
<b>B</b>	<b>Solving the cosmic ray transport equation</b>	<b>125</b>
B.1	GALPROP	125
	<b>Bibliography</b>	<b>131</b>

---

## Abstract

When a star dies, it leaves a mark on its surrounding environment. The energy from the supernova explosion forms an expanding shock wave that interacts with interstellar and circumstellar material, creating what we know as a supernova remnant (SNR). If the original star has a mass  $\geq 8M_{\odot}$ , this can also lead to the formation of a rapidly rotating neutron star called a pulsar. As these objects evolve, they interact with the surrounding environment, producing *non-thermal* and *thermal* emission. For an SNR, its non-thermal emission arises from a population of relativistic particles being accelerated at the shock front of the SNR, while its thermal emission arises from the shock front heating ejecta and swept-up interstellar medium to X-ray emitting temperatures. For pulsars, their non-thermal emission arises from relativistic particles being accelerated at the termination shock of a pulsar wind. These particles interact with surrounding magnetic fields and ambient photon fields producing synchrotron and inverse Compton emission which we observe as a pulsar wind nebula (PWN), while its thermal emission arises from the surface of the neutron star. These properties of SNRs and pulsars provide a unique window into studying the acceleration, injection, propagation and interaction of highly energetic particles called cosmic rays with the interstellar medium. In addition, they provide information about the evolution, and dynamics of these objects; properties of the shock fronts; details about the original progenitor star; and the impact that these objects have on their surroundings. The research presented here focuses on analysing the intimate connection between cosmic rays, the non-thermal emission arising from SNRs interacting with molecular clouds, and pulsar wind nebulae; as well as analysing the observational and evolutionary properties of these objects.

In this thesis we model the propagation of cosmic rays through the Galaxy in an attempt to characterise a standard cosmic ray background with uncertainties, to reveal the origin of the cosmic ray electron positron anomaly. Furthermore, we analyse the  $\gamma$ -ray emission from SNRs Kes 79 and MSH 11–61A, which are known to be interacting with molecular clouds, as well as the non-thermal X-ray emission arising from the PWN of PSR J1741-2054. We find that the emission from both SNRs most likely arises from the decay of neutral pions that resulted from the interaction of relativistic ions which are accelerated at the shock-front of a SNR, with ambient material. For PSR J1741-2054, we characterise the properties, minimum magnetic field and minimum energy of the particle population that produces the observed diffuse synchrotron emission that surrounds and trails the

pulsar.

In addition, we characterise the X-ray emission arising from Kes 79, MSH 11–61A and PSR J1741-2054, in an attempt to shed light on the origin and nature of these objects and their emission. Using X-ray data from *XMM-Newton* and *Suzaku* respectively, we probe the temperature, ionisation state, and elemental abundance of the shocked gas of each SNR. This allows us to determine their evolutionary properties, properties of the shock, and mass of the original progenitor; and constrain the density of the X-ray emitting plasma. Using *Chandra*, we determined the temperature of PSR J1741-2054, as well as characterised its proper motion, velocity, direction of motion, and presence of small scale structure immediately surrounding the pulsar.

---

## List of research outputs

- Paper I** *Extracting the size of the cosmic electron-positron anomaly*. Katie Auchettl, Csaba Balázs. ApJ, 749 (2012) 184.  
arXiv:1106.4138 [astro-ph].
- Paper I(a)** *The cosmic  $e^\pm$  anomaly* (conference version A). Katie Auchettl, Csaba Balázs. Appeared in Proceedings of the 14th Workshop “What Comes Beyond the Standard Models”, July 2011 Bled, DMFA-Zaloznistvo, Ljubljana, Vol. 12, No. 2, pg. 1 - 8.  
arXiv:1306.4704 [hep-ph].
- Paper I(b)** *The status of the  $e^\pm$  cosmic-ray anomaly* (conference version B). Katie Auchettl, Csaba Balázs. J. Phys. Conf. Ser. 384, 012016,  
DOI:10.1088/1742-6596/384/1/012016
- Paper I(c)** *The  $e^\pm$  cosmic-ray anomaly* (conference version C). Csaba Balázs, Katie Auchettl. PoS ICHEP2012 (2013) 431  
URL: <http://inspirehep.net/record/1257211>
- Paper I(d)** *Uncertainties in Dark Matter Indirect Detection* (book chapter). Katie Auchettl, Csaba Balázs. Title: Open Questions in Cosmology. Editor: Gonzalo J. Olmo.  
ISBN 978-953-51-0880-1, DOI:10.5772/52052
- Paper II** *Fermi-LAT Observations of Supernova Remnant Kesteven 79*. Katie Auchettl, Patrick Slane, Daniel Castro. ApJ, 783 (2014), 32.  
arXiv:1401.2745 [astro-ph].
- Paper III** *Multi-wavelength analysis of the Galactic supernova remnant MSH 11–61A*. Katie Auchettl, Patrick Slane, Daniel Castro, Adam Foster, Randall K. Smith. Accepted to ApJ.  
arXiv:1507.08012 [astro-ph].
- Paper IV** *X-ray analysis of the proper motion and pulsar wind nebula for PSR J1741-2054*. Katie Auchettl, Patrick Slane, Roger W. Romani, Bettina Posselt, George G. Pavlov, Oleg Kargaltsev, C-Y. Ng, Tea Temim, Martin. C. Weisskopf, Andrei Bykov, Douglas A. Swartz. ApJ, 804 (2015), 68.  
arXiv:1501.03225 [astro-ph].



---

## General Declaration

Monash University

Declaration for thesis based or partially based on conjointly published or unpublished work

### General Declaration

In accordance with Monash University Doctorate Regulation 17.2 Doctor of Philosophy and Research Master's regulations the following declarations are made:

I hereby declare that this thesis contains no material which has been accepted for the award of any other degree or diploma at any university or equivalent institution and that, to the best of my knowledge and belief, this thesis contains no material previously published or written by another person, except where due reference is made in the text of the thesis.

This thesis includes four (4) original papers published in peer reviewed journals. The core theme of this thesis was to analyse the intimate connection between cosmic rays, supernova remnants and pulsar wind nebula, and to characterise the X-ray properties of these objects. The ideas, development and writing up of all the papers in the thesis were the principal responsibility of myself, the candidate, working within the School of Physics and Astronomy in conjunction with the Smithsonian Astrophysical Observatory (SAO) at the Harvard-Smithsonian Centre for Astrophysics under the supervision of Associate Professor Csaba Balazs, Dr. Jasmina Lazendic-Galloway and Dr. Patrick Slane (SAO).

The inclusion of co-authors reflects the fact that the work came from active collaboration between researchers and acknowledges input into team-based research. The contribution of the PhD Candidate to each of the papers arising from the thesis is declared overleaf.



Katie Amanda Auchettl

June, 2015

Thesis chapter	Publication Title	Status	Nature and extent of candidate's contribution
2	<i>Extracting the size of the cosmic electron-positron anomaly</i>	Published	Wrote a majority of the code needed to randomly sample the parameter space of the GALPROP program using the Monash sungrid cluster. Wrote some of the code needed to perform the Bayesian analysis. Performed the statistical analysis and interpretation of the results. Wrote majority of the paper.
2	<i>The cosmic <math>e^\pm</math> anomaly</i> (conference version A)	Published	As above; contributed to writing the proceedings.
2	<i>The status of the <math>e^\pm</math> cosmic-ray anomaly</i> (conference version B)	Published	As above; contributed to writing the proceedings.
2	<i>The <math>e^\pm</math> cosmic-ray anomaly</i> (conference version C)	Published	As above; did not contribute to writing the proceedings.
2	<i>Uncertainties in Dark Matter Indirect Detection</i> (book chapter)	Published	As above; co-wrote the chapter.
3	<i>Fermi-LAT observations of supernova remnant Kesteven 79</i>	Published	Performed data reduction for both the X-ray and $\gamma$ -ray data.; analysed and interpreted results; wrote paper.
4	<i>Multi-wavelength analysis of Galactic supernova remnant MSH 11-61A</i>	Published	Performed data reduction for both the X-ray and $\gamma$ -ray data.; analysed and interpreted results; wrote paper.
5	<i>X-ray analysis of the proper motion and pulsar wind nebula for PSR J1741-2054</i>	Published	Performed data reduction and analysis of the X-ray data, as well as interpretation of X-ray results; wrote paper.

---

## Acknowledgements

For me, writing the acknowledgements is the hardest part of writing a thesis. I am always worried that I have forgotten one of the very many people that were an integral part of me getting to this point. I didn't do this myself, but with the help of every single one of you. I hope that I haven't forgotten anyone, I am sorry if I have. It was unintentional.

I am incredibly indebted to my three supervisors: Patrick Slane, Csaba Balazs, and Jasmina Lazendic-Galloway. Each have provided invaluable guidance and support over the course of my PhD studies, and for many years before my time as a PhD candidate.

Jasmina, you were the one who ignited my passion, excitement and curiosity for research in astrophysics. From the first time I stepped into your office as a third year undergraduate and you showed me those *Chandra* images of SNRs, I was hooked. Since then, your absolute unwavering support, confidence, advocacy and encouragement for me to take every opportunity (and even finding them for me when I was blind to them), has really made me realise just how incredibly lucky I am.

Csaba, your continual encouragement, and support that you have given me to go out and explore and understand the theoretical foundations of physics has lead to many opportunities I didn't think possible. You took me as an undergraduate student who was just curious about the foundations and opened up a completely new and wonderful world for me. In addition, your willingness to allow me to wander off and explore different research topics outside of your traditional field of research has been invaluable.

Pat, you took the excitement and passion that Jasmina had initiated and provided the accelerant. Your support, mentorship, and patience as I caught up with astronomy due to my physics background, encouragement to discover and understand the details as well as the bigger picture, your ability to explain any concept from the bottom up and enthusiasm for what we do has made the last nearly three years unforgettable. I can't thank you enough for the opportunities you have given me and for taking a chance on the theoretical physicist who was just an astrophysicist in disguise.

I would also like to thank several collaborators who contributed directly or indirectly with the work presented in this thesis or to my training as an astrophysicists through your discussions, support and encouragement. In particular,

thank you to Daniel Castro, Laura Lopez, Enrico Ramirez-Ruiz, Randall Smith, Adam Foster, Josh Wing, Roger W. Romani, Bettina Posselt, Tea Temim, C-Y. Ng, George G. Pavlov, Martin. C. Weisskopf, Andrei Bykov, Oleg Kargaltsev, Aytap Sezer and James Guillochon.

I am gratefully for the financial support of an Australian Postgraduate Award (APA) during my time in Australia, as well as to Pat for the continual financial support during my time in Boston. In addition, I would like to thank Csaba and by extension the Australian Research Council Centre for Particle Physics at the Terascale (CoEPP) for their travel support to go to Boston.

I have been very lucky to be a part of two different departments during my PhD. I would like to thank the School of Physics and Astronomy and all of its staff for its support throughout my candidature even when I was on the other side of the world. In particular Jean Pettigrew who has always made me realise just how lucky we are to be her “physics children” and for her to be our “mother hen”. As well as David Paganin, Julia Barnes, Jenny McCabe, Theo Hughes, Lincoln Turner, Catherine Buchanan, Steven Morton, Alexis Bishop, Yuri Levin and Michael Morgan. I would also like to thank the Monash Research Graduate School (MRGS) for allowing me to take the opportunity presented at the Harvard-Smithsonian Centre for Astrophysics. I would like to thank the Smithsonian Astrophysical Observatory for providing the predoctoral fellowship opportunity. It has opened so many doors that I would have never expected. Special thanks to the staff in the HEAD, and IT division at the Harvard-Smithsonian Center for Astrophysics. In particular Donna Wyatt for looking after all the international researchers who are trying to navigate the waters associated with being in a new country. As well as Frank Nigro, Kyle Welsh, Wendy Roberts and the CF for the computer support.

Spending my time in two departments has lead me to come across many postgraduate students, past-postgraduate students, postdocs, officemates and non-physicists that have provided me with friendship, and support, and have formed a part of my second family. In particular, I have to specially thank my boys: Jeremy Brown, Martijn Jasperse, Elliot Hutchinson and Wan Zahidi Zakwan. I love you guys to bits. No matter if we are together, or on other sides of the world you guys always make me laugh with your silly antics, conversations, and pictures. I am so lucky to have you guys in my life! In addition (in no particular order): Rhiannon Murrie, Tessa Charles, Marcin Kowalczyk, Kathryn Waldron, Tom Hyde and Teigen Bywater, Chris and Melissa Lee, Shane Landry, Rhys Dunstan, Daniel Guthrie, Luke Zoltan Kelley, Maria Drout and Mark Wilson, Christopher Faesi, Katy Wyman, Laura Colquhoun, Sarah Wellons, Laura Schaefer and Zavi Dogic, Ragnhild Lunnan, Moritz, Lauren and Johann Guenther, Katja and Tobi Poppenhaeger, Cecilia Garraffo, Katia Melo and Felipe Andrade Santos, Esra Bulbul, Valerie Gerard and Adrian, Lola Piscopo and Josh Wing, Florian Rodler,

Laura Lopez, Eric Morganson and the PSIons from all around the world. But of course, this an incredibly small subsection of many many people I have come across and who have been a part of this whole experience (I wrote the list out but I needed nearly a whole page for all your names!)

Finally, this thesis would not have been possible without the support, encouragement and love of my family; especially to my Mum, Dad, Rebecca and Gaby. Thank you for allowing me to wander around the world on my journey, and supporting me even when we are many timezones and flight hours apart. And of course, I must thank Lucas Hackl, for his love, and support. You fill my life with joy. Here is to the next adventure together!

Thank you all!

*For Mum, Dad, Rebecca, and Gaby.*

---

# Introduction

## 1.1 Supernovae

Supernovae (SNe) are violent explosions which mark the end of the evolution of some classes of stars. They are among the most energetic events in the universe, releasing approximately  $10^{53}$  erg of energy into its surrounding environment. Supernovae play an important role in the Universe (Filippenko, 1997). They can trigger star formation; they influence the chemical content and physical state of the interstellar medium (ISM); they produce compact objects such as neutron stars and black holes; part of their energy is converted into cosmic rays; and due to their detectability up to redshifts of  $\sim 1.9$  (Riess et al., 2007; Suzuki et al., 2012; Jones et al., 2013) they are used as “standard candles” for measuring the rate of expansion of our Universe (Perlmutter et al., 1998; Garnavich et al., 1998).

SNe are commonly observed using optical wavelengths and are classified according to their light curves, and optical spectra near maximum brightness (Filippenko, 1997). Traditionally, SNe are classified into two broad classes based on the presence (or lack thereof) of Balmer series hydrogen absorption lines in their spectra (Minkowski, 1941). SNe without these hydrogen (H) lines in their spectra are classified as Type I, while those with H lines are classified as Type II. These broad categories are also split into subclasses based on the presence or absence of absorption features from other elements or due to the shape of their light curves. The diversity of SNe is thought to arise from the different progenitor stars and different environments in which that these progenitors are located.

Type I SNe are split into three categories: Type Ia, Type Ib, and Type Ic. Type Ia SN have strong silicon (Si) II absorption lines, Type Ib have weak Si II absorption and strong helium (He) lines, while Type Ic have weak Si II but no He absorption lines. The lack of absorption lines in the optical spectra of Type I suggest that the progenitor of these SNe have no outer hydrogen envelope (and helium for Type Ic) as a result of stellar wind mass loss (Heger et al. 2003) or binary interaction (Podsiadlowski et al. 1992).

Type II SNe are split into four subclasses based on the shapes of their light

curves. Type II-P show a near constant (“plateau”) luminosity for a number of weeks after maximum light, while Type II-L have a linear decrease in luminosity with time after maximum light. Type II-b is an intermediate class between Type Ib and Type II, in that initially their spectra mimics Type II explosions but at later times they evolve into Type Ib. Type II-n is characterised by narrow H line emission.

Type Ia are thought to result from the thermonuclear explosion of a carbon-oxygen white dwarf that has reached the Chandrasekhar mass ( $\sim 1.4 M_{\odot}$ ) due to accretion from a companion (Nomoto, 1982; Hillebrandt & Niemeyer, 2000). This type of explosion results in complete destruction of the progenitor(s) with no compact object left over. One of the big research topics in Type Ia research is to determine the configuration of the progenitor system. Currently there are two main progenitor system scenarios: single degenerate and double degenerate. In the single degenerate scenario, the white dwarf accretes hydrogen from either a main sequence star or an evolved companion until its mass exceeds the Chandrasekhar limit and collapses under its own gravity. In the double degenerate case there are two white dwarfs that merge and as their combined mass exceeds the Chandrasekhar limit, this results in the product of this merger collapsing under its own gravity. The ejecta of Type Ia SNe are very iron rich.

In comparison, core-collapse (CC) SNe, comprising of Type Ib, Type Ic and Type II, result from massive ( $M \geq 8M_{\odot}$ ), fuel-depleted stars collapsing under their own gravity (Woosley & Janka, 2005). This collapse is triggered by the formation of an iron (Fe) core, as no energy can be gained from nuclear fusion of Fe. Depending on the mass of the progenitor star, the core will collapse into either a neutron star, or a black hole. Type II-P is the most common core collapse SN and the progenitors of these are red supergiants that have most of their H envelopes intact (Chevalier, 2005). The progenitors of Type II-L and Type II-b have substantially smaller H envelopes due to stellar wind mass loss, or binary interactions. The narrow H emission observed in Type II-n most likely arises from a dense circumstellar environment created by the significant mass loss by its progenitor. The ejecta of core collapse SNe consists primarily of stellar material and explosive nucleosynthesis products, with carbon, oxygen, neon and magnesium being the dominant elements produced (Woosley & Weaver, 1995; Thielemann et al., 1996).

## 1.2 Supernova remnants

A core collapse supernova explosion releases roughly  $10^{53}$  erg of energy, with 99% of this energy being radiated away in the form of neutrinos. The other 1% is converted into  $\sim 10^{51}$  erg of kinetic energy which forms an expanding shock-wave

of ejected material (ejecta) and swept-up ISM and/or stellar material expelled by stellar winds pre-SN. The result of the complex interaction between the stellar ejecta and the surrounding environment gives rise to what is known as a supernova remnant (SNR). These objects can last for tens of thousands of years and emit radiation across the entire electromagnetic spectrum. Currently there are 294 Galactic SNRs that have been detected as extended objects in the radio band, with nearly 40% of these being detected in X-rays and 30% detected in optical (Green, 2014). SNRs play a central role in the dynamics and chemical evolution of galaxies, and in the distribution of heavy elements that are produced in SN explosions.

### 1.2.1 Dynamical evolution

The evolution of an SNR can be divided into four stages, which are determined by the relationship between the mass of the ejecta ( $M_{ej}$ ) and the mass of the swept-up ISM ( $M_{ISM}$ ) (Woltjer, 1972).

#### Free Expansion

In the free expansion (or ejecta dominated) phase  $M_{ej} \gg M_{ISM}$ , thus the expansion of the shock is unimpeded by the low-density ISM. Assuming that the explosion energy is transformed into the kinetic energy of the ejecta  $E_0$ , the velocity ( $v_s$ ) of this free expansion can be expressed as

$$v_s = (2E_0/M_{ej})^{1/2}, \quad (1.1)$$

where the radius of the shock is defined by

$$R_s = v_s t \quad (1.2)$$

where  $t$  is the SNR age. Typically, the ejecta from a Type Ia is expelled into the surrounding medium with a velocity of  $\sim 10^4$  km s $^{-1}$ , while for a core collapse event the ejecta has a velocity of  $\sim 5000$  km s $^{-1}$  (Reynolds, 2008). As the typical speed of sound in the surrounding environment is approximately 1-10 km s $^{-1}$ , the ejecta forms a shock-wave that has a very large Mach-number ( $M \geq 10^3$ ). This phase will last until  $M_{ISM}$  is comparable to  $M_{ej}$ . The mass of ISM swept-up by the forward shock is

$$M_{ISM} \sim \frac{4\pi}{3} R_s^3 \rho_0 = \frac{4\pi}{3} R_s^3 \mu m_H n_0 \quad (1.3)$$

where  $\rho_0$  is the initial density of the interstellar medium,  $\mu = 1.36$  is the mean atomic weight per hydrogen atom,  $m_H$  is the mass of the hydrogen atom and  $n_0$  is the density of the ISM. The free expansion ends when the shock-front has a radius of

$$R_s \sim \left( \frac{3M_{ej}}{4\pi m_H \mu n_0} \right)^{1/3}. \quad (1.4)$$

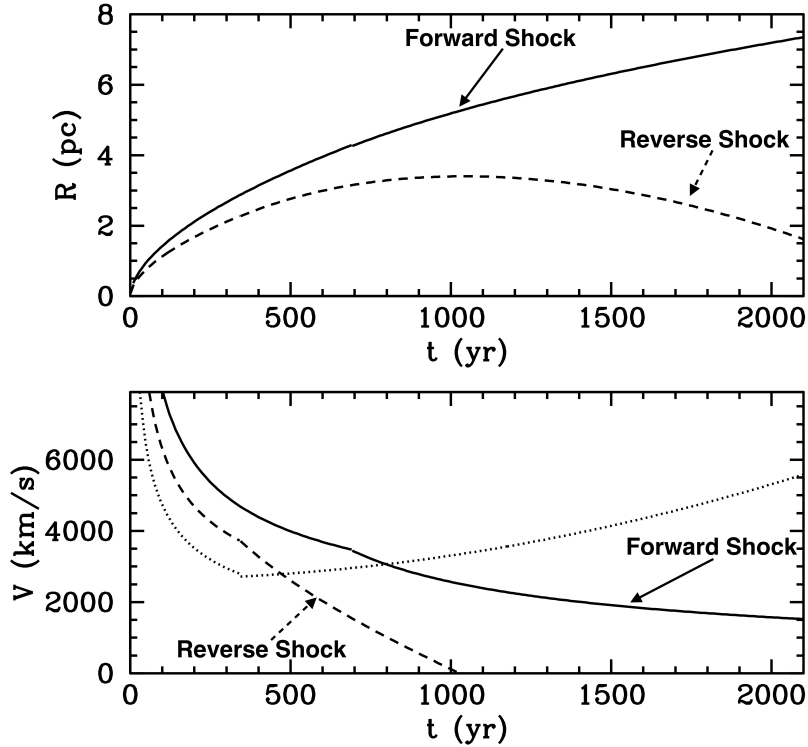


Figure 1.1: *Top*: Shock radius and *Bottom*: shock velocity as a function of time, as modelled by Truelove & McKee (1999). In the top figure the solid line represents the forward shock of the SNR, the dashed line corresponds to the reverse shock, while in the bottom figure, the dotted line represents the velocity of the shock in the Fe-L ejecta frame. Figure adapted from Vink (2012).

and corresponds to a timescale of

$$t \sim \frac{R_s}{v_s} \sim M_{ej}^{5/6} E_0^{-1/2} \rho^{-1/3}, \quad (1.5)$$

which is typically a few hundred years (Truelove & McKee, 1999).

### Sedov Phase (Adiabatic Phase)

As the expanding ejecta are decelerated due to the mass of the swept-up ISM, a reverse shock is produced which compresses and heats the inner ejecta to temperatures as high as  $10^7$  Kelvin (McKee, 1974). The forward shock and reverse shock are separated by a boundary called the “contact discontinuity”. As radiative losses are negligible compared to the kinetic energy of the ejecta ( $E_0$ ), the expansion of the remnant becomes adiabatic. When  $M_{ISM} > M_{ej}$ , the mass of the swept-up ISM becomes hydrodynamically important and the SNR enters the Sedov-Taylor phase. At this point all ejecta are shocked (i.e. the reverse shock reaches the centre of the remnant), and the evolution of the SNR can be

approximated assuming an adiabatic point explosion in a uniform medium with density  $\rho$  (Shklovskii, 1962). Taylor (1950) and Sedov (1959) determined that the radius and velocity of the shock-wave under these assumptions can be described by:

$$R_s = \left( \zeta \frac{E_0 t^2}{\rho_0} \right)^{1/5} \quad (1.6)$$

and.

$$v_s = \frac{dR_s}{dt} = \frac{2}{5} \left( \zeta \frac{E_0}{\rho_0} \right)^{1/5} t^{-3/5} = \frac{2R_s}{5t}, \quad (1.7)$$

where  $\zeta$  is a dimensionless constant that depends on the adiabatic heat index ( $\gamma$ )<sup>1</sup>. During this phase, the SNR will have a temperature of:

$$T = \frac{3\mu m_H}{16k_B} v_s^2. \quad (1.8)$$

where  $k_B$  is Boltzmann's constant. The Sedov-Taylor phase can last up to tens of thousands of years, and by the end of this phase a significant fraction of the initial kinetic energy has been converted into thermal energy of the swept-up ISM (Chevalier, 1974).

In Figure 1.1, the radius and velocity of the shock as a function of time is shown. These plots are based on the model by Truelove & McKee (1999), whose analytical model takes into account the transition from the free expansion phase to the Sedov-Taylor phase.

### Snow plough phase

The Sedov phase ends when the shockwave cools to the point that significant radiative cooling occurs and the adiabatic approximation breaks down (Reynolds, 2008). When this occurs the remnant enters the snow plough phase. Here radiative cooling has become dynamically important and the total energy contained in the SNR is no longer conserved. If the shock-front of the SNR is interacting with a non-uniform medium, the transition of the remnant into this phase can vary between different regions. Once the majority of the shock-front has become radiative, the material immediately behind the shock cools much more efficiently compared to the low density material in the centre of the remnant. This hotter inner region can provide significant pressure on the shock as this hot gas is still expanding adiabatically. At this point, the remnant will expand with a radius of

$$R_s \propto t^{2/7}, \quad (1.9)$$

and is in what is called the pressure-driven snowplough phase (McKee & Ostriker, 1977). As the interior gas cools, the pressure becomes negligible and the shock-front

---

<sup>1</sup>Here  $\zeta = \frac{75(\gamma-1)}{8\pi}$ , thus for an an ideal monoatomic, non-relativistic gas where  $\gamma = 5/3$ ,  $\zeta \sim 1.99$ .

will expand following

$$R_s \propto t^{1/4} \quad (1.10)$$

due to momentum conservation. This stage of evolution is called the momentum conserving snowplough stage (Cioffi et al., 1988). The transition between the Sedov phase and radiative snow plough occurs (assuming a uniform ISM) when

$$t = 2.9 \times 10^4 \left( \frac{E_0}{10^{51}} \right)^{4/17} n_0^{-9/17} \text{ year}, \quad (1.11)$$

where  $n_0$  is the number density of the ISM (Blondin et al., 1998). This corresponds to a radius of

$$R = 19 \left( \frac{E_0}{10^{51}} \right)^{5/17} n_0^{-7/17} \text{ pc} \quad (1.12)$$

and a total swept up mass of

$$M = 10^3 \left( \frac{E_0}{10^{51}} \right)^{15/17} n_0^{-4/17} M_\odot. \quad (1.13)$$

### Disappearance Phase

As the velocity of the shockwave decreases to below the speed of sound in the ISM ( $< 10$  km) and the temperature of the remnant becomes comparable to the ISM ( $\sim 10^4$  K), the remnant will disperse into the surrounding medium ISM and thus disappear. This is called the dissipative phase. The whole evolution of an SNR lasts for approximately  $10^6$  years (Reynolds, 2008).

Although this picture of SNR evolution is helpful for providing an explanation of some of the general features of SNRs, it oversimplifies their dynamics. In reality, these remnants are interacting with magnetic fields, inhomogeneities in the surrounding material and ejecta, and different initial ejecta and ISM density profiles to what was assumed above. Other complications such as asymmetries in the SN explosion, particle acceleration occurring at the shock and the interaction with nearby molecular clouds can substantially effect the evolution of a given object. Furthermore core-collapse SNe can leave rapidly rotating neutron stars which modify the surrounding unshocked ejecta. All these factors result in the diversity of the morphological structure of SNRs in all wavelengths.

### 1.2.2 Morphologies of supernova remnants

Supernova remnants are classified according to their radio and X-ray morphology. Depending on their progenitor, environment and evolutionary stage, SNRs can appear very different from each other and very different at different wavelengths. There are three main SNR morphologies: shell-type, composite type and mixed-morphology.

### Shell-like

Approximately 80% of known Galactic SNRs are classified as shell-type due to their limb-brightened morphology in radio (and sometimes X-ray) wavelengths. This emission resembles a ring-like structure that is often incomplete. The radio emission observed in these remnants arises from a population of non-thermal GeV electrons emitting synchrotron radiation with a frequency  $\nu$ . This emission has a spectral index,  $\alpha$ , ranging between  $-0.7$  and  $-0.3$ , where the radio flux  $S_\nu \propto \nu^\alpha$ . The X-ray emission observed in these remnants is often spatially correlated with the observed radio emission. Cassiopeia A (G111.7-2.1), Tycho (G120.1+1.4) and Kepler (G4.5+6.8) are well-known examples of shell-like SNRs whose X-ray emission is primarily thermal in nature (see Figure 1.2a). The observed thermal X-rays arise from an optically-thin plasma that has been compressed and heated to X-ray emitting temperatures ( $\sim 10^6 - 10^8$  K) by the reverse shock of the SNR. As such the resulting emission is comprised of a bremsstrahlung continuum and line emission from heavy elements. Well known examples of shell-like SNRs whose X-ray emission arises from predominantly non-thermal emission are SN1006 (G327.6+14.6) and RX J1713.7-3946 (G347.3-0.5). These X-rays arise from relativistic electrons being accelerated to TeV energies by the shock-front of the SNR (see Figure 1.2b).

### Composite

Composite type SNRs have both shell-like and centre-filled morphologies in radio and X-ray wavelengths. The central non-thermal emission arises from a pulsar wind nebula (PWN) that is produced by a pulsar which formed during a core-collapse SNe, and can be described by a flat power law spectrum<sup>2</sup>. The shell of the remnant shows a much steeper spectrum compared to its center, due to the interaction of the shock wave with the surrounding environment. Typical examples of this type of remnant are the Vela SNR (G263.9-3.3), G21.5-0.9, G292.0+1.8 (see Figure 1.3a) or G327.1-1.1 (see Figure 1.3b) and about 10% of Galactic SNRs fall into this category.

### Mixed-morphology

Mixed Morphology (MM) SNRs are characterised by centre filled, thermal X-ray emission which arises from swept-up, shock-heated ISM and a bright shell of synchrotron radio emission (Rho & Petre, 1998; Cox et al., 1999). These remnants differ from the other classes of SNRs, as there is no spatial correlation between the radio and X-ray emission. At present, there are  $\sim 40$  known MM SNRs (see Table 4 of Vink 2012), which corresponds to  $\sim 13\%$  of all Galactic SNRs, and

---

<sup>2</sup>See Section 1.3 for more details.

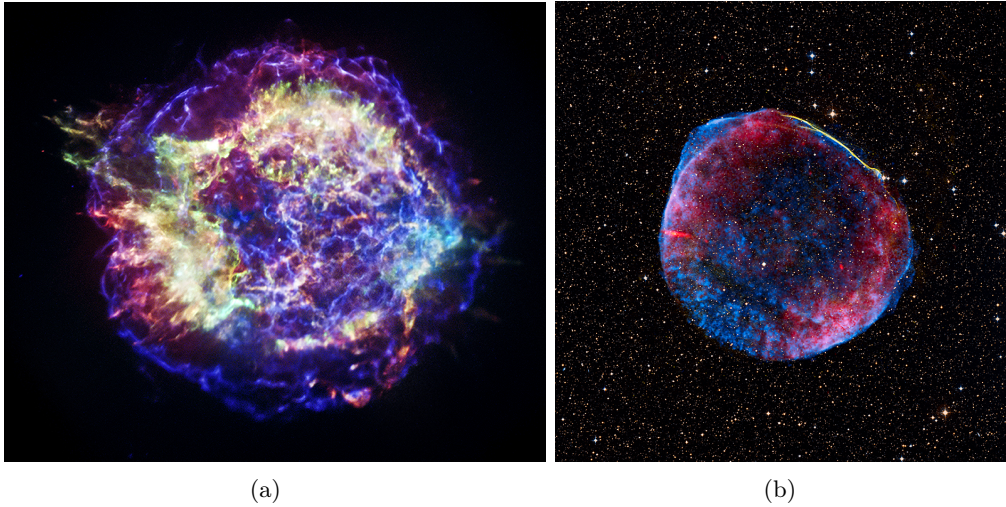


Figure 1.2: (a) X-ray image of shell-type SNR Cassiopeia A taken with the *Chandra* X-ray Observatory. Here red corresponds to 0.5-1.5 keV, green to 1.5-2.5 keV and blue to 4.0-6.0 keV (Stage et al., 2006). (b) Composite image of shell-type SNR SN1006. Here blue corresponds to X-rays observed using *Chandra* (Cassam-Chenaï et al., 2008), yellow corresponds to optical observations of the north-western region of the remnant using University of Michigan’s 0.9 metre Curtis Schmidt telescope at the NSF Cerro Tololo Inter-American Observatory (Winkler & Long, 1997) and red corresponds to radio observations using NRAO Very Large Array and Green Bank Telescope (Dyer et al., 2004)

nearly 25% of all X-ray detected SNRs (Aschenbach, 1993). Well known examples of this type are W44 (G34.7+0.4) (Figure 1.4a), W49B (G43.3+0.2) (Figure 1.4b) and IC443 (G189.1+3.0).

MM SNRs tend to be middle aged ( $\geq 10^4$  years old), are located in high density regions, are known to be interacting with nearby molecular clouds due to the association with 1720 MHz OH masers (e.g., Frail et al. 1994; Claussen et al. 1997; Frail & Mitchell 1998) and are often associated with sources of GeV (e.g., Abdo et al. 2009a, Abdo et al. 2010b, Castro & Slane, 2010, Abdo et al., 2010a, Uchiyama et al. 2012, Ackermann et al. 2013a, Hanabata et al. 2014) and TeV  $\gamma$ -ray emission (e.g., Aharonian et al. 2008a, Acciari et al. 2009, Brun et al. 2011, Aleksić et al. 2012). In addition, their X-ray spectra show evidence of ejecta in the form of super-solar abundances (e.g., Shelton et al. 2004, Lazendic & Slane 2006, Bocchino et al. 2009, Pannuti et al. 2010), their plasmas appear to be nearly isothermal in nature (e.g., Slane et al. 2002) which contradicts the temperature profile of a Sedov remnant, and they also exhibit overionisation/recombination as a result of the rapid cooling of the plasma (e.g., Kawasaki et al. 2002, Yamaguchi et al. 2009, Miceli et al. 2010, Sawada & Koyama 2012, Lopez et al. 2013a).

The evolutionary sequence leading to these unusual X-ray properties are not well understood, and the morphology and characteristics of these SNRs are difficult

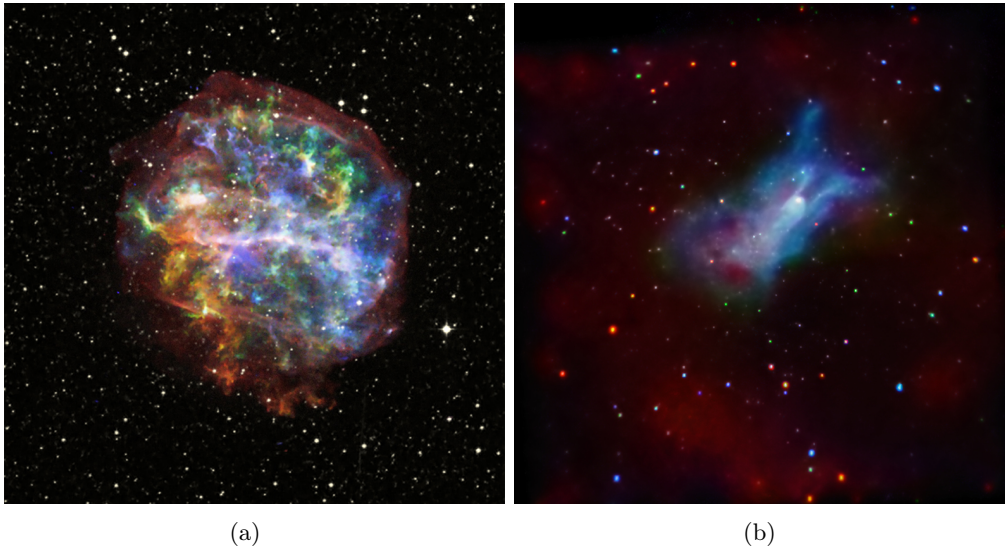


Figure 1.3: (a) Composite image of the X-ray and optical emission of G292.0+1.8. Here the X-rays are represented by red (0.58-0.71 keV & 0.88-0.95 keV), orange (0.98-1.10 keV), green (1.28-1.43 keV), and blue (1.81-2.05 and 2.40-2.62 keV) (Park et al., 2007), while the optical emission is shown in white (Ghavamian et al., 2005). The pulsar is located slightly below and to the left of the centre of G292.0+1.8.(b) *Chandra* X-ray image of Composite SNR G327.1-1.1 (Temim et al., 2009). Here red corresponds to 0.5-1.5 keV, green to 1.5-2.5 keV and blue to 2.5-6.0 keV.

to explain using standard SNR evolution models (Section 1.2.1). As a consequence there have been numerous models invoked to explain their characteristics. One possible model (White & Long, 1991) assumes that the SNR is evolving in a medium filled with many small dense, cold cloudlets. These cloudlets are small enough that they do not affect the passage of the shock, and are sufficiently dense that they are neither blown apart nor swept up. Once the shock has passed, the cloudlets slowly evaporate via saturated thermal conduction, filling the interior of the SNR with a relatively dense gas that emits in X-rays. White & Long (1991) derived a Sedov-like solution to describe the evolution of an SNR in this environment using two additional parameters: the cloud evaporation timescale and the ratio of the mass in the clouds to that of the intercloud material. For different combinations of these two parameters, the X-ray brightness and temperature profiles obtained can reproduce the observed X-ray morphology of MM SNRs. Slane et al. (2002) successfully modelled the X-ray emission of MSH 11-61A using the White & Long (1991) model.

Another possible scenario is that thermal conduction (Cui & Cox, 1992) and turbulent mixing (Shelton et al., 2004) result in the transport of heat and material to the centre of the remnant, increasing its central density, and smoothing the temperature gradient behind the shock (Cox et al., 1999). Numerical simulations

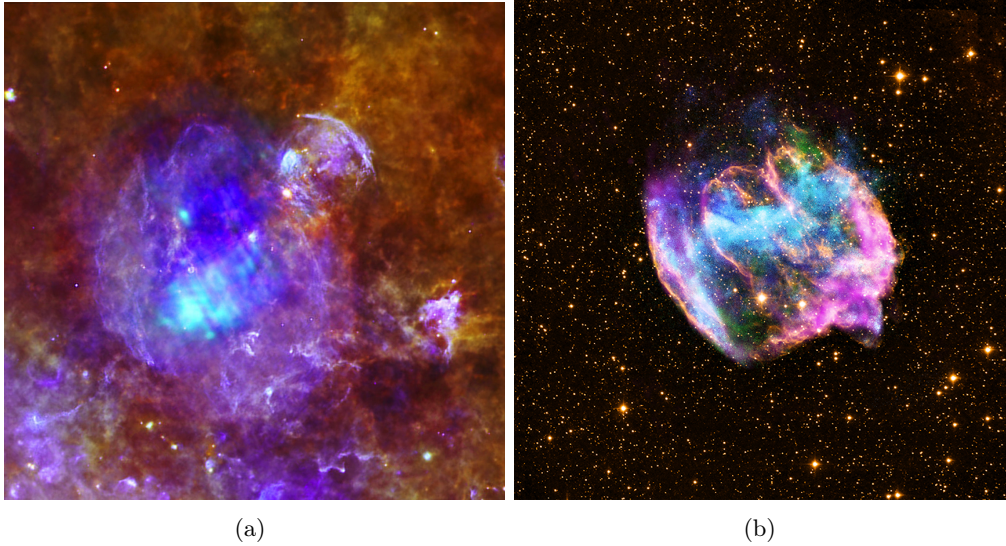


Figure 1.4: (a) Multiwavelength image of MM SNR W44. Here blue ( $70 \mu m$ ), green ( $160 \mu m$ ), and red ( $250 \mu m$ ) corresponds to infra-red emission as observed using Herschel Photodetecting Array Camera and Spectrometer (PACS) and spectral and photometric imaging receiver (SPIRE) instrument (Nguyen Luong et al., 2011; Nguyen-Lu’o’ng et al., 2013). Highlighted in blue is the X-ray emission of W44 as observed using XMM-Newton (Harrus et al., 2006). (b) Composite image of MM SNR W49B. Here the radio emission from the remnant as detected by the VLA is highlighted in magenta (Lacey et al., 2001), the infra-red emission as measured by WIRC instrument on the Hale 200 inch (5 m) telescope on Mount Palomar is shown in yellow (Keohane et al., 2007), and the X-ray emission as observed using *Chandra* is shown as green and blue (Lopez et al., 2013b).

of this model (e.g., Shelton et al. 1999; Velázquez et al. 2004) have been able to reproduce the central bright X-ray emission of MM SNRs but are unable to fully explain temperature and brightness distributions of some remnants such as W44.

### 1.2.3 Heating collisionless plasmas to X-ray emitting temperatures

As mentioned in Section 1.2.1, the shock-front of the SNR will heat and compress the surrounding medium and ejecta, leaving a hot, ionised, X-ray emitting plasma behind. Due to the low ambient densities encountered by SNRs ( $\leq 1 \text{ cm}^{-3}$ ), these shock fronts are collisionless<sup>3</sup> and one can describe the nature of these shocks using the Rankine-Hugoniot relations (Macquorn Rankine, 1870; Hugoniot, 1889), which describes the relationship between density ( $\rho$ ), velocity ( $v$ ) and pressure ( $P$ ) of the gas upstream of the shock (denoted by subscript 1) to those downstream

<sup>3</sup>In a collisionless shock, the transition between the upstream and downstream regions of the shock is much smaller than the mean free path of collisions. This means that Coulomb collisions which produce a mean free path much larger than the size of the system are replaced with magnetic field and charged particle interactions in the form of plasma instabilities, which typically have a shorter mean free path.

(denoted by subscript 2). These conditions are derived using conservation of mass, momentum and energy across a planar, adiabatic shock front, while assuming that external sources such as magnetic pressure, diffusive terms and radiation energy losses are negligible. For a non-radiative shock with a sonic Mach number of  $M = v_1/c_s = (v_1^2\rho_1/\gamma P_1)^{1/2}$ , where  $c_s$  is the speed of sound and is equal to  $(\gamma P_1/\rho_1)^{0.5}$ , the conditions are:

$$\rho_1 v_1 = \rho_2 v_2 \quad (1.14)$$

$$P_1 + \rho_1 v_1^2 = P_2 + \rho_2 v_2^2 \quad (1.15)$$

$$\frac{1}{2}v_1^2 + \frac{\gamma}{\gamma-1} \frac{P_1}{\rho_1} = \frac{1}{2}v_2^2 + \frac{\gamma}{\gamma-1} \frac{P_2}{\rho_2}, \quad (1.16)$$

where  $\gamma$  is the specific heat ratio (adiabatic index). Equations 1.14, 1.15, 1.16 have the solutions:

$$r = \frac{\rho_2}{\rho_1} = \frac{v_1}{v_2} = \frac{(\gamma+1)M_1^2}{(\gamma-1)M_1^2+2}, \quad (1.17)$$

where  $r$  is the compression ratio and

$$\frac{P_2}{P_1} = \frac{2\gamma M_1^2 - (\gamma-1)}{\gamma+1}. \quad (1.18)$$

Assuming an ideal gas with a pressure given by  $P = (\rho kT)/m$ , Equation 1.18 becomes

$$\frac{P_2}{P_1} = \frac{\rho_2 k_B T_2 / m}{\rho_1 k_B T_1 / m} = \frac{\rho_2 T_2}{\rho_1 T_1}, \quad (1.19)$$

where  $m$  is the mass of the particle,  $k_B$  is Boltzmann's constant, and  $T$  is the temperature of the shock. Assuming a strong shock ( $M \sim P_2/P_1 \gg 1$ ), the equations 1.17, 1.19 become:

$$r = \frac{\rho_2}{\rho_1} = \frac{v_1}{v_2} \sim \frac{\gamma+1}{\gamma-1} \quad (1.20)$$

$$P_2 \sim \frac{2\gamma}{\gamma+1} M_1^2 P_1 = \frac{2}{\gamma+1} \rho_1 v_1^2, \quad (1.21)$$

respectively. Using Equations 1.18 and 1.19, we can derive a relationship for the temperature upstream and downstream of the shock

$$\frac{T_2}{T_1} = \frac{[(\gamma-1)M_1^2+2][2\gamma M_1^2 - (\gamma-1)]}{(\gamma+1)^2 M_1^2}. \quad (1.22)$$

For a strong shock this becomes

$$T_2 \sim \frac{2\gamma(\gamma-1)}{(\gamma+1)^2} T_1 M_1^2 = \frac{2(\gamma-1)mv_1^2}{(\gamma+1)^2 k_B}. \quad (1.23)$$

For a non-relativistic mono-atomic gas where  $\gamma = 5/3$ , the temperature of the electrons, protons and other ions in the post-shocked gas (the gas that is downstream of the shock) is:

$$k_B T_i = \frac{3}{16} m_i v_1^2, \quad (1.24)$$

where  $m_i$  is the mass of the particle species. From Equation 1.24 it can be inferred that heavier particle species are heated much more efficiently than light particle species. For an SNR in the adiabatic phase, whose shock front has a velocity of  $\sim 1000 \text{ km s}^{-1}$ , we expect the temperature of the post shock gas to be  $k_B T_s \sim 1.0 \text{ keV}$ , which corresponds to X-ray wavelengths.

#### 1.2.4 Ionisation equilibrium of the X-ray emitting plasma in a SNR

The shock-front of the SNR does not produce electrons and ions with similar temperatures, but Coulomb interactions between the hotter ion species and the cooler electrons will gradually drive the two populations into temperature equilibrium. The rate at which these Coulomb collisions occur and thus the rate in which temperature equilibrium occurs is

$$\frac{dT_e}{dt} = \frac{T_i - T_e}{\tau_{eq}}, \quad (1.25)$$

where  $T_i$  and  $T_e$  is the temperature of the ions and electrons respectively and  $\tau_{eq}$  is the timescale for equilibration (Zeldovich & Raizer, 1966; Itoh, 1984). Assuming a Maxwellian distribution, the timescale for equilibrium is:

$$\tau_{eq} \sim 10^9 n_e^{-1} \left( \frac{k_B T_e}{1 \text{ keV}} \right)^{3/2} \left( \frac{\ln \Lambda}{30.9} \right)^{-1} \text{ s}, \quad (1.26)$$

where  $n_e$  is the electron density,  $T_e$  is the electron temperature, and  $\ln \Lambda$  is the Coulomb logarithm defined by  $\ln \Lambda = 30.9 - \ln[n_e^{1/2} (k_B T_e / 1 \text{ keV})^{-1}]$  (Spitzer, 1965). For typical densities of  $n_e \sim 1 \text{ cm}^{-3}$  and temperatures of  $\sim 1 \text{ keV}$  that are commonly found in post shock gases of SNRs, the timescale is approximately  $10^4$  years, which is much longer than the age of many SNRs. This timescale can be shorter if the SNR is in a dense environment or if electrons are heated via other means.

Due to the relatively low densities that SNRs expand into, the plasma of an SNR is typically observed out of ionisation equilibrium. A useful way to characterise the ionisation state of an SNR plasma is to use the ionisation temperature  $kT_z$ . This describes the extent to which the ions are stripped of their electrons and is determined by taking the line ratio of an element and comparing it to the ratio of this element in a plasma found in collisional equilibrium (Kawasaki et al., 2002, 2005). By comparing  $kT_z$  to the temperature of the electrons ( $T_e$ ), one can classify the ionisation state of a collisionless plasma in the following way:

1. When  $kT_z < kT_e$ , the rate of ionisation is greater than the rate of recombination (Itoh, 1977), and a plasma in this state is classified as an *ionising* or *non-equilibrium ionisation* (NEI) plasma.

2. When  $kT_z = kT_e$ , the rate of ionisation and recombination is the same and the plasma is in *collisional ionisation equilibrium* (CIE).
3. When  $kT_z > kT_e$ , the rate of recombination is greater than the rate of ionisation. A plasma with these properties is called an *overionised* or *recombining* plasma. Recombining plasma is thought to be produced by rapid cooling of electrons either by thermal conduction (Kawasaki et al., 2002), adiabatic expansion via rarefaction and recombination (Itoh & Masai, 1989) or the interaction with dense cavity walls or molecular clouds (Dwarkadas, 2005).

The ionisation state of a plasma can be described using the following differential equation, assuming a given temperature  $T$

$$\frac{1}{n_e} \frac{df_i}{dt} = \alpha_{i-1}(T)f_{i-1} - [\alpha_i(T) + \beta_{i-1}(T)]f_i + \beta_i(T)f_{i+1}, \quad (1.27)$$

where  $f_i$  is the ionisation fraction of a given atomic species in the  $i$ -th ionisation state,  $n_e$  is the number density of electron,  $\alpha_i$  and  $\beta_i$  represent the ionisation and recombination rate coefficients for the  $i$ -th ionised ion (Gronenschild & Mewe, 1982). Solving Equation 1.27 we can estimate the characteristic ionisation timescale ( $\tau$ ) for a plasma to reach ionisation equilibrium (i.e.  $\sum_i \frac{df_i}{dt} = 0$ ) (Masai, 1984; Hughes & Helfand, 1985; Kaastra & Jansen, 1993; Smith & Hughes, 2010). For temperatures relevant for young SNRs ( $kT_e = 0.5\text{-}5.0$  keV),  $\tau = n_e t \sim 10^{12} \text{ cm}^{-3} \text{ s}$ . For typical electron number densities of  $n_e \sim 1 \text{ cm}^{-3}$  in the ISM, SNRs are expected to have an NEI plasma for  $\sim 3 \times 10^4$  years. Figure 1.5 shows the maximum ionisation timescale for a number of elements found in SNRs as a function of temperature. It also highlights the timescale in which these elements are within 10% of their equilibrium value.

### 1.2.5 Thermal emission from an X-ray emitting plasma

As shown in Section 1.2.3, the shock front of an SNR will heat ejecta and swept-up ISM to X-ray emitting temperatures. The thermal emission observed from these plasmas arises from continuum and line emission. Thermal continuum emission observed in SNRs arises from three main emission processes (Kaastra et al., 2008): Bremsstrahlung (or free-free emission), radiative recombination (free-bound emission), and two-photon decay, while line emission (bound-bound emission) arises from collisional excitation.

#### Bremsstrahlung

Bremsstrahlung continuum emission arises from the interaction between charged particles (such as free electrons and ions in an ionised plasma) via Coulomb forces. It is also referred to as “free-free” emission as the initial and end state

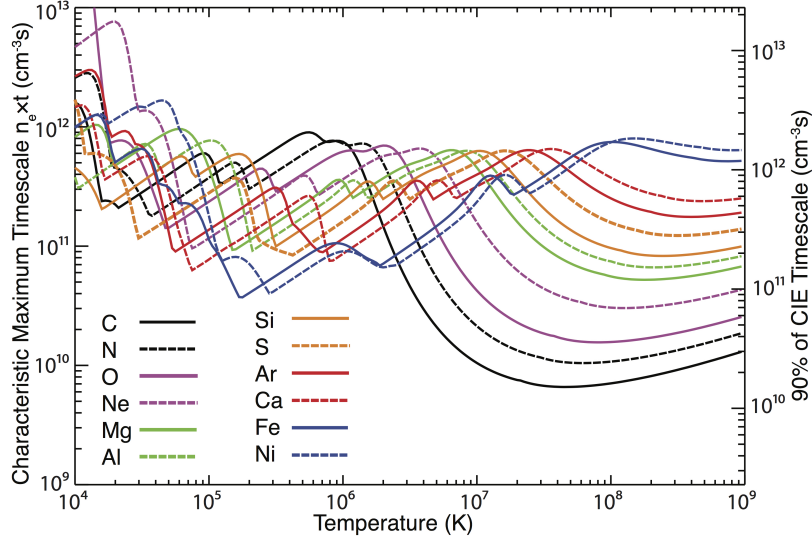


Figure 1.5: Plotted on the left axis is the density-weighted time-scale ( $n_e t$  in units of  $\text{cm}^{-3} \text{s}$ ) for carbon (C), nitrogen (N), oxygen (O), neon (Ne), magnesium (Mg), aluminium (Al), sulfur (S), silicon (Si), argon (Ar), calcium (Ca), iron (Fe), and nickel (Ni). Plotted on the right axis is the density-weighted time-scale for all ions to be within 10% of their equilibrium value. Both right and left axes are plotted against temperature in Kelvin (Smith & Hughes, 2010).

of the charged particle species involved in this interaction are unbound. For an optically-thin thermal plasma with solar abundances, this emission is dominated by electrons with a Maxwell-Boltzmann distribution that are interacting with hydrogen (protons) and helium ions. Free electrons interacting with heavy ions from SNR ejecta can also be an important or a dominant contribution (e.g., Vink et al. 1996). Bremsstrahlung emission has a characteristic shape that is dependent on the electron velocity distribution and is given by:

$$\frac{dE}{dV dt d\nu} = \frac{2^5 \pi e^6}{3 m_e c^3} \left( \frac{2\pi}{2k_B m_e} \right)^{1/2} Z_i^2 n_e n_i g_{ff} T_e^{-1/2} \exp\left(-\frac{h\nu}{k_B T_e}\right) \text{ erg s}^{-1} \text{ cm}^{-3} \text{ Hz}^{-1}, \quad (1.28)$$

where  $e$  is the electron charge,  $m_e$  is the mass of the electron,  $c$  is the speed of light,  $T_e$  is the electron temperature,  $n_e$  is the electron number density,  $n_i$  is the ion number density,  $Z$  is the number charge of the ion,  $\nu$  is the frequency of emission,  $h$  is the planck constant,  $k_B$  is Boltzmann's constant, and  $g_{ff} \sim 1$  is the Gaunt-factor<sup>4</sup> (Rybicki & Lightman, 1979).

---

<sup>4</sup> $g_{ff} = (3k_B T_e / \pi h \nu)^{-1/2}$

Table 1.1: The binding energies  $E_{bind}$  (in keV) of H-like and He-like ions. These energies are observed as the sharp energy seen in a RRC (Thompson et al., 2009).

Element	H-like	He-like
	He-RRC	H-RRC
Mg	1.763	1.958
Si	2.439	2.666
S	3.225	3.482
Ar	4.121	4.406
Ca	5.128	5.440
Fe	8.830	9.194

### Radiative recombination

Free-bound emission arises from a free electron that is captured into the bound state of an ion. This capture emits a photon with energy equal to the kinetic energy of the electron plus the binding energy of the newly recombined electron. As the kinetic energy of an electron is not quantised, this will produce a continuum of emission. This continuum emission will have sharp edges at the binding energy of the shell, as electrons are statistically more likely to be captured by atomic shells with a high principal quantum number, whose potential energy is small. This spectrum of radiation is called the “radiative recombination continuum” (RRC), whose shape is described by:

$$\frac{dE}{dV dt d\nu} = \left( \frac{16}{2\pi m_e k_B T_e} \right)^{1/2} n_e n_i \sigma_{rrc} \frac{E_\gamma \kappa}{k_B T_e} \exp\left( -\frac{\kappa}{k_B T_e} \right), \quad (1.29)$$

where  $n_e$  and  $n_i$  is the electron and ion number density,  $E_\gamma$  is the energy of the emitted photon,  $E_{bind}$  is the electron binding energy,  $\kappa = E_\gamma - E_{bind}$ , and  $\sigma_{rrc}$  is the recombination cross section to level  $n$  at the the electron energy  $E_\gamma - E_{bind}$ , assuming a Maxwell-Boltzmann distribution (Tucker & Gould, 1966)<sup>5</sup>. RRCs are usually observed as a perturbation on top of a bremsstrahlung continuum and a recombining plasma will have strong RRC features. Table 1.1 lists the RRC binding energies for a number of major elements found in SNRs.

### Two photon emission

Two photon emission arises from an electron that has been excited from a metastable state such as  $1s \rightarrow 2s$ , and cannot decay to the  $1s$  shell as this transition is forbidden since  $\Delta S = 0$ . To return to the ground state, the electron will emit two photons whose combined energy is equal to the energy difference of

<sup>5</sup>For a complete derivation see <http://www.atomdb.org/Physics/rrc.pdf>

the  $1s$  shell and  $2s$  shell. This process is not dominant in the plasmas found in SNRs (Raymond & Smith, 1977).

### Line emission

Line emission arises from the excitation of an ion by an electron, which then reverts back to a lower state or its ground state by emitting a photon that has discrete energies corresponding to the difference between the initial and final state of the ion. For hydrogen and hydrogen-like ions (ions that have been stripped of all but one or two electrons) the energy of the photon absorbed and emitted from this process is given by the Rydberg formula:

$$E = Z^2 R_y \left( \frac{1}{n^2} - \frac{1}{m^2} \right) \text{eV}, \quad (1.30)$$

where  $Z$  is the atomic number of the ion,  $R_y \sim 13.6$  eV is Rydberg constant,  $n$  and  $m$  are the principal quantum numbers of the discrete levels where  $m > n$ . Transitions from  $m = 2 \rightarrow \infty$  to  $n = 1$  are called the Lyman series and each transition is labelled sequentially using Greek letters (i.e.,  $m = 2 \rightarrow n = 1$  is called  $\text{Ly}\alpha$ ,  $m = 3 \rightarrow n = 1$  is called  $\text{Ly}\beta$  etc.). Table 1.2 lists the expected line energies for H-like ions from the  $\text{Ly}\alpha$  and  $\text{Ly}\beta$  transitions.

The line emission observed in SNRs arise from transitions occurring within elements that have been stripped of all but one or two of their electrons. As a consequence, these originally complex multi-electron atoms can be treated as if they were simple hydrogen-like (H-like) or helium-like (He-like) atoms. When an electron in one of these ions transitions from an excited state to the ground state ( $n = 1$ ) this transition is called a K-shell transition, while a transition from an excited state to the  $n = 2$  state is called an L-shell transition. A K-shell transition in a H-like atom will produce a prominent emission line, while a K-shell transition in He-like atoms will produce a triplet that consists of a resonance<sup>6</sup>, intercombination<sup>7</sup> and forbidden<sup>8</sup> line. Table 1.2 lists the common K-shell transitions observed in SNRs.

Line emission observed in SNRs from different elements provide a useful tool for characterising the properties of the X-ray emitting plasmas. At these temperatures, most elements are stripped of all but one or two of their electrons leading to H-like and He-like ions. Elements with atomic number greater than 6 (i.e., Carbon

<sup>6</sup>The resonance line is produced by an electron jumping between the ground state and the first energy level in an atom or ion e.g.,  $1s2p [^1P_1] \rightarrow 1s^2 [^1S_0]$ .

<sup>7</sup>This spectral line arises from the transition of an electron between two levels with different spin quantum number, i.e.,  $1s2p [^3P_{2,1}] \rightarrow 1s^2 [^1S_0]$ .

<sup>8</sup>A forbidden line arises from an atomic transition that is traditionally forbidden by the electric dipole selection rules. Even though they are forbidden there is a small probability of their spontaneous occurrence, should an atomic nucleus, atom or molecule be raised to an excited state. The K-shell forbidden line usually arises from the following transition  $1s2s [^3S_1] \rightarrow 1s^2 [^1S_0]$ .

Table 1.2: Common line emission seen in the X-ray spectra of SNRs. Here all transitions are listed in keV (Thompson et al., 2009). Under the He-like elements,  $R$  corresponds to the resonance line,  $I$  is the intercombination line and  $F$  is the forbidden line.

Element	H-like		He-like		
	Ly $\alpha_1$	Ly $\beta_1$	K $\alpha(R)$	K $\alpha(I)$	K $\alpha(F)$
C	0.3675	0.4356	0.3079	0.3044	0.2990
N	0.5004	0.5930	0.4307	0.4263	0.4198
O	0.6537	0.7746	0.5740	0.5687	0.5611
Ne	1.0220	1.2110	0.9220	0.9150	0.9051
Mg	1.4726	1.7488	1.3522	1.3431	1.3311
Si	2.0061	2.3766	1.8650	1.8547	1.8394
S	2.6277	3.1067	2.4606	2.4488	2.4303
Ar	3.3230	3.9357	3.1396	3.1263	3.1041
Ca	4.1075	4.8641	3.9024	3.8878	3.8612
Fe	6.9732	8.2526	6.7004	6.6823	6.6366
Ni	8.1017	9.5869	7.8056	7.7864	7.7316

and beyond) dominate the observed line emission in X-rays and their strength is dependent on both the electron temperature and the ionisation timescale.

### 1.3 Pulsars and their Pulsar Wind Nebulae

The core collapse of a massive star ( $\geq 8M_{\odot}$ ) can lead to the formation of a very dense, very compact stellar remnant called a neutron star. These objects have strong magnetic fields ( $B \sim 10^9 - 10^{13}$  Gauss), theoretical radii of  $\sim 12$  km, masses of  $\sim 1.4M_{\odot}$  and are rapidly rotating with a periods of  $\sim 0.001 - 10$  seconds (Lattimer & Prakash, 2007). The rapid rotation produces a highly relativistic magnetised wind of particles and electromagnetic fields called a pulsar wind. As this wind is travelling much faster than the speed of sound in the ambient medium, a termination shock (standing shock-wave) is produced. At the shock, the velocity of the wind becomes subrelativistic (Kennel & Coroniti, 1984). As this relativistic wind interacts with the surrounding magnetic fields and photon fields, the particles emit non-thermal radiation via synchrotron and inverse Compton (IC) emission (see Section 1.4.3 for more details), which we observe as a pulsar wind nebula (PWN). Observationally, PWNs vary dramatically depending on the properties of its pulsar such as its spin-down energy, space velocity, the interaction of the PWN with its surrounding medium and the evolutionary stage of the ejecta from PWN's host SNR. The most famous example of a PWN is the Crab Nebula (see Figure 1.6a), which is the result of a supernova explosion that was observable in AD 1054. At the heart of the Crab is a 33 ms pulsar that is powering a bright synchrotron

nebula, while the shock-front of the SNR remains undetected (for more details see the review by [Hester 2008](#) about its properties).

### 1.3.1 The properties of the central pulsar

The emission of a PWN is powered by the rotational spin-down energy,  $E_{rot}$ , of its central pulsar. A pulsar spins down from an initial period  $P_0$  following  $\dot{\Omega} \propto \Omega^n$ , where  $\Omega$  is the angular velocity and is equal to  $2\pi/P$ ,  $n$  is the braking index and  $P$  is the rotational period of the pulsar. The rate at which the rotational energy of the pulsar is dissipated (or the spin-down luminosity) is given by:

$$\dot{E} = -\mathcal{I}\Omega\dot{\Omega} = -\frac{dE_{rot}}{dt} \equiv 4\pi^2\mathcal{I}\frac{\dot{P}}{P^3} \quad (1.31)$$

where  $\dot{P}$  is the rate at which the period of the pulsar decaying and  $\mathcal{I}$  is the moment of inertia of the neutron star ([Gaensler & Slane, 2006](#)). Typically  $\mathcal{I} = 10^{45}$  g cm<sup>-2</sup>, assuming a uniform sphere. Pulsars that produce an observable PWN have a  $\dot{E} > 10^{34}$  erg s<sup>-1</sup> ([Gotthelf, 2004](#)), although it is expected that all pulsars are accompanied by a PWN as all pulsars produce a wind ([Kargaltsev & Pavlov, 2008](#)).

Assuming that the braking index  $n \neq 1$ , the age of the pulsar is given by ([Manchester & Taylor, 1977](#)):

$$\tau = \frac{P}{(n-1)\dot{P}} \left[ 1 - \left( \frac{P_0}{P} \right)^{n-1} \right] \quad (1.32)$$

If a pulsar spins down via magnetic dipole radiation (corresponding to a braking index of 3), Equation 1.32 becomes:

$$\tau = \frac{P}{2\dot{P}}, \quad (1.33)$$

assuming  $P_0 \ll P$ . This corresponds to the characteristic age of the pulsar. Equation 1.33 often underestimates the actual age of the pulsar ([Gaensler & Slane, 2006](#)). The spin-down luminosity of a pulsar evolves as a function of time following:

$$\dot{E} = \dot{E}_0 \left( 1 + \frac{t}{\tau_0} \right)^{-\frac{(n+1)}{(n-1)}} \quad (1.34)$$

where  $\tau_0$  is the initial spin down timescale of the pulsar ([Pacini & Salvati, 1973](#)). The period of a pulsar evolves similarly:

$$P = P_0 \left( 1 + \frac{t}{\tau_0} \right)^{\frac{1}{n-1}}. \quad (1.35)$$

### 1.3.2 Evolution of a pulsar wind nebula

When a pulsar is born, it is embedded in the slowly moving unshocked ejecta of its progenitor that is freely expanding into the surrounding medium. As the expansion velocity of the PWN is much faster than the speed of the slowly moving ejecta, the PWN drives a shock into the the expanding ejecta. Assuming a spherically symmetric expansion, the radius of the PWN ( $R_{PWN}$ ) evolves as:

$$R_{PWN} \propto \left( \frac{\dot{E}_0 t^3}{\rho(t)} \right)^{1/5} \quad (1.36)$$

where  $\dot{E}_0$  is the initial spin down luminosity,  $\rho(t)$  is the density of the surrounding SNR medium described by  $\rho(t) = 3M_{ej}/4\pi R_{SNR}^3(t)$ ,  $M_{ej}$  is the ejected mass and  $R_{SNR}(t)$  is given by Equation 1.2 (van der Swaluw et al., 2001).

As the host SNR enters the Sedov-Taylor stage, a reverse shock is produced which moves inward, and collides and compresses the PWN. The motion of the pulsar and any asymmetries in the expansion of the SNR will result in the morphology of the PWN to be highly distorted. Once the interaction between the reverse shock and PWN has subsided, the PWN will expand into hot, shocked ejecta. During this phase it will expand with a radius described by Equation 1.36, where  $R_{SNR}$  is given by Equation 1.6. At this point, the pulsar could have travelled at a distance equal to or larger than the equivalent PWN radius of a stationary pulsar. If this is the case, the pulsar will escape its original PWN, leaving behind a “relic” radio emitting PWN, while creating a new, smaller PWN (van der Swaluw et al., 2004).

As the PWN moves closer to the edge of the remnant, the velocity of the PWN becomes supersonic compared to the velocity of the expanding ejecta. This will cause the PWN to form a bow shock structure (see Section 1.3.3), that is tightly confined due to the ram pressure resulting from the pulsar’s motion. The pulsar will escape the SNR at the time:

$$t_{cross} \propto \left( \frac{E_{snr}}{\rho_{ISM} v_p^5} \right)^{1/3}, \quad (1.37)$$

where  $E_{snr}$  is the explosion energy of the SNR ( $\sim 10^{51}$  erg),  $\rho_{ISM}$  is the density of the ISM and  $v_p$  is the velocity of the pulsar (van der Swaluw et al., 2003). Outside the SNR, the pulsar is highly supersonic resulting in a bow-shock PWN with a large Mach number.

### 1.3.3 The morphology of pulsar wind nebulae

Before the launch of high resolution X-ray satellites like the *Chandra X-ray Observatory* or *XMM-Newton*, only a small number of PWN were detected using radio observations (Manchester et al., 2005). Since then, *Chandra* and *XMM*

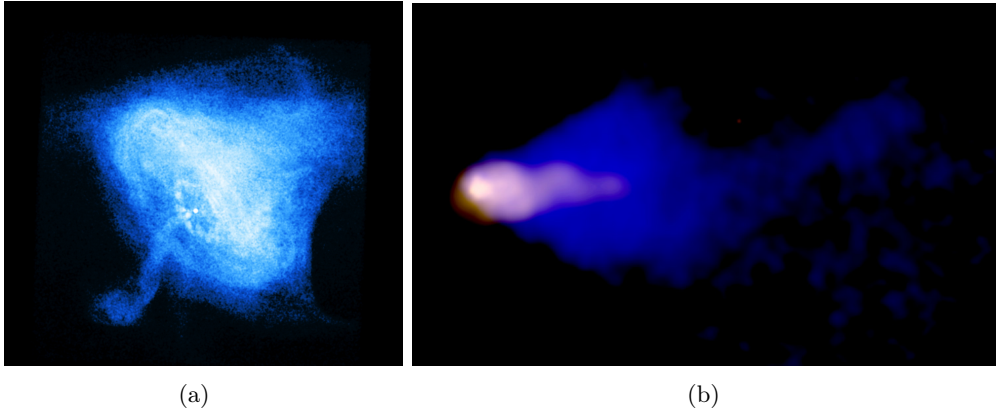


Figure 1.6: (a) The most famous example of toroidal and jet like morphology of a PWN is shown in this *Chandra* X-ray image of the Crab nebula (Weisskopf et al., 2000). (b) Typical example of the bow-shock and trail morphology of a PWN. This is the Mouse (PSR J1747-2958) PWN and highlighted in blue is the radio emission as detected using the VLA, while the X-ray emission as observed using *Chandra* is highlighted in yellow (Gaensler et al., 2004).

have revealed that pulsar wind nebulae (PWNe) have a wide range of shapes and morphologies. PWNe can be separated based on their morphology. They can either show a torus and/or a jet like feature (see Figure 1.6a), or a bowshock and/or a trail (see Figure 1.6b) or have a combination of these features. These morphologies are dependent on the outflow geometry of the pulsar wind, velocity of the pulsar and direction of motion of the pulsar. As a pulsar rotates, it produces an expanding, toroidal magnetic field. Due to conservation of energy flux along the field lines, the Lorentz factor of the pulsar wind will have a spatial variation which will cause the wind to become anisotropic, resulting in a toroidal like structure of the wind. In addition, the magnetic field will collimate the outflow of the pulsar wind producing a jet-like structure along the axis of rotation (Komissarov & Lyubarsky, 2004; Bogovalov et al., 2005).

Pulsars can be born with high space velocities that arise from a kick given due to the asymmetry of the supernova explosion that formed the neutron star (Lai, 2004). As described in Section 1.3.2, the pulsar will eventually escape its original PWN and propagate through the shocked ejecta of its host SNR. Once the pulsar has travelled at least two thirds of the host SNRs radius, the motion of the pulsar becomes supersonic resulting in the formation of a bow shock structure observable in X-ray and radio wavelengths (van der Swaluw et al., 2003). The bow shock morphology is characterised by an extended trail with the pulsar surrounded by a Mach cone. The pulsar is found at the apex of this feature. When the pulsar escapes its host SNR, it will propagate through the neutral gas of the ISM, and the PWN will also become detectable using  $H\alpha$  measurements.

### 1.3.4 Emission from a pulsar and its nebula

The pulsar wind produces a population of highly relativistic electrons and positrons. These particles will interact with surrounding magnetic fields and ambient photon fields producing non-thermal emission in the form of synchrotron and inverse Compton radiation (see Section 1.4.3 for more details about each mechanism). The emission of a PWN is dominated by synchrotron emission, which is observable in radio to X-ray wavelengths. This emission can be easily discernible from the emission of its host SNR whose emission is generally dominated by thermal processes (see Section 1.2.5). The synchrotron spectrum of a PWN can be characterised by a broken power law distribution where its spectral ( $\alpha$ ) and photon ( $\Gamma$ ) index for the radio and X-ray emission ranges from  $-0.3 \leq \alpha \leq 0$  and  $\Gamma \sim 2$  respectively<sup>9</sup> (Gaensler & Slane, 2006). The radio morphology of a PWN can be unstructured, while X-ray observations reveal a wide range of features (see Section 1.3.3). The size of a PWN as observed in X-rays is usually much smaller than its radio or optical counterpart, since high energy particles have a shorter lifetime compared to lower energy particles. This effect is called synchrotron burn off. However, there are cases where the X-ray and radio morphology of a PWN is the same size (e.g 3C58 or G21.5-0.9). Apart from SNRs, pulsars and their nebulae are thought to be one of the main sources that contribute to the electron positron anomaly that is discussed in Section 1.4.

The X-ray emission from a neutron star consists of a non-thermal component that arises from the magnetosphere of the pulsar and a thermal component that arises from the surface of the neutron star (Pavlov & Zavlin, 2003; Özel, 2013). Typically, for young pulsars the non-thermal emission dominates the observed X-ray spectrum, while for older pulsars both components can be resolved. The non-thermal emission arises from synchrotron radiation from relativistic electrons and positrons being accelerated by the very strong magnetic fields close to the neutron star surface. This emission can usually be fit using a power law spectrum whose photon index  $\Gamma$  ranges from 1 - 2. The thermal component is thought to arise from either relativistic particles hitting the neutron star surface at the magnetic poles (Ruderman & Sutherland, 1975; Arons, 1981; Harding & Muslimov, 1998, 2001, 2002) or from the bulk of the neutron star which is radiating heat from the interior (Schaab et al., 1999). Analysing these components provides information about the properties related to particle acceleration in the magnetosphere, the geometry of the magnetic field, and equation of state of the dense matter at the interior of the neutron star.

---

<sup>9</sup>The synchrotron radio emission can be characterised by  $S_\nu \propto \nu^\alpha$ , where  $S_\nu$  is the flux density at a frequency  $\nu$  and  $\alpha$  is the spectral index. For X-rays, the synchrotron emission is described by  $N_E \propto E^{-\Gamma}$ , where  $N_E$  is the number of X-ray photons emitted with energy between  $E$  and  $E + dE$ . Here  $\Gamma$  is the photon index and is equal to  $1 - \alpha$ , where  $\alpha$  is the spectral index.

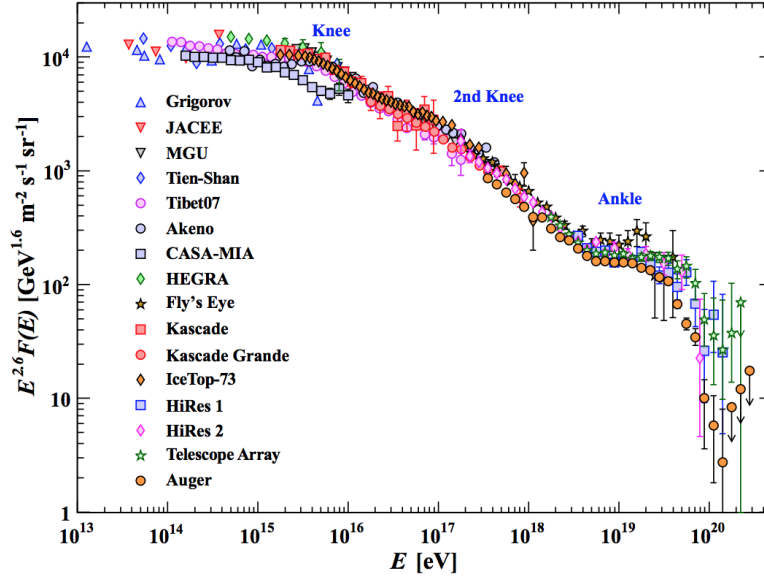


Figure 1.7: The all particle cosmic ray spectrum as measured from air shower experiments as a function energy (eV). The differential energy spectrum has been multiplied by  $E^{2.6}$  so that features of the steep spectrum are easily observable. The “knee” and “ankle” of the cosmic-ray spectrum are highlighted. Figure from (Olive & Particle Data Group, 2014).

## 1.4 Cosmic rays and their non thermal emission

Since the discovery of cosmic rays (CRs) by Viktor Hess in 1912 (Hess, 1912), numerous ground-based, balloon and space-based experiments have attempted to measure the energy distribution of these extra-terrestrial particles, over many decades of energies (Figure 1.7). The spectrum of cosmic rays, which extends from  $10^{10}$  eV to about  $10^{20}$  eV, can be modelled using a broken powerlaw. Below the “knee” of the spectrum ( $E_{knee} \sim 10^{15}$  eV), the spectrum can be described by a powerlaw with an index of 2.7, while above the “knee”, the index steepens to about 3.0 – 3.2. At around  $10^{18}$  eV there is another spectral break called the “ankle”, where the spectrum starts to flatten. The presence of these two spectral breaks is thought to be intimately linked to the origin of CRs. Below the “knee” of the spectrum, the CRs are thought to be Galactic in origin since their gyro-radius in the interstellar magnetic field is less than the radius of the Galaxy, while CRs with energies greater than the “knee” are thought to be extra-Galactic in origin (Hillas, 1972).

Galactic CR have an energy density of about  $1 \text{ eV cm}^{-3}$ , which corresponds to an injection rate of approximately  $5 \times 10^{40}$  erg/s (Longair, 2011), assuming our Galaxy can be approximated by a cylinder with radius of 15 kpc and thickness of 200 pc and lifetime of a CR is about  $10^6$  years (Lukasiak et al., 1994). Baade &

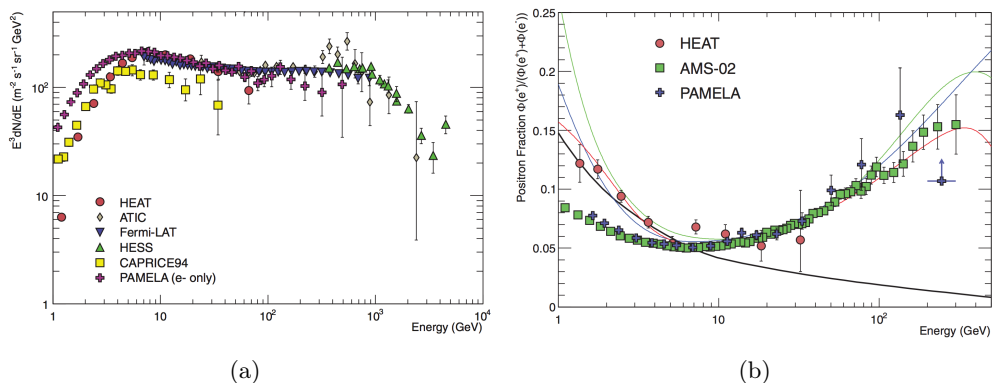


Figure 1.8: (a) Electron plus positron sum as measured by HEAT, ATIC, *Fermi*-LAT, H.E.S.S., CAPRICE94, as well as the electron spectrum measured by PAMELA. This spectrum is multiplied by  $E^3$  to highlight the features of this differential spectrum. (b) The ratio of positrons to electrons+positrons (positron fraction), as measured by HEAT, AMS-02 and PAMELA. Black line represents the theoretical prediction assuming standard production mechanisms (Moskalenko & Strong, 1998). The green, blue and red lines correspond to the models of the positron fraction produced by dark matter decay, modification of cosmic ray propagation physics and pulsars, respectively. Figures adapted from (Olive & Particle Data Group, 2014).

Zwicky (1934) showed using simple energetic arguments that SNRs can naturally explain the observed energy density. Ginzburg & Syrovatskii (1964) suggested that SNR shock-waves are the best candidate for accelerating Galactic CRs as only a small percentage (1-10%) of their total explosion energy would be needed to be converted into relativistic particles to explain the observed energy density.

SNRs are typically discovered using radio observations, with a large number of the SNRs in Green’s supernova remnant catalogue (Green, 2014) identified as extended radio sources with non-thermal radio spectra. Shklovskii (1953) first proposed that the observed radio emission arose from synchrotron emission, implying that SNRs were sources of non-thermal, power-law populations of electrons being accelerated to high energies. Since then, discoveries of synchrotron X-ray emission from other SNRs such as SN1006 (Koyama et al., 1995; Reynolds, 1998), RX J1713.7-3946 (Koyama et al., 1997; Slane et al., 1999; Uchiyama et al., 2007) and Tycho (Hwang et al., 2002; Warren et al., 2005), as well as  $\gamma$ -ray emission from SNRs such as IC443 (Abdo et al., 2010c; Ackermann et al., 2013b), W44 (Abdo et al., 2010b; Ackermann et al., 2013b), W41, MSH 17-39, and G337.0-0.1 (Castro et al., 2013a), have indicated that SNRs can accelerate particles to close to the “knee” of the CR spectrum (Reynolds, 1998), cementing the idea that SNRs accelerate cosmic rays at their shocks. In addition to measuring the all particle cosmic ray spectrum shown in Figure 1.7, balloon born and space based experiments have measured the distribution of high energy electrons and positrons at Earth (see Figure 1.8). These experiments include HEAT (Barwick et al., 1997; Beatty et al.,

2004); Golden et al. (1996); CAPRICE96 (Boezio et al., 2000); AMS-01 (Alcaraz et al., 2000b; AMS-01 Collaboration et al., 2007), AMS-02 (Aguilar et al., 2013); ATIC (Chang et al., 2008); PAMELA (Adriani et al., 2009b,a), *Fermi*-LAT (Abdo et al., 2009b; Ackermann et al., 2010); and H.E.S.S. (Aharonian et al., 2008b, 2009b). Over the last couple of years, these measurements have generated a lot of interest due to the discovery of an excess of electrons and positrons compared to what is theoretically expected. Electrons and positrons undergoing diffusive propagation (for more details see Section 1.4.2) are expected to produce a flat spectrum above  $\sim 5$  GeV due to strong radiative energy losses (Olive & Particle Data Group, 2014), while the positron fraction,  $e^+/(e^+ + e^-)$ , is expected to decrease above  $\sim 10$  GeV (Moskalenko & Strong, 1998). Experiments taken prior to 2008 such as HEAT, and AMS-1, seemed to agree with theoretical predictions when taking into account the systematic errors. However, ATIC measured an excess of electrons between about 300 – 800 GeV, peaking at  $\sim 600$  GeV, while the *Fermi*-LAT measured an excess in electrons and positrons over a similar energy range without confirming the peak excess (Figure 1.8a). Similarly PAMELA and AMS-02 measured the electron to positron ratio and found that above 10 GeV this ratio increases (Figure 1.8b). This observed excess is unable to be explained using conventional mechanisms such as the production of charged particles arising from the collision of cosmic rays with the ISM. As a consequence the excess is thought to arise from either individual nearby sources such as SNRs (e.g. Shaviv et al. 2009; Fujita et al. 2009; Blasi 2009; Mertsch & Sarkar 2011) and pulsars and their PWN (e.g. Hooper et al. 2009; Yüksel et al. 2009; Grasso et al. 2009; Malyshev et al. 2009; Gendeleev et al. 2010; Blasi & Amato 2011; Profumo 2012). Additionally, other explanations include modification of CR propagation physics, or dark matter decay and/or annihilation (see Panov (2013) and references there within).

Apart from detecting electrons and positrons, a number of balloon and space based experiments such as Ryan et al. (1972), SOKOL (Ivanenko et al., 1993), RUNJOB (Hareyama & RUNJOB Collaboration, 2006), CREAM (Ahn et al., 2010; Yoon et al., 2011), ATIC-2 (Wefel et al., 2008), CAPRICE98 (Boezio et al., 2003), IMAX (Menn et al., 2000), RICH2 (Diehl et al., 2003), JACEE (Asakimori et al., 1998), CAPRICE94 (Boezio et al., 1999), BESS (Haino et al., 2004), AMS-01 (Alcaraz et al., 2000a), PAMELA (Adriani et al., 2011), AMS-02 (Consolandi & AMS-02 Collaboration, 2014) and *Fermi*-LAT (Ackermann et al., 2014) have measured the flux of protons over energies of 1 -  $10^6$  GeV (see Figure 1.9). Unlike the all particle spectrum which is well measured to energies close to the knee of the CR spectrum, data is statistically limited to energies well below the knee. This is due to the large experimental uncertainties associated with determining the fluxes and energies of protons. Below  $\sim 100 - 200$  GeV, the proton spectrum derived by PAMELA agrees well with older experiments such as CAPRICE98 and

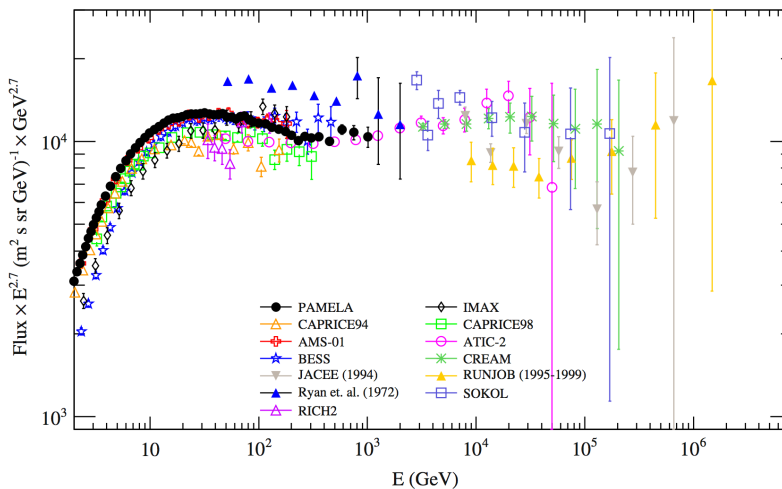


Figure 1.9: The local CR proton spectrum as determined from multiple experiments. This spectrum is multiplied by  $E^{2.7}$  to highlight features in the spectrum. Figure from Boezio (2014).

BESS, while above this energy PAMELA is consistent with data from the ATIC-2 and CREAM experiments. The data collected by ATIC-2, CREAM and PAMELA experiments seems to indicate the presence of either a spectral break or spectral hardening above  $\sim 230 - 240$  GeV (Adriani et al., 2011). The proton spectrum derived by AMS-01 agrees well with the PAMELA data but shows no spectral hardening. AMS-01 is instead consistent with a simple power-law above  $\sim 50$  GeV. In addition, data from newer observations by AMS-02 or *Fermi*-LAT do not confirm or disprove the presence of the spectral break, but do indicate a flatter proton spectrum at high energies. The flattening of the proton spectrum at high energies has been confirmed by an analysis of the  $\gamma$ -ray spectrum arising from very dense molecular clouds in the Gould belt (Neronov et al., 2012; Kachelrieß & Ostapchenko, 2012).

Similar to the observed excess of electrons and positrons, this observed spectral hardening cannot be explained using conventional cosmic-ray propagation mechanisms, which predicts that the cosmic-ray proton spectrum is well described by a single powerlaw up to the knee. As a consequence this hardening is thought to arise from the presence of local sources such as a nearby SNRs (e.g., Thoudam & Hörandel 2012, 2013), variation in the injection spectrum at the source (e.g., from SNR: Biermann et al. 2010; Yuan et al. 2011), from multiple sources with different spectral indices and different maximal energies (e.g., Zatsepin & Sokolskaya 2006), from a local component dominating up to  $\sim 200$  GeV (e.g., Erlykin & Wolfendale 2012), from variation in the diffusion coefficient (e.g., Vladimirov et al. 2012) or from the spatial change of the CR diffusion properties in different regions of the

Galaxy (e.g., Tomassetti 2012).

### 1.4.1 Diffusive shock acceleration

As the observational evidence for SNRs accelerating CRs increased, a number of authors proposed mechanisms to explain how SNRs were able to accelerate particles up to such high energies. Fermi (1949) proposed a simple mechanism that naturally resulted in a powerlaw energy distribution of accelerated particles while taking into account the presence of a magnetic field. In this mechanism, collisions occur between charged particles and molecular material via magnetic mirroring<sup>10</sup>, which will cause these particles to gain energy after scattering. This mechanism is called second order Fermi acceleration as the energy gain is second order in  $\Delta E/E \sim (u/v)^2$ , where  $u$  is the velocity of the molecular material and  $v$  is the velocity of the particle. However this mechanism is not sufficient to efficiently accelerate particles such that it would explain the observed CR spectrum.

Axford et al. (1977), Krymskii (1977), Bell (1978a), Blandford & Ostriker (1978) and Bell (1978b) determined simultaneously that a shock-wave can naturally enhance the effects of the second order Fermi acceleration. As the shock-wave of a SNR propagates, these particles will scatter back and forth across the shock due to turbulence in the form of Alfvén waves, resulting in first order energy gains in  $\Delta v/v$ , where  $\Delta v = v_1 - v_2$  is the difference in the flow velocity of upstream ( $v_1$ ) and downstream ( $v_2$ ) of the shock, and  $v$  is the velocity of the particle (Figure 1.10). This process is called first-order Fermi acceleration, or more commonly known as diffusive shock acceleration (DSA), and it naturally produces a powerlaw distribution of accelerated particles in the following way (Bell, 1978a,b; Malkov & O’C Drury, 2001; Longair, 2011).

When a relativistic particle with energy  $E_0$  is scattered across the shock-front of an SNR, it will gain energy such that its new energy is given by  $E = \alpha E_0$ , where  $\alpha = 1 + \frac{4\Delta v}{3v}$ . After  $k$  crossings, we expect  $N_k = N_0 \mathcal{P}^k$  particles with energy  $E_k = E_0 \alpha^k$  to be remaining in the acceleration region with a probability of  $\mathcal{P} = 1 - \frac{4v_2}{c}$ . Here  $N_0$  is the initial number of particles in the region of acceleration. Eliminating  $k$  gives:

$$\frac{\ln(N_k/N_0)}{\ln(E_k/E_0)} = \frac{\ln(\mathcal{P})}{\ln(\alpha)} \sim -\frac{3v_2}{\Delta v}, \quad (1.38)$$

to first order and assuming that  $(v_2/v, \Delta v/v) \ll 1$ . Rearranging this yields

$$\frac{N_k}{N_0} = \left(\frac{E_k}{E_0}\right)^{\ln \mathcal{P} / \ln \alpha} \sim \left(\frac{E_k}{E_0}\right)^{-\frac{3v_2}{\Delta v}} \quad (1.39)$$

<sup>10</sup>Magnetic mirroring is when a charge particle is reflected from a region of high magnetic field density to a region of low magnetic field density.

which gives the differential energy spectrum

$$\frac{dN(E)}{dE} \propto E^{-\frac{3v_2}{\Delta v}-1} \sim E^{-\frac{r+2}{r-1}} \quad (1.40)$$

where  $r = v_1/v_2$  is the shock compression ratio and is given by Equation 1.20, assuming a strong shock. For a non-relativistic mono-atomic gas where  $\gamma = 5/3$ , Equation 1.40 simplifies to:

$$\frac{dN(E)}{dE} \propto E^{-2}. \quad (1.41)$$

This agrees well with the observed spectral index of the CR spectrum shown below the ‘‘knee’’ (Figure 1.7), as well as with the spectral index of the synchrotron spectrum of SNRs.

Applying DSA to a powerlaw distribution of charged particles being accelerated by the shock-front of an SNR, Lagage & Cesarsky (1983) determined that SNRs can accelerate particles up to  $\sim 10^{14}$  eV, assuming that the acceleration time scale is similar to the age of the remnant and that the diffusion coefficient ( $D$ ) of CRs (see Equation 1.43) is proportional to the gyro-radius of the particle. This further supports the evidence that SNRs are the origin of the CRs below the ‘‘knee’’ of the CR spectrum.

Particle acceleration will affect the dynamics of the supernova remnant, producing non-linear effects on the system that cannot be ignored. These include the modification of the adiabatic index of the plasma. As the number of relativistic non-thermal particles increases,  $\gamma$  will become softer ( $\gamma \rightarrow 4/3$ ), resulting in increased compressibility of the gas (see Equation 1.17), and thus higher acceleration efficiency. Additionally, efficient particle acceleration will result in energy-dependent diffusion, which will cause higher energy particles to escape the shock producing a flatter non-thermal spectrum, as well as enhanced turbulence up and down stream of the shock-front and modification of the ionisation structure of the plasma (e.g., Patnaude et al. 2009, Reynolds 2008 and references therein).

### 1.4.2 Cosmic-ray propagation

The propagation of Galactic cosmic rays with energies less than  $10^{17}$  eV is best described using a diffusion model with added convection (Strong et al., 2007). Diffusion of cosmic ray particles provides a simple explanation of the highly isotropic distribution of high energy charged particles and their noticeable retention in the Galaxy. Diffusion results from the scattering of the cosmic rays on random magnetohydrodynamic (MHD) waves and inhomogeneities in the Galactic magnetic field. The random nature of the Galactic magnetic field causes charged CRs to undergo a random walk in space. The energy distribution of the CRs is modified by energy losses experienced by their interaction with the ISM and the interstellar radiation fields (ISRF). Galactic wind-driven convection, re-acceleration due to

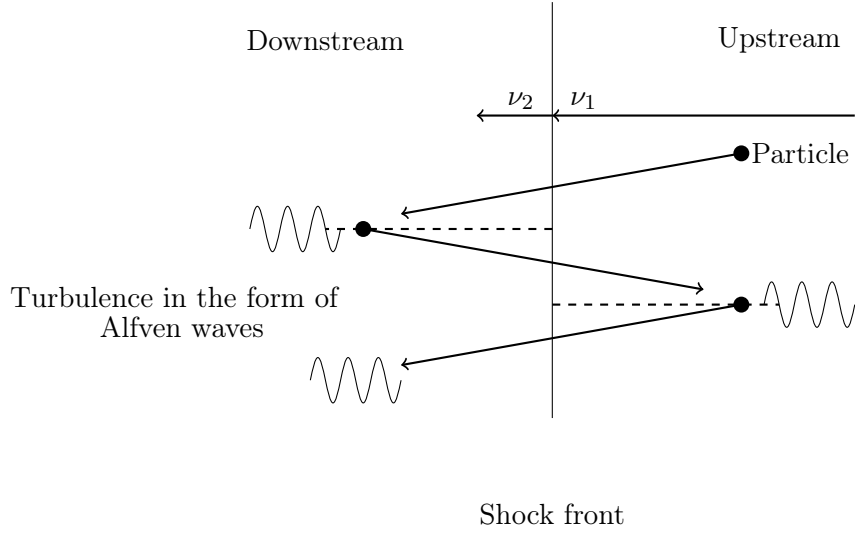


Figure 1.10: Schematic diagram of diffusive shock acceleration. Here  $\nu_1$  is the flow velocity upstream of the shock, while  $\nu_2$  is the velocity downstream of the shock.

interstellar shocks, fragmentation and radioactive decays for heavy and unstable nuclei, also modify the energy distribution. As a consequence, the CR spectrum that one measures on Earth differs substantially from the spectrum emitted from the source (Fan et al., 2010).

The density  $\psi(\vec{r}, p, t)$  (per unit particle momentum  $p$ ) of a particular CR species at a Galactic radius  $r$ , can be calculated by solving the cosmic ray transport equation which has the general form (Strong et al., 2007):

$$\begin{aligned} \frac{\partial \psi(\vec{r}, p, t)}{\partial t} = & q(\vec{r}, p, t) + \vec{\nabla} \cdot (D_{xx} \vec{\nabla} \psi - \vec{V} \psi) + \frac{\partial}{\partial p} \left( p^2 D_{pp} \frac{\partial}{\partial p} \frac{1}{p^2} \psi \right) \\ & - \frac{\partial}{\partial p} \left[ \dot{p} \psi - \frac{p}{3} (\vec{\nabla} \cdot \vec{V}) \psi \right] - \frac{1}{\tau_f} \psi - \frac{1}{\tau_r} \psi \end{aligned} \quad (1.42)$$

Here  $q(\vec{r}, p, t)$  is the source term, which encaptures the production mechanism, spallation and decay of primary or secondary CRs<sup>11</sup>. The source(s) of the CRs are assumed to be concentrated near the Galactic plane and have a distribution similar to known astrophysical objects such as SNRs, and pulsars. The spatial diffusion coefficient  $D_{xx}$ , describes the transport of the CR species through turbulent magnetic fields. This transport can be either isotropic or anisotropic, and can be influenced by the CRs themselves (Strong et al., 2007). Generally,  $D_{xx}$  has the generic form:

$$D_{xx} = D_{xx0} \beta \left( \frac{R}{\text{GeV}} \right)^\delta \quad (1.43)$$

<sup>11</sup>Primary CRs are particles that are accelerated at an astrophysical object such as an SNR, while secondary CRs arise from the decay of a primary cosmic ray.

where  $\beta = \frac{v}{c}$ , and  $R = \frac{pc}{eZ}$  is the magnetic rigidity<sup>12</sup>. Here  $Z$  is the effective nuclear charge of the particle,  $p$  is its momentum,  $e$  is its charge, and  $c$  is the speed of light. The constant exponent  $\delta$  indicates the power law dependence of the spatial diffusion coefficient  $D_{xx}$ . Different regions of the energy spectrum can have different  $\delta$  values, producing a discontinuity in the spatial diffusion coefficient  $D_{xx}$ . This artificial break in  $D_{xx}$  is introduced so that one can fit observed CR ratios such as the Boron/Carbon ratio over all energies (Strong & Moskalenko, 1998). The value of the diffusion coefficient can be estimated from modelling CR data and typically has a value of  $D_{xx} \sim (3 - 5) \times 10^{28} \text{ cm}^2 \text{ s}^{-1}$  at 1 GeV.

In addition to spatial diffusion, the random scattering of CR particles on turbulent MHD waves leads to diffusive re-acceleration (not be confused with diffusive shock acceleration). This is described by the diffusion coefficient  $D_{pp}$  and is related to the spatial diffusion coefficient  $D_{xx}$  by:

$$D_{pp}D_{xx} = \frac{4p^2v_A^2}{3\delta(4 - \delta^2)(4 - \delta)\omega}, \quad (1.44)$$

Here  $v_a$  is the Alfvén speed<sup>13</sup>, and  $\omega$  characterises the level of MHD turbulence experienced by the CR. This is also known as the ratio of MHD energy density to the magnetic field energy density.

In the transport equation, the convection velocity is described by  $\vec{V}$ . This is a function of Galactic radius  $r$  and depends on the properties of the Galactic wind. The convection velocity is assumed to have cylindrical symmetry and increases linearly with height  $z$  from the Galactic plane. Apart from transporting particles through the Galaxy, convection also causes adiabatic energy losses (or gains) in the non-uniform flow of gas ( $\vec{\nabla} \cdot \vec{V}$ ). The momentum gained (or lost) due to the particles interactions with the ISM and Galactic magnetic fields is described by  $\dot{p}$ . The last two terms of the transport equation,  $\tau_f$ , describes the time-scale for energy loss due to fragmentation. This parameter depends on the total spallation cross section and gas density  $n(r)$  which can be estimated using atomic and molecular gas surveys. The parameter  $\tau_r$  describes the timescale for radioactive decay.

To solve Equation 1.42, the boundary conditions depend on the diffusion model that one uses, but  $\psi = 0$  is assumed at the halo boundary where particles are expected to escape into the intergalactic space. The diffusion of CRs is modelled using either a leaky-box or a weighted-slab model. The leaky-box model assumes that CRs are injected into the Galaxy by sources that are distributed uniformly throughout. The escape time of these particles is independent of their position in the Galaxy and this model assumes uniform molecular gas and interstellar

<sup>12</sup>The rigidity of a particle describes a particle's resistance to deflection by a magnetic field.

<sup>13</sup>Alfvén speed describes the speed of an Alfvén wave, which is a special type of MHD wave (Strong & Moskalenko, 1998). An Alfvén wave results from the interaction of the magnetic fields and electric currents that occur within a plasma

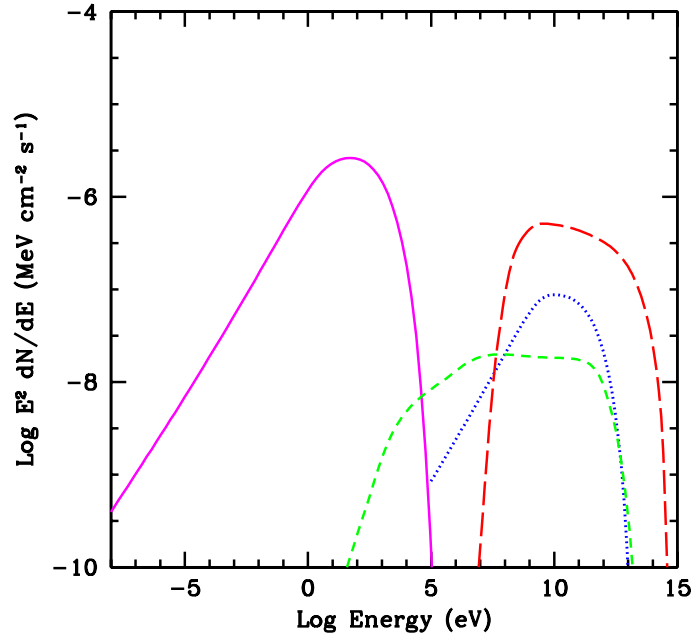


Figure 1.11: The non-thermal emission expected from a SNR accelerating electrons and protons at the shock-front. The magenta curve represent synchrotron emission from relativistic electrons, the dotted blue curve is from inverse Compton scattering off CMB photons, the dashed green curve is from non-thermal bremsstrahlung from the relativistic electrons interacting with ambient material and the red long-dashed curve corresponds in pion decay. This figure has been adapted from [Slane et al. \(2014\)](#).

radiation fields. This model best describes the propagation of CRs if diffusion is fast and there is a non-zero probability that CRs are reflected at the boundaries of the halo, or when the Galaxy can be described by a flat-halo model<sup>14</sup>. The weighted-slab model consists of separating the astrophysical and nuclear physics parts of the transport equation into two separate calculations, which are then combined. Unfortunately this model breaks down for low energy CRs or strong dependences on energy losses and nuclear cross sections, but is best used when there is no convective transport and the diffusion coefficient depends on particle energy and position in the Galaxy ([Strong & Moskalenko, 1998](#)).

### 1.4.3 Non-thermal emission from accelerated particles

The interaction of particles, accelerated at the shock-front of an SNR, with surrounding material such circumstellar material, molecular clouds, magnetic

<sup>14</sup>A flat-halo model assumes that the distance from the galactic plane  $Z_h$  is much less than the radius of the galactocentric radius,  $R$

fields, interstellar radiation fields (from starlight and dust), and/or the cosmic microwave background leads to non-thermal emission that is divided into two main categories. There is *leptonic* emission which results from the interaction of an electron or a positron with one of the above targets and results in synchrotron radiation, inverse Compton (IC) scattering or non-thermal Bremsstrahlung. There is also *hadronic* emission that arises from the decay of a neutral pion ( $\pi^0$ ) into two  $\gamma$ -ray photons, which is produced in a proton-proton collision. Figure 1.11 presents the expected emission of each process from a SNR undergoing efficient particle acceleration. Over the last 10 years or so, there have been numerous observations establishing that there is a population of particles that can be accelerated to the “knee” of the CR energy spectrum. Evidence for SNRs accelerating relativistic electrons arises from the detection of non-thermal X-ray emission from a number of SNRs such as SN1006 (Koyama et al., 1995; Reynolds, 1998), Vela Jr. (Aschenbach, 1998), RX J1713.7-3946 (Koyama et al., 1997; Slane et al., 1999; Uchiyama et al., 2007) and Tycho (Hwang et al., 2002; Warren et al., 2005) and from the detection of GeV and TeV  $\gamma$ -ray emission from SNRs such as Tycho (Acciari et al., 2011; Morlino & Caprioli, 2012), RX J1713.7-3946 (Muraishi et al., 2000; Abdo et al., 2011), G166.0+4.3 (Araya, 2013), and RCW86 (Aharonian et al., 2009a; Yuan et al., 2014). Evidence in favour of SNRs accelerating protons at their shock-front has dramatically increased since the *Fermi* satellite launched in 2008. The *Fermi*-LAT detector provided the necessary coverage in the GeV energy band, that was crucial for being able to distinguish between emission arising from  $\pi^0$ -decay, non-thermal bremsstrahlung or IC scattering. Modelling of the  $\gamma$ -ray and broadband emission of SNRs such as W51C (Abdo et al., 2009a); G349.7+0.2, CTB 37A, 3C 391, G8.7-0.1 (Castro & Slane, 2010); W41, MSH 17-39, and G337.7-0.1 (Castro et al., 2013b), has established that  $\pi^0$ -decay dominates their  $\gamma$ -ray emission. *Fermi*-LAT observations of SNR W44 and IC443 show clear evidence of the characteristic pion decay feature at 67.5 MeV in their  $\gamma$ -ray spectra, confirming that protons are accelerated at the shock-front of an SNR (Ackermann et al., 2013a). For PWN, their non-thermal emission is dominated by leptonic emission as discussed in Section 1.3.4.

## Synchrotron

Synchrotron emission, which is predominantly observed in radio and X-ray wavelengths, arises from the interaction of a relativistic, charged particle with a magnetic field with strength  $B$ . For an electron with energy  $E$ , mass  $m_e$  and charge  $e$ , the rate at which electrons lose energy to synchrotron emission is:

$$\left(\frac{dE}{dt}\right)_{syn} = -\frac{4}{3}c\sigma_T\beta^2\gamma^2U_B, \quad (1.45)$$

where  $c$  is the speed of light,  $\sigma_T = \frac{8}{3}\pi r_e^2$  is the Thomson cross section where  $r_e$  is the classical electron radius<sup>15</sup>,  $\beta \equiv v/c$ ,  $\gamma$  is the Lorentz factor and  $U_B = B^2/8\pi$  is the energy density of the magnetic field (Pacholczyk, 1970; Reynolds, 2008).

The frequency ( $\nu$ ) at which an electron emits most strongly is described by:

$$\nu_c = \frac{3e}{4\pi m_e^3 c^4} \sin\theta E^2 B, \quad (1.46)$$

where  $\theta$  is the pitch angle<sup>16</sup> of the electron (Pacholczyk, 1970). This corresponds to a typical frequency of  $\nu_c \sim 1.5$  GHz for electrons with an energy of 1 GeV and  $\nu_c \sim 3.75 \times 10^9$  GHz, or  $E = h\nu_c \sim 15$  keV for electrons with an energy of 50 TeV, assuming a magnetic field of 100  $\mu$ G.

The synchrotron spectrum of a powerlaw distribution of electrons described by  $N(E)dE \propto E^{-\delta}dE$ , where  $\delta$  is the particle distribution index, is:

$$\epsilon_\nu d\nu = -\left(\frac{dE}{dt}\right)_{syn} N(E)dE, \quad (1.47)$$

where  $\epsilon_\nu$  is the synchrotron emissivity (Pacholczyk, 1970). Integrating over  $E$  yields:

$$\epsilon_\nu \propto B^{\frac{\delta+1}{2}} \nu^\Gamma \quad (1.48)$$

where  $\Gamma = \frac{1-\delta}{2}$  is the synchrotron photon index. For a constant magnetic field, Equation 1.48 becomes a simple power law  $\epsilon_\nu \propto \nu^\Gamma$ . DSA predicts  $\delta = 2$  for a non-relativistic, mono-atomic gas with  $\gamma = 5/3$  (see Equation 1.41), which corresponds to a synchrotron emission index of 0.5, which is consistent with the radio spectral index of SNRs (Green, 2014).

To produce synchrotron radiation emission, the ratio of the total energy density of CRs,  $U_{CR} = (1 + \kappa)U_e$ , to the total energy density of the magnetic field  $U_B$ , where  $U_e \propto B^{-3/2}$ , and  $U_B \propto B^2$  is equal to

$$\frac{(1 + \kappa)U_e}{U_B} = \frac{4}{3}. \quad (1.49)$$

This corresponds to the condition in which the total energy ( $U_{total} = (1-\kappa)U_e + U_B$ ) is minimised. The energy in relativistic particles in which this relation holds is

$$E_{min} \sim C(1 + \kappa)^{4/7} V^{3/7} L_{syn}^{4/7}, \quad (1.50)$$

where  $\kappa$  is the ion to electron energy ratio,  $L_{syn}$  is the synchrotron luminosity and  $C$  is a function dependent on energy, electron charge, speed of light and the mass of the electron in Gaussian cgs units (near page 171 of Pacholczyk 1970). The corresponding energy in the magnetic field in which this condition holds is

$$B_{min} \sim (D(1 + \kappa)L_{syn})^{2/7} V^{-2/7}, \quad (1.51)$$

<sup>15</sup>The classical radius of the electron is defined as  $r_e = \frac{e^2}{m_e c^2}$ .

<sup>16</sup>The pitch angle is the angle between the particle's velocity vector and the magnetic field.

where  $D$  is a function similar to  $C$  (see pg. 171 of [Pacholczyk 1970](#)).

The synchrotron lifetime of a source is defined by ([Gaisser et al., 1998](#))

$$\tau \sim 1.3 \times 10^{10} \left( \frac{B}{1 \mu\text{G}} \right)^{-2} \left( \frac{E}{1 \text{ GeV}} \right)^{-1} \text{ yr.} \quad (1.52)$$

For electrons with an energy of 1 GeV, interacting in an average ISM magnetic field of about 3  $\mu\text{G}$ , the synchrotron lifetime is approximately  $1.4 \times 10^9$  years, while for an electron with energy of 100 TeV, the synchrotron lifetime is about  $1.4 \times 10^4$  years.

### Inverse Compton scattering

Inverse Compton scattering arises from the interaction of a relativistic electron with a low energy photon (seed photon) in the background radiation fields. This scattering will transfer some of the energy of the electron to the photon, producing a photon whose final energy is larger than its initial energy. For SNRs, the dominant radiation field which provides the seed photons is the cosmic microwave background, while contributions from starlight and infra-red sources are no more than about 10%. This scattering process results in  $\gamma$ -ray emission up to tens of TeV and its cross section is determined by the energies of the interacting photon ( $E_\gamma$ ) and electron ( $E_e$ ).

The total cross-section of IC scattering is given by:

$$\sigma_{IC} = \frac{3\sigma_T}{8\kappa} \left[ \left( 1 - \frac{2}{\kappa} - \frac{2}{\kappa^2} \right) \ln(1 + 2\kappa) + \frac{1}{2} + \frac{4}{\kappa} - \frac{1}{2(1 + 2\kappa)^2} \right], \quad (1.53)$$

where  $\kappa = E_\gamma/E_e$ , and  $\sigma_T = \frac{8\pi}{3} \left( \frac{e^2}{m_e c^2} \right)^2 \sim 6.7 \times 10^{-25} \text{ cm}^{-2}$  is the Thomson cross section ([Coppi & Blandford, 1990](#)). In the non-relativistic Thomson regime, where  $E_e \gg E_\gamma$  in the rest frame of the electron, the cross-section reduces to  $\sigma_{IC} \sim \sigma_T(1 - 2\kappa)$ , while in the ultra-relativistic Klein-Nishina regime where  $E_e \ll E_\gamma$ , the cross-section becomes  $\sigma_{IC} \sim (3/8)\sigma_T\kappa^{-1} \ln(4\kappa)$  ([Aharonian, 2004](#)).

The energy loss experienced by the electron (or another way to look at it is the net gain of energy by the seed photon) due to IC in the Thomson regime is described by

$$\left( \frac{dE}{dt} \right)_{IC} = -\frac{4}{3} c \sigma_T \beta^2 \gamma^2 U_\gamma \quad (1.54)$$

where  $U_\gamma$  is the energy density of the photon field which the electron upscatters. In the Klein-Nishina regime, Equation 1.54 becomes

$$\left( \frac{dE}{dt} \right)_{IC} = -\frac{3}{8} \frac{\sigma_T c U_\gamma}{E_\gamma} \left( \ln(4\kappa) - \frac{11}{6} \right). \quad (1.55)$$

For a powerlaw distribution of electrons described by  $N(E)dE \propto E^{-\delta}dE$ , the IC spectrum in the Thomson regime is  $\propto E^{-\Gamma} \equiv E^{-(1+\delta)/2}$  ([Ginzburg & Syrovatskii, 1964](#)), while in the Klein-Nishina region it is  $\propto (E_\gamma/E_e)^{-\Gamma} (\ln(4E_e^2)) \equiv (E_\gamma/E_e)^{-(1+\delta)/2} (\ln(4E_e^2))$  ([Blumenthal & Gould, 1970](#)).

### Non-thermal Bremsstrahlung

Bremsstrahlung emission arises when a charged particle, such as an electron is decelerated due to it being deflected by the Coulomb field of a neighbouring charged particle. The Bremsstrahlung cross-section for an electron with energy  $E$  is given by:

$$\sigma_{brem} = \frac{3\alpha\sigma_T}{8\pi} \left[ \left[ 1 + \left( 1 - \frac{E_\gamma}{E_e} \right)^2 \right] \phi_1 - \frac{2}{3} \left( 1 - \frac{E_\gamma}{E_e} \right) \phi_2 \right] \quad (1.56)$$

where  $\sigma_T$  is the Thomson cross-section,  $\alpha$  is the fine structure constant,  $\phi_1, \phi_2$  are energy dependent-scattering functions,  $E_\gamma$  is the energy of the emitted photon and  $E_e$  is the energy of the relativistic electron (Bethe & Heitler, 1934; Schlickeiser, 2002; Stanev, 2010). For an unshielded charge,  $\phi_1 = \phi_2 = Z^2\phi$ , where  $Z$  is the atomic number of the atom that the electron is interacting with and  $\phi = 4(\ln[\frac{2E_e}{mc^2}(\frac{E_e - E_\gamma}{E_\gamma})] - \frac{1}{2})$ .

The energy loss experienced by an electron due to Bremsstrahlung emission was derived by Bethe & Heitler (1934) and is given by

$$\left( \frac{dE}{dt} \right)_{Brem} = \frac{4nZ}{A} \alpha r_e^2 E \left[ \ln \left( \frac{191}{Z^{1/3}} + \frac{1}{18} \right) \right] \quad (1.57)$$

where  $n$  is the number density of the ambient gas, and  $A$  is the mass number of the atom that the electron is interacting with. The lifetime of electrons undergoing bremsstrahlung is given by

$$\tau_{brem} = -E \left( \frac{dt}{dE} \right)_{Brem} \quad (1.58)$$

where  $(dt/dE)_{Brem}$  is the inverse of Equation 1.57. Assuming that the electron is being decelerated by the Coulomb field of a hydrogen atom, the cooling time becomes (Aharonian, 2004)

$$\tau_{brem} \sim 4 \times 10^7 \left( \frac{n}{1 \text{ cm}^{-3}} \right) \text{ yrs.} \quad (1.59)$$

As  $\tau_{brem}$  is independent of the energy of the electron or emitted photon, this implies that Bremsstrahlung does not change the original electron spectrum. Thus for a powerlaw distribution of electrons as described previously, the corresponding Bremsstrahlung spectrum  $\propto E_\gamma^{-\Gamma}$ , where  $\Gamma = \delta$  (Gaisser et al., 1998).

### Neutral Pion Decay

Through inelastic collisions with molecular material, accelerated protons will produce a neutral pion ( $\pi^0$ ) (as well as other mesons) that will subsequently decay into two  $\gamma$ -ray photons. To be able to produce a  $\pi^0$ , the protons involved in

the interaction must have a minimum energy of  $E_{min} = m_p c^2 (1 + 2m_\pi/m_p + m_\pi^2/2m_p^2) \sim 1.2$  GeV.

For energies ( $E_p - m_p c^2$ ) greater than 1 GeV, the inelastic proton-proton cross section can be approximated by:

$$\sigma_{pp}(E_p) \sim 30 \left[ 0.95 + 0.06 \ln \left( \frac{E_p - m_p c^2}{1 \text{ GeV}} \right) \right] \text{mb}, \quad (1.60)$$

where  $E_p = \gamma m_p c^2$  is the energy of the proton,  $m_p$  is the mass of the proton, and  $1 \text{ mb} = 10^{-27} \text{ cm}^2$  (Aharonian & Atoyan, 2000).

The spectrum of secondary particles generated from a proton-proton collision is defined by

$$q_{\pi^0} = \frac{cn}{f_\pi} \sigma_{pp}(\mathcal{E}) N_p(\mathcal{E}) \quad (1.61)$$

where  $\mathcal{E} = (m_p c^2 + \frac{E_\pi}{f_\pi})$ ,  $f_\pi$  is the fraction of the proton kinetic energy ( $E_p - m_p c^2$ ) that is transferred to a  $\pi^0$  during the collision (coefficient of inelasticity), and  $N_p$  is the energy distribution of protons. The corresponding spectrum of  $\gamma$ -rays that are produced from the decay of  $\pi^0$  is:

$$q_\gamma = 2 \int_{E_{min}}^{\infty} \frac{q_{\pi^0}}{\sqrt{E_\pi^2 - m_\pi^2 c^4}} dE_\pi, \quad (1.62)$$

where the minimum proton energy to produce a photon with energy,  $E_\gamma$ , is  $E_{min} = E_\gamma + (m_{\pi^0}^2 c^4)/4E_\gamma$  (Dermer, 1986). Assuming that the  $\pi^0$  decays isotropically, the resulting  $\gamma$ -ray spectrum will be symmetric around  $m_\pi/2 = 68$  MeV.

Relativistic protons have a characteristic cooling time of:

$$\tau_{pp} = \frac{1}{n \sigma_{pp} f c} \sim 6 \times 10^7 \left( \frac{n}{1 \text{ cm}^{-3}} \right)^{-1} \text{yr} \quad (1.63)$$

where  $n$  is the density of the ambient medium (Aharonian & Atoyan, 1996). One can see that the lifetime of the protons is independent of energy, thus the  $\gamma$ -ray spectrum observed from  $\pi^0$  decay has the same energy spectrum as the original proton spectrum above the minimum energy. Thus for a powerlaw distribution of protons described by  $N(E)dE \propto E^{-\delta} dE$ , the corresponding  $\gamma$ -ray spectrum arising from the  $\pi^0$  decay is  $\propto E_\gamma^{-\Gamma}$ , where  $\Gamma = \delta$  (Hinton & Hofmann, 2009).

## 1.5 Observational signatures of SNRs interacting with their surroundings

As discussed in Section 1.1, supernova remnants that result from core-collapse SNe are often born in regions with dense molecular clouds (MCs). The interaction of an SNR with a molecular cloud can significantly affect the evolution and emission of these objects. In addition, the interaction of an SNR shock-front with dense

molecular material can reveal the presence of energetic particles being accelerated at the shock. These remnants are ideal, indirect laboratories that one can use to detect and analyse  $\gamma$ -rays arising from  $\pi^0$  decay (Section 1.4.3), as this emission can be significantly enhanced in these environments. The interaction of the SNR's shockwave with dense molecular material can be inferred from a number of observational signatures such as hydroxyl (OH) maser emission, excitation line ratios, broad molecular lines, HI and radiative shocks (see Slane et al., 2014 and reference therein).

### 1.5.1 Maser emission

The word maser stands for “microwave amplification of simulated emission of radiation” and is a naturally occurring source of stimulated<sup>17</sup>, monochromatic line emission. The frequency of a maser arises from the difference in two energy levels of an atomic species that has been pumped such that a population inversion<sup>18</sup> has occurred.

The most direct tracer of an SNR shock-front interacting with a molecular cloud is the detection of a Hydroxyl 1720 MHz maser (Frail et al., 1994, 1996), and currently about 10% of the known Galactic SNRs have an OH maser (Brogan et al., 2013). To form the OH maser, one requires temperatures of 50 – 125 Kelvin, densities of  $n = 10^3 - 10^5 \text{ cm}^{-3}$  and an OH column density of  $10^{16} - 10^{17} \text{ cm}^{-2}$  (Lockett et al., 1999). The population inversion required to produce the OH maser line is maintained by the shock-front of the SNR colliding with molecular hydrogen ( $H_2$ ), as well as X-ray emission from the SNR or CRs being accelerated at the shock front (Wardle, 1999). These masers are coincident with regions of high density or where there are other indications of shock interaction. They have narrow, simple line profiles, low magnetic field strength and a low polarisation (Brogan et al., 2013). As the conditions for forming an OH maser are so strict, the absence of an OH maser does not indicate that there is no SNR/MC interaction.

Apart from OH masers, the methanol ( $\text{CH}_3\text{OH}$ ) molecule can be collisionally pumped producing a number of bright maser transitions at 36.169 GHz, and 44.070 GHz, with weaker emission at 84.521 GHz and 95.169 GHz (Frail 2011, Pihlström et al. 2014 and references there within). These masers are excited over densities of  $n = 10^5 - 10^6 \text{ cm}^{-3}$  and temperatures of 80 – 200 Kelvin, which is a much wider range than the OH maser. As a consequence,  $\text{CH}_3\text{OH}$  masers could be produced much closer to the molecular shock front. Pihlström et al. (2014) performed a targeted search for methanol masers in a sample of Galactic SNRs known to have

---

<sup>17</sup>Simulated emission arises when an incoming photon with a frequency  $\nu$  interacts with an excited atom, causing it to transition to a lower energy state. This interaction produces a photon that has the same properties (frequency, direction etc.) as the incoming photon.

<sup>18</sup>A population inversion occurs when the the number of particles in the excited state  $n + 1$  is greater than the number of particles in the less excited state  $n$ .

OH masers. They discovered multiple CH<sub>3</sub>OH masers in G1.4-0.1 and W28, but due to the limited angular coverage of the VLA observations, they were unable to determine whether CH<sub>3</sub>OH masers are better tracers of SNR/MC interaction compared to OH masers.

### 1.5.2 Line and molecular emission

As a shock propagates into a high density region, the post-shocked gas will cool and radiate primarily via infra-red, UV, and optical line emission. The type of emission is dependent on the type of shock (Raymond, 1979; Hollenbach & McKee, 1989). Emission generated by a continuous shock (C-type) will be composed of entirely IR emission lines such as the vibrational or rotational transitions of H<sub>2</sub>, carbon monoxide (CO) and water (H<sub>2</sub>O). These transitions will occur in weakly ionised molecular gas, whose shock is travelling less than 40 – 50 km s<sup>-1</sup>. For a discontinuous shock (J-type), the emission will be dominated by visible lines from transitions such as [O II], [N II] and [S II] and a few strong infra-red lines such as [O I] (63 μm), [Fe II] (26 μm), [C II] (157.7 μm). These transitions will be found behind the shock front of the remnant and are produced predominantly in ionised or neutral atomic gas that have fast shocks ( $\nu_s > 40 - 50 \text{ km s}^{-1}$ ). SNR IC443 has strong line emission from multiple transitions, highlighting that the shock-front of the SNR is interacting with its surrounding environment (see Slane et al. 2014 and references there within for more details).

In addition, the detection of molecular line broadening or asymmetric profiles of enhancement of excitation line ratios such as <sup>12</sup>CO(J = 2 → 1)/<sup>12</sup>CO(J = 1 → 0) provide evidence of shock-interaction (Seta et al. 1998, Slane et al. 2014 and references).

Apart from providing evidence in favour of the SNR shock-front interacting with surrounding material, studying maser and line emission also provides an independent estimation of the kinetic distance to the molecular cloud and thus the SNR that it is interacting with. In addition, masers provide a means of estimating the strength of the magnetic field in a SNR (Brogan et al., 2000).

## 1.6 Thesis outline

The research presented in this thesis uses and builds on the current knowledge presented in this chapter, with the aim of attempting to shed light on the intimate connection between CRs, the non-thermal emission arising from SNRs interacting with MCs and PWNe; as well as analysing the observational and evolutionary properties of these objects. These studies were completed using the imaging and spectral capabilities of the X-ray satellites *Chandra X-ray Observatory*, *XMM-Newton*, and *Suzaku*, as well as the  $\gamma$ -ray satellite the *Fermi Gamma-ray Space*

*Telescope*. In addition, theoretical models for the non-thermal emission produced by the shock-front of an SNR, the propagation of CRs through the Galaxy as well as models for the X-ray emission from SNRs and PWNe, were used to shed light on the properties of these objects.

In the following chapters I present four published works associated with understanding the origin, propagation and emission of CRs, as well as the properties of the astrophysical objects that accelerate these particles. Each chapter begins with a brief introduction that gives the context of the paper, a declaration of my contribution to the published works as well as the contribution of co-authors, and then the published work itself. In my final chapter, I summarise the results of the previous chapters and highlight potential avenues for future work associated with this research topic. Accompanying these chapters are two Appendices which give more detail related to Bayesian Inference, as well as solving the CR transport equation which models how CRs diffuse through our Galaxy.

---

# Extracting the size of the cosmic electron-positron anomaly

---

*Extracting the size of the cosmic electron-positron anomaly*

Katie Auchettl, Csaba Balázs

Published in ApJ, 749 (2012) 184

DOI: 10.1088/1742-6596/384/1/012016

e-Print: [arXiv:1106.4136](https://arxiv.org/abs/1106.4136) [astro-ph]

---

---

***The cosmic  $e^\pm$  anomaly***

(Conference version A)

*Not reproduced here due to close similarity to paper*

Katie Auchettl, Csaba Balázs.

Published in Proceedings of the Bled Workshops in Physics 12 (2011) 2, 1

Conference: C11-07-11.4

*XIV Workshop ‘What Comes Beyond the Standard Models’*

e-Print: [arXiv:1306.4704](https://arxiv.org/abs/1306.4704) [hep-ph]

---

***The status of the  $e^\pm$  cosmic-ray anomaly***

(Conference version B)

*Not reproduced here due to close similarity to paper*

Katie Auchettl, Csaba Balázs.

Published in J. Phys.: Conf. Ser. 384, 012016,

Conference: C11-09-26.2

*35<sup>th</sup> International Conference on High Energy Physics*

DOI: [10.1088/1742-6596/384/1/012016](https://doi.org/10.1088/1742-6596/384/1/012016)

---

***The  $e^\pm$  cosmic-ray anomaly***

(Conference version C)

*Not reproduced here due to close similarity to paper*

Csaba Balázs, Katie Auchettl

Published in PoS ICHEP2012 (2013) 431

Conference: C11-09-26.2

*35<sup>th</sup> International Conference on High Energy Physics*

---

***Uncertainties in Dark Matter Indirect Detection***

(Book chapter)

*Not reproduced here due to close similarity to paper*

Katie Auchettl, Csaba Balázs.

Published in Open Questions in Cosmology

ISBN: 978-953-51-0880-1

DOI: [10.5772/52052](https://doi.org/10.5772/52052)

---

## 2.1 Introductory remarks

Cosmic rays provide a unique and powerful way to probe some of the highest energy processes in our Galaxy. Measuring the fluxes of these particles allows us to gain insight into the nature of particle production in different astrophysical phenomena such as supernova remnants, pulsars or dark matter, while also allowing us to study how cosmic rays propagate through the Galaxy. Experiments such as *ATIC* (Chang et al., 2008), *PAMELA* (Adriani et al., 2009b,a), *AMS-02* (Aguilar et al., 2013) and the *Fermi-LAT* (Abdo et al., 2009b; Ackermann et al., 2010), have established that the flux of cosmic-ray electrons and positrons cannot be explained by assuming conventional cosmic ray propagation physics. This has led to a myriad of models in an attempt to explain this discrepancy ranging from the modification of the cosmic-ray propagation to requiring an extra injection spectrum of electrons and positrons. However, the existence, statistical significance, and the properties of this discrepancy is dependent on the theoretical prediction and uncertainty of the cosmic-ray background. As the origin and physics of cosmic ray diffusion is not well understood, this makes estimating the cosmic ray background challenging due to the large number of free or unconstrained parameters in our propagation models. A large number of models found in the literature, which attempt to explain this electron positron anomaly overlook this fact and use a description of the cosmic-ray background that has no uncertainties.

In this paper, we attempt to characterise the cosmic-ray background with uncertainties and establish whether there exists a statistically significant anomalous contribution to the electron/positron fluxes measured at Earth. We do this by establishing which parameters in the cosmic ray propagation model has the greatest influence on the flux of electrons and positrons. Using cosmic-ray data from a number of different experiments, we perform a Bayesian analysis to determine the one sigma credibility regions of the relevant propagation parameters. Based on these credibility regions, we predict the cosmic-ray background with uncertainties. Subtracting this background prediction from the *Fermi-LAT* electron-positron sum and *PAMELA* positron fraction, we isolate and characterise the anomalous contribution to the electron positron flux. We briefly compare this model-independent result to some theoretical models of the anomaly.

Our method for tackling this problem is described in Section 3 of paper that is shown overleaf, while our results are presented in Section 4. Figure 2 highlights the one sigma credibility regions of the propagation parameters that affect the electron/positron flux the most, while Figure 3 presents our estimate of the cosmic ray background with uncertainties and the size and shape of the cosmic ray anomaly.

## 2.2 Declaration for thesis chapter 2

### Declaration by candidate

In the case of the paper(s) contained in Chapter 2, the nature and extent of my contribution to the work was the following:

<b>Paper</b>	<b>Nature of contribution</b>	<b>Extent of contribution (%)</b>
I	Wrote a majority of the code needed to randomly sample the parameter space of the GALPROP program using the Monash sungrid cluster. Wrote some of the code needed to perform the Bayesian analysis. Performed the statistical analysis and interpretation of the results. Wrote majority of the paper.	85%
I(a)	As above; contributed to writing the proceedings.	75%
I(b)	As above; contributed to writing the proceedings.	75%
I(c)	As above; did not contribute to writing the proceedings.	60%
I(d)	As above; co-wrote book chapter	60%

The following co-authors contributed to the work. If co-authors are students at Monash University, the extent of their contribution in percentage terms is stated:

<b>Name</b>	<b>Nature of contribution</b>	<b>Extent of contribution (%)</b>
Csaba Balázs	Contributed to the initial idea, discussions and code related to Bayesian analysis; provided guidance in interpreting results; provided supervisory advice; contributed to paper write up. Where applicable, wrote or contributed to the writing of the conference proceedings and book chapter.	

The undersigned hereby certify that the above declaration correctly reflects the nature and extent of the candidate's and co-authors' contributions to this work.

**Signatures:**

Katie Auchetl:



Date: 15th June 2015

Patrick Slane:



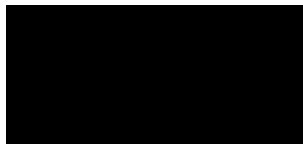
Date: 15th June 2015

Csaba Balázs:



Date: 15th June 2015

Jasmina Lazendic-Galloway:



Date: 15th June 2015

## 2.3 Published material: Paper I

Begins overleaf.

## EXTRACTING THE SIZE OF THE COSMIC ELECTRON–POSITRON ANOMALY

KATIE AUCHETTL<sup>1,2</sup> AND CSABA BALÁZS<sup>1,2</sup>

School of Physics, Monash University, Melbourne, Victoria 3800, Australia  
Received 2011 May 30; accepted 2012 February 11; published 2012 April 5

### ABSTRACT

We isolated the anomalous part of the cosmic electron–positron flux within a Bayesian likelihood analysis. Using 219 recent cosmic-ray spectral data points, we inferred the values of selected cosmic-ray propagation parameters. In the context of the propagation model coded in GalProp, we found a significant tension between the electron–positron related and the rest of the fluxes. Interpreting this tension as the presence of an anomalous component in the electron–positron related data, we calculated background predictions for *PAMELA* and *Fermi*-LAT based on the non-electron–positron related fluxes. We found a deviation between the data and the predicted background even when uncertainties, including systematics, were taken into account. We identified this deviation with the anomalous electron–positron contribution. We briefly compared this model-independent signal to some theoretical results predicting such an anomaly.

*Key words:* astroparticle physics – cosmic rays – diffusion – Galaxy: general – ISM: general – methods: statistical

*Online-only material:* color figures

### 1. INTRODUCTION

Over the last few decades observations of cosmic rays established an increasingly significant and puzzling deviation from theoretical predictions. Several experiments, such as TS (Golden et al. 1994), AMS (Alcaraz et al. 2000), CAPRICE (Boezio et al. 2001), MASS (Grimani et al. 2002), and HEAT (Barwick et al. 1997; Beatty et al. 2004), provided a hint of an excess of high-energy positrons in our locality. Recent measurements of the *PAMELA* satellite confirmed these suspicions by establishing an excess in the positron fraction over the theoretical predictions for energies above 10 GeV (Adriani et al. 2009). The *PAMELA* data appear to significantly deviate from the background predictions even when sizeable experimental and theoretical uncertainties are taken into account (Delahaye et al. 2009b, 2010, 2011; Mertsch 2010).

A possible excess in the electron–positron sum was also indicated by AMS (Aguilar et al. 2002), PPB-BETS (Torii et al. 2008), and HESS (Aharonian et al. 2008, 2009). The exceptionally precise measurement of the local electron+positron flux by the *Fermi*-LAT satellite, at first glance, seems to partially confirm the electron+positron excess above 100 GeV (Ackermann et al. 2010). The deviation between the *Fermi*-LAT data (especially the 2010 release) and the theoretical background calculation produced by the numerical code GalProp by Strong & Moskalenko (1998) appears to be significant. These results were recently confirmed by the *PAMELA* collaboration, which measured the cosmic-ray electron flux in a similar energy range and found it to be consistent with the *Fermi*-LAT data.

The deviation between the measurements and the predicted backgrounds prompted numerous attempts to explain it by invoking new physics ranging from modification of the cosmic-ray propagation (Stawarz et al. 2010; Cowsik & Burch 2009; Katz et al. 2009; Blasi 2009; Hu et al. 2009; Dado & Dar 2010; Perelstein & Shakya 2010, 2011), through supernova remnants (Ahlens et al. 2009; Shaviv et al. 2009; Fujita et al. 2009; Hooper et al. 2009a, 2009b; Yuksel et al. 2009; Profumo

2011; Malyshev et al. 2009; Barger et al. 2009; Grasso et al. 2009; Mertsch & Sarkar 2009; Malyshev 2009), to dark matter annihilation (Cirelli et al. 2009; Arkani-Hamed et al. 2009; Cholis et al. 2009; Harnik & Kribs 2009; Allahverdi et al. 2009; Calmet & Majee 2009; Shirai et al. 2009, 2010; Chen et al. 2009, 2010; Hamaguchi et al. 2009a, 2009b; Okada & Yamada 2009; Fukuoka et al. 2009; Bai et al. 2009; Chen 2009; Mardon et al. 2009; Demir et al. 2010; Hooper & Tait 2009; Choi & Yaguna 2010; Feldman et al. 2009a, 2009b; Yin et al. 2009; Ibarra & Tran 2009; Nardi et al. 2009; Ishiwata et al. 2009; De Lope Amigo et al. 2009; Arvanitaki et al. 2009; Buchmuller et al. 2009; Ibarra et al. 2010; He 2009; Brun et al. 2009; Ibe et al. 2009; Guo & Wu 2009; Bi et al. 2009; Hisano et al. 2005; March-Russell et al. 2008; Dent et al. 2010; Zavala et al. 2010; Feng et al. 2010; Backovic & Ralston 2010). Serpico (2011) summarizes the present situation of these speculations.

The existence and statistical severity of the electron–positron anomaly depend on the theoretical prediction of the cosmic-ray background. While the origin of the cosmic rays is not fully understood, their local observation, coupled with other astrophysical measurements, enables us to build and constrain a model of particle production and propagation in our Galaxy. Such a model is based on the relatively well understood features of particle diffusion within the Milky Way. The diffusion is described by the transport equation, subject to an initial source distribution and boundary conditions. The local electron and positron fluxes are calculated by solving this transport equation. Besides the lack of precise knowledge of the cosmic-ray sources, the background prediction is challenging because the propagation model has numerous free parameters, such as the convection velocities, spatial diffusion coefficients, or momentum loss rates.

Motivated by possible new physics buried in the *Fermi*-LAT data, in this work we attempt to determine the size of the anomalous contribution in the cosmic electron–positron flux. Our strategy involves the following main steps:

1. Finding the cosmic-ray propagation parameters that influence the electron–positron flux measured by *Fermi*-LAT and *PAMELA* the most.
2. Subjecting cosmic-ray data, other than the *Fermi*-LAT and *PAMELA* electron–positron measurements, to a Bayesian

<sup>1</sup> Monash Centre for Astrophysics, Monash University, Victoria 3800, Australia.

<sup>2</sup> ARC Centre of Excellence for Particle Physics at the Tera-scale, Monash University, Victoria 3800, Australia.

likelihood analysis, to determine the 68% ( $1\sigma$ ) credibility regions of the relevant propagation parameters.

3. Calculating a background prediction, with uncertainties, for *Fermi*-LAT and *PAMELA*, based on the determined  $1\sigma$  credibility regions of the propagation parameters.
4. Subtracting the background prediction from the *Fermi*-LAT and *PAMELA* measurement to isolate the anomalous part of the spectrum.

Since in the process of the likelihood analysis we determine the uncertainty of the electron–positron background, we can also quantify the statistical significance of the deviation between the cosmic-ray data and the theoretical background calculation.

When contrasted with the earlier literature, our work contains two main novel results: (1) demonstration of a significant tension between the electron–positron related and the rest of the cosmic-ray data in the context of the propagation model coded in GalProp, and (2) the extraction of the anomalous part of the electron–positron flux. We were able to obtain these results because we use more data than other similar studies (Maurin et al. 2001, 2002, 2010; Putze et al. 2010; Lin et al. 2010; Trotta et al. 2011). We used the numerical code GalProp in the Bayesian framework, extending the analysis of Trotta et al. (2011) to quantify the uncertainty in the background contribution of cosmic-ray spectra. Unlike Lin et al. (2010), we do not use gamma-ray data because some components of the gamma-ray flux are thought to be affected by the same (or similar) anomalous contributions as the electron–positron flux. Leaving out the calculation of gamma-ray propagation also speeds up our numerical calculations. We decided to include gamma-ray data in our analysis at a later stage.

While the numerical analysis by Trotta et al. (2011) is very similar to ours, the choice of the free diffusion and nuisance parameters are different. More importantly, the use of substantially more experimental data (219 data points altogether compared to 76 in Trotta et al. 2011) enables us to constrain the background prediction well enough to isolate the anomalous part of the  $e^+e^-$  flux. The experimental data we use come from multiple instruments, over a wide energy range, as discussed in Section 3.3.

## 2. COSMIC-RAY PROPAGATION

Cosmic rays are highly energetic particles that have their origins locally and remotely in the visible universe (Ginzburg & Syrovatskii 1964; Blandford & Eichler 1987; Stawarz et al. 2010; Aharonian et al. 2011). They are divided into two main categories: primary and secondary. Primary cosmic rays are particles that are accelerated by astrophysical objects, such as supernova remnants. These cosmic rays interact with interstellar matter to create secondary cosmic rays (Blandford & Eichler 1987; Delahaye et al. 2009b; Nakamura et al. 2010; Aharonian et al. 2011). The majority of cosmic-ray electrons, for example, are likely to originate from supernova remnants, while cosmic-ray positrons are believed to be mainly produced via secondary production processes such as spallation and nucleosynthesis (Blandford & Eichler 1987; Adriani et al. 2009; Delahaye et al. 2009a; Nakamura et al. 2010; Aharonian et al. 2011).

Cosmic-ray propagation through the Galaxy is typically quantified using the diffusion model (Ginzburg et al. 1990; Schlickeiser 2002; Ptuskin et al. 2006; Strong et al. 2007). Diffusion of cosmic rays provides a simple explanation for the highly isotropic distribution of high-energy-charged particles and their noticeable retention in the Galaxy. Diffusion results from the

particle scattering of cosmic rays on random magnetohydrodynamic (MHD) waves and inhomogeneities in the Galactic magnetic field. The random nature of the Galactic magnetic field causes the trajectories of the cosmic rays to become jumbled, causing them to undergo a random walk in space (Ginzburg & Syrovatskii 1964; Strong et al. 2007; Cotta et al. 2011; Aharonian et al. 2011). The energy distribution of cosmic rays is modified by energy losses experienced by these particles as they propagate through the Galaxy. Energy losses arise due to the interaction of the cosmic rays with the interstellar medium (ISM) and interstellar radiation fields. Re-acceleration due to interstellar shocks and Galactic winds powered by convection also contribute (Strong & Moskalenko 1998; Strong et al. 2007; Fan et al. 2010), while for heavy and unstable nuclei, fragmentation processes also need to be taken into account.

The diffusion model assumes homogeneous propagation of charged particles within the Galactic disk (similar to one of the simplest models of propagation, called the leaky box model), but it also takes into account cooling effects. The density  $\psi(\vec{r}, p, t)$  (per unit particle momentum  $p$ ) of a particular cosmic-ray species at a Galactic radius of  $\vec{r}$  can be calculated solving the cosmic-ray transport equation, which has the general form (Strong et al. 2007)

$$\begin{aligned} \frac{\partial \psi(\vec{r}, p, t)}{\partial t} = & q(\vec{r}, p, t) + \vec{\nabla} \cdot (D_{xx} \vec{\nabla} \psi - \vec{V} \psi) \\ & + \frac{\partial}{\partial p} \left( p^2 D_{pp} \frac{\partial}{\partial p} \frac{1}{p^2} \psi \right) \\ & - \frac{\partial}{\partial p} \left( \dot{p} \psi - \frac{p}{3} (\vec{\nabla} \cdot \vec{V}) \psi \right) - \frac{1}{\tau_f} \psi - \frac{1}{\tau_r} \psi. \end{aligned} \quad (1)$$

Here  $q(\vec{r}, p, t)$  is the source term that depends on the production mechanism of primary and secondary cosmic-ray contributions. The spatial diffusion coefficient  $D_{xx}$  describes the scattering of cosmic-ray species through turbulent magnetic fields. This propagation can be isotropic or anisotropic and can be influenced by the cosmic rays themselves (Strong et al. 2007). Generally,  $D_{xx}$  has the form

$$D_{xx} = D_{0xx} \beta \left( \frac{R}{\text{GeV}} \right)^\delta, \quad (2)$$

where  $\beta = v/c$  and  $R = pc/eZ$  is the magnetic rigidity of the particles that describes a particle's resistance to deflection by a magnetic field. Here,  $Z$  is the effective nuclear charge of the particle,  $v$  is its velocity,  $p$  is its momentum,  $e$  is its charge, and  $c$  is the speed of light. The energy of high-momentum cosmic-ray electrons and positrons, for example, can be approximated by  $E \simeq eR$  (Hillas 1984). The constant exponent  $\delta$  indicates the power-law dependence of the spatial diffusion coefficient  $D_{xx}$ . Different regions of the energy spectra can have different  $\delta$  values, producing a discontinuity in the derivative of  $D_{xx}$ . This artificial kink is introduced so that one can fit the B/C ratio data over all energies (Strong & Moskalenko 1998).

In Equation (1),  $\vec{V}$  describes the convection velocity, which is a function of Galactic radius  $r$  and depends on the characteristics of the Galactic winds. The convection velocity is assumed to have a cylindrical symmetry and increase linearly with height  $z$  from the Galactic plane. Apart from transporting particles through the Galaxy, convection also causes the adiabatic energy losses (or gains) of cosmic rays due to their interaction with the

non-uniform flow of gas (Galactic winds) with an inhomogeneous magnetic field. This is represented by the term  $\vec{\nabla} \cdot \vec{V}$ .

Diffusion in momentum space (diffusive re-acceleration) is described by the coefficient  $D_{pp}$ . This arises from the scattering of cosmic-ray particles on randomly moving MHD waves. Diffusion in momentum is related to spatial diffusion via

$$D_{pp}D_{xx} = \frac{4p^2v_A^2}{3\delta(4-\delta^2)(4-\delta)w}. \quad (3)$$

Here,  $v_A$  is the Alfvén speed, and the parameter  $w$  characterizes the level of hydromagnetic turbulence experienced by the cosmic rays in the ISM (Seo & Ptuskin 1994). This parameter is also known as the ratio of MHD energy density to the magnetic field energy density. In the last two terms of Equation (1) the parameter  $\tau_f$  is the timescale of the fragmentation loss and  $\tau_r$  is the radioactive decay timescale.

Observations of galaxies other than ours suggest that cosmic rays are diffusing in a cylindrical slab, whose height is dependent on the Galaxy itself (Delahaye et al. 2009a). Consequently, the transport equation (generalized and simplified) is solved in a diffusive region shaped as a solid flat cylinder. This cylinder, parameterized by the coordinates  $(\vec{r}, \phi, z)$ , encloses the Galactic plane with height  $2L$  in the  $z$ -direction ( $z \in [-L, L]$ ) and a radius of  $R = 20$  kpc in the  $\vec{r}$  direction. The solar system is located at  $(\vec{r}, \phi, z) = (8.5 \text{ kpc}, 0, 0)$ , while the boundary conditions imposed on this scenario allow the cosmic-ray density to vanish at the surface of the flat cylinder and particles may propagate freely outside it and escape. The rate of energy loss,  $b(E)$ , is determined by the photon density, strength of the magnetic field, and the Thomson scattering cross section associated with the cosmic rays.

To obtain an explicit analytic solution for a particular cosmic-ray species, it is possible to solve the simplified version of the transport equation, such as

$$\frac{\partial \psi(E, \vec{r})}{\partial t} = D_{xx} \nabla^2 \psi(E, \vec{r}) + \frac{\partial}{\partial E} [b(E)\psi(E, \vec{r})] + q(E, \vec{r}) \quad (4)$$

for electrons (Delahaye et al. 2008), using a Green's function method (Baltz & Edsjö 1998). However, in most cases that require a realistic description of the astrophysical environment that produces the experimentally observed cosmic-ray spectra, an analytical solution is not possible. Hence, a numerical solution is pursued.

The numerical Galactic cosmic-ray propagation package GalProp calculates the propagation of relativistic charged particles and their diffuse emission produced during their propagation through the Galaxy. GalProp solves the propagation equation numerically for  $Z \geq 1$  nuclei, as well as for electrons and positrons on a two-dimensional spatial grid with cylindrical symmetry in the Galaxy (Strong et al. 2007). It also has the capability of solving the diffusion equation in three dimensions. GalProp starts with the heaviest primary element defined by the user, and the propagated solution is used to compute the source term for the secondary products of this element. This process is continued until protons, secondary electrons, positrons, and anti-protons are produced and a steady-state solution is obtained. The cosmic-ray spectrum is used to compute the gamma rays and energy losses such as synchrotron radiation experienced by the cosmic rays. These are computed in conjunction with realistic maps of the interstellar gas distributions and radiation fields

based on current HI and CO surveys and detailed theoretical calculations of the Galactic magnetic field (Strong et al. 2007).

The input parameter file for GalProp has a number of free parameters that are available for the author to define. The main free parameters determine the geometry of the model (radius, height of cylinder, and grid spacing), the distribution of cosmic-ray sources (which is usually chosen to represent an even distribution of supernova remnants), the primary cosmic-ray spectral shape and the isotropic composition of the sources (Strong et al. 2007), and the spatial and momentum diffusion coefficients and their dependence on the particle rigidity (Grasso et al. 2009). These can be classified into a number of subsets: the diffusion of cosmic rays, the primary cosmic-ray sources, and radiative energy losses of these primary cosmic rays. The diffusion subset is described by the parameters defined above:

$$D_{0xx}, \delta, L, v_A, \partial \vec{V} / \partial z. \quad (5)$$

The most relevant parameters in the primary cosmic-ray source subset are

$$R_{\text{ref}}^{e^-}, \gamma^{e^-}, R_{\text{ref}}^{\text{nucleus}}, \gamma^{\text{nucleus}}. \quad (6)$$

Here,  $\gamma^{e^-}$  is the primary source electron injection index. This specifies the steepness of the electron injection spectrum,  $dq(p)/dp \propto p^{\gamma^{e^-}}$ , below a reference rigidity  $R_{\text{ref}}^{e^-}$ . There is also a separate injection index for nuclei defined by  $\gamma^{\text{nucleus}}$  above  $R_{\text{ref}}^{\text{nucleus}}$ . For further details we refer the reader to Strong et al. (2007).

### 3. BAYESIAN INFERENCE

Our aim is to isolate the anomalous part of the *Fermi*-LAT and *PAMELA* electron-positron fluxes. To do this, first we need to know the non-anomalous, standard astrophysical background contributing to *Fermi* and *PAMELA*. To extract this background and to determine its uncertainty, we use the cosmic-ray measurements, which appear to be consistent with the background estimates. First, we determine the values of the Galactic propagation parameters most favored by this part of the data and extract the uncertainties of these parameters. Then we use these parameter values to calculate the  $e^-$  and  $e^+$  background and its uncertainty and compare this to the measurements of *Fermi* and *PAMELA*. This way we are able to isolate the size and uncertainty of the contribution of the (possible) new source(s) in the electron-positron related fluxes.

To extract the values of the propagation parameters  $P = \{p_1, \dots, p_N\}$  favored by the experimental data  $D = \{d_1, \dots, d_M\}$ , we utilize Bayesian inference. In the Bayesian framework the probability density of a certain theoretical parameter  $p_i$  acquiring a given value is given by the marginalized posterior probability distribution

$$\mathcal{P}(p_i|D) = \int \mathcal{P}(P|D) \prod_{i \neq j=1}^N dp_j, \quad (7)$$

where the integral is carried out over the full range of the parameters. According to Bayes' theorem, the posterior probability density over the full parameter space is calculated as

$$\mathcal{P}(P|D) = \mathcal{L}(D|P) \frac{\mathcal{P}(P)}{\mathcal{E}(D)}. \quad (8)$$

Here, the likelihood function  $\mathcal{L}(D|P)$  is the conditional probability density of the theoretical predictions for the data with given parameter values  $P$ . Data-independent information on the parameter distribution is folded in via the prior distribution  $\mathcal{P}(P)$ , and the Bayesian evidence  $\mathcal{E}(D)$ , for our purposes, acts as a normalization factor.

The likelihood function, in our case, is calculated as

$$\mathcal{L}(D|P) = \prod_{i=1}^M \frac{1}{\sqrt{2\pi}\sigma_i} \exp(-\chi_i^2(D, P)/2), \quad (9)$$

where

$$\chi_i^2(D, P) = \left( \frac{d_i - t_i(P)}{\sigma_i} \right)^2. \quad (10)$$

The log-likelihood  $\chi_i^2$  contrasts the central value of the  $i$ th data point  $d_i$  with the theoretical prediction  $t_i$  for given parameter values  $P$ , in terms of the combined theoretical and experimental uncertainty  $\sigma_i$ .

For parameter estimation the Bayesian evidence only plays the role of an irrelevant normalization. Nevertheless, it is useful to calculate  $\mathcal{E}(D)$  when assessing the validity of the hypothesis quantified as the theory parameterized by  $P$ . The evidence is easily calculated using the normalization of the posterior density

$$\int \mathcal{P}(P|D) \prod_{j=1}^N dp_j = 1. \quad (11)$$

This enables us to recast Bayes' theorem in the integral form

$$\mathcal{E}(D) = \int \mathcal{L}(D|P) \mathcal{P}(P) \prod_{j=1}^N dp_j. \quad (12)$$

Once the posterior distribution is known, we can determine the credibility intervals for each of the parameters. We define a credibility region  $\mathcal{R}_x$  for parameter  $p_i$  by the collection of minimal-sized parameter regions supporting  $x\%$  of the total probability:

$$x = \int_{\mathcal{R}_x} \mathcal{P}(p_i|D) dp_i. \quad (13)$$

In plain terms, a 68% credibility interval is the minimal parameter region that contains 68% of the area under the posterior distribution. This region gives the value of the parameter at  $1\sigma$  certainty. Combined credibility regions over multi-dimensions of the parameter space can be similarly defined as the minimal region satisfying

$$x = \int_{\mathcal{R}_x} \mathcal{P}(p_i, p_j|D) dp_i dp_j. \quad (14)$$

### 3.1. Parameter Choice

The calculation of the posterior probability distributions  $\mathcal{P}(p_i|D)$  requires us to numerically integrate over the parameter region where the (cumulative) likelihood function is non-negligible. The CPU demand to reliably sample the posterior density depends on the number of free theoretical parameters  $N$  and the speed of the numerical implementation. In the case of the diffusion model encoded in GalProp the number of free input parameters is around a hundred, and for a given set of parameters

the code runs for several minutes on a single CPU. This makes it unfeasible to attempt the calculation of the posterior without simplifications.

Fortunately, both the number of relevant free parameters and the running time can be substantially reduced. To reduce the dimension of the parameter space, we tested the robustness of the electron–positron flux against the variation of nearly all individual parameters and found that it is mostly sensitive to the following propagation parameters:

$$P = \{\gamma^{e^-}, \gamma^{\text{nucleus}}, \delta_1, \delta_2, D_{0xx}\}. \quad (15)$$

Here,  $\gamma^{e^-}$  and  $\gamma^{\text{nucleus}}$  are the primary electron and nucleus injection indices parameterizing an injection spectrum without a break,  $\delta_1$  and  $\delta_2$  are spatial diffusion coefficients below and above a reference rigidity  $\rho_0$ , and  $D_{0xx}$  determines the normalization of the spatial diffusion coefficient.

We found that the electron–positron spectra are fairly insensitive to the rest of the parameters. We also found that the electron–positron spectrum is sensitive to not only the power-law dependence of the spatial diffusion coefficient  $D_{xx}$ , but the presence of a kink therein. So following Strong et al. (2004), we introduce two coefficients  $\delta_1$  and  $\delta_2$  that parameterize this power-law dependence in Equation (2) below and above a reference rigidity. We fix this reference rigidity to 4 GeV as in Strong et al. (2004).

Our calculations also confirmed the findings of a recent study by Cotta et al. (2011) that the electron–positron flux is sensitive to the change of the Galactic plane height  $L$ . Indeed, Seo & Ptuskin (1994) have shown that there is a connection between  $L$  and  $D_{0xx}$ :

$$D_{0xx} = \frac{2c(1-\delta)L^{1-\delta}}{3\pi w\delta(\delta+2)}. \quad (16)$$

Thus, varying the cylinder height amounts to the redefinition of  $D_{0xx}$  as also noticed by Di Bernardo et al. (2011b). In the light of this, we fix  $L$  to 4 kpc and use  $D_{0xx}$  as a free parameter.

We treat the normalizations of the  $e^-$ ,  $e^+$ ,  $\bar{p}/p$ , B/C, (SC+Ti+V)/Fe, and Be-10/Be-9 fluxes as theoretical nuisance parameters.

$$P_{\text{nuisance}} = \{\Phi_{e^-}^0, \Phi_{e^+}^0, \Phi_{\bar{p}/p}^0, \Phi_{B/C}^0, \Phi_{(SC+Ti+V)/Fe}^0, \Phi_{Be-10/Be-9}^0\}. \quad (17)$$

They are kept free because the electron–positron flux is either directly or indirectly sensitive to these parameters. On the other hand, prior information is available for these parameters, enabling us to reduce them to the nuisance level. Since GalProp calculates normalizations based on local cosmic-ray measurements, the results of this calculation can be used as a guideline to the central values of the nuisance parameters. The uncertainties of the normalizations can be reliably estimated by an initial scan over the full parameter space.<sup>3</sup>

Varying the parameters listed in Equations (15) and (17), we confirmed the result of Trotta et al. (2011) that the electron+positron flux of *Fermi*-LAT can be well reproduced by the theoretical calculation. We also found that by changing these parameters the theory can match well the latest *PAMELA* electron spectrum (Adriani et al. 2011) and the latest *PAMELA* positron

<sup>3</sup> During our analysis of  $e^\pm$  related or other data, we found that the posterior for  $\Phi_{e^\pm}^0$  prefers about 10% lower normalization than the value GalProp determines. Since these normalizations form part of our parameters in our plots, we use the posterior normalizations rather than the GalProp ones.

**Table 1**  
Cosmic-ray Experiments and Their Energy Ranges over which We Have Chosen the Data Points for Our Analysis

Measured Flux	Experiment	Energy (GeV)	Number of Data Points
$e^+ + e^-$	AMS (Aguilar et al. 2002)	0.60–0.91	3
	<i>Fermi</i> -LAT (Ackermann et al. 2010)	7.05–886	47
	HESS (Aharonian et al. 2008, 2009)	918–3480	9
$e^+/(e^+ + e^-)$	<i>PAMELA</i> (Adriani et al. 2010a)	1.65–82.40	16
$e^-$	<i>PAMELA</i> (Adriani et al. 2011)	1.11–491.4	39
Anti-proton/proton	<i>PAMELA</i> (Adriani et al. 2010b)	0.28–129	23
Boron/carbon	IMP8 (Moskalenko et al. 2002)	0.03–0.11	7
	ISEE3 (Krombel & Wiedenbeck 1988)	0.12–0.18	6
	Lezniak & Webber (1978)	0.30–0.50	2
	HEAO3 (Engelmann et al. 1990)	0.62–0.99	3
	<i>PAMELA</i> (et al. 2008)	1.24–72.36	8
	CREAM (Ahn et al. 2008)	91–1433	3
(Sc+Ti+V)/Fe	ACE (Davis et al. 2000)	0.14–35	20
	SANRIKU (Hareyama 1999)	46–460	6
Be-10/Be-9	Wiedenbeck & Greiner (1980)	0.003–0.029	3
	Garcia-Munoz et al. (1981)	0.034–0.034	1
	Wiedenbeck & Greiner (1980)	0.06–0.06	1
	ISOMAX98 (Hams et al. 2001)	0.08–0.08	1
	ACE-CRIS (Davis et al. 2000)	0.11–0.11	1
	ACE (Yanasak et al. 2001)	0.13–0.13	1
	AMS-02 (Burger 2004)	0.15–9.03	15

**Notes.** We split the data into two groups: electron–positron flux related (first five lines in the table) and the rest. We perform two independent Bayesian analyses to show the significant tension between the two data sets.

fraction data (Adriani et al. 2010a). (We defer the discussion of the quantitative details to the results section.) This demonstrates that varying the selected parameters gives us enough flexibility to fit all the observed features of the electron–positron spectra.

While the Galactic propagation of GeV or higher energy cosmic rays is relatively well understood, the propagation of a few GeV or lower energy electrons and positrons in the turbulent, magnetized ISM remains a formidable challenge (Prantzos et al. 2011). Local effects, such as solar modulation and the geomagnetic cutoff, significantly affect cosmic rays at lower energies (Pesce-Rollins & Fermi LAT Collaboration 2009). Since solar modulation effects, based on the force field model, are built into GalProp, we take these effects into account by varying the value of the modulation potential in the code. Following Gast & Schael (2009), we assume a charge-sign-dependent modulation, that is, positively and negatively charged cosmic rays are modulated differently by the Sun. Gast & Schael (2009) conclude that the effect of this charge-dependent modulation on (*PAMELA*) positrons is substantial. They also show that the modulation effect on the  $\bar{p}/p$  ratio is comparable to the statistical uncertainties. As described in the next section, we absorb this effect in the systematic uncertainties of the  $\bar{p}/p$  data. Heavier nuclei (B, C, Sc, Ti, V, Fe, and Be) can carry higher positive charges than that of the proton, but their charge-to-mass ratio is still lower. Since the modulation potential is proportional to the charge-to-mass ratio, the modulation effect on heavier nuclei is even milder. Considering that we use the ratio of their fluxes, most of the modulation effect cancels since they are positively charged. So the modulation effect on heavier nuclei can also be safely absorbed in the systematic uncertainties.

To be able to compare with experimental data, we set the positron (electron) modulation potential in GalProp to  $\phi^+ = 442$  (2) MV. These values were determined by Gast & Schael

(2009) for *PAMELA*. Usoskin et al. (2011) showed that the time dependence of the solar modulation potential is not substantial over the period of *PAMELA*’s data taking, and about the same average values can be used for *Fermi*-LAT. We set the rest of the GalProp parameters to the values promoted by Strong et al. (2004).

### 3.2. Statistical and Numerical Issues

In order to extract the most favored values of the propagation parameters, we have to calculate the posterior distribution  $\mathcal{P}(p_i|D)$  using suitable Bayesian priors  $\mathcal{P}(p_j)$ . Assuming no prior knowledge justifies the use of uniform priors. Since we have previous knowledge about the order of magnitude of our parameters, we use uniform priors for the propagation parameters (rather than for some functions, such as log, of them). For the nuisance parameters prior knowledge is available in the form of a scan over GalProp predictions that are based on local measurements of cosmic-ray fluxes different from those listed in Table 1. Thus, for our nuisance parameters we use normally distributed priors.

When evaluating  $\sigma_i$  for the log likelihood in Equation (10), following Trotta et al. (2011), we ignore theoretical uncertainties and combine statistical and systematic experimental uncertainties in quadrature

$$\sigma_i^2 = \sigma_{i,\text{statistical}}^2 + \sigma_{i,\text{systematic}}^2. \quad (18)$$

This can be done for *Fermi*-LAT and the latest *PAMELA*  $e^-$  flux. Unfortunately, systematic uncertainties are not available for the rest of the cosmic-ray measurements. When this is the case, as an estimate of the systematics, we define  $\sigma_i$  as the rescaled statistical uncertainty

$$\sigma_i^2 = \sigma_{i,\text{statistical}}^2 / \tau_i. \quad (19)$$

For simplicity, in this study, we use the same scale factor  $\tau_i$  for all data points where systematic uncertainty is not available. To remain mostly consistent with the work of Trotta et al. (2011), we set this common scale factor to a conservative value that they use:  $\tau_i = 0.2$ . We checked that our conclusions only mildly depend on this choice.

We note that systematic errors in the data are not necessarily normally distributed point-to-point errors. In fact, typically systematic errors are correlated, such as a systematic shift in the energy scale, and could be described by various probability distributions other than a Gaussian. Unfortunately, these probability distributions are not provided by even those experimental collaborations that indicate a confidence interval for their systematic errors. In the lack of this information, we use the simplest ansatz that is adopted by most authors in the literature. This estimate of the systematic errors is a simplified approximation of a more complicated situation. Nevertheless, for astrophysical data it captures the essence of systematic uncertainties. After all, the simplest cosmic-ray flux is a falling power-law spectrum. For this case a systematic shift in the energy scale, for example, can be re-interpreted as a systematic normalization shift of the spectrum. Part of this shift is absorbed by our normalization nuisance parameters, and part of it is approximated as Gaussian error.<sup>4</sup>

Due to the simplicity of the posterior density (Trotta et al. 2011) and its relatively low dimensionality, we sample the parameter space  $P$  and  $P_{\text{nuisance}}$  according to a simple algorithm. We select random model points from the parameter space according to a uniform distribution for  $P$  and normally distributed for  $P_{\text{nuisance}}$ . While this sampling technique is less efficient than the Monte Carlo based ones, it enables us to trivially parallelize the numerical calculation. It also allows us to simply check the robustness of our results against the change of certain assumptions such as the prior, the scale factor  $\tau$ , or the adequateness of the sampling.

The simplicity of the likelihood function and the high number of data points used in this analysis also make convergence testing relatively simple. To test the validity of our results, we can evaluate an approximate value of the posterior means, variances, and the evidence adopting the procedure described by Tierney & Kadane (1986). To assure the adequacy of the sampling, we can simply increase the number of samples of the posterior density until the numerically calculated evidence is within 5% of the one obtained by the Laplace method. During this procedure, we found that to extract the posterior probabilities presented in this paper about one million samples of the posterior density were required over the parameter space in Equations (15) and (17). The gathering of this sample consumed about  $2 \times 10^5$  CPU hours.

### 3.3. Experimental Data

We included 219 of the most recent experimental data points in our statistical analysis. These contained 114 electron–positron related and 105 boron/carbon, anti-proton/proton, (Sc+Ti+V)/Fe, and Be-10/Be-9 cosmic-ray flux measurements. As a number of experiments have energy ranges that overlap, we chose the most recent experimental data points in those energy ranges.

For  $e^+ + e^-$  we used the most recent data from AMS by Aguilar et al. (2002), *Fermi*-LAT by Ackermann et al. (2010), and HESS by Aharonian et al. (2008, 2009). The energy ranges in which we use each experiment are listed in Table 1. The AMS experiment reported an excess in high-energy positrons

for energies greater than 10 GeV. The *Fermi*-LAT collaboration reported a high-precision measurement of the  $e^+ + e^-$  spectrum for energies from 7 GeV to 1 TeV using its Large Area Telescope (LAT). This spectrum extended their previously published electron–positron spectrum over an energy range of 20 GeV to 1 TeV (Abdo et al. 2009) and is flatter than results reported by earlier experiments. HESS’s atmospheric Cerenkov telescope reported a significant steepening of the electron plus photon spectrum above 1 TeV.

The *PAMELA* collaboration measured the flux of the positron fraction  $e^+/(e^+ + e^-)$ , between 1.5 and 100 GeV (Adriani et al. 2009). They observed that this differential positron fraction falls slower than expected for energies above 10 GeV. This behavior is different from that of the background of secondary positrons produced during propagation of cosmic rays in the Galaxy. Recently *PAMELA* released the measurement of the  $e^-$  flux alone (Adriani et al. 2011), robustly confirming the  $e^+ + e^-$  spectrum by *Fermi*-LAT.

Cosmic-ray anti-protons can be used to study the production of primary and secondary cosmic rays and their transport throughout the Galaxy. Detailed anti-proton spectra require a large number of measurements over a larger energy range, with good statistics. Previous balloon-borne experiments such as CAPRICE98 (Boezio et al. 2001) and HEAT (Beach et al. 2001) detected only a small number of anti-protons with limited statistics. The *PAMELA* satellite experiment (Adriani et al. 2010b) provided a comprehensive measurement of the anti-proton/proton flux ratio for an energy range of 1–100 GeV. *PAMELA*’s spectrum follows the same trend as other recent anti-proton/proton ratio measurements. The energy range over which we use the *PAMELA* experiment for the anti-proton/proton ratio is listed in Table 1.

In comparison to primary/primary or secondary/secondary cosmic-ray ratios, stable secondary-to-primary cosmic-ray ratios, such as boron/carbon and (Sc+Ti+V)/Fe ratios, are the most sensitive to variation in the propagation of cosmic rays in the Galaxy. Their sensitivity arises from the fact that primary cosmic rays are generated by the original source while secondary cosmic rays are created by the interaction of their primaries with the ISM (Childers & Duvernois 2008). Primary/primary and secondary/secondary cosmic-ray ratios have a low sensitivity to variation in the propagation parameters as the denominator and numerator are produced by similar propagation mechanisms. The boron/carbon and (Sc+Ti+V)/Fe ratios provide an indication (over different energy ranges) of the amount of interstellar material that primary cosmic rays traverse as a function of energy (Childers & Duvernois 2008). The experiments used to define the B/C and (Sc+Ti+V)/Fe ratios for our analysis are found in Table 1.

In conjunction with stable secondary/primary ratios such as the boron/carbon ratio, unstable isotope ratios such as Beryllium-10/Beryllium-9 can be used to constrain the time it takes for cosmic rays to propagate through the Galaxy (Malinin 2004). In this work we use Be-10/Be-9 data from various experiments, such as ISOMAX98 (Hams et al. 2001), ACE-CRIS (Davis et al. 2000), ACE (Yanasak et al. 2001), and AMS-02 (Burger 2004).

## 4. RESULTS

### 4.1. Is There a Cosmic-ray Anomaly?

We begin our results section by investigating the question whether the present cosmic-ray data can be used to justify

<sup>4</sup> We thank the referee of our manuscript for pointing out this issue.

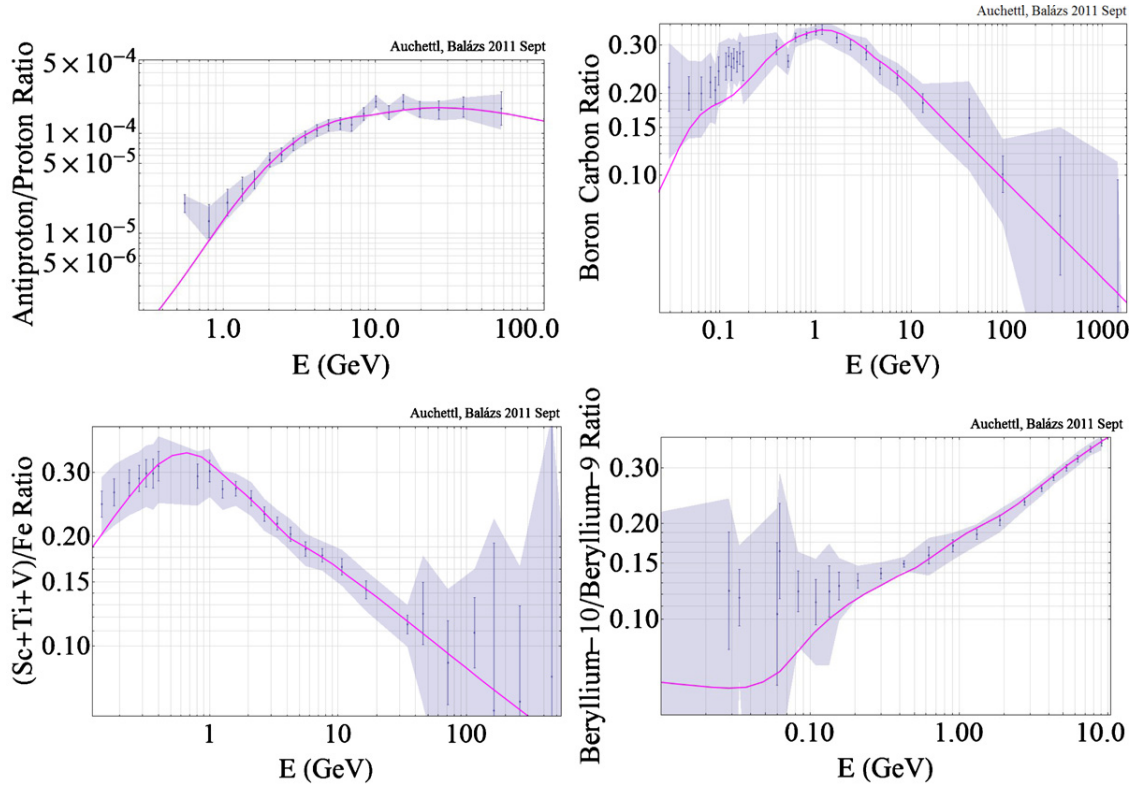


**Figure 1.** Best-fit curves compared to non-electron–positron related data. The curves were calculated using the most probable parameter values inferred from the  $\bar{p}/p$ , B/C, (Sc+Ti+V)/Fe, and Be data. These most probable values correspond to the peak values of the posterior probabilities shown in red in Figure 2. The best-fit curves pass through the estimated systematic error bands, shown in gray.

(A color version of this figure is available in the online journal.)

the existence of an anomaly in the cosmic electron–positron spectrum. Both the reality of an anomaly in the *PAMELA*  $e^+/(e^+ + e^-)$  flux and the absence of such in the anti-proton flux have been questioned by Katz et al. (2009) and Kane et al. (2009), respectively. Recently, Trotta et al. (2011) argued that the *Fermi*-LAT data can be well matched by the diffusion model, as encoded in GalProp, simply by adjusting the parameters of the propagation model. Their Figure 8 clearly shows that the *Fermi*-LAT data agree reasonably well with the propagation model that was their best fit to 76 cosmic-ray spectral data points. Trotta et al. (2011) also acknowledge that the “positron fraction, shown in the right panel of Figure 8, does not agree with the *PAMELA* data (Adriani et al. 2009), but this was expected since secondary positron production in the general ISM is not capable of producing an abundance that rises with energy.” In other words, they conclude that *PAMELA* cannot be fitted by simply adjusting the propagation parameters. We take this as an important indication that the cosmic-ray anomaly is real and requires a detailed investigation rather than the adjustment of the propagation model to explain it.

The hypothesis that the adjustment of the propagation parameters does not solve the cosmic-ray anomaly is further supported by the fact that not all cosmic-ray data can be fitted well with a single set of these parameters. It is already evident from Figures 7 and 8 of Trotta et al. (2011) that the best fit of the propagation parameters to the rest of the cosmic-ray data does not fit well AMS, *Fermi*, and HESS simultaneously. This is exactly what we find in our analysis. Our best fit for all cosmic-ray data excluding AMS, *Fermi*, HESS, and *PAMELA* data with electron and/or positron fluxes gives a  $\chi^2$  per degree of freedom of 0.34. As a consequence, the best-fit curves all pass through the esti-

mated systematic error bands, shown in gray, in Figure 1. When this fit is compared to the AMS, *Fermi*, HESS, and *PAMELA* electron and/or positron flux, the  $\chi^2$  per degree of freedom we obtain is 24, which signals considerable tension bordering exclusion. The converse also holds. By changing the propagation parameters, we can find an ideal fit for the electron–positron related fluxes with  $\chi^2$  per degree of freedom of 1.0. But for the rest of the cosmic-ray data the same fit results in a  $\chi^2$  per degree of freedom of 3.1, which is a significant pull for 105 degrees of freedom. These discrepancies signal a statistically significant tension between the electron–positron measurements and the rest of the cosmic-ray data.

To further investigate the tension, we divide the cosmic-ray data into two groups: 114 measurements containing observations of electron and/or positron fluxes (AMS, *Fermi*, HESS, and *PAMELA*), and the remaining 105 data points (anti-proton/proton, boron/carbon, (Sc+Ti+V)/Fe, Be-10/Be-9). We perform a Bayesian analysis independently on these two sets of data, extracting the preferred values of the propagation parameters. Remarkably, we found that we can obtain information about the electron–positron related propagation parameters from the rest of the data because the propagation of the cosmic rays is entangled for several reasons. First, certain propagation parameters, most importantly for us  $D_{0xx}$ , are species independent. Second, the transport equation includes nuclear fragmentation and decay, which directly contributes to the secondary electron–positron fluxes. Third, since their energy density is comparable to the interstellar radiation and magnetic fields, various species of cosmic rays affect each other’s dynamics.

Due to the correlations pointed out above, certain parameters of the electron–positron propagation are constrained even if no

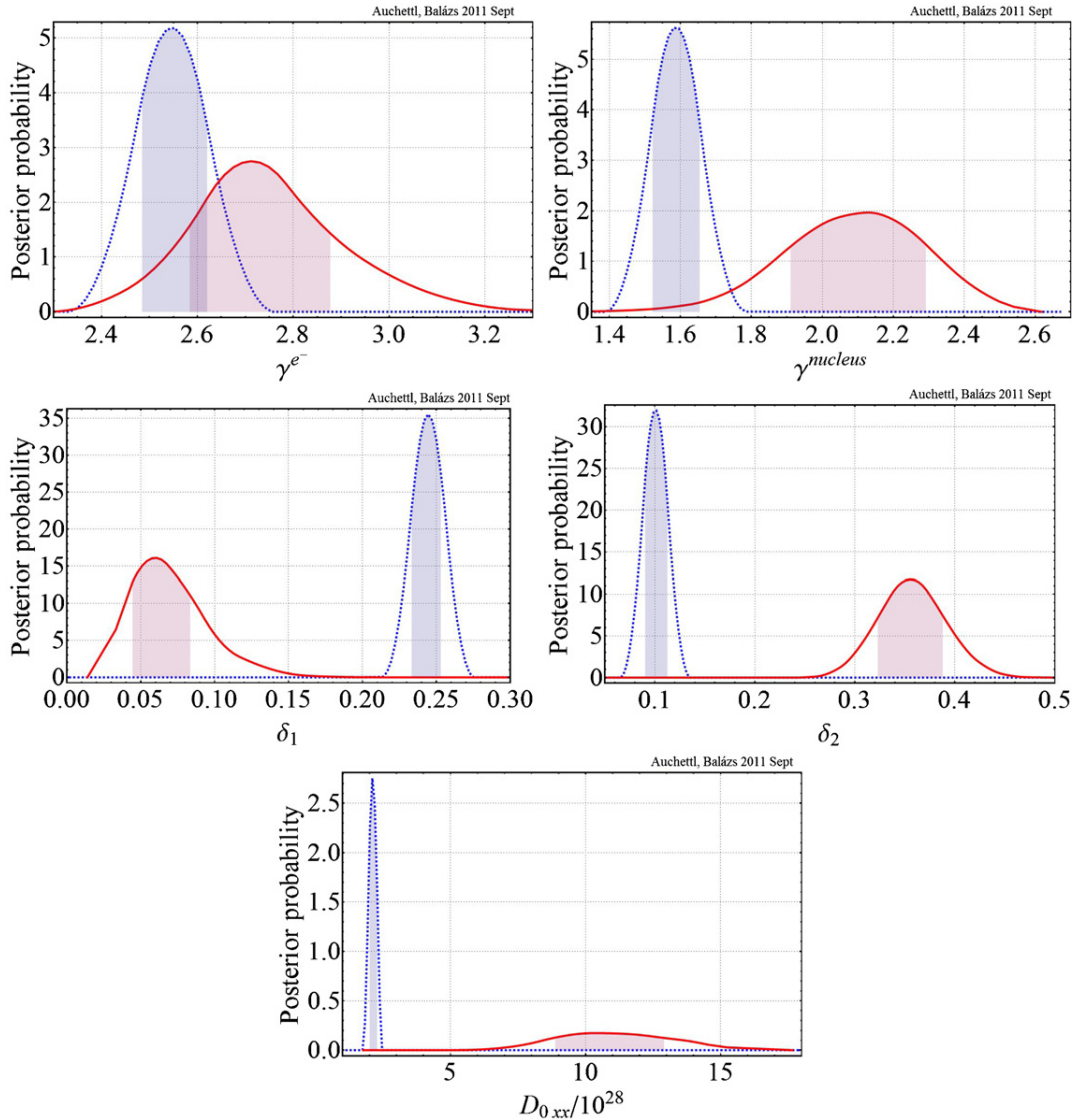


**Figure 2.** Marginalized posterior probability distributions of propagation parameters listed in Equation (15). The dashed blue curves show results with likelihood functions containing electron and/or positron flux data, while the solid red curves contain only the rest of the cosmic-ray data. Shaded areas show the 68% credibility regions. A statistically significant tension between the electron–positron data and the rest is evident in the three lower frames.

(A color version of this figure is available in the online journal.)

electron–positron related data are used in our fit. Unfortunately, the injection indices remain virtually unconstrained. In order to fix those parameters, we resorted to using a minimal amount of information from the electron–positron related fluxes. We decided to use data points from the  $e^- + e^+$  spectrum because (1) they span the widest energy range, and the end points of the  $e^- + e^+$  spectrum, partially due to their high uncertainty, appeared to agree with the theoretical predictions even before we set out to find the most optimal parameter values; (2) in the low-energy region they are relatively insensitive for solar modulation effects; and (3) in the mid-energy range the  $e^- + e^+$  theoretical prediction develops an insensitivity to the values of the propagation parameters (cf. the distinct bow-tie shape of the theory uncertainty band).

With this in mind, we included four  $e^\pm$  related data points in the analysis together with the  $\bar{p}/p$ , B/C, (Sc+Ti+V)/Fe, and Be data. These were the lowest energy point of AMS, the highest energy point of HESS, and the 19.40 GeV and 29.20 GeV data points of *Fermi*-LAT. We have checked that

our result is robust against this choice and does not bias the final conclusion.

Figure 2 clearly shows that the two subsets of cosmic-ray data are inconsistent with the hypothesis that the cosmic-ray propagation model and/or sources implemented in GalProp provide a good theoretical description. The five frames display the marginalized posterior probability densities of our selected propagation parameters. Dashed blue curves show results with likelihood functions containing only electron–positron related flux data (AMS, *Fermi*, HESS, and *PAMELA*), while the likelihood functions for the solid red curves contain only the rest of the cosmic rays (anti-proton/proton, boron/carbon, (Sc+Ti+V)/Fe, Be-10/Be-9). Shaded areas show the 68% credibility regions for the parameters. Table 2 shows the numerical values of the best fits and the 68% credibility ranges for the propagation parameters.

In the first two frames, showing the posterior densities of the electron and nucleus injection indices  $\gamma^{e^-}$  and  $\gamma^{\text{nucleus}}$ , there is a mild but tolerable tension between the electron–positron related

**Table 2**  
Best-fit Values of the Propagation Parameters and Their 68% Credibility Ranges

Parameter	Fit for the $e^\pm$ Related Data		Fit for the Rest of the Data	
	Best-fit Value	68% Cr Range	Best-fit Value	68% Cr Range
$\gamma^{e^-}$	2.55	{2.45, 2.60}	2.71	{2.54, 2.92}
$\gamma^{\text{nucleus}}$	1.60	{1.51, 1.69}	2.10	{1.88, 2.92}
$\delta_1$	0.24	{0.23, 0.26}	0.06	{0.04, 0.08}
$\delta_2$	0.10	{0.08, 0.12}	0.35	{0.32, 0.39}
$D_{0xx} [\times 10^{28}]$	2.17	{1.85, 2.19}	11.49	{8.86, 13.48}

**Notes.** Numerical values are shown for both fits: including the electron–positron related cosmic-ray data only and including the rest of the data.

and the rest of the cosmic-ray data. The last three frames, on the other hand, indicate statistically significant tension between the  $e^+e^-$  and the rest of the data. The 68% credibility regions for the spatial diffusion coefficients  $\delta_1$  and  $\delta_2$  and that of  $D_{0xx}$  fall far away from each other when determined using the two different cosmic-ray data sets. Although it is not shown, it is easily inferred that not even the 99% credibility regions overlap. It appears that by adjusting the cosmic-ray parameters we can indeed achieve a good fit to either the electron–positron related fluxes or the rest of the data but not both simultaneously.

Our interpretation of the tension between the electron–positron fluxes and the rest of the cosmic-ray data is the following. The measurements of *PAMELA* and *Fermi-LAT* are affected by new physics that is unaccounted for by the propagation model and/or cosmic-ray sources included in our calculation. We base this hypothesis partly on the earlier quoted statement of Trotta et al. (2011) that “secondary positron production in the general ISM is not capable of producing an abundance that rises with energy.” The behavior of the *PAMELA*  $e^+/(e^+ + e^-)$  data is unexpected based on general theoretical principles, and when it is fit by adjusting the propagation parameters, it leads to a bad fit to the rest of the data. An anomaly in *PAMELA*  $e^+/(e^+ + e^-)$  is also expected to produce an anomaly in the *Fermi-LAT*  $e^+ + e^-$  and the *PAMELA*  $e^-$  spectra.

We note that the recently released *PAMELA*  $e^-$  flux (Adriani et al. 2011), which is included among our electron–positron related data, considerably increases this tension. We checked that without the inclusion of the *PAMELA*  $e^-$  flux the tension is noticeably milder. This, as well as the effect of the extra data that we use, probably explains why this tension was not detected by Trotta et al. (2011).

#### 4.2. What is the Size of the Anomaly?

We attempt to extract the size of the new physics signal, after arriving to the conclusion that new physics is buried in the electron–positron fluxes. Based on our findings, our working hypothesis is that the new physics is affecting the electron–positron fluxes but hardly influences the rest of the cosmic rays. Under this hypothesis the cosmic-ray propagation parameters can be determined from the unbiased data: anti-proton/proton, boron/carbon, (Sc+Ti+V)/Fe, Be-10/Be-9. This means that we can use the central values and credibility regions of the parameters determined using these data to calculate a background prediction for all cosmic-ray data including the electron–positron fluxes. Once we quantify the background, we can subtract it from the electron–positron data to see whether there is a statistically significant signal that can be extracted.

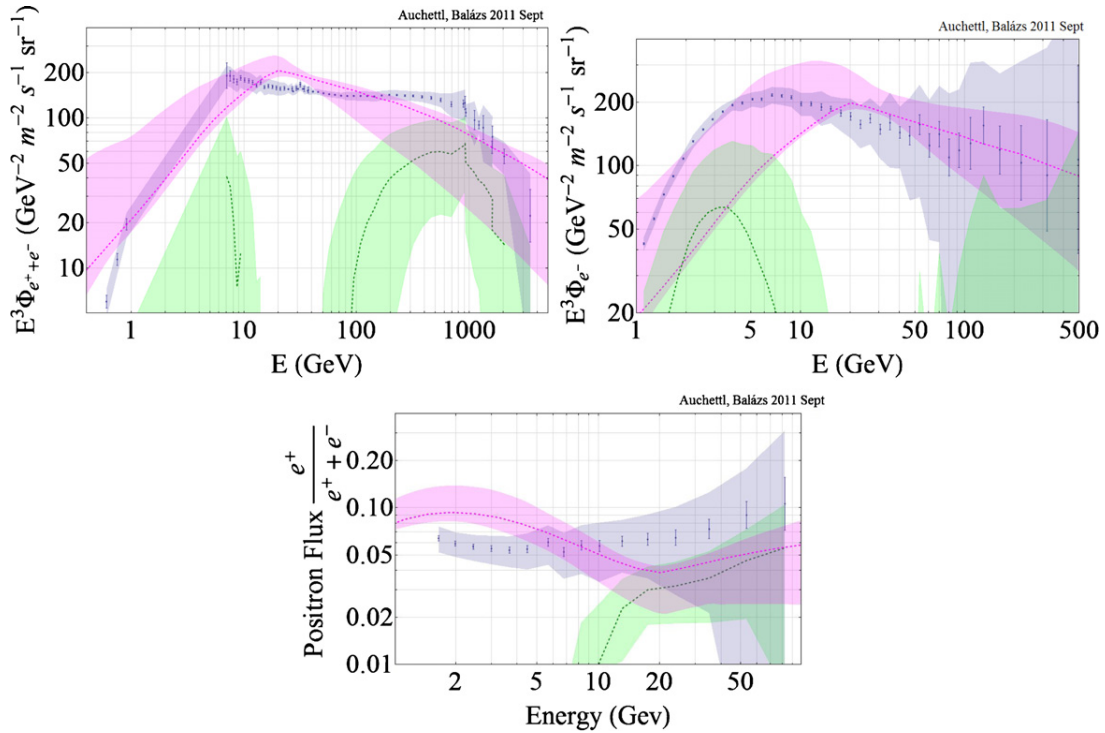
In the first step, we use the central values of the propagation parameters determined earlier using  $\bar{p}/p$ , B/C, (Sc+Ti+V)/Fe, Be-10/Be-9 to calculate a central value prediction for the *PAMELA* and *Fermi-LAT* electron–positron fluxes. Then we use all the scanned points in the parameter space lying within the 68% credibility region of all the five scanned parameters to establish a  $1\sigma$  band around this central value. We will refer to this band as the  $1\sigma$  uncertainty of the background. We overlay this uncertainty band on the *Fermi-LAT* electron+positron and the *PAMELA* electron and positron fraction fluxes.

Figure 3 shows the comparison of the measured electron–positron fluxes and their backgrounds. Statistical and systematic uncertainties combined in quadrature are shown for *Fermi-LAT* and *PAMELA*  $e^-$ , while ( $\tau = 0.2$ ) scaled statistical uncertainties are shown for *PAMELA*  $e^+/(e^+ + e^-)$  as gray bands. Our background prediction is overlaid as magenta bands. The central value and the  $1\sigma$  uncertainty of the calculated anomaly are displayed as green dashed lines and bands. As the first frame shows, the *Fermi-LAT* measurements deviate from the predicted background both below 10 GeV and above 100 GeV.

As we shall discuss later, the low-energy deviation might be due to the inadequacies of the propagation model, so here we concentrate on the deviation between the background and the measurements above 100 GeV. In our interpretation this is a weak but statistically significant signal of the presence of new physics in the electron+positron flux. Based on the difference between the central values of the data and the background, a similar conclusion can be drawn from *PAMELA*. Unfortunately, the sizable uncertainties for the *PAMELA* measurements prevent us from claiming a statistically significant deviation.<sup>5</sup>

After having determined the background for the electron–positron fluxes, we can subtract the background from the measured flux to obtain the size of the new physics signal. We determine the central value of the signal by subtracting the central value of the background from the central value of the data. The  $1\sigma$  uncertainty of the signal is the quadratically combined experimental and background uncertainty. Results for the electron–positron anomaly are also shown in Figure 3. As expected based on the background predictions, a non-vanishing anomaly can be established for the *Fermi-LAT*  $e^+ + e^-$  flux,

<sup>5</sup> Recently the *Fermi* collaboration revealed a very preliminary positron fraction measurement nicely confirming the *PAMELA* results (Mitthumsiri 2011). Even though the *Fermi-LAT* makes use of only Earth’s magnetic field, it appears to have less systematic uncertainties than that of *PAMELA*. If the officially published *Fermi-LAT* measurement will indeed reduce the systematic errors to the level of *PAMELA*’s statistical ones, our background will deviate from it, revealing a signal also in the positron fraction.



**Figure 3.** Electron–positron fluxes measured by *Fermi*-LAT and *PAMELA* (gray bands) with the extracted size of the electron–positron anomaly (green bands). Combined statistical and systematic uncertainties are shown for *Fermi*-LAT and *PAMELA*  $e^-$ , while ( $\tau = 0.2$ ) scaled statistical uncertainties are shown for *PAMELA*  $e^+/(e^+ + e^-)$ . Our background predictions (magenta bands) are also overlaid.

(A color version of this figure is available in the online journal.)

while no anomaly with statistical significance can be claimed for *PAMELA* due to the large uncertainties.

#### 4.3. What Is the Source of the Anomaly?

Based on the available evidence, we can only speculate about the origin of the discrepancy between the data and predictions of the cosmic electron–positron spectra. Since the publication of the first *PAMELA* positron fraction measurement by Adriani et al. (2009), speculation has been abundant. The first obvious assumption is that some aspect of the propagation model used in the present calculation is insufficient for the proper description of the electron–positron fluxes arriving at Earth (Stawarz et al. 2010; Donato & Serpico 2011; Arakida & Kuramata 2011; Tawfik & Saleh 2010). In this case there exists no anomaly in the data. One such plausible effect, which is missed by the two-dimensional calculation in GalProp, is the spectral hardening of cosmic rays caused by non-steady sources (Cowsik & Lee 1979; Pohl & Esposito 1998; Pohl et al. 2003). It would be an interesting exercise to repeat our analysis using a different calculation, such as DRAGON by Maccione et al. (2010) (Evoli et al. 2008; Di Bernardo et al. 2010), USINE by Maurin et al. (2011), PPPC4DMID by Cirelli et al. (2011), or the code of Buesching et al. (2003), to confirm these possibilities.<sup>6</sup>

Assuming that the propagation model satisfactorily describes physics over the Galaxy, the next reasonable thing is to suspect local effects modifying the electron–positron distribution (Pesce-Rollins & Fermi LAT Collaboration 2009). Further suspicion falls on the lack of sources included in the calculation (Di Bernardo et al. 2011b; de Vega et al. 2010; Blum 2011; Frandsen

et al. 2011). Possible new sources of cosmic rays to account for the anomaly have been proposed in two major categories. The first category is known astrophysical objects with unknown or uncertain parameters (Lavalle 2011). These could be supernova remnants, pulsars, various objects in the Galactic center, etc. (Kawanaka et al. 2011; Kashiyama et al. 2011; Pato et al. 2010; Yuan et al. 2011; Guo et al. 2011; Di Bernardo et al. 2011a). Finally, more exotic explanations call for new astronomical and/or particle physics phenomena, such as dark matter (Pieri et al. 2011; Abidin et al. 2010; Josan & Green 2010; Cheng et al. 2011; Ko & Omura 2011; Cirelli et al. 2011; Cholis & Goodenough 2010; Palomares-Ruiz & Siegal-Gaskins 2010; Anderson 2010; Zaharijas et al. 2010; Yang 2010; Borriello et al. 2012; Kajiyama & Okada 2011; Finkbeiner et al. 2011; Buckley et al. 2011; Kyae 2010; Logan 2011; Hutsi et al. 2010; Feldman et al. 2010; Arina et al. 2010; Cholis 2011; Chen et al. 2011; Lineros 2010; Dugger et al. 2010; Vincent et al. 2010; Mohanty et al. 2010; Bell et al. 2011b; Kang et al. 2011; Haba et al. 2011; Cline 2010; Ishiwata et al. 2010; Barger et al. 2010; Kang & Li 2011; Carone et al. 2010; Cirelli & Cline 2010; Masina & Sannino 2011; Porter et al. 2011; Hutsi et al. 2011; Sanchez & Holdom 2011; Zavala et al. 2011; Ke et al. 2011; Zhu 2011; Bell et al. 2011a).

Possible deviations from the predicted background can occur for energies above 100 GeV, as electron propagation is limited by energy losses via inverse Compton scattering of interstellar dust and CMB light and synchrotron radiation due to the Galactic magnetic field. This results in a relatively short lifetime and a rapidly decreasing intensity of the cosmic ray, as energy increases. Hence, a large fraction of the detected electrons and positrons above 100 GeV are hypothesized to come from individual nearby sources that are within a few kiloparsecs of the Earth (Delahaye et al. 2009a; Grasso et al. 2009). Random

<sup>6</sup> We thank the referee of our manuscript for alerting us to some of the possibilities discussed and for suggesting some of the references in this paragraph.

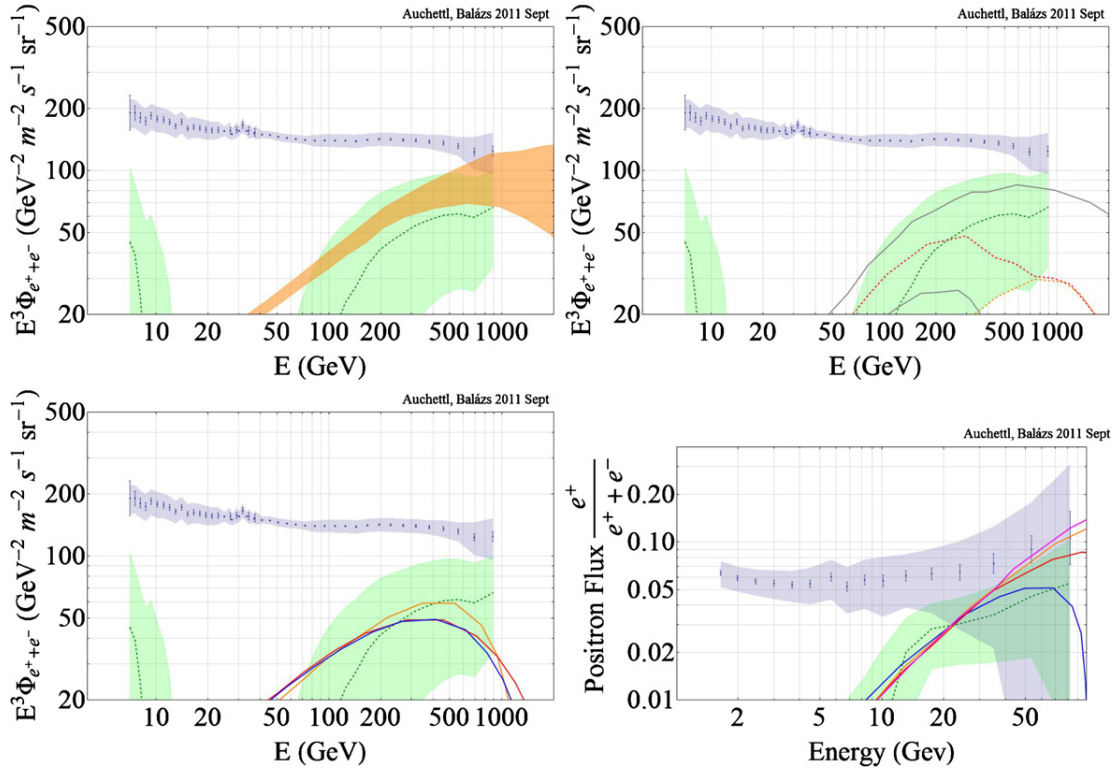


**Figure 4.** Comparison of the signal extracted in this work to potential explanations of the electron–positron cosmic-ray anomaly. The various theoretical predictions come from Ahlers et al. (2009), Grasso et al. (2009), Bergstrom et al. (2009), and Cholis et al. (2009). Currently the comparison is fairly inconclusive, but with more data it will be possible to shrink the uncertainty in the determination of the signal. Then various suggestions can be confirmed or ruled out.

(A color version of this figure is available in the online journal.)

fluctuations in the injection spectrum and the spatial distribution of those nearby sources produce significant differences in the most energetic part of the observed electron and positron spectrum. This can be the indication of new physics from either an astrophysical object(s) or dark matter.

Whatever the source of the anomaly is, if the size of the anomaly can be isolated, then the source will have to match that size. Figure 4 compares our extracted signal to a few attempts to match the anomaly that we randomly selected from the recent literature. The first frame shows the prediction of Ahlers et al. (2009) for unaccounted energetic electrons and positrons produced by supernova remnants. The top right frame features contributions from additional electron–positron primary sources (nearby pulsars or particle dark matter annihilation) calculated by Grasso et al. (2009). The bottom left frame contains predictions of Bergstrom et al. (2009) for anomalous electron–positron sources from dark matter annihilations. Similar to this, dark matter annihilation contributions suggested by Cholis et al. (2009) are shown in the last frame.

The contributions of various new sources typically come with their own (theoretical) uncertainties. In some of the cases this uncertainty is unknown; thus, it is hard to draw any conclusion by comparing these speculations to our isolated signal. In the cases where the theoretical uncertainty is known, currently it tends to be large enough to prevent us from judging the validity of the given explanation. Nevertheless, based on the present amount of information, we can already select a few scenarios that are more favored than some others. By adding more data to our analysis, it is possible to shrink the uncertainty of the signal. Similarly, in most cases, the theoretical model of a given new source can be constrained further, producing a narrower

prediction. With time, more data, and more precise calculations, the various suggestions of the cosmic electron–positron anomaly can be ruled out or confirmed.

## 5. CONCLUSIONS

We subjected a wide range of cosmic-ray observations to a Bayesian likelihood analysis, motivated by the possibility of new physics contributing to the measurements of *PAMELA* and *Fermi-LAT*. In the context of the propagation model coded in *GalProp*, we found a significant tension between the electron–positron related data and the rest of the cosmic-ray fluxes. This tension can be interpreted as the failure of the model to describe all the data simultaneously or as the effect of a missing source component.

Since the *PAMELA* and *Fermi-LAT* data are suspected to contain a component unaccounted for in *GalProp*, we extracted the preferred values of the cosmic-ray propagation parameters from the non-electron–positron related measurements. Based on these parameter values, we calculated background predictions, with uncertainties, for *PAMELA* and *Fermi-LAT*. We found a deviation between the *PAMELA* and *Fermi-LAT* data and the predicted background even when uncertainties, including systematics, were taken into account. Interpreting this as an indication of new physics, we subtracted the background from the data, isolating the size of the anomalous component.

The signal of new physics in the electron+positron spectrum was found to be non-vanishing within the calculated uncertainties. Thus, the use of 219 cosmic-ray spectral data points within the Bayesian framework allowed us to confirm the existence of new physics effects in the electron+positron flux in a model-independent fashion. Using the statistical techniques, we were

able to extract the size, shape, and uncertainty of the anomalous contribution in the electron+positron cosmic-ray spectrum. We briefly compared the extracted signal to some theoretical results predicting such an anomaly.

The authors are indebted to R. Cotta, A. Donea, J. Lazendic-Galloway, Y. Levin, A. Mazumdar, N. Sahu, and T. Porter for invaluable discussions on various aspects of cosmic-ray physics and likelihood analysis. K.A. is thankful to P. Chan for help with issues of parallel computing, to M. Jasperse for assistance in Mathematica programming, and to J. Lazendic-Galloway, T. Porter, and A. Vladimirov for help with GalProp. This research was funded in part by the Australian Research Council under Project ID DP0877916 and in part by the Project of Knowledge Innovation Program (PKIP) of Chinese Academy of Sciences, Grant No. KJCX2.YW.W10. The use of Monash University Sun Grid, a high-performance computing facility, is also gratefully acknowledged.

## REFERENCES

- Abdo, A. A., Ackermann, M., Ajello, M., et al. 2009, *Phys. Rev. Lett.*, **102**, 181101
- Abidin, Z., Afanasev, A., & Carlson, C. E. 2010, arXiv:1006.5444
- Ackermann, M., Ajello, M., Atwood, W. B., et al. 2010, *Phys. Rev. D*, **82**, 092004
- Adriani, O., Barbarino, G., Bazilevskaya, G., et al. 2010a, *Astropart. Phys.*, **34**, 1
- Adriani, O., Barbarino, G. C., Bazilevskaya, G. A., et al. 2009, *Nature*, **458**, 607
- Adriani, O., Barbarino, G. C., Bazilevskaya, G. A., et al. 2010b, *Phys. Rev. Lett.*, **105**, 121101
- Adriani, O., Barbarino, G. C., Bazilevskaya, G. A., et al. 2011, *Phys. Rev. Lett.*, **106**, 201101
- Aguilar, M., Alcaraz, J., Allaby, J., et al. 2002, *Phys. Rep.*, **366**, 331
- Aharonian, F., Akhperjanian, A. G., Anton, G., et al. 2009, *A&A*, **508**, 561
- Aharonian, F., Akhperjanian, A. G., Barres de Almeida, U., et al. 2008, *Phys. Rev. Lett.*, **101**, 261104
- Aharonian, F., Bykov, A., Parizot, E., Ptuskin, V., & Watson, A. 2011, arXiv:1105.0131
- Ahlers, M., Mertsch, P., & Sarkar, S. 2009, *Phys. Rev. D*, **80**, 123017
- Ahn, H. S., Allison, P. S., Bagliesi, M. G., et al. 2008, *Astropart. Phys.*, **30**, 133
- Alcaraz, J., Alpat, B., Ambrosi, G., et al. 2000, *Phys. Lett. B*, **484**, 10
- Allahverdi, R., Dutta, B., Richardson-McDaniel, K., & Santoso, Y. 2009, *Phys. Rev. D*, **79**, 075005
- Anderson, B. 2010, arXiv:1012.0863
- Arakida, H., & Kuramata, S. 2011, *Int. J. Mod. Phys. A*, **26**, 911
- Arina, C., Josse-Michaux, F.-X., & Sahu, N. 2010, *Phys. Lett. B*, **691**, 219
- Arkani-Hamed, N., Finkbeiner, D. P., Slatyer, T. R., & Weiner, N. 2009, *Phys. Rev. D*, **79**, 015014
- Arvanitaki, A., Dimopoulos, S., Dubovsky, S., et al. 2009, *Phys. Rev. D*, **80**, 055011
- Backovic, M., & Ralston, J. P. 2010, *Phys. Rev. D*, **81**, 056002
- Bai, Y., Carena, M., & Lykken, J. 2009, *Phys. Rev. D*, **80**, 055004
- Baltz, E. A., & Edsjö, J. 1998, *Phys. Rev. D*, **59**, 023511
- Barger, V., Gao, Y., Keung, W. Y., Marfatia, D., & Shaughnessy, G. 2009, *Phys. Lett. B*, **678**, 283
- Barger, V., Gao, Y., McCaskey, M., & Shaughnessy, G. 2010, *Phys. Rev. D*, **82**, 095011
- Barwick, S. W., Beatty, J. J., Bhattacharyya, A., et al. 1997, *ApJ*, **482**, L191
- Beach, A. S., Beatty, J. J., Bhattacharyya, A., et al. 2001, *Phys. Rev. Lett.*, **87**, A261101
- Beatty, J. J., Bhattacharyya, A., Bower, C., et al. 2004, *Phys. Rev. Lett.*, **93**, 241102
- Bell, N. F., Dent, J. B., Jacques, T. D., & Weiler, T. J. 2011a, *Phys. Rev. D*, **84**, 103517
- Bell, N. F., Dent, J. B., Jacques, T. D., & Weiler, T. J. 2011b, *Phys. Rev. D*, **83**, 013001
- Bergstrom, L., Edsjo, J., & Zaharijas, G. 2009, *Phys. Rev. Lett.*, **103**, 031103
- Bi, X.-J., He, X.-G., & Yuan, Q. 2009, *Phys. Lett. B*, **678**, 168
- Blandford, R., & Eichler, D. 1987, *Phys. Rep.*, **154**, 1
- Blasi, P. 2009, *Phys. Rev. Lett.*, **103**, 051104
- Blum, K. 2011, *J. Cosmol. Astropart. Phys.*, **JCAP11(2011)037**
- Boezio, M., Bonvicini, V., Schiavon, P., et al. 2001, *ApJ*, **561**, 787
- Borriello, E., Maccione, L., & Cuoco, A. 2012, *Astropart. Phys.*, **35**, 537
- Brun, P., Delahaye, T., Diemand, J., Profumo, S., & Salati, P. 2009, *Phys. Rev. D*, **80**, 035023
- Buchmuller, W., Ibarra, A., Shindou, T., Takayama, F., & Tran, D. 2009, *J. Cosmol. Astropart. Phys.*, **JCAP09(2009)021**
- Buckley, M. R., Hooper, D., & Tait, T. M. P. 2011, *Phys. Lett. B*, **702**, 216
- Buesching, I., Kopp, A., Pohl, M., & Shlickeiser, R. 2003, in 28th International Cosmic Ray Conference, Vol. 4, ed. T. Kajita, Y. Asaoka, A. Kawachi, Y. Matsubara, & M. Sasaki (Tokyo: Universal Academy Press), 1985
- Burger, J. 2004, *Eur. Phys. J. C*, **33**, 941
- Calmet, X., & Majee, S. K. 2009, *Phys. Lett. B*, **679**, 267
- Carone, C. D., Erlich, J., & Primulando, R. 2010, *Phys. Rev. D*, **82**, 055028
- Chen, C.-H. 2009, arXiv:0905.3425
- Chen, C.-H., Geng, C.-Q., & Zhuridov, D. V. 2009, *J. Cosmol. Astropart. Phys.*, **JCAP10(2009)001**
- Chen, C.-H., Geng, C.-Q., & Zhuridov, D. V. 2010, *Eur. Phys. J.*, **C67**, 479
- Chen, N., Feldman, D., Liu, Z., Nath, P., & Peim, G. 2011, *Phys. Rev. D*, **83**, 023506
- Cheng, H.-C., Huang, W.-C., Low, I., & Menon, A. 2011, *J. High Energy Phys.*, **JHEP03(2011)019**
- Childers, J. T., & Duvernois, M. A. 2008, in 30th International Cosmic Ray Conference, Vol. 2, ed. R. Caballero, J. C. D'Olivo, G. Medina-Tanco et al. (Mexico City: Universidad Nacional Autonoma de Mexico), 183
- Choi, K.-Y., & Yaguna, C. E. 2010, *Phys. Rev. D*, **81**, 023502
- Cholis, I. 2011, *J. Cosmol. Astropart. Phys.*, **JCAP09(2011)007**
- Cholis, I., Finkbeiner, D. P., Goodenough, L., & Weiner, N. 2009, *J. Cosmol. Astropart. Phys.*, **JCAP12(2009)007**
- Cholis, I., & Goodenough, L. 2010, *J. Cosmol. Astropart. Phys.*, **JCAP09(2010)010**
- Cirelli, M., & Cline, J. M. 2010, *Phys. Rev. D*, **82**, 023503
- Cirelli, M., Corcella, G., Hektor, A., et al. 2011, *J. Cosmol. Astropart. Phys.*, **JCAP03(2011)051**
- Cirelli, M., Kadastik, M., Raidal, M., & Strumia, A. 2009, *Nucl. Phys. B*, **813**, 1
- Cline, J. M. 2010, arXiv:1005.5001
- Cotta, R. C., Conley, J. A., Gainer, J. S., Hewett, J. L., & Rizzo, T. G. 2011, *J. High Energy Phys.*, **JHEP01(2011)064**
- Cowsik, R., & Burch, B. 2009, arXiv:0905.2136
- Cowsik, R., & Lee, M. A. 1979, *ApJ*, **228**, 297
- Dado, S., & Dar, A. 2010, *Mem. Soc. Astron. Italiana*, **81**, 132
- Davis, A. J., Mewaldt, R. A., Binns, W. R., et al. 2000, in AIP Conf. Ser. 528, Acceleration and Transport of Energetic Particles Observed in the Heliosphere, ed. R. A. Mewaldt, J. R. Jokipii, M. A. Lee, E. Möbius, & T. H. Zurbuchen (Melville, NY: AIP), 421
- Delahaye, T., Armand, F., Pohl, M., & Salati, P. 2011, *A&A*, **531**, A37
- Delahaye, T., Laval, J., Lineros, R., Donato, F., & Fornengo, N. 2010, *A&A*, **524**, A51
- Delahaye, T., Lineros, R., Donato, F., Fornengo, N., & Salati, P. 2008, *Phys. Rev. D*, **77**, 063527
- Delahaye, T., Brun, P., Donato, F., et al. 2009a, arXiv:0905.2144
- Delahaye, T., Lineros, R., Donato, F., et al. 2009b, *A&A*, **501**, 821
- De Lope Amigo, S., Cheung, W. M.-Y., Huang, Z., & Ng, S.-P. 2009, *J. Cosmol. Astropart. Phys.*, **JCAP06(2009)005**
- de Vega, H., Falvella, M., & Sanchez, N. 2010, arXiv:1009.3494
- Demir, D. A., Everett, L. L., Frank, M., Selbuz, L., & Turan, I. 2010, *Phys. Rev. D*, **81**, 035019
- Dent, J. B., Dutta, S., & Scherrer, R. J. 2010, *Phys. Lett. B*, **687**, 275
- Di Bernardo, G., Evoli, C., Gaggero, D., Grasso, D., & Maccione, L. 2010, *Astropart. Phys.*, **34**, 274
- Di Bernardo, G., Evoli, C., Gaggero, D., et al. 2011a, arXiv:1101.1830
- Di Bernardo, G., Evoli, C., Gaggero, D., et al. 2011b, *Astropart. Phys.*, **34**, 528
- Donato, F., & Serpico, P. D. 2011, *Phys. Rev. D*, **83**, 023014
- Dugger, L., Jeltema, T. E., & Profumo, S. 2010, *J. Cosmol. Astropart. Phys.*, **JCAP12(2010)015**
- Engelmann, J. J., Ferrando, P., Soutoul, A., Goret, P., & Juliusson, E. 1990, *A&A*, **233**, 96
- Evoli, C., Gaggero, D., Grasso, D., & Maccione, L. 2008, *J. Cosmol. Astropart. Phys.*, **JCAP10(2008)018**
- Fan, Y.-Z., Zhang, B., & Chang, J. 2010, *Int. J. Mod. Phys. D*, **19**, 2011
- Feldman, D., Liu, Z., & Nath, P. 2009a, *Phys. Rev. D*, **79**, 063509
- Feldman, D., Liu, Z., Nath, P., & Nelson, B. D. 2009b, *Phys. Rev. D*, **80**, 075001
- Feldman, D., Liu, Z., Nath, P., & Peim, G. 2010, *Phys. Rev. D*, **81**, 095017
- Feng, J. L., Kaplinghat, M., & Yu, H.-B. 2010, *Phys. Rev. Lett.*, **104**, 151301
- Finkbeiner, D. P., Goodenough, L., Slatyer, T. R., Vogelsberger, M., & Weiner, N. 2011, *J. Cosmol. Astropart. Phys.*, **JCAP05(2011)002**
- Frandsen, M. T., Masina, I., & Sannino, F. 2011, *Phys. Rev. D*, **83**, 127301
- Fujita, Y., Kohri, K., Yamazaki, R., & Ioka, K. 2009, *Phys. Rev. D*, **80**, 063003

- Fukuoka, H., Kubo, J., & Suematsu, D. 2009, *Phys. Lett. B*, **678**, 401
- Garcia-Munoz, M., Guzik, T. G., Margolis, S. H., Simpson, J. A., & Wefel, J. P. 1981, in 17th International Cosmic Ray Conference, Vol. 9, ed. T. Montmerle (Saclay: Centre de Saclay), 195
- Gast, H., & Schael, S. 2009, in 31st International Cosmic Ray Conference, ed. W. Bednarek & M. Giller (Lodz: University of Lodz), 1
- Ginzburg, V. L., Dogiel, V., Berezhinsky, V., Bulanov, S., & Ptuskin, V. 1990, *Astrophysics of Cosmic Rays* (Weinheim: Wiley-VCH)
- Ginzburg, V. L., & Syrovatskii, S. I. 1964, *The Origin of Cosmic Rays* (New York: Macmillan)
- Golden, R. L., Grimani, C., Kimbell, B. L., et al. 1994, *ApJ*, **436**, 769
- Grasso, D., Profumo, S., Strong, A. W., et al. 2009, *Astropart. Phys.*, **32**, 140
- Grimani, C., Stephens, S. A., Cafagna, F. S., et al. 2002, *A&A*, **392**, 287
- Guo, W.-L., & Wu, Y.-L. 2009, *Phys. Rev. D*, **79**, 055012
- Guo, Y., Feng, Z., Yuan, Q., Liu, C., & Hu, H. 2011, arXiv:1101.5192
- Haba, N., Kajiyama, Y., Matsumoto, S., Okada, H., & Yoshioka, K. 2011, *Phys. Lett. B*, **695**, 476
- Hamaguchi, K., Nakaji, K., & Nakamura, E. 2009a, *Phys. Lett. B*, **680**, 172
- Hamaguchi, K., Nakamura, E., Shirai, S., & Yanagida, T. T. 2009b, *Phys. Lett. B*, **674**, 299
- Hams, T., Barbier, L. M., Bremerich, M., et al. 2001, in 27th International Cosmic Ray Conference, Vol. 5 (Hamburg), 1655
- Hareyama, M. 1999, in 26th International Cosmic Ray Conference, Vol. 3, ed. D. Kieda, M. Salamon, & B. Dingus (Salt Lake City), 105
- Harnik, R., & Kribs, G. D. 2009, *Phys. Rev. D*, **79**, 095007
- He, X.-G. 2009, *Mod. Phys. Lett. A*, **24**, 2139
- Hillas, A. M. 1984, *Ann. Rev. Astron. Astrophys.*, **22**, 425
- Hisano, J., Matsumoto, S., Nojiri, M. M., & Saito, O. 2005, *Phys. Rev. D*, **71**, 063528
- Hooper, D., Blasi, P., & Serpico, P. D. 2009a, *J. Cosmol. Astropart. Phys.*, **JCAP01(2009)025**
- Hooper, D., Stebbins, A., & Zurek, K. M. 2009b, *Phys. Rev. D*, **79**, 103513
- Hooper, D., & Tait, T. M. P. 2009, *Phys. Rev. D*, **80**, 055028
- Hu, H.-B., Yuan, Q., Wang, B., et al. 2009, *ApJ*, **700**, L170
- Hutsi, G., Chluba, J., Hektor, A., & Raidal, M. 2011, *A&A*, **535**, A26
- Hutsi, G., Hektor, A., & Raidal, M. 2010, *J. Cosmol. Astropart. Phys.*, **JCAP07(2010)008**
- Ibarra, A., & Tran, D. 2009, *J. Cosmol. Astropart. Phys.*, **JCAP02(2009)021**
- Ibarra, A., Tran, D., & Weniger, C. 2010, *J. Cosmol. Astropart. Phys.*, **JCAP01(2010)009**
- Ibe, M., Murayama, H., & Yanagida, T. T. 2009, *Phys. Rev. D*, **79**, 095009
- Ishiwata, K., Matsumoto, S., & Moroi, T. 2009, *Phys. Rev. D*, **79**, 043527
- Ishiwata, K., Matsumoto, S., & Moroi, T. 2010, *J. High Energy Phys.*, **JHEP12(2010)006**
- Josan, A. S., & Green, A. M. 2010, *Phys. Rev. D*, **82**, 083527
- Kajiyama, Y., & Okada, H. 2011, *Nucl. Phys. B*, **848**, 303
- Kane, G., Lu, R., & Watson, S. 2009, *Phys. Lett. B*, **681**, 151
- Kang, Z., & Li, T. 2011, *J. High Energy Phys.*, **JHEP02(2011)035**
- Kang, Z., Li, T., Liu, T., Tong, C., & Yang, J. M. 2011, *J. Cosmol. Astropart. Phys.*, **JCAP01(2011)028**
- Kashiyama, K., Ioka, K., & Kawanaka, N. 2011, *Phys. Rev. D*, **83**, 023002
- Katz, B., Blum, K., & Waxman, E. 2009, *MNRAS*, **405**, 1458
- Kawanaka, N., Ioka, K., Ohira, Y., & Kashiyama, K. 2011, *ApJ*, **729**, 93
- Ke, J., Luo, M., Wang, L., & Zhu, G. 2011, *Phys. Lett. B*, **698**, 44
- Ko, P., & Omura, Y. 2011, *Phys. Lett. B*, **701**, 363
- Krombel, K. E., & Wiedenbeck, M. E. 1988, *ApJ*, **328**, 940
- Kyae, B. 2010, *J. Phys. Conf. Ser.*, **259**, 012103
- Lavalle, J. 2011, *MNRAS*, **414**, 985
- Lezniak, J. A., & Webber, W. R. 1978, *ApJ*, **223**, 676
- Lin, T., Finkbeiner, D. P., & Dobler, G. 2010, *Phys. Rev. D*, **82**, 023518
- Lineros, R. A. 2010, *J. Phys. Conf. Ser.*, **259**, 012101
- Logan, H. E. 2011, *Phys. Rev. D*, **83**, 035022
- Maccione, L., Evoli, C., Gaggero, D., Di Bernardo, G., & Grasso, D. 2010, DRAGON: A Public Code to Compute the Propagation of High-energy Cosmic Rays in the Galaxy (Harburg: Luca Maccione, Deutsches Elektronen)
- Malinin, A. G. 2004, *Phys. At. Nucl.*, **67**, 2044
- Malyshev, D. 2009, *J. Cosmol. Astropart. Phys.*, **JCAP07(2009)038**
- Malyshev, D., Cholis, I., & Gelfand, J. 2009, *Phys. Rev. D*, **80**, 063005
- March-Russell, J., West, S. M., Cumberbatch, D., & Hooper, D. 2008, *J. High Energy Phys.*, **JHEP07(2008)058**
- Mardon, J., Nomura, Y., & Thaler, J. 2009, *Phys. Rev. D*, **80**, 035013
- Masina, I., & Sannino, F. 2011, *J. Cosmol. Astropart. Phys.*, **JCAP1108(2011)018**
- Maurin, D., Donato, F., Taillet, R., & Salati, P. 2001, *ApJ*, **555**, 585
- Maurin, D., Putze, A., & Derome, L. 2010, *A&A*, **516**, A67
- Maurin, D., Putze, A., Derome, L., et al. 2011, USINE—A Galactic Cosmic-ray Propagation Code (Como, Italy)
- Maurin, D., Taillet, R., & Donato, F. 2002, *A&A*, **394**, 1039
- Mertsch, P. 2010, arXiv:1012.4239
- Mertsch, P., & Sarkar, S. 2009, *Phys. Rev. Lett.*, **103**, 081104
- Mitthumsiri, W. 2011, in Fermi Symposium, ed. W. Mitthumsiri (Rome, Italy), 9
- Mocchiutti, E., et al. 2008, in Proc. 21st European Cosmic Ray Symposium (ECRS 2008), ed. P. Kiraly, K. Kudela, M. Stehlik, & A. W. Wolfendale (Kóscice: Institute of Experimental Physics, Slovak Academy of Sciences), 396
- Mohanty, S., Rao, S., & Roy, D. 2010, arXiv:1009.5058
- Moskalenko, I. V., Strong, A. W., Ormes, J. F., & Potgieter, M. S. 2002, *ApJ*, **565**, 280
- Nakamura, K., & Particle Data Group 2010, *J. Phys. G: Nucl. Part. Phys.*, **37**, 075021
- Nardi, E., Sannino, F., & Strumia, A. 2009, *J. Cosmol. Astropart. Phys.*, **JCAP01(2009)043**
- Okada, N., & Yamada, T. 2009, *Phys. Rev. D*, **80**, 075010
- Palomares-Ruiz, S., & Siegal-Gaskins, J. M. 2010, arXiv:1012.2335
- Pato, M., Lattanzi, M., & Bertone, G. 2010, *J. Cosmol. Astropart. Phys.*, **JCAP12(2010)020**
- Perelstein, M., & Shakya, B. 2010, *Phys. Rev. D*, **82**, 043505
- Perelstein, M., & Shakya, B. 2011, *Phys. Rev. D*, **83**, 123508
- Pesce-Rollins, M., & Fermi LAT Collaboration 2009, arXiv:0907.0387
- Pieri, L., Lavalle, J., Bertone, G., & Branchini, E. 2011, *Phys. Rev. D*, **83**, 023518
- Pohl, M., & Esposito, J. A. 1998, *ApJ*, **507**, 327
- Pohl, M., Perrot, C., Grenier, I., & Digel, S. 2003, *A&A*, **409**, 581
- Porter, T. A., Johnson, R. P., & Graham, P. W. 2011, *ARA&A*, **49**, 155
- Prantzos, N., Boehm, C., Bykov, A., et al. 2011, *Rev. Mod. Phys.*, **83**, 1001
- Profumo, S. 2011, *Central European J. Phys.*, **10**, 1
- Ptuskin, V. S., Moskalenko, I. V., Jones, F. C., Strong, A. W., & Zirakashvili, V. N. 2006, *ApJ*, **642**, 902
- Putze, A., Derome, L., & Maurin, D. 2010, *A&A*, **516**, A66
- Sanchez, C. G., & Holdom, B. 2011, *Phys. Rev. D*, **83**, 123524
- Schlickeiser, R. 2002, *Cosmic Ray Astrophysics* (Berlin: Springer)
- Seo, E. S., & Ptuskin, V. S. 1994, *ApJ*, **431**, 705
- Serpico, P. D. 2011, *Astrophysical Models for the Origin of the Positron Excess* (North Holland: Astroparticle Physics), 1
- Shaviv, N. J., Nakar, E., & Piran, T. 2009, *Phys. Rev. Lett.*, **103**, 111302
- Shirai, S., Takahashi, F., & Yanagida, T. T. 2009, *Phys. Lett. B*, **680**, 485
- Shirai, S., Takahashi, F., & Yanagida, T. T. 2010, *Prog. Theor. Phys.*, **122**, 1277
- Stawarz, L., Petrosian, V., & Blandford, R. D. 2010, *ApJ*, **710**, 236
- Strong, A. W., & Moskalenko, I. V. 1998, *ApJ*, **509**, 212
- Strong, A. W., Moskalenko, I. V., & Ptuskin, V. S. 2007, *Ann. Rev. Nucl. Part. Sci.*, **57**, 285
- Strong, A. W., Moskalenko, I. V., & Reimer, O. 2004, *ApJ*, **613**, 962
- Tawfik, A., & Saleh, A. 2010, arXiv:1010.5390
- Tierney, L., & Kadane, J. B. 1986, *J. Am. Stat. Assoc.*, **81**, 82
- Torii, S., Yamagami, T., Tamura, T., et al. 2008, arXiv:0809.0760
- Trotta, R., Jóhannesson, G., Moskalenko, I. V., et al. 2011, *ApJ*, **729**, 106
- Usoskin, I. G., Bazilevskaia, G. A., & Kovaltsov, G. A. 2011, *J. Geophys. Res. (Space Phys.)*, **116**, A02104
- Vincent, A. C., Xue, W., & Cline, J. M. 2010, *Phys. Rev. D*, **82**, 123519
- Wiedenbeck, M. E., & Greiner, D. E. 1980, *ApJ*, **239**, L139
- Yanasak, N. E., Wiedenbeck, M. E., Binns, W. R., et al. 2001, *Adv. Space Res.*, **27**, 727
- Yang, J.-M. 2010, *Mod. Phys. Lett. A*, **25**, 976
- Yin, P.-F., Yuan, Q., Liu, J., et al. 2009, *Phys. Rev. D*, **79**, 023512
- Yuan, Q., Zhang, B., & Bi, X.-J. 2011, *Phys. Rev. D*, **84**, 043002
- Yüksel, H., Kistler, M. D., & Stanev, T. 2009, *Phys. Rev. Lett.*, **103**, 051101
- Zaharijas, G., Cuoco, A., Yang, Z., & Conrad, J. 2010, arXiv:1012.0588
- Zavala, J., Vogelsberger, M., Slatyer, T. R., Loeb, A., & Springel, V. 2011, *Phys. Rev. D*, **83**, 123513
- Zavala, J., Vogelsberger, M., & White, S. D. M. 2010, *Phys. Rev. D*, **81**, 083502
- Zhu, G. 2011, *Phys. Rev. D*, **83**, 076011



---

*Fermi-LAT* observations of  
supernova remnant Kesteven  
79

---

*Fermi-LAT observations of supernova remnant Kesteven 79*

Katie Auchettl, Patrick Slane, Daniel Castro

Published in ApJ, 783 (2014), 32

DOI: 10.1088/0004-637X/783/1/328

e-Print: [arXiv:1401.2745](https://arxiv.org/abs/1401.2745) [astro-ph]

---

### 3.1 Introductory remarks

Supernova remnants (SNRs) that arise from core collapse supernovae evolve in and interact with complex, dense environments. This environment, which was the birth place of their progenitor, is shaped by the winds and mass loss of the original star as well as the presence of dense molecular clouds. This dense molecular material strongly impacts the properties and evolution of these remnants. The interaction of the SNR shock front with this dense material is highlighted by distinct signatures such as 1720 MHz OH masers, and line emission. One advantage of studying SNRs interacting with molecular clouds is that these remnants are ideal for revealing the presence of energetic particles being accelerated at the shock-front. These relativistic particles will produce  $\gamma$ -ray emission from either leptonic processes such as inverse Compton scattering, or non-thermal Bremsstrahlung; or from hadronic emission due to pion-decay. Due to this degeneracy, a means of distinguishing between these mechanisms is crucial for our understanding of the origin of this observed emission. In regions of high density, the  $\gamma$ -ray emission arising from pion-decay is enhanced, providing the ideal laboratory to detect and analyse this type of emission.

In this paper, we present our analysis of the GeV  $\gamma$ -ray emission coincident with Galactic SNR Kes 79 that was detected using the *Fermi Gamma-ray Space Telescope*. Kes 79 is thought to be interacting with a nearby molecular cloud based on the detection of a broad OH absorption feature, and strong  $^{12}\text{CO}$   $J = 1 \rightarrow 0$ , and  $\text{HCO}^{12}$   $J = 1 \rightarrow 0$  emission found in the direction of the molecular cloud. We investigate the origin of this emission by performing broadband modelling of its non thermal emission using both leptonic and hadronic processes, and conclude via energetic arguments that the emission is most likely hadronic in nature. We estimate the density of the  $\gamma$ -ray emitting material and compare this to the inferred density derived from multiple archival *XMM-Newton* observations of Kes 79. We find that the density derived from our  $\gamma$ -ray modelling is larger than that derived from our X-ray analysis, consistent with scenarios presented by other studies such as [Castro & Slane \(2010\)](#). We perform a similar analysis for SNR Kes 78, which is known to be interacting with a molecular cloud due to the detection of an OH maser, but due to the large uncertainties in the  $\gamma$ -ray background model, we are unable to conclude if there is any significant GeV  $\gamma$ -ray emission associated with this remnant. In addition to our  $\gamma$ -ray analysis, we also perform a spatially resolved analysis of the thermal X-ray emission from Kes 79, and derive the evolutionary properties of the remnant.

In Section 2 of the paper found overleaf, we describe our analysis of the *Fermi-LAT* data for both Kes 79 and Kes 78. In Section 3 we describe our analysis of the *XMM-Newton* observations of Kes 79, and in Section 4 we present our  $\gamma$ -ray modelling of the broadband non-thermal emission of Kes 79. Figure 1 shows the

$\gamma$ -ray count maps of both Kes 79 and Kes 78, with the detection significance overlaid, while Figure 5 presents the broadband non-thermal emission of Kes 79 and our model of this emission.

## 3.2 Declaration for thesis chapter 3

### Declaration by candidate

In the case of the paper(s) contained in Chapter 3, the nature and extent of my contribution to the work was the following:

<b>Paper</b>	<b>Nature of contribution</b>	<b>Extent of contribution (%)</b>
II	Performed data reduction for both the X-ray and $\gamma$ -ray data; analysed and interpreted results; wrote paper.	90%

The following co-authors contributed to the work. If co-authors are students at Monash University, the extent of their contribution in percentage terms is stated:

<b>Name</b>	<b>Nature of contribution</b>	<b>Extent of contribution (%)</b>
Patrick Slane	Contributed to the initial idea and discussion; provided supervisory advice; provided guidance on the interpretation of the X-ray results; provided comments on the draft of the paper.	
Daniel Castro	Developed the code which models the $\gamma$ -ray emission arising from pion-decay, inverse Compton scattering, non-thermal bremsstrahlung and synchrotron; provided guidance on how to reduce the $\gamma$ -ray data; provided comments on the draft of paper.	

The undersigned hereby certify that the above declaration correctly reflects the nature and extent of the candidate's and co-authors' contributions to this work.

**Signatures:**

Katie Auchetl:



Date: 15th June 2015

Patrick Slane:



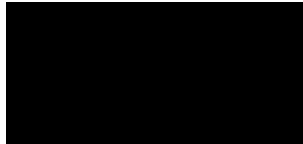
Date: 15th June 2015

Csaba Balázs:



Date: 15th June 2015

Jasmina Lazendic-Galloway:



Date: 15th June 2015

### 3.3 Published material: Paper II

Begins overleaf.

## FERMI-LAT OBSERVATIONS OF SUPERNOVA REMNANTS KESTEVEN 79

KATIE AUCHETTL<sup>1,2,3,4</sup>, PATRICK SLANE<sup>1</sup>, AND DANIEL CASTRO<sup>5</sup>

<sup>1</sup> Harvard-Smithsonian Center for Astrophysics, 60 Garden Street, Cambridge, MA 02138, USA

<sup>2</sup> School of Physics, Monash University, Melbourne, Victoria 3800, Australia

<sup>3</sup> Monash Centre for Astrophysics, Monash University, Victoria 3800, Australia

<sup>4</sup> ARC Centre of Excellence for Particle Physics at the Tera-scale, Monash University, Victoria 3800, Australia

<sup>5</sup> MIT-Kavli Center for Astrophysics and Space Research, 77 Massachusetts Avenue, Cambridge, MA 02139, USA

Received 2013 August 22; accepted 2014 January 6; published 2014 February 10

### ABSTRACT

In this paper, we report on the detection of  $\gamma$ -ray emission coincident with the Galactic supernova remnant (SNR) Kesteven 79 (Kes 79). We analyzed approximately 52 months of data obtained with the Large Area Telescope on board the *Fermi Gamma-ray Space Telescope*. Kes 79 is thought to be interacting with adjacent molecular clouds, based on the presence of strong  $^{12}\text{CO } J = 1 \rightarrow 0$  and  $\text{HCO}^+ J = 1 \rightarrow 0$  emission and the detection of 1720 MHz line emission toward the east of the remnant. Acceleration of cosmic rays is expected to occur at SNR shocks, and SNRs interacting with dense molecular clouds provide a good testing ground for detecting and analyzing the production of  $\gamma$ -rays from the decay of  $\pi^0$  into two  $\gamma$ -ray photons. This analysis investigates  $\gamma$ -ray emission coincident with Kes 79, which has a detection significance of  $\sim 7\sigma$ . Additionally, we present an investigation of the spatial and spectral characteristics of Kes 79 using multiple archival *XMM-Newton* observations of this remnant. We determine the global X-ray properties of Kes 79 and estimate the ambient density across the remnant. We also performed a similar analysis for Galactic SNR Kesteven 78 (Kes 78), but due to large uncertainties in the  $\gamma$ -ray background model, no conclusion can be made about an excess of GeV  $\gamma$ -ray associated with the remnant.

**Key words:** gamma rays: ISM – ISM: individual objects (Kesteven 79, G33.6+0.1, Kesteven 78, G32.8–0.1) – ISM: supernova remnants

*Online-only material:* color figures

### 1. INTRODUCTION

Supernova remnants (SNRs) have long been regarded as efficient accelerators of Galactic cosmic rays (CRs). As predicted by diffusive shock acceleration, the shock front of an SNR is expected to naturally accelerate electrons and ions with a power law momentum distribution (e.g., Malkov & O’C Drury 2001), which produces non-thermal emission from the SNR. The existence of this population of particles is inferred directly from  $\gamma$ -rays, while the nature of the  $\gamma$ -ray emission and the efficiency of the particle acceleration is characterized using observations in multiple wavelengths. Non-thermal X-ray emission from a number of SNRs such as SN 1006 (Koyama et al. 1995; Reynolds 1998), Vela Jr. (Aschenbach 1998), RX J1713.7–3946 (Uchiyama et al. 2007), and Tycho (Warren et al. 2005) has established that a population of relativistic electrons can be accelerated to TeV energies at SNR shocks. Ground-based measurements of TeV  $\gamma$ -ray emission from SNRs such as Tycho (Acciari et al. 2011; Morlino & Caprioli 2012) suggest that there is a population of particles that are being accelerated to energies approaching the knee ( $E_{\text{knee}} \sim 10^{15}$  eV) of the CR energy spectrum. Even with this evidence, there has been an ongoing debate in the literature (reviewed in Reynolds 2008) as to whether this  $\gamma$ -ray emission arises from relativistic hadrons interacting with the ambient medium (hadronic in origin), inverse Compton scattering, or non-thermal bremsstrahlung emission from high-energy electrons (leptonic origin).

Gamma-rays can be produced from the decay of a neutral pion into two photons. This decay results from the interaction of relativistic ions with ambient material via proton–proton interactions (Claussen et al. 1997). The two  $\gamma$ -rays in the neutral pion’s rest frame have an energy of  $\frac{1}{2}m_{\pi}c^2 = 67.5$  MeV, where  $m_{\pi}$  is the rest mass of  $\pi^0$  and  $c$  is the speed of light. Molecular

clouds (MCs) are a large source of protons, hence SNRs that are known to be interacting with dense MCs provide effective targets for detecting and analyzing emission from accelerated hadrons. The interaction of an SNR’s shockwave with dense molecular material is often inferred from the detection of 1720 MHz hydroxyl (OH) masers in the direction of the SNR (Hewitt et al. 2009). Additionally, the combination of the detection of molecular line broadening and/or asymmetric profiles, the enhancement of excitation line ratios such as  $J = 2 \rightarrow 1/J = 1 \rightarrow 0$ , and the detection of [Fe II] or H<sub>2</sub> line emission due to rotational–vibrational coupling or morphological agreement of molecular features with SNR features all provide persuasive evidence for SNR–MC interactions (Chen et al. 2013).

Observations of GeV to TeV  $\gamma$ -rays allow one to identify  $\pi^0$ -decay signatures that can provide information about the parent accelerated protons. Compared to other  $\gamma$ -ray telescopes such as the Energetic Gamma-Ray Experiment Telescope, the Large Area Telescope (LAT) on board the *Fermi Gamma-ray Space Telescope* has significantly improved the sensitivity and resolution in the MeV–GeV energy range, providing new opportunities for studying astrophysical objects such as SNRs. Since its launch, there have been multiple reports of the detection of GeV  $\gamma$ -ray emission from a large number of SNRs using data obtained from the *Fermi*-LAT, such as IC443 (Abdo et al. 2010b; Ackermann et al. 2013), W44 (Abdo et al. 2010a; Ackermann et al. 2013), W41, MSH17–39, G337.0–0.1 (Castro et al. 2013), G349.7–0.5, CTB 37A, 3C 391, G8.7–0.1 (Castro & Slane 2010), and Tycho (Giordano et al. 2012). Using these measurements, many authors have modeled the  $\gamma$ -ray spectra of these remnants to determine the mechanism behind this emission. However, it has been difficult to unequivocally establish whether the  $\gamma$ -ray emission arises from the interaction of relativistic protons with the surrounding ambient medium or

from inverse Compton or non-thermal bremsstrahlung emission. Observations of RX J1713.7–3946 using the *Fermi*-LAT have suggested that the  $\gamma$ -ray emission is dominated by leptonic processes (Ellison et al. 2010; Abdo et al. 2011). However, assuming that the SNR is interacting with a clumpy interstellar medium, Inoue et al. (2012) concluded that the  $\gamma$ -rays resulted from pion decay. Gamma-ray data from the *Fermi*-LAT has also been combined with other MeV-GeV observations, such as AGILE observations of SNR W44, which strongly suggested that  $\pi^0$ -decay dominates the observed  $\gamma$ -ray emission (Giuliani et al. 2011). This conclusion was confirmed by Ackermann et al. (2013), who detected the characteristic pion-decay feature in the  $\gamma$ -ray spectra of W44 and IC443 using the *Fermi*-LAT.

Kes 79 (G33.6+0.1) is a Galactic SNR that was first discovered by Caswell et al. (1975) using the 408 MHz Molonglo and 5000 MHz Parkes radio continuum survey. The remnant appears to consist of two concentric incomplete radio shells with several short, bright radio filaments toward the center of the remnant (Velusamy et al. 1991; Frail & Clifton 1989). Using single-based line interferometry over a limited range of velocities, Caswell et al. (1975) produced an H I absorption spectrum in the direction of Kes 79, which was used to estimate a lower limit of 7 kpc for the kinematic distance. This distance estimate implies that the diameter of Kes 79 has a lower limit of 20 pc. This is several times the size of a young SNR (less than a thousand years old), implying that Kes 79 is at least several thousand years old (Green & Dewdney 1992). This conclusion was also obtained by Sun et al. (2004), who derived a Sedov age of 5.9–7.8 kyr using a shock temperature of 0.4–0.7 keV.

Using the Dominion Radio Astrophysical Observatory, Green (1989) detected an unusually broad 1667 MHz OH absorption feature coincident with Kes 79. It was found at a position  $(\alpha_{J1950}, \delta_{J1950}) = (18^{\text{h}}50^{\text{m}}10^{\text{s}}, +00^{\circ}35'00'')$ , with local standard of rest (LSR) velocity between +95 and +115 km s<sup>-1</sup>. This absorption feature coincides with a nearby MC found at the same velocity, which suggests that the remnant's shock wave is interacting with this MC. The CO survey conducted by Scoville et al. (1987) reveals a large elongated MC at a velocity of 100 km s<sup>-1</sup> overlapping the eastern and southeastern region of Kes 79. The suggestion that Kes 79 is interacting with nearby MCs is also supported by the detection of extended, bright <sup>12</sup>CO  $J = 1 \rightarrow 0$  emission and strong HCO<sup>+</sup>  $J = 1 \rightarrow 0$  emission from the east and southeastern regions of Kes 79 at a velocity of 105 km s<sup>-1</sup> by using the NRAO 12 m telescope (Green & Dewdney 1992). As the mean hydrogen density of the MC associated with Kes 79 is much less than the density required to produce significant HCO<sup>+</sup> emission, the authors suggested that the observed HCO<sup>+</sup> emission arises from the interaction with the SNR shock. Using the Parkes telescope, Green et al. (1997) detected 1720 MHz line emission from Kes 79, while Zubrin & Shulga (2008) reported on the detection of a 95 GHz methanol maser. However, observations with the 12 m Arizona Radio Observatory and Very Large Array (VLA) failed to confirm the methanol maser detection (Frail 2011). These observations provide additional evidence for a kinematic distance of  $\sim 7$  kpc.

Sun et al. (2004) used a 30 ks *Chandra* ACIS-I observation to reveal the rich structure of the X-ray emission of Kes 79, implying a complicated surrounding environment. There are many bright and faint X-ray filaments, three partial X-ray shells, a loop in the southwest and a “protrusion” toward the northeast. Nearly all of these spatial structures have a corresponding radio structure. Using the semi-analytic, thin-shell approximation

for an SNR shock crossing a density jump derived by Chen et al. (2003), Sun et al. (2004) derived an average value of 0.36 cm<sup>-3</sup> for the ambient density. Using two 30 ks archival *XMM* observations, Giacani et al. (2009) derived a global X-ray spectrum, which indicated dominant emission from Mg, Si, S, and Fe, consistent with results derived using *ASCA* (Sun & Wang 2000; Tsunemi & Enoguchi 2002).

Kes 78 (G32.8–0.1) is a Galactic SNR that was first identified in a 408 MHz and 5000 MHz radio continuum survey by Kesteven (1968) and Caswell et al. (1975), respectively. It is an elongated shell type SNR that is 20'  $\times$  10' in diameter and has a partially brightened non-thermal radio shell with a spectral index of  $-0.5$  (Kassim 1992). In the literature, there are multiple estimates of the distance of Kes 78 using a number of different measurements, (e.g., Caswell et al. 1975; Allakhverdiev et al. 1983; Gosachinskii & Khersonskii 1985; Case & Bhattacharya 1998; Boumis et al. 2009; Xu & Zhang 2009). Zhou & Chen (2011) used H I absorption spectra at different LSR velocities and the association of Kes 78 with an MC at an LSR velocity of  $\sim 81$  km s<sup>-1</sup> to derive a distance of 4.8 kpc. Gosachinskii & Khersonskii (1985), using H I observations, estimated the age of the remnant to be  $\sim 1.2 \times 10^5$  yr.

Koralesky et al. (1998) detected a single, 86.1 km s<sup>-1</sup> 1720 MHz OH maser at a position of  $(\alpha_{J2000}, \delta_{J2000}) = (18^{\text{h}}51^{\text{m}}48^{\text{s}}04, 00^{\circ}10'35'')$  using the VLA. This maser is coincident with the eastern edge of Kes 78's radio shell. The detection of this maser indicates that the SNR shock-wave is interacting with the surrounding MCs. Observations of <sup>12</sup>CO reveal that Kes 78 is coincident with dense MCs found toward the east of the remnant where the OH maser emission arises (Zhou & Chen 2011). The distribution of <sup>12</sup>CO traces out the eastern radio shell of the remnant and it indicates that Kes 78 is expanding into a CO cavity. Elevated <sup>12</sup>CO  $J = 2 \rightarrow 1/J = 1 \rightarrow 0$  ratios along the boundary of the SNR also suggest the presence of perturbations in the molecular gas due to the interaction of the SNR shock (Zhou & Chen 2011). The kinematic distance to Kes 78 implied by the association of MCs is  $4.8_{-0.7}^{+3.1}$  kpc.

Zhou & Chen (2011) detected X-rays arising from the northeastern region of the radio shell using *XMM-Newton*. This emission can be modeled using a low density, under-ionized plasma with a temperature of  $kT \sim 1.5$  keV. The H.E.S.S. collaboration reported an extended very high energy (VHE)  $\gamma$ -ray source, HESS J1852–000, that could be associated with the eastern edge of the remnant interacting with a nearby molecular cloud or with a previously undiscovered pulsar-wind nebula (Kosack et al. 2011).<sup>6</sup>

In this paper, we study the  $\gamma$ -ray emission coincident with Kes 79 and Kes 78 and investigate the nature of this emission by modeling the broadband spectrum. Additionally, we perform a spatial and spectral analysis of archival *XMM* data for Kes 79 and report on the X-ray properties of this remnant. In Section 2, we describe how the *Fermi*-LAT data are analyzed and present the results of this analysis. In Section 3, we present our method and the results of our spatial and spectral analysis of archival *XMM* data for Kes 79, while in Section 4, we discuss the implication of the results obtained.

## 2. FERMI-LAT OBSERVATIONS OF SNR Kes 79 AND Kes 78

For this study, 52 months of data, collected from 2008 August to 2012 December using the *Fermi Gamma-ray Space*

<sup>6</sup> <http://www.mpi-hd.mpg.de/hfm/HESS/pages/home/som/2011/02/>

Telescope Large Area Telescope (*Fermi*-LAT), were analyzed. As previously detailed in Ackermann et al. (2012), only events belonging to the “Pass7 V6” source class were selected for this study. Using this source class reduces the residual background of the data. We used the “Pass7 version 6” instrument response function (IRF), which was generated by using data recorded in-flight and incorporates effects that were not included in the pre-launch analysis such as accidental coincidence effects in the detectors (Ackermann et al. 2012). For the IRFs that we used in this analysis, the systematic uncertainties in the effective area of the *Fermi*-LAT are 10% at 100 MeV, decreasing to 5% at 560 MeV, and increasing to 10% at 10 GeV.<sup>7</sup> To reduce the effect of terrestrial albedo  $\gamma$ -rays on the data, we selected events coming from zenith angles smaller than  $100^\circ$ . To further decrease the effects of these terrestrial  $\gamma$ -rays, we also excluded events that were detected when the rocking angle of the LAT was greater than  $52^\circ$ . The analysis included data from circular regions within a radius of  $20^\circ$ , centered on Kes 79 and Kes 78. The  $\gamma$ -ray data in the direction of Kes 79 and Kes 78 were analyzed using the Fermi Science Tools v9r27p1.<sup>8</sup>

To obtain morphological, positional, and spectral information about the remnant, the maximum likelihood fitting technique, *glike*, was used. Likelihood analysis was used on the *Fermi*-LAT data due to the low detection rates of  $\gamma$ -rays and the large point spread function (PSF) of the *Fermi*-LAT. *glike* calculates the parameters that best fit the emission model by maximizing the joint probability of the data, given a specific emission model (Mattox et al. 1996). *glike* uses diffuse Galactic and isotropic emission models to account for the  $\gamma$ -rays generated by CRs interacting with background photons, the interstellar medium, the extragalactic diffuse, and residual backgrounds. It also includes known  $\gamma$ -ray sources by placing them at fixed positions and calculating the background contribution from these sources to the data. The  $\gamma$ -ray emission from the Milky Way is described by the mapcube file `gal_2yearp7v6_v0.fits`, while the table `iso_p7v6source.txt` models the isotropic emission arising from extragalactic diffuse and residual backgrounds.<sup>9</sup>

### 2.1. Spatial Analysis

Gamma-ray data, with energy ranging from 2 to 200 GeV converted in the front section of the LAT, were selected to determine the spatial characteristics of the  $\gamma$ -ray emission from Kes 79 and Kes 78. These events were chosen as they improve the angular resolution of the data. The  $1\sigma$  containment radius angle for front-selected photons in this energy band is  $\leq 0.3^\circ$ . Test statistic (TS) maps constructed using *gtlmap* allow one to determine the detection significance as well as the position and extent of the source. The TS is defined as the logarithmic ratio of the likelihood of a point source being found at a given position on a spatial grid, to the likelihood of the model without the additional source,  $2 \log(L_{ps}/L_{null})$ . The image resolution of these TS maps is defined by the size of the grid used for this analysis; we set the grid to be  $0.05^\circ$ .

To analyze the surrounding neighborhood of the remnant, we generated count maps of  $1^\circ \times 1^\circ$  regions centered around Kes 79 and Kes 78. The count maps were smoothed by a

Gaussian of width similar to the PSF of the events selected and are presented in Figure 1. The radio emission from Kes 79 and Kes 78, as observed during the VLA Galactic plane survey, are overlaid as the green contours (Stil et al. 2006). Possibly associated with Kes 79 is an unresolved  $\gamma$ -ray source designated as 2FGL J1852.7+0047c in the *Fermi*-LAT Second Source Catalogue, while possibly associated with Kes 78 is an unresolved  $\gamma$ -ray source designated as 2FGL J1850.7–0014c. In the Second Source Catalogue, these two *Fermi*-LAT sources are characterized by photon power law indexes of  $\Gamma = 2.53 \pm 0.21$  and  $\Gamma = 2.85 \pm 0.18$ , respectively. The photon flux of these sources over an energy of 1 GeV–100 GeV is  $(1.8 \pm 0.5) \times 10^{-9}$  photons  $\text{cm}^{-2} \text{s}^{-1}$  and  $(4.3 \pm 0.9) \times 10^{-9}$  photons  $\text{cm}^{-2} \text{s}^{-1}$ , respectively. The position and extent of each of these  $\gamma$ -ray sources are plotted as a magenta circle, in Figure 1.

To determine the significance of the detection of the  $\gamma$ -ray emission from Kes 79 and Kes 78, we generated a TS map for each remnant. For Kes 79, we calculated the TS map over an energy range of 0.2–2 GeV and obtained a detection significance of  $\sim 7\sigma$ . The TS map is presented as the cyan contours overlaid in Figure 1(a). The TS contours suggest that the  $\gamma$ -ray emission in this region is associated with Kes 79. For Kes 78, we calculated a TS map over an energy range of 1 GeV–3.2 GeV and overlaid the TS map as cyan contours in Figure 1(b). We select this range, as the resolution of the *Fermi*-LAT below 1 GeV is significantly affected by the large uncertainty in the Galactic diffuse emission model. The TS contours do not show a concentration (or peak) of flux at the centroid of Kes 78, in contrast to the significant  $\gamma$ -ray emission seen in the region centered on Kes 79 (Figure 1(a)). The detection significance of  $\sim 5$ – $6\sigma$  in the region of Kes 78 is equal to or less than the detection significance seen everywhere in the field of view, indicating that the observed  $\gamma$ -ray emission is dominated by uncertainties in the background model or by  $\gamma$ -ray emission spilling over from nearby sources. Thus, it is not possible to claim an excess of GeV  $\gamma$ -ray emission associated with the remnant.

### 2.2. Spectral Analysis

The spectral energy distribution characteristics of the *Fermi*-LAT emission coincident with Kes 79 are produced by using events with an energy of 0.2–200 GeV. This energy range is selected for multiple reasons, including avoiding source confusion, avoiding the large flux uncertainties that arise below 0.2 GeV due to limitations of the Galactic diffuse model, and reducing the influence that the rapidly changing effective area of the instrument at low energies has on the data. We perform the spectral analysis by modeling the flux at each energy bin and then estimate the parameters that best fit the data using the maximum likelihood technique *glike*. We also included in the likelihood fits background sources from the 24 month *Fermi*-LAT Second Source Catalogue (Nolan et al. 2012) that are found within a  $20^\circ$  circular region centered on Kes 79.<sup>10</sup> For Kes 79, all evident background sources were identified in the *Fermi*-LAT Second Source Catalogue and the associated parameters from the catalog were used.

For each energy bin, the normalization of the diffuse Galactic component was left free to account for correlations between close-by sources. In addition to using the statistical uncertainties from the likelihood analysis, the systematic uncertainty associated with the Galactic diffuse emission was also considered by

<sup>7</sup> <http://fermi.gsfc.nasa.gov/ssc/data/analysis/LATcaveats.html>

<sup>8</sup> The Fermi Science Support Center has made publically available the Science Tools package and related documentation at <http://fermi.gsfc.nasa.gov/ssc>.

<sup>9</sup> The most up to date `gal_2yearp7v6_v0.fits` and `iso_p7v6source.txt` where obtained from <http://fermi.gsfc.nasa.gov/ssc/data/access/lat/BackgroundModels.html>.

<sup>10</sup> The data for these sources is made available by the Fermi Science Support Center and is found at [http://fermi.gsfc.nasa.gov/ssc/data/access/lat/2yr\\_catalog/](http://fermi.gsfc.nasa.gov/ssc/data/access/lat/2yr_catalog/).

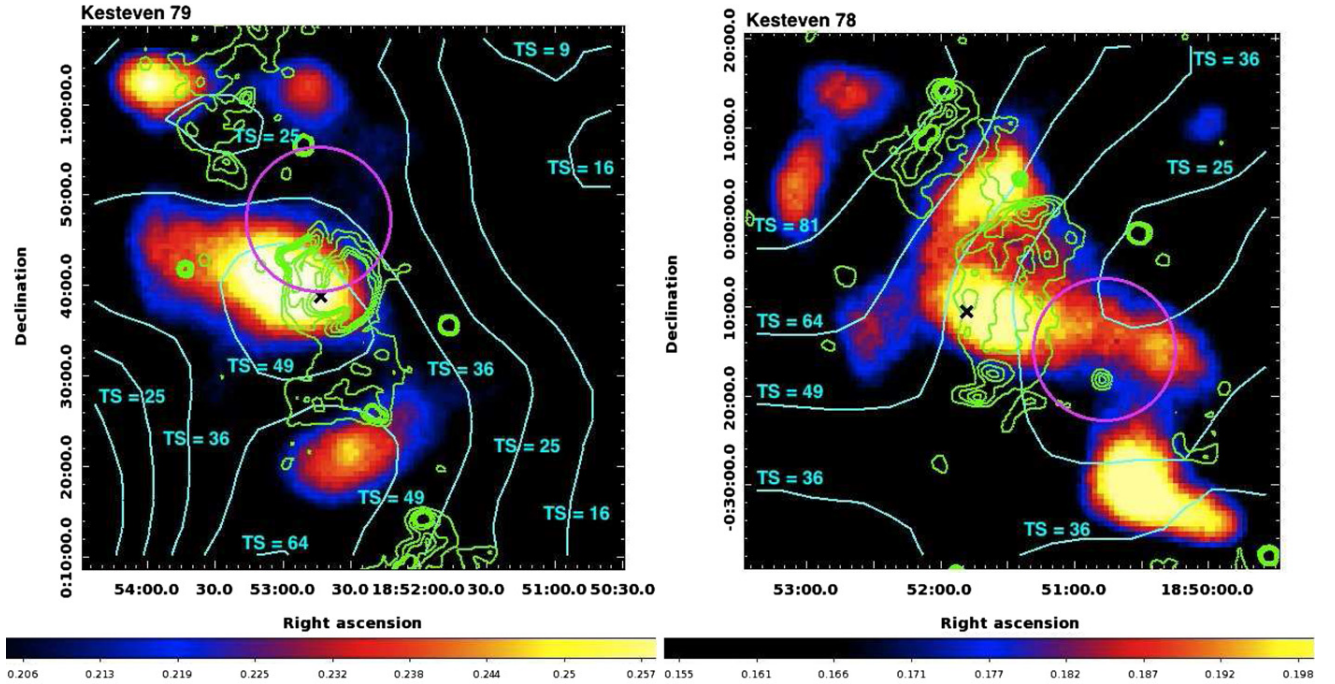


**Figure 1.** Smoothed *Fermi*-LAT count maps of events with energy of 2–200 GeV in a region  $1^\circ \times 1^\circ$  surrounding Kes 79 and Kes 78, respectively (units are counts degree $^{-2}$ ). The pixel binning is  $0'01$  and the maps are smoothed with Gaussians of width 0.2 arcmin. The magenta circles correspond to the *Fermi*-LAT sources, 2FGL J1852.7+0047c and 2FGL J1850.7–0014c, located near Kes 79 and Kes 78, respectively. The radio emission observed during the VLA Galactic plane survey are overlaid as the green contours (Stil et al. 2006), while the *Fermi*-LAT TS map contours are shown in cyan. The square root of the TS value is approximately equal to the detection significance. The position of the 1667 MHz OH absorption feature for Kes 79 and the position of the 1720 MHz OH maser for Kes 78 are indicated by the black crosses. The scale corresponds to the number of counts degree $^{-2}$ .

(A color version of this figure is available in the online journal.)

artificially altering the normalization of the Galactic background by  $\pm 6\%$  from the best-fit value at each energy bin. This method is modeled from similar treatments presented in Castro & Slane (2010) and Castro et al. (2012).

The  $\gamma$ -ray spectrum of the *Fermi*-LAT sources coincident with Kes 79 is shown in Figure 2. Upper limits are plotted as blue triangles. The  $\gamma$ -ray spectrum of Kes 79 can be fitted using a simple power law with a spectral index of  $2.6 \pm 0.1$ , while an exponential cut-off power law with  $E_{\text{cut}} = 2.7 \pm 0.6$  GeV and a spectral index of  $2.00 \pm 0.4$  significantly improves the fit. Assuming a distance of 7 kpc to Kes 79, the luminosity of this  $\gamma$ -ray source for an energy range of 0.1–100 GeV is  $6.1 \times 10^{35}$  erg s $^{-1}$ . Both the simple power law and exponential cut-off models for Kes 79 are shown in Figure 2 as the green dotted and cyan dashed plots, respectively. The parameters that define these best fits, along with the detection significance and positional information of Kes 79, are summarized in Table 1.

### 3. XMM-NEWTON OBSERVATIONS AND ANALYSIS

For Kes 79 we analyzed 21 archival *XMM-Newton* observations which were found within a radius of 12 arcmin of the centroid of Kes 79 (see Table 2). These observations were performed over a period of five years and have an effective exposure time of  $\sim 447$  ks and  $\sim 456$  ks for the MOS1 and MOS2 detector, respectively. All *XMM-Newton* observations simultaneously acquired EPIC-MOS, and EPIC-pn observations, with the pn detector operating in “small window” mode, while the MOS cameras operated in “full frame” mode. For all observations, the full SNR was included in the field of view of the MOS cameras, while only part of the remnant was detected by

EPIC-pn due to it operating in “small window” mode. Thus for this analysis, we only used data from the MOS cameras.

Giacani et al. (2009) used the *XMM-Newton* observations 204970201 and 204970301 to compare the morphology of the X-ray emission and 324 MHz VLA observations of Kes 79, while Halpern & Gotthelf (2010) used the EPIC-pn observations of 16 of the *XMM-Newton* observations listed in Table 2 to perform a dedicated series of timing observations of PSR J1852+0040 found in Kes 79. We re-analyzed all 21 archival EPIC MOS observations previously presented in the literature using the *XMM-Newton* Science Analysis System (SAS) version 12.0.1 and the most up to date calibration files.<sup>11</sup> All analyses were completed by starting from the observational data files. For the MOS cameras, we selected single to quadruple patterned events. For both spectral and imaging analysis, all event files were filtered such that all flagged events were removed and periods of high background and/or photon flare contamination were removed as suggested in the current SAS analysis threads and XMM-Newton Users Handbook.<sup>12</sup> We generated count rate histograms for all observations with energies above 10 keV to determine the time intervals where the emission from the MOS cameras was affected by periods of high background and/or photon flares. The effective exposures of the MOS1 and MOS2 observations after filtering are shown in Table 2.

<sup>11</sup> Documentation related to the SAS package, as well as its download, is distributed by XMM-Newton Science Operations Center at <http://xmm.esac.esa.int/sas/>.

<sup>12</sup> [http://xmm.esac.esa.int/external/xmm\\_user\\_support/documentation/uhb/index.html](http://xmm.esac.esa.int/external/xmm_user_support/documentation/uhb/index.html)

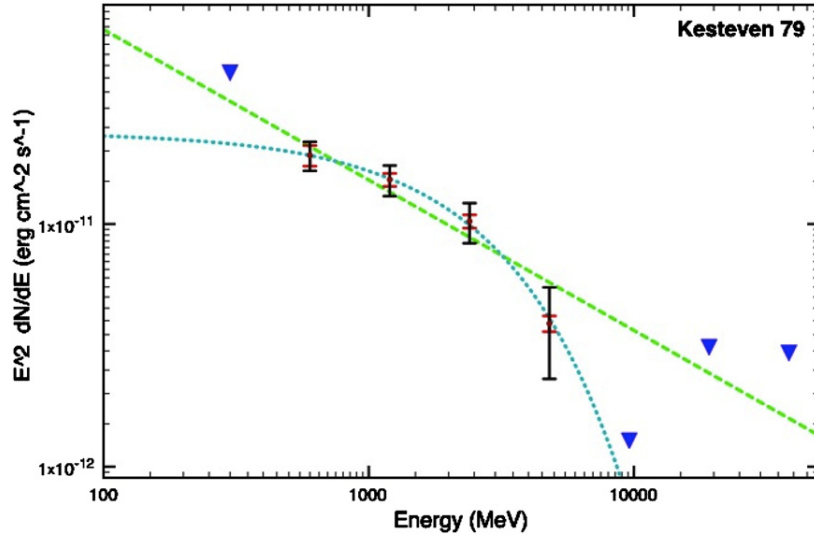


**Figure 2.** *Fermi*-LAT gamma-ray spectrum of Kesteven 79. The statistical errors are plotted in black, systematic errors are plotted in red, and upper limits are plotted in blue. The simple power law models and exponential cut-off model described by the parameters in Table 1 are shown as the green dotted line and the cyan dashed line, respectively.

(A color version of this figure is available in the online journal.)

**Table 1**  
The Spatial and Spectral Fit Parameters for the Kes 79 *Fermi*-LAT Data

Name	Spatial		Spectral Fit						
	R.A. (deg)	Decl. (deg)	$F(0.1\text{--}100\text{ GeV})$ ( $10^{-7}$ photons $\text{GeV cm}^{-2} \text{s}^{-1}$ )	$\Gamma_{\text{pwl}}$	$\chi^2_{\text{pwl}}$ (dof)	$\Gamma_{\text{cut}}$	$E_{\text{cut}}$ (GeV)	$\chi^2_{\text{exp}}$ (dof)	TS Value
Kes 79	283.121	+0.645	$0.63^{+0.70}_{-0.30}$	$2.62 \pm 0.12$	2.87(2)	$2.00 \pm 0.38$	$2.71 \pm 0.64$	0.27(1)	$\sim 7\sigma$

**Table 2**  
Archival *XMM-Newton* Observations of Kes 79 and Their Corresponding Total and Effective Exposure Times as Used in Our Analysis

Obs. ID	R.A. (J2000)	Decl. (J2000)	Observation Date	Exposure (ks)	MOS 1		MOS 2	
					Good Exposure (ks)	Good Exposure (ks)	Good Exposure (ks)	Good Exposure (ks)
204970201	18 52 35.54	+00 39 40.4	2010 Apr 18	31.4		28.7		30.3
204970301	18 52 35.65	+00 39 36.4	2010 Apr 23	31.4		30.9		30.5
400390201	18 52 34.90	+00 39 42.4	2010 Jun 8	30.4		28.7		29.4
400390301	18 52 42.56	+00 40 52.2	2003 Jul 20	34.5		34		33.6
550670201	18 52 34.72	+00 39 48.7	2009 Aug 19	26.9		21.6		21.8
550670301	18 52 34.61	+00 39 46.3	2009 Aug 21	35.4		30.4		30.5
550670401	18 52 34.64	+00 39 48.1	2009 Aug 23	40.4		36.1		35.5
550670501	18 52 34.68	+00 39 43.0	2009 Aug 29	34.1		32.7		33.1
550670601	18 52 34.82	+00 39 43.7	2010 Aug 10	40.4		34.7		34.1
550670901	18 52 42.67	+00 40 48.5	2003 Sep 17	26.9		25		25.4
550671001	18 52 42.53	+00 40 49.0	2003 Sep 16	27.9		23.5		24.5
550671101	18 52 42.31	+00 40 50.4	2003 Sep 25	23.0		19.0		18.7
550671201	18 52 42.49	+00 40 52.2	2003 Sep 23	27.9		17.7		19.4
550671301	18 52 42.24	+00 40 58.1	2004 Sep 4	26.9		22.2		22.7
550671401	18 52 42.67	+00 40 48.4	2003 Sep 17	5.93		5.4		5.3
550671501	18 52 42.28	+00 40 52.0	2003 Sep 25	6.42		0.0		4.3
550671601	18 52 42.49	+00 40 52.0	2003 Sep 23	5.63		5.0		5.1
550671701	18 52 42.24	+00 40 57.9	2004 Sep 4	4.43		3.7		3.8
550671801	18 52 41.92	+00 41 02.9	2004 Sep 22	28.9		25.4		25
550671901	18 52 42.10	+00 40 58.4	2004 Sep 10	31.4		18.1		19.5
550672001	18 52 42.10	+00 40 58.3	2004 Sep 10	5.13		3.8		3.6

### 3.1. Imaging

To analyze the morphology of Kes 79, we produced an image of the entire remnant by combining all 21 filtered observations of MOS1 and MOS2 using the SAS task *emosaic*. This task

produces a single exposure-corrected intensity image of the SNR. For each camera, we generated maps in the energy bands 0.5–1.195 keV, 1.195–1.99 keV, and 1.99–7.00 keV.

The *XMM-Newton* EPIC MOS mosaic image of Kes 79 in the 0.5–7.0 keV band is presented in Figure 3(a). The

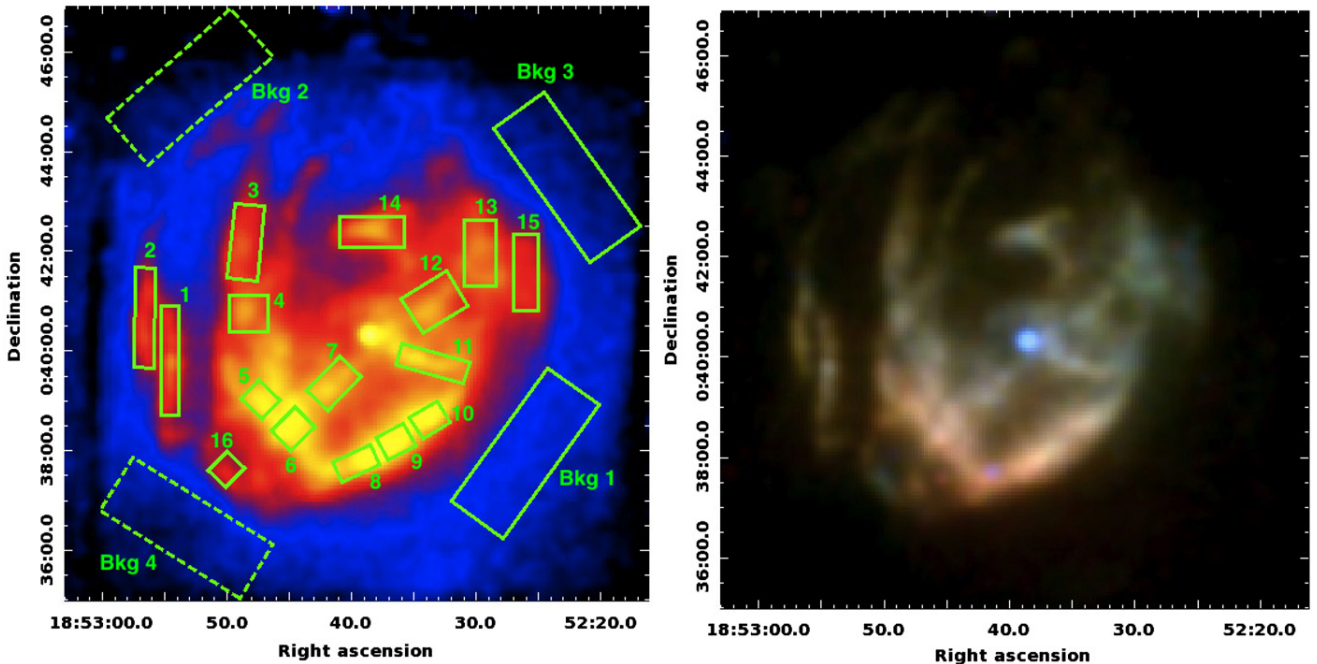


**Figure 3.** (a) A 0.5–7 keV exposure corrected image of the X-ray emission from Kes 79. This was created using the *XMM-Newton* SAS task *mosaic*. The image has been smoothed with a Gaussian function of width  $3''$ . Overlaid in green are the regions we use for spectral extraction, described in Section 3.2, and the four background regions we used. (b) Exposure corrected RGB image of SNR Kes 79 created using EPIC MOS1 and MOS2 data. Red corresponds to the 0.5–1.195 keV energy band, green to 1.195–1.99 keV, and blue to 1.99–7.00 keV. The RGB image has been smoothed with a Gaussian function of width  $3''$ . The relative intensity levels of the different color images have been adjusted to highlight spectral structures of the emission.

(A color version of this figure is available in the online journal.)

X-ray emission observed with *XMM-Newton* corresponds well to the rich spatial structure observed by Sun et al. (2004) using 29.3 ks of *Chandra* data. A large majority of the emission comes from the center of the remnant, with faint X-ray emission toward the northeast. There are multiple faint and bright X-ray filaments and evidence of multiple partial shells highlighted by bright X-ray emission toward the south. Also observable in this image is the X-ray emission from the pulsar PSR J1852+0040. Our mosaic image mimics the 0.5–5 keV *XMM* image of Kes 79 by Giacani et al. (2009).

With the aim of analyzing any possible spectral variation in Kes 79, we also created an RGB image of the remnant, which is found in Figure 3(b). We generated this image by combining images of events from the MOS1 and MOS2 cameras in the energy bands 0.5–1.195 keV (red), 1.195–1.99 keV (green), and 1.99–7.00 keV (blue). The relative intensities of the color images have been adjusted in the RGB representation to highlight all structures. This image reveals a very filamentary and clumpy morphology, with the southern shell producing a significant amount of soft X-rays. The pulsar, which has a hard spectrum, is seen as the bright blue dot in the center of the image.

### 3.2. Spectroscopy

The aim of our spectral analysis of Kes 79 is to perform a spatially resolved spectral study of the remnant. To do this, we analyze the variation in the spectral parameters in different regions of the remnant.

For our analysis, we used *XMM* observations that had a good exposure time of 10 ks or more, as the event files with less than this amount produced spectra with less than 100 counts. The X-ray spectra were extracted from the filtered and cleaned event files using the SAS task *evselect*. The tasks *arfgen* and *rmfgen*

were used to generate a spectral response and effective area file for each extracted region.

The background of *XMM-Newton* consists of the Cosmic X-ray background and a time-variable non-X-ray background resulting from electronic noise, solar protons, and CRs interacting with the detector (Kuntz & Snowden 2008). Above  $\sim 5$  keV, the X-ray spectrum for these observations is dominated by background. We accounted for the background of each observation by selecting four source-free regions as shown in Figure 3(a). Four background regions were selected to ensure that any gaps due to mosaicking would not affect the spectra obtained.

The combined spectra were analyzed with the X-ray software XSPEC version 12.8.0, over an energy range of 0.5–10 keV. Each energy bin was required to have a minimum of 25 counts and the reduced  $\chi^2$  statistic was used as the best-fit model discriminator. To investigate the emission of the remnant, we used the non-equilibrium ionization (NEI) plasma emission models, PSHOCK and VPSHOCK (Borkowski et al. 2001). These models describe a plane-parallel shock front interacting with a plasma and are characterized by a constant electron temperature ( $kT$ ) and an upper and lower limit on the ionization timescale ( $\tau_l = n_e t_l$  and  $\tau_u = n_e t_u$ ). The absorption, upper limit of the ionization timescale, temperature, normalization of both models, and the abundances of Ne, Mg, Si, and S, were left as free parameters. All other elemental abundances were frozen to the solar values of Wilms et al. (2000) once we verified that their variation did not significantly improve the model fit of the data. As these NEI models do not include atomic data for the Argon emission, an additional Gaussian component with a width of 0.01 keV and line energy of 3.1396 keV was added to account for this feature in the spectra fitting. The normalization of this additional component was left free.

### 3.2.1. Spectral Properties of Individual Regions

To investigate the spectral variation across Kes 79, we perform a spatially resolved spectral analysis by extracting X-ray spectra from 16 regions shown in green in Figure 3(a). These regions were selected as they correspond to variations in the color distribution in the RGB image or variation in the flux as observed in the X-ray image. To increase the signal-to-noise ratio, we combined the X-ray spectra extracted for all 16 MOS1 and MOS2 observations with good time events of 10 ks or greater, producing combined MOS1 and combined MOS2 X-ray spectra for each region. This was done by using the HEASOFT tasks *mathpha*, *fparkey*, *marfrmf*, and *addrmf*. The combined spectra for all regions were grouped using the FTOOLS command *grppha*.

Initially, the spectra from all extracted regions were fitted using a single component model (VPSHOCK) and the XSPEC absorption model TBABS (Wilms et al. 2000). By itself, TBABS\*VPSHOCK was able to account reasonably well for the X-ray emission below  $\sim 3$  keV, but it failed to fit the higher energy component of the spectrum, and as a consequence the fits resulted in relatively large reduced chi-squared values ( $\chi^2/(\text{dof}) > 1.80$ ). Subsequently, we fitted the spectra of each region with a two-component plasma model, VPSHOCK+PSHOCK, and TBABS. The parameters of the best-fit models for all extracted spectra are shown in Table 3, where the uncertainties correspond to the 90% confidence level.

All regions require two thermal components, indicating that the plasma of Kes 79 contains a soft and hard temperature component. The temperatures derived for the hard component in regions 3–14 range between  $0.61 \pm 0.03$  and  $1.36 \pm 0.3$  keV, while for the filamentary structures encompassed by regions 1–2, the hard temperatures are equal to  $0.55^{+0.03}_{-0.01}$  keV and  $0.49 \pm 0.03$  keV, respectively. The derived VPSHOCK temperatures for regions 3–14 are, on average, comparable to the temperature derived by Sun et al. (2004) and Giacani et al. (2009), who used a single component NEI model, while the temperature of the filamentary structures are lower than global temperatures derived by Sun et al. (2004) and Giacani et al. (2009). The soft plasma (PSHOCK) component of Kes 79's X-ray emitting material is highly isothermal in nature, with all regions requiring a temperature of  $\sim 0.24$  keV.

All region-specific spectra are similar to each other, with strong emission lines coming from Si, S, and Mg, with some requiring Ne and Ar. All regions in the high  $kT$  component have super-solar abundances (e.g., larger than  $\sim 2$  times solar abundance) of Si and S, while Mg has  $\sim 1.5$  times solar abundance. We thus associate this component with shocked ejecta. All regions require approximately solar abundances of Ne, with the exception of region 7, which has an enhancement of Ne. Region 15 has the largest elemental abundances out of all the regions analyzed, with Mg, Si, and S requiring super-solar abundances. The inner regions closest to the X-ray position of the pulsar (regions 7, 11, and 12), and the filament described by region 2, all require the highest abundances of Mg, Si, and S overall. All regions require enhanced abundances of Mg, Si, and S, which indicates that the ejecta component is found everywhere throughout the remnant, implying that we observed X-ray emission from shocked ejecta. The abundances obtained in this analysis are larger than the values obtained by Sun et al. (2004) using their ionization equilibrium collisional plasma model or NEI collisional plasma models. This arises from the fact that in our analysis, we use the abundance table by Wilms et al. (2000), while Sun et al. (2004) uses the table derived by Anders & Grevesse (1989).

The shocked ejecta, modeled using VPSHOCK, have an ionization timescale of  $\sim 10^{11} \text{ cm}^{-3} \text{ s}$  in all regions. These values agree well with the ionization timescales derived by Sun et al. (2004) and Giacani et al. (2009). The ionization timescale of the material swept up by the forward shock as derived using the PSHOCK model is fixed to  $1 \times 10^{12} \text{ cm}^{-3} \text{ s}$ , as initial spectral analysis yielded ionization timescales of this magnitude. The high ionization timescale of all regions indicates that the soft plasma component is in ionization equilibrium (Vink 2012), while the hard plasma component across the whole remnant is far from ionization equilibrium.

The derived hydrogen column density for each region ranges between  $(2.08^{+0.03}_{-0.04} - 2.75^{+0.03}_{-0.04}) \times 10^{22} \text{ cm}^2$ . These values are higher than the estimated absorbing column density derived by Sun et al. (2004) using *Chandra* data ( $\sim 1.6 \times 10^{22} \text{ cm}^2$ ) and Giacani et al. (2009) using *XMM-Newton* data ( $\sim 1.5 \times 10^{22} \text{ cm}^2$ ). This discrepancy most likely arises from the fact that we use a different abundance table in our analysis and a two-component plasma model. These derived values indicate that the X-ray spectrum of Kes 79 is heavily absorbed by interstellar material.

### 3.2.2. Global Spectral Properties

To investigate the average spectral properties of Kes 79, we extracted a global X-ray spectrum from a circular region centered at  $(\alpha_{J2000}, \delta_{J2000}) = (18^{\text{h}}52^{\text{m}}41^{\text{s}}.31, +0^{\circ}40'52''.97)$  with a radius of 4.70 arcmin. This region enclosed the complete SNR as observed in X-rays. The background spectrum was extracted using the four source-free regions shown in Figure 3(a). We did this for each observation with good exposure times of 10 ks or greater and all spectra are binned with a minimum of 25 counts. We fit all 16 MOS1 and MOS2 observations simultaneously over an energy range of 0.5–10 keV. Similar to the spatial X-ray analysis, a single-component VPSHOCK model with enhanced abundances of Si, S, and Mg produced unsatisfactory fits, and was improved when we added a thermal component (PSHOCK) ( $\chi^2/(\text{dof}) = 1.07$ ). Figure 4 shows the global X-ray spectrum of Kes 79, while the values of these best-fit parameters with their corresponding  $1\sigma$  uncertainties are found in Table 4. This result implies that the plasma of Kes 79 consists of a hard component with a plasma temperature of  $0.77^{+0.006}_{-0.001}$  keV and a soft component with a temperature of  $0.24^{+0.0002}_{-0.001}$  keV. This is consistent with our fits of the individual regions. The temperatures derived by Sun et al. (2004) and Giacani et al. (2009) using *Chandra* and *XMM* data is similar to the temperature of the hard plasma component. The best-fit absorbing column density is  $N_{\text{H}} = 2.35^{+0.003}_{-0.01} \times 10^{22} \text{ cm}^2$  and is higher than values obtained by Sun et al. (2004) and Giacani et al. (2009) using a single NEI plasma model. Using the Anders and Grevesse abundance table, we obtained a column density similar to that obtained by Sun et al. (2004) and Giacani et al. (2009).

Using the best fit of the global X-ray spectrum and the total count rate, we derive an unabsorbed flux, for an energy range of 0.5–10 keV, of  $9.8 \times 10^{-10} \text{ erg cm}^{-2} \text{ s}^{-1}$  and a luminosity of  $5.6 \times 10^{36} \text{ erg s}^{-1}$  assuming a distance of 7 kpc. The luminosity derived in this analysis is a factor of two larger than the flux obtained by Sun et al. (2004) using *Chandra* and this most likely arises from the fact that we use a two component NEI plasma model, while Sun et al. (2004) uses a one component NEI model for their analysis.

### 3.2.3. X-ray Characteristics of Kes 79

Using the PSHOCK+VPSHOCK model parameters summarized in Table 3, we derive the density of the X-ray emitting

Table 3

Results from Fitting the Two-component Model, the VPSHOCK+PSHOCK Model, and the XSPEC Absorption Model TBABS to the 16 Different Regions Defined in Figure 3(a) with the 90% Confidence Ranges

Region	TBABS	Soft Component (PSHOCK)			Hard Component (VPSHOCK)						$\chi^2/(dof)$	
	nH ( $10^{22} \text{ cm}^{-2}$ )	kT (keV)	$\tau_w$ ( $10^{12} \text{ s cm}^{-3}$ )	Norm $\text{cm}^{-5}$ ( $10^{-2}$ )	kT (keV)	$\tau$ ( $10^{11} \text{ s cm}^{-3}$ )	Norm $\text{cm}^{-5}$ ( $10^{-3}$ )	Ne	Mg	Si		S
1	$2.43 \pm 0.05$	$0.19 \pm 0.01$	1	$5.94^{+2.5}_{-2.0}$	$0.55^{+0.03}_{-0.01}$	$2.76^{+0.6}_{-0.7}$	$3.61^{+0.1}_{-0.5}$	...	$1.29 \pm 0.8$	$2.31^{+0.1}_{-0.2}$	$2.50 \pm 0.3$	1.19
2	$2.51^{+0.06}_{-0.03}$	$0.20 \pm 0.02$	1	$3.14^{+2.5}_{-1.3}$	$0.49 \pm 0.03$	$2.61^{+0.9}_{-0.6}$	$3.41^{+1.0}_{-1.1}$	...	$1.42 \pm 0.1$	$2.69 \pm 0.3$	$2.83^{+0.5}_{-0.4}$	1.10
3	$2.48^{+0.04}_{-0.02}$	$0.25 \pm 0.01$	1	$3.77^{+1.2}_{-0.3}$	$0.78^{+0.02}_{-0.04}$	$1.56 \pm 0.2$	$2.71^{+0.6}_{-0.2}$	...	$1.52^{+0.08}_{-0.1}$	$2.53^{+0.2}_{-0.1}$	$2.53 \pm 0.2$	1.24
4	$2.14^{+0.02}_{-0.03}$	$0.22 \pm 0.01$	1	$3.62^{+0.3}_{-0.4}$	$0.69^{+0.01}_{-0.02}$	$1.99^{+0.3}_{-0.1}$	$3.51^{+0.4}_{-0.2}$	...	$1.44^{+0.06}_{-0.05}$	$2.18^{+0.09}_{-0.06}$	$2.33 \pm 0.12$	1.32
5	$2.12^{+0.02}_{-0.01}$	$0.23 \pm 0.005$	1	$4.00^{+1.2}_{-0.6}$	$0.75 \pm 0.02$	$1.74 \pm 0.2$	$3.89 \pm 0.3$	...	$1.39^{+0.05}_{-0.04}$	$2.11^{+0.06}_{-0.05}$	$2.06 \pm 0.1$	1.34
6	$2.27 \pm 0.03$	$0.25^{+0.009}_{-0.003}$	1	$3.72^{+0.7}_{-0.4}$	$0.80^{+0.03}_{-0.01}$	$2.44^{+0.2}_{-0.3}$	$4.40^{+0.09}_{-0.54}$	...	$1.40 \pm 0.04$	$1.94 \pm 0.06$	$1.88^{+0.12}_{-0.08}$	1.35
7	$2.08^{+0.03}_{-0.04}$	$0.26 \pm 0.01$	1	$3.67^{+0.4}_{-0.6}$	$1.05^{+0.05}_{-0.09}$	$9.25^{+0.16}_{-0.07}$	$1.34^{+0.6}_{-0.2}$	$1.79 \pm 0.27$	$1.84^{+0.13}_{-0.19}$	$3.23^{+0.44}_{-0.48}$	$2.87^{+0.30}_{-0.46}$	1.43
8	$2.09^{+0.02}_{-0.04}$	$0.25^{+0.02}_{-0.01}$	1	$2.35^{+0.4}_{-0.6}$	$0.67^{+0.03}_{-0.02}$	$3.31^{+0.6}_{-0.5}$	$4.08^{+0.6}_{-0.4}$	...	$1.41^{+0.07}_{-0.05}$	$2.07 \pm 0.1$	$2.25 \pm 0.2$	1.38
9	$2.30 \pm 0.03$	$0.23 \pm 0.01$	1	$4.09 \pm 0.1$	$0.73^{+0.04}_{-0.02}$	$2.34^{+0.2}_{-0.3}$	$3.15^{+0.3}_{-0.6}$	$1.28^{+0.3}_{-0.1}$	$1.56^{+0.2}_{-0.1}$	$2.35^{+0.3}_{-0.1}$	$2.33^{+0.3}_{-0.1}$	1.36
10	$2.61^{+0.02}_{-0.04}$	$0.26^{+0.003}_{-0.005}$	1	$5.74^{+0.3}_{-0.2}$	$0.90 \pm 0.2$	$1.57 \pm 0.10$	$4.54^{+0.3}_{-0.2}$	$0.94 \pm 0.1$	$1.28^{+0.06}_{-0.07}$	$2.03^{+0.09}_{-0.08}$	$1.97 \pm 0.1$	1.34
11	$2.62^{+0.03}_{-0.02}$	$0.25^{+0.003}_{-0.004}$	1	$7.78^{+0.7}_{-2.2}$	$0.80^{+0.01}_{-0.03}$	$1.59 \pm 0.1$	$5.14^{+0.7}_{-0.6}$	$1.18^{+0.1}_{-0.2}$	$1.70^{+0.05}_{-0.06}$	$2.72 \pm 0.2$	$2.42 \pm 0.1$	1.34
12	$2.75^{+0.03}_{-0.04}$	$0.23 \pm 0.01$	1	$8.65^{+3.0}_{-1.8}$	$0.81^{+0.03}_{-0.05}$	$0.96^{+0.06}_{-0.05}$	$3.12^{+0.6}_{-0.5}$	...	$2.09^{+0.1}_{-0.2}$	$4.39^{+0.2}_{-0.4}$	$3.63^{+0.3}_{-0.2}$	1.53
13	$2.50^{+0.06}_{-0.04}$	$0.23 \pm 0.02$	1	$3.03^{+1.6}_{-0.7}$	$0.61 \pm 0.03$	$3.66^{+0.7}_{-1.1}$	$4.71 \pm 0.8$	$0.84^{+0.2}_{-0.1}$	$1.34 \pm 0.06$	$2.01^{+0.2}_{-0.1}$	$2.17^{+0.2}_{-0.1}$	1.18
14	$2.53^{+0.04}_{-0.07}$	$0.23 \pm 0.02$	1	$3.49 \pm 1.2$	$0.65^{+0.03}_{-0.04}$	$2.92 \pm 0.8$	$4.14 \pm 0.9$	$0.91 \pm 0.2$	$1.35 \pm 0.1$	$2.04 \pm 0.2$	$2.13 \pm 0.2$	1.22
15	$2.45 \pm 0.1$	$0.22^{+0.03}_{-0.02}$	1	$1.56 \pm 0.1$	$1.36 \pm 0.3$	$0.41 \pm 0.09$	$0.17 \pm 0.01$	...	$2.38^{+0.5}_{-0.6}$	$5.81^{+2.3}_{-1.7}$	$4.14^{+1.6}_{-1.1}$	1.09
16	$2.51^{+0.05}_{-0.06}$	$0.24 \pm 0.02$	1	$3.08^{+1.6}_{-1.0}$	$0.62 \pm 0.03$	$3.60^{+1.4}_{-0.9}$	$4.65^{+0.9}_{-0.5}$	$0.56 \pm 0.2$	$1.34^{+0.09}_{-0.08}$	$2.04^{+0.3}_{-0.2}$	$2.21 \pm 0.2$	1.18

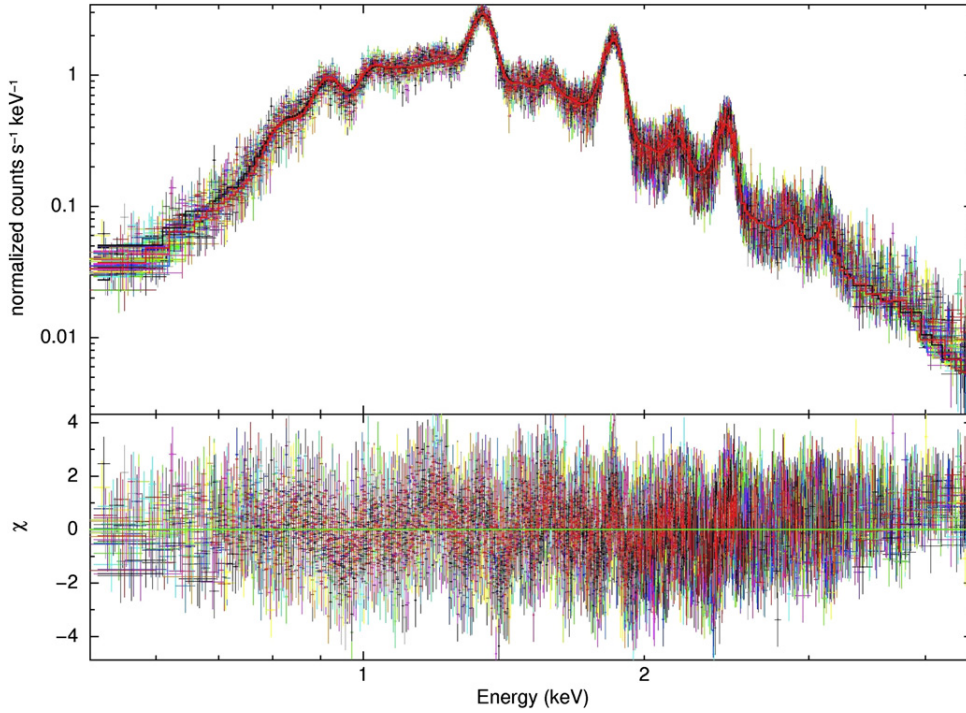


**Figure 4.** MOS1 and MOS2 spectrum extracted from 16 *XMM-Newton* observations with good time intervals of 10 ks or more for the whole of Kes 79. These spectra have been fitted simultaneously with a two-component plasma model, VPSHOCK+PSHOCK, and the XSPEC absorption model TBABS described by the parameters in Table 4. The X-ray spectra are overlaid with the fitted VPSHOCK+PSHOCK model and their chi-square residuals are shown. The combined MOS1 and MOS2 X-ray spectra derived for each region shown in Figure 3(a) all have features similar to the global X-ray spectrum shown here. (A color version of this figure is available in the online journal.)

**Table 4**

Results from Fitting the Two-component Model and the VPSHOCK+PSHOCK Model to the Whole SNR with 90% Confidence Ranges

Parameters	Global Fit
$n_H$ ( $10^{22}$ cm $^{-2}$ )	$2.35^{+0.003}_{-0.001}$
<i>Soft component (PSHOCK)</i>	
$kT$ (keV)	$0.24^{+0.0002}_{-0.001}$
$\tau$ ( $10^{12}$ s cm $^{-3}$ )	1
Norm (cm $^{-5}$ )	$0.67^{+0.0002}_{-0.001}$
Absorbed flux for 0.5–10 keV (erg cm $^{-2}$ s $^{-1}$ )	$2.65 \times 10^{-12}$
Unabsorbed flux for 0.5–10 keV (erg cm $^{-2}$ s $^{-1}$ )	$7.68 \times 10^{-10}$
<i>Hard component (VPSHOCK)</i>	
$kT$ (eV)	$0.78^{+0.006}_{-0.001}$
$\tau$ ( $10^{11}$ s cm $^{-3}$ )	$1.57 \pm 0.03$
Norm cm $^{-5}$	$0.06^{+0.01}_{-0.02}$
Mg	$1.41^{+0.02}_{-0.01}$
Si	$2.33 \pm 0.02$
S	$2.28 \pm 0.03$
Absorbed flux for 0.5–10 keV (erg cm $^{-2}$ s $^{-1}$ )	$7.90 \times 10^{-12}$ erg cm $^{-2}$ s $^{-1}$
Unabsorbed flux for 0.5–10 keV (erg cm $^{-2}$ s $^{-1}$ )	$2.09 \times 10^{-10}$ erg cm $^{-2}$ s $^{-1}$
$\chi^2$ /(dof)	1.07
Total luminosity (0.5–10 keV)	$5.6 \times 10^{36}$ erg s $^{-1}$

material and how it changes across the remnant. In our calculations, we set the radius ( $R$ ) of Kes 79 to 4.7 arcmin, which corresponds to a physical size of  $9.6 d_7$  pc. For each individual region, the X-ray emitting volume was estimated by taking an area equivalent to the extracted SNR regions (Figure 3(a)) and projecting this area through a shell (front and back) with a thickness of  $R/12$ . The volume emission measure (EM), which de-

scribes the amount of plasma available to produce the observed X-ray flux, is defined as  $EM \sim \int n_e n_H dV_X \sim n_e n_H f V_X$ , where  $n_e$  is the post-shock electron density,  $n_H$  is the mean hydrogen density, and  $f$  is a volume filling factor. The EM is estimated using the normalization of the X-ray spectral fits using  $K = (10^{-14}/4\pi d^2)EM$ . Assuming a strong shock, the ambient density can be calculated using  $n_0^2 = (Kd^2\pi)/(4.8 \times 10^{-14} f V_X)$ . From this, we can calculate the ambient density ( $n_0$ ) across the remnant (i.e., for each region). These  $n_0$  calculations are summarized in Table 5. The inferred ambient density across the remnant ranges from  $n_0 = (1.81 \pm 0.5 - 4.85^{+1.1}_{-0.9}) f^{-1/2} d_7^{-1/2}$  cm $^{-3}$ . These high ambient density values indicate that the remnant is expanding into a dense environment. The ambient density is highest in regions 5, 6, 9, 10, 11, and 16, which are predominantly toward the south and southeast of the remnant. This observation is consistent with the presence of a nearby MC overlapping the eastern and southeastern regions of Kes 79. The presence of X-ray emission in these regions may imply the interaction of the remnant's shock-wave with the MC.

Our estimates of the ambient density are an order of magnitude larger than the estimated ambient density by Sun et al. (2004). This results from the higher column density derived using the Wilms et al. (2000) abundance table. This absorption hides a significant soft component, which comprises a large total mass and results in a high derived density. The temperature derived by Sun et al. (2004) using the three non-ionization equilibrium models in their paper have approximately intermediate values of the soft and hard temperature components derived from our spatial dependent and global X-ray spectra (Tables 3 and 4, respectively). This could imply that the short *Chandra* observation could not distinguish between the two plasma components suggested by our extracted X-ray spectra and instead

**Table 5**  
Derived Ambient Density Estimates for the 16 Different  
Regions Shown in Figure 3(a)

Region	Ambient Density ( $d_7 f^{-0.5} \text{ cm}^{-3}$ )
1	$3.39^{+2.2}_{-2.0}$
2	$2.52^{+2.2}_{-1.6}$
3	$2.49^{+1.4}_{-0.6}$
4	$3.15^{+0.9}_{-1.0}$
5	$4.29^{+2.3}_{-1.7}$
6	$3.59^{+1.6}_{-1.2}$
7	$3.08^{+1.0}_{-1.2}$
8	$2.68^{+1.1}_{-1.4}$
9	$3.95 \pm 0.6$
10	$4.85^{+1.1}_{-0.9}$
11	$4.29^{+1.3}_{-2.3}$
12	$3.94^{+2.3}_{-1.8}$
13	$2.34^{+1.7}_{-1.1}$
14	$2.55 \pm 1.5$
15	$1.81 \pm 0.5$
16	$3.51^{+2.5}_{-2.0}$

**Notes.** These values are calculated from the best-fit parameters of our two component plasma models, VPSHOCK+PSHOCK, and the XSPEC absorption model TBABS shown in Table 3.

represents an average of the soft and hard components summed along the line of sight.

In the Sedov phase of evolution, the SNR radius scales as  $R \propto n_0^{-1/5}$ , at a given age. Thus, while our analysis indicates a somewhat non-uniform ambient medium, the overall behavior can be reasonably approximated by assuming evolution in a uniform medium (Hnatyk & Petruk 1999). When calculating the global characteristics of Kes 79, we estimate the volume of the X-ray emitting region ( $V_X$ ) by assuming that the plasma fills a spherical shell with a radius of  $9.6 d_7$  pc, a thickness of two times  $R/12$  and the X-ray parameters listed in Table 4. The shock temperature can be derived by using  $T_{\text{sh}} = 0.79 T_X$ , where  $T_X$  is the temperature inferred from the X-ray fit, assuming electron-ion temperature equilibrium. Using the global temperature for the soft component (PSHOCK) which is suggested to be the forward shock component, we obtain a shock temperature of  $T_{\text{sh}} \sim 0.19$  keV. The forward shock velocity is determined using  $v_{\text{sh}} = [(16kT_{\text{sh}})/(3\mu m_{\text{H}})]^{1/2}$ , where  $\mu = 0.604$  is the mean atomic weight,  $k$  is Boltzmann's constant and  $m_{\text{H}}$  is the mass of hydrogen. We obtain a shock velocity of  $v_{\text{sh}} \sim 400 \text{ km s}^{-1}$ , assuming electron-ion temperature equilibrium. The Sedov age of the remnant is related to the forward shock velocity by  $t_{\text{SNR}} = 2r_{\text{sh}}/5v_{\text{sh}}$ . Assuming the SNR radius of  $r_{\text{sh}} = 4.7$  arcmin, we derive an age of  $\sim 9400 d_7$  yr. Our spatial X-ray analysis described by the model parameters in Table 3 gives a  $t_{\text{age}}$  between  $\sim 9000$ – $10600$  yr whose average is approximately the  $t_{\text{age}}$  that we derived in the global analysis. Sun et al. (2004), using different X-ray model parameters, derived an age of Kes 79 of 5400–7500 yr, while Giacani et al. (2009), using VLA radio data, derived an upper limit of  $t_{\text{age}} < 15 \times 10^3$  yr. The explosion energy is calculated using  $E_{\text{SNR}} = 0.7r_{\text{sh}}^5 m_p n_0 t_{\text{SNR}}^{-2}$  and we obtain  $E_{\text{SNR}} \sim 3.7 \times 10^{50} f^{-1/2} d_7^{-5/2}$  erg. This value is lower than the canonical  $10^{51}$  erg. This low value for the explo-

sion energy has been inferred from X-ray observations of a number of other SNRs, e.g., G272.2–3.2 (Harrus et al. 2001) and G299.2–2.9 (Park et al. 2007). Castro et al. (2011), suggested that such low inferred explosion energies could be a signature of efficient CR acceleration during the evolution of the SNR, consistent with the detection of  $\gamma$ -rays from Kes 79 (see below). The X-ray emitting mass is calculated using  $M_X = 1.4n_{\text{H}}m_{\text{H}}fV$  and we obtain  $M_X \sim 160 f^{1/2} d_7^{5/2} M_{\odot}$  of swept-up ISM.

## 4. DISCUSSION

Non-thermal X-ray and  $\gamma$ -ray emission from SNRs indicate that a population of particles are being accelerated to VHEs by the SNR shock front.  $\gamma$ -rays can be produced by leptonic mechanisms such as inverse Compton scattering, non-thermal bremsstrahlung, or by hadronic mechanisms via the decay of neutral pions generated during proton-proton interactions. SNR shocks are not the only astrophysical sources capable of producing  $\gamma$ -rays. Pulsars can also contribute to the observed  $\gamma$ -ray emission and their contribution should also be considered before we assume that the  $\gamma$ -ray sources are products of particles being accelerated at the SNR shock.

### 4.1. Pulsar Contribution to $\gamma$ -rays

In the first *Fermi*-LAT Pulsar catalog, Abdo et al. (2010c) determined that the spectra of pulsars detected in the *Fermi*-LAT energy band are best described by a power-law distribution with an exponential cut-off of 1–5 GeV, with the exception of the Crab pulsar, which can be described using an exponential cut-off of  $>100$  GeV (Aliu et al. 2011). This result was confirmed and presented in the second *Fermi*-LAT Pulsar catalog (Abdo et al. 2013) in which the *Fermi*-LAT collaboration analyzed three years of *Fermi*-LAT data and detected with high confidence 117  $\gamma$ -ray pulsars above an energy of 0.1 GeV. Most recently, a preliminary analysis of pulsars detected by the *Fermi*-LAT satellite by Saz Parkinson & *Fermi*-LAT Collaboration (2012) indicated that a number of pulsars show possible evidence of high-energy emission with a cut-off energy  $>10$  GeV. The spectra of the source coincident with Kes 79 can be best fit using an exponential cut-off of  $E_{\text{cut}} \sim 2.62$  GeV and  $E_{\text{cut}} \sim 1.5$  GeV, respectively, which falls within the expected range for  $E_{\text{cut}}$  for  $\gamma$ -ray pulsars. As a consequence, the hypothesis that the observed  $\gamma$ -ray emission could be due to the presence of a pulsar cannot be ruled out straight away.

Within a  $5^\circ$  region centered on the observed  $\gamma$ -ray emission of Kes 79 (Figure 1(a)), there are three pulsars in the Australian Telescope National Facility (ATNF) Pulsar Catalogue (Manchester et al. 2005),<sup>13</sup> whose spin down power is sufficient to produce the  $\gamma$ -ray flux of Kes 79 if, at the distance of the pulsar, all of that power goes into  $\gamma$ -rays. An upper limit on the  $\gamma$ -ray flux of each ATNF pulsar is calculated by using the distance to the pulsar listed in the catalog, and by assuming that 100% of the spin down power,  $\dot{E}$ , is converted into  $\gamma$ -rays. The upper limit on the pulsar's  $\gamma$ -ray flux is comparable to the observed  $\gamma$ -ray flux of Kes 79. This indicates that these three pulsars could potentially contribute to the observed  $\gamma$ -rays. The pulsars would also have to be located such that the *Fermi*-LAT's PSF could not resolve them as separate sources. At 0.6 GeV, which corresponds to the energy of the first data point of Kes 79's  $\gamma$ -ray spectrum, the resolution of the PSF of the *Fermi*-LAT is

<sup>13</sup> The ATNF Catalogue contains the positional and physical characteristics of 1509 pulsars, which can be found at <http://www.atnf.csiro.au/research/pulsar/psrcat>.

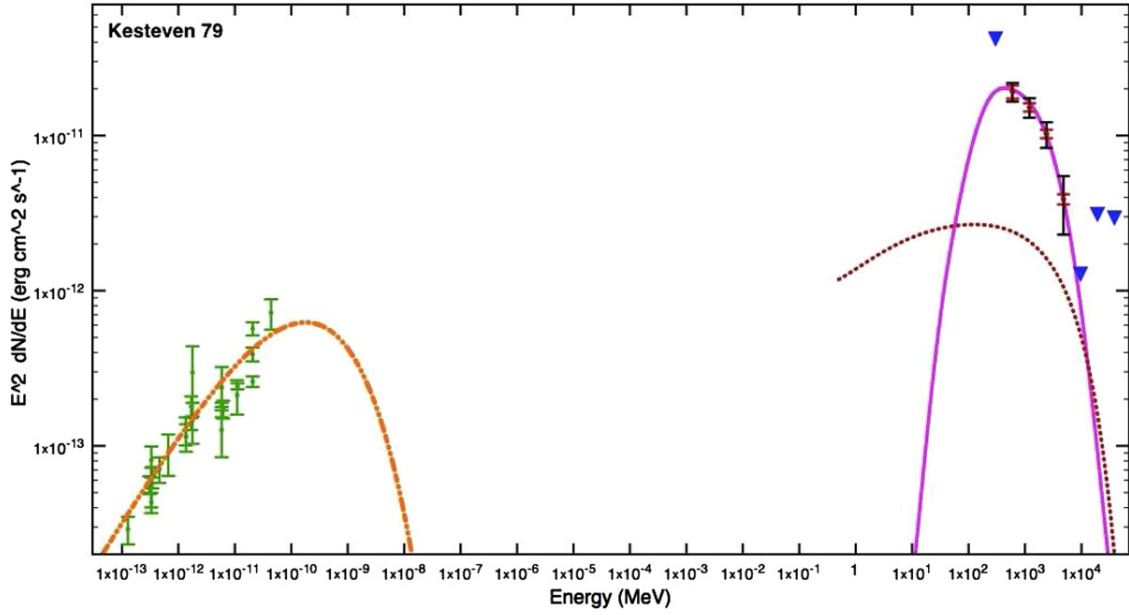


**Figure 5.** Broadband fits to radio (green data points) and *Fermi*-LAT  $\gamma$ -ray data points (as described in Figure 2) of Kes 79. The pion decay, non-thermal bremsstrahlung, and synchrotron models defined by the parameters in Table 6 are shown as the solid magenta line, dotted dark red line, and dot-dashed orange line, respectively. The corresponding IC model falls below the plotted axis.

(A color version of this figure is available in the online journal.)

$\sim 1^\circ$  for front events at 68% containment.<sup>14</sup> All three pulsars are at a distance of  $1.23$  or more from the centroid of the  $\gamma$ -ray emission, thus making it highly unlikely that any of these pulsars are contributing significantly to the observed  $\gamma$ -ray emission of Kes 79. The 105 ms X-ray pulsar, PSR J1852+00040, discovered by Gotthelf et al. (2005) and Seward et al. (2003) to be associated with Kes 79, has a spin down power  $\dot{E} = 3 \times 10^{32}$  erg s<sup>-1</sup> (Halpern & Gotthelf 2010). If all of this spin down energy is converted into  $\gamma$ -rays at the distance of the pulsar, it is incapable of producing the  $\gamma$ -ray flux we observe. Thus, we can state with confidence that this pulsar is not producing the observed  $\gamma$ -ray emission of Kes 79.

#### 4.2. Hadronic Origin of $\gamma$ -rays

As there is a lack of evidence in favor of significant  $\gamma$ -ray contribution from a pulsar, it is reasonable to assume that the observed  $\gamma$ -rays associated with Kes 79 arise from the SNR itself, a prospect made particularly likely by the high ambient density implied by our X-ray analysis in Section 3. This is supported by the presence of strong  $\text{HCO}^+ J = 1 \rightarrow 0$  and  $^{12}\text{CO} J = 1 \rightarrow 0$  emission found toward the east of the remnant and the fact that the remnant is thought to be interacting with dense molecular material (Scoville et al. 1987; Green 1989). In order to investigate the nature of the  $\gamma$ -ray emission, we first model the  $\gamma$ -ray spectrum, assuming that the  $\gamma$ -rays are produced predominantly by the decay of accelerated hadrons.

To reproduce the observed  $\gamma$ -ray spectrum of Kes 79, we use a model that simultaneously calculates the  $\gamma$ -ray emission, assuming a distribution of electrons and protons being accelerated at the SNR shock front. The  $\pi^0$  decay model is based on a proton-proton interaction model by Kamae et al. (2006) with a scaling factor of 1.85 for helium and heavy nuclei (Mori 2009). The synchrotron and inverse Compton emission models are based on Baring et al. (1999) and the non-thermal

bremsstrahlung emission is modeled using the description in Bykov et al. (2000). To generate the momentum distribution of protons (or electrons) being accelerated by the SNR shock wave, we adopt a power law spectrum with an exponential cut-off, as expected from classical diffusive shock theory. This is described by

$$\frac{dN_i}{dp} = a_i p^{-\alpha_i} \exp\left(-\frac{p}{p_{0i}}\right), \quad (1)$$

where  $i$  is the particle species,  $a_i$  is the normalization of the particle distribution, and  $p_{0i}$  is the exponential particle momentum cut-off. This particle distribution is transformed from momentum space to energy space, such that the exponential cut-off is defined by an input energy,  $E_{0i}$ . The integrals of each particle species distribution are summed and set such that the sum is equal to the assumed total energy in accelerated particles,  $E_{\text{CR}} = \epsilon E_{\text{SN}}$ , where  $\epsilon$  is the efficiency of the SNR in depositing energy into CRs.

Figure 5 shows the model fits to the broadband emission observed from Kes 79. The radio spectrum of Kes 79, shown as the green data points in Figure 5(a), is a combination of multiple observations by Kundu & Velusamy (1967), Kesteven (1968), Beard & Kerr (1969), Altenhoff et al. (1970), Dulk & Slee (1972), Dickel (1973), Caswell et al. (1975, 1981), Becker & Kundu (1975), Dickel & Denoyer (1975), Slee (1977), Angerhofer et al. (1977), Kassim (1989, 1992), Kovalenko et al. (1994), and Giacani et al. (2009). We have plotted the pion decay model that adequately reproduces the observed  $\gamma$ -ray spectrum of Kes 79 as the solid magenta line, while the orange dot-dashed line corresponds to the synchrotron model which sufficiently reproduces the radio spectrum of each remnant, assuming an electron-positron ratio ( $K_{\text{ep}}$ ) of 0.01. For completeness, we have also plotted the non-thermal bremsstrahlung contribution for Kes 79 as the dotted dark red line, while the corresponding IC model falls below the plotted axis. In Table 6, we have listed the parameters which reproduce the pion-decay, synchrotron, non-thermal bremsstrahlung and IC models observed in Figure 5.

<sup>14</sup> [http://www.slac.stanford.edu/exp/glast/groups/canda/lat\\_Performance.htm](http://www.slac.stanford.edu/exp/glast/groups/canda/lat_Performance.htm)

**Table 6**  
Model Parameters and Density Estimates for the Pion Decay Model for Kesteven 79

Object	Distance (kpc)	$\alpha_{\text{proton}}$	$\alpha_{\text{elec}}$	$E_0^{\text{proton}}$ (GeV)	$E_0^{\text{elec}}$ (GeV)	Magnetic Field ( $\mu\text{G}$ )	Ambient Density $n_0$ ( $\text{cm}^{-3}$ )	X-Ray Density $n_X$ ( $\text{cm}^{-3}$ )	$n_X$ Reference
Kes 79	7	4.09	3.8	12	12	180	14.5	$4_{-0.7}^{+0.9} d_7 f^{-0.5}$	Table 5

The  $\gamma$ -ray spectrum of Kes 79 is adequately described by a pion-decay model with a proton distribution that has a power law index of  $\alpha_p = 4.09$  and a proton cut-off energy of  $E_0^p \sim 12$  GeV. The cut-off energy for the proton spectrum required to model the  $\gamma$ -ray spectrum of Kes 79 under this hadronic-dominated scenario is rather low given that we expect cut-off energies for protons to be well in excess of a TeV (Reynolds 2008). This discrepancy could arise from efficient CR acceleration being suppressed in dense surrounding environments due to the suppression of Alfvén waves by ion-neutral collisions. This allows particles being accelerated by the SNR shock to escape the emission volume (Malkov et al. 2011, 2012).

To model the radio spectrum of Kes 79 using synchrotron emission, we assume that the cut-off energy of the electrons to be the same as the cut-off energy of the pion-decay model, as there is no non-thermal X-ray data to constrain the cut-off energy of the electron population. To reproduce the radio spectrum of Kes 79, we required an electron distribution with a power law index of  $\alpha_e = 3.8$  and a magnetic field of  $180 \mu\text{G}$ . The magnetic field required to model the radio spectrum of Kes 79 is larger than the average interstellar magnetic field ( $3\text{--}5 \mu\text{G}$ ) and could arise from the magnetic fields being amplified by the shock-wave compressing the surrounding medium during the acceleration process.

If one makes reasonable assumptions about the fraction,  $\epsilon$ , of total supernova explosion energy,  $E_{\text{SN}}$ , used to accelerated CRs, as well as the shock compression ratio,  $r$ , one can use this model to estimate the density of the surrounding medium with which the SNR shock wave is interacting. For this analysis, we set  $r = 4$  and we assume that  $\epsilon = 0.4$ . This is a conservatively high estimate of the amount of supernova explosion energy expected to be converted into accelerating CRs. In Table 6, we summarize the estimated density of the  $\gamma$ -ray emitting material as well as the density of the X-ray emitting material derived in the literature and from our X-ray analysis.

When fitting the  $\gamma$ -ray spectrum of Kes 79 using a pion-decay model, we obtained a density of  $14.5 \text{ cm}^{-3}$ . This density is much larger than the values derived from the X-ray measurements listed in Table 5. This inferred density enhancement could indicate that the shock-wave of the SNR is interacting with cold, dense clumps of material (ISM or ejecta) that form due to instabilities in the post-shock flow (Castro & Slane 2010; Inoue et al. 2012). These cold dense clumps do not radiate significantly in X-rays. If these clumps of material have a high filling factor, then the densities inferred from the X-ray emission would significantly underestimate the local mean density. This scenario is consistent with a CO survey conducted by Scoville et al. (1987), which revealed a large elongated MC that overlaps the eastern and south eastern region of Kes 79. MCs are known to be clumpy in nature, with dense clumps of molecular material occupying only a fraction of the actual MC volume. This clumpy material can have a density of  $n_{\text{H}} \sim 5\text{--}25 \text{ atoms cm}^{-3}$  (Chevalier 1999) or an ambient density of  $n_0 \sim 1.25\text{--}6.25 \text{ cm}^{-3}$ , if we assume  $n_0 = n_{\text{H}}/4$ . Our inferred ambient densities (Table 5) across the remnant fall within this range, supporting the original

conclusion that Kes 79 is interacting with a dense molecular material that does not radiate significantly in X-rays.

Alternatively, highly energetic particles accelerated by the remnant’s shock-wave could escape the acceleration region and stream ahead of the shock. These escaped particles can interact with the dense gas upstream of the shock, enhancing the detected  $\gamma$ -ray emission. A number of authors such as Aharonian & Atoyan (1996), Gabici et al. (2009), and Fujita et al. (2009) have shown that dense MCs in the vicinity of an SNR can significantly influence the  $\gamma$ -ray flux. However, the escaping particles in this scenario come predominantly from the higher energy part of the particle spectrum, leading to inconsistencies between the predicted and observed  $\gamma$ -ray spectrum.

#### 4.3. Leptonic Origin of $\gamma$ -rays

An alternative scenario is that the  $\gamma$ -ray emission coincident with Kes 79 arises from a non-thermal population of electrons in the form of IC or bremsstrahlung radiation. Bykov et al. (2000) and other authors have proposed this mechanism as the main production mechanism of  $\gamma$ -rays in SNRs. For completeness, we tested whether IC or non-thermal bremsstrahlung could be the dominant mechanism producing the  $\gamma$ -ray spectra of Kes 79. In order for the non-thermal bremsstrahlung to dominate the GeV  $\gamma$ -ray emission, the electron-to-proton ratio,  $K_{\text{ep}}$ , must be larger than  $\sim 0.2$  (Gaisser et al. 1998). Local observations of the CR abundance ratio imply that  $K_{\text{ep}} \sim 0.01$  (Gaisser et al. 1998), while models of the  $\gamma$ -ray emission from SNRs such as RX J1713.7–3946 suggest even smaller values of this ratio (Ellison et al. 2010).

Assuming that electrons make up approximately 1% of the relativistic particle energy budget (i.e.,  $K_{\text{ep}} = 0.01$ ), we determined that in order to reproduce the  $\gamma$ -ray spectrum of Kes 79, the total electron energy would be  $1 \times 10^{51}$  erg. This is equal to the entire canonical SN explosion energy, making it difficult to assert that IC is the dominant mechanism behind the  $\gamma$ -ray emission of Kes 79.

To test whether non-thermal bremsstrahlung is the dominant mechanism producing the  $\gamma$ -rays of Kes 79, we used the highest ambient density value derived in our X-ray analysis (see Table 5), as this would give us a lower limit on the total energy in accelerated electrons. Assuming  $K_{\text{ep}} = 0.01$ , we obtained a lower limit of  $6.1 \times 10^{50}$  erg for the total electron energy. This implies a total relativistic particle energy that is far in excess of the mechanical energy of an SNR. This fact makes it unlikely that non-thermal bremsstrahlung is the dominant mechanism behind the observed  $\gamma$ -rays of Kes 79.

## 5. CONCLUSION

In summary, using 52 months of *Fermi*-LAT data, we searched for  $\gamma$ -ray emission from SNR Kes 79, which is found to be interacting with MCs. Assuming that the main production mechanism for the observed  $\gamma$ -ray emission arises from pion decay, the inferred ambient density is high. This is consistent with observations of dense MCs near Kes 79. However, these estimates are

larger than the density derived from X-ray observations found in the literature. A pulsar association with the observed  $\gamma$ -ray emission is also considered for completeness as well as leptonic origin of the  $\gamma$ -ray emission. For Kes 79, an SNR origin of the emission is the most likely scenario, while a hadronic origin of the  $\gamma$ -rays was the most energetically favored mechanism. Additionally, we performed a spatial and spectral analysis of Kes 79 using 16 archival *XMM-Newton* observations and inferred an ambient density that is much smaller than the inferred ambient density from modeling the observed  $\gamma$ -ray emission. These results are consistent with scenarios represented by Castro & Slane (2010) and Abdo et al. (2009). We also performed a similar analysis for SNR Kes 78, but due to the uncertainties in the background  $\gamma$ -ray model or from  $\gamma$ -ray emission spilling over from nearby sources, we were unable to conclude that there is an excess of GeV  $\gamma$ -ray emission associated with this remnant.

The authors thank Dr. Thomas M. Dame for his in depth discussions in regards to the association and interaction of Kes 79 with its surrounding molecular cloud. K.A. thanks Dr. Jasmina Lazendic-Galloway for her helpful discussions in regards to the X-ray analysis. This work was partially funded by NASA grant NNX 11AQ096. P.S. acknowledges support from NASA contract NAS8-03060. D.C. acknowledges support for this work provided by NASA through SAO contract SV3-73016 to MIT for Support of the Chandra X-Ray Center, which is operated by the SAO under contract NAS8-03060.

## REFERENCES

- Abdo, A., Ackermann, M., Ajello, M., et al. 2009, *ApJL*, 706, L1  
 Abdo, A., Ackermann, M., Ajello, M., et al. 2010a, *Sci*, 327, 1103  
 Abdo, A., Ackermann, M., Ajello, M., et al. 2010b, *ApJ*, 712, 459  
 Abdo, A., Ackermann, M., Ajello, M., et al. 2010c, *ApJS*, 187, 460  
 Abdo, A., Ackermann, M., Ajello, M., et al. 2011, *ApJ*, 734, 28  
 Abdo, A., Ajello, M., Allafort, A., et al. 2013, *ApJS*, 208, 17  
 Acciari, V. A., Aliu, E., Arlen, T., et al. 2011, *ApJL*, 730, L20  
 Ackermann, M., Ajello, M., Albert, A., et al. 2012, *ApJS*, 203, 4  
 Ackermann, M., Ajello, M., Allafort, A., et al. 2013, *Sci*, 339, 807  
 Aharonian, F. A., & Atayan, A. M. 1996, *A&A*, 309, 917  
 Aliu, E., Arlen, T., Aune, T., et al. 2011, *Sci*, 334, 69  
 Allakhverdiev, A. O., Guseinov, O. K., Kasumov, F. K., & Iusifov, I. M. 1983, *Ap&SS*, 97, 287  
 Altenhoff, W. J., Downes, D., Goad, L., Maxwell, A., & Rinehart, R. 1970, *A&AS*, 1, 319  
 Anders, E., & Grevesse, N. 1989, *GeCoA*, 53, 197  
 Anghofer, P. E., Becker, R. H., & Kundu, M. R. 1977, *A&A*, 55, 11  
 Aschenbach, B. 1998, *Natur*, 396, 141  
 Baring, M. G., Ellison, D. C., Reynolds, S. P., Grenier, I. A., & Goret, P. 1999, *ApJ*, 513, 311  
 Beard, M., & Kerr, F. J. 1969, *AuJPh*, 22, 121  
 Becker, R. H., & Kundu, M. R. 1975, *AJ*, 80, 679  
 Borkowski, K. J., Lyerly, W. J., & Reynolds, S. P. 2001, *ApJ*, 548, 820  
 Boumis, P., Xilouris, E., Alikakos, J., et al. 2009, *A&A*, 499, 789  
 Bykov, A., Chevalier, R., Ellison, D., & Uvarov, Y. 2000, *ApJ*, 538, 203  
 Case, G. L., & Bhattacharya, D. 1998, *ApJ*, 504, 761  
 Castro, D., & Slane, P. 2010, *ApJ*, 717, 372  
 Castro, D., Slane, P., Carlton, A., & Figueroa-Feliciano, E. 2013, *ApJ*, 774, 36  
 Castro, D., Slane, P., Ellison, D. C., & Patnaude, D. J. 2012, *AJ*, 756, 88  
 Castro, D., Slane, P., Patnaude, D. J., & Ellison, D. C. 2011, *ApJ*, 734, 85  
 Caswell, J. L., Clark, D., Crawford, D. F., & Green, A. J. 1975, *AuJPA*, 37, 1  
 Caswell, J. L., Milne, D. K., & Wellington, K. J. 1981, *MNRAS*, 195, 89  
 Caswell, J. L., Murray, J. D., Roger, R. S., Cole, D. J., & Cooke, D. J. 1975, *A&A*, 45, 239  
 Chen, Y., Jiang, B., Zhou, P., et al. 2013, arXiv:1304.5367  
 Chen, Y., Zhang, F., Williams, R. M., & Wang, Q. D. 2003, *ApJ*, 595, 227  
 Chevalier, R. A. 1999, *ApJ*, 511, 798  
 Claussen, M., Frail, D., Goss, W. M., & Gaume, R. 1997, *ApJ*, 489, 143  
 Dickel, J. R. 1973, *AuJPh*, 26, 369  
 Dickel, J. R., & Denoyer, L. K. 1975, *AJ*, 80, 437  
 Dulc, P., & Slee, O. 1972, *AuJPh*, 25, 429  
 Ellison, D. C., Patnaude, D. J., Slane, P., & Raymond, J. 2010, *ApJ*, 712, 287  
 Frail, D. A. 2011, *MmSAI*, 82, 703  
 Frail, D. A., & Clifton, T. R. 1989, *ApJ*, 336, 854  
 Fujita, Y., Ohira, Y., Tanaka, S. J., & Takahara, F. 2009, *ApJL*, 707, L179  
 Gabici, S., Casanova, S., & Aharonian, F. A. 2009, in AIP Conf. Proc. 1085, High Energy Gamma-ray Astronomy, ed. F. A. Aharonian, W. Hofmann, & F. Rieger (Melville, NY: AIP), 265  
 Gaisser, T., Protheroe, R., & Stanev, T. 1998, *ApJ*, 492, 219  
 Giacani, E., Smith, M. J. S., Dubner, G., et al. 2009, *A&A*, 507, 841  
 Giordano, F., Naumann-Godo, M., Ballet, J., et al. 2012, *ApJL*, 744, L2  
 Giuliani, A., Cardillo, M., Tavani, M., et al. 2011, *ApJL*, 742, L30  
 Gosachinski, I., & Khersonskii, V. K. 1985, *Ap&SS*, 108, 303  
 Gotthelf, E. V., Halpern, J. P., & Seward, F. D. 2005, *ApJ*, 627, 390  
 Green, A. J., Frail, D. A., Goss, W. M., & Otrupcek, R. 1997, *AJ*, 114, 2058  
 Green, D. A. 1989, *MNRAS*, 238, 737  
 Green, D. A., & Dewdney, P. E. 1992, *MNRAS*, 254, 686  
 Halpern, J. P., & Gotthelf, E. V. 2010, *ApJ*, 709, 436  
 Harrus, I. M., Slane, P. O., Smith, R. K., & Hughes, J. P. 2001, *ApJ*, 552, 614  
 Hewitt, J. W., Yusef-Zadeh, F., & Wardle, M. 2009, *ApJL*, 706, L270  
 Hnatyk, B., & Petruk, O. 1999, *A&A*, 344, 295  
 Inoue, T., Yamazaki, R., Inutsuka, S.-i., & Fukui, Y. 2012, *ApJ*, 744, 71  
 Kamae, T., Karlsson, N., Mizuno, T., Abe, T., & Koi, T. 2006, *ApJ*, 647, 692  
 Kassim, N. 1992, *AJ*, 103, 943  
 Kassim, N. E. 1989, *ApJS*, 71, 799  
 Kesteven, M. J. L. 1968, *AuJPh*, 21, 369  
 Koralesky, B., Frail, D., Goss, W. M., Claussen, M., & Green, A. J. 1998, *AJ*, 116, 1323  
 Kosack, K., Chaves, R. C. G., & Acero, F. 2011, in Proc. 32nd International Cosmic Ray Conference (ICRC2011), Vol. 7 (Beijing: IUPAP), 75  
 Kovalenko, A. V., Pynzar', A. V., & Udal'tsov, V. A. 1994, *ARep*, 38, 95  
 Koyama, K., Petre, R., Gotthelf, E., et al. 1995, *Natur*, 378, 255  
 Kundu, M. R., & Velusamy, T. 1967, *AnAp*, 30, 723  
 Kuntz, K. D., & Snowden, S. L. 2008, *A&A*, 478, 575  
 Malkov, M. A., Diamond, P. H., & Sagdeev, R. Z. 2011, *NatCo*, 2, 194  
 Malkov, M. A., Diamond, P. H., & Sagdeev, R. Z. 2012, *PhPl*, 19, 082901  
 Malkov, M. A., & O' C Drury, L. 2001, *RPPH*, 64, 429  
 Manchester, R. N., Hobbs, G. B., Teoh, A., & Hobbs, M. 2005, *AJ*, 129, 1993  
 Mattox, J., Bertsch, D., Chiang, J., et al. 1996, *ApJ*, 461, 396  
 Mori, M. 2009, *Aph*, 31, 341  
 Morlino, G., & Caprioli, D. 2012, *A&A*, 538, A81  
 Nolan, P. L., Abdo, A. A., Ackermann, M., et al. 2012, *ApJS*, 199, 31  
 Park, S., Slane, P. O., Hughes, J. P., et al. 2007, *ApJ*, 665, 1173  
 Reynolds, S. P. 1998, *ApJ*, 493, 375  
 Reynolds, S. P. 2008, *ARA&A*, 46, 89  
 Saz Parkinson, P. M., & Fermi-LAT Collaboration, 2012, in AIP Conf. Proc. 1505, High Energy Gamma-ray Astronomy, ed. F. A. Aharonian, W. Hofmann, & F. M. Rieger (Melville, NY: AIP), 293  
 Scoville, N. Z., Yun, M. S., Sanders, D. B., Clemens, D. P., & Waller, W. H. 1987, *ApJS*, 63, 821  
 Seward, F. D., Slane, P. O., Smith, R. K., & Sun, M. 2003, *ApJ*, 584, 414  
 Slee, O. B. 1977, *AuJPA*, 43, 1  
 Stil, J. M., Taylor, A., Dickey, J., et al. 2006, *AJ*, 132, 1158  
 Sun, M., Seward, F. D., Smith, R. K., & Slane, P. O. 2004, *ApJ*, 605, 742  
 Sun, M., & Wang, Z. R. 2000, *AdSpR*, 25, 549  
 Tsunemi, H., & Enoguchi, H. 2002, *PASJ*, 54, 735  
 Uchiyama, Y., Aharonian, F. A., Tanaka, T., Takahashi, T., & Maeda, Y. 2007, *Natur*, 449, 576  
 Velusamy, T., Becker, R. H., & Seward, F. D. 1991, *AJ*, 102, 676  
 Vink, J. 2012, *A&ARv*, 20, 49  
 Warren, J. S., Hughes, J. P., Badenes, C., et al. 2005, *ApJ*, 634, 376  
 Wilms, J., Allen, A., & McCray, R. 2000, *ApJ*, 542, 914  
 Xu, J.-W., & Zhang, H.-R. 2009, arXiv:0909.0394  
 Zhou, P., & Chen, Y. 2011, *ApJ*, 743, 4  
 Zubrin, S. Y., & Shulga, V. M. 2008, in Proc. 15th Young Scientists' Conference on Astronomy and Space Physics, ed. V. Y. Choliy & G. Ivashchenko (Kyiv: Kyivskiy Universytet), 41



---

Multi-wavelength analysis of  
Galactic supernova remnant  
MSH 11–61A

---

*Multi-wavelength analysis of Galactic supernova remnant MSH 11–61A*

Katie Auchettl, Patrick Slane, Daniel Castro, Adam Foster, Randall K. Smith

Accepted for publication in ApJ

e-Print: [arXiv:1507.08012](https://arxiv.org/abs/1507.08012) [astro-ph]

---

## 4.1 Introductory remarks

As mentioned in the previous chapter, supernova remnants (SNRs) found near molecular clouds are ideal candidates for studying the emission arising from a population of relativistic particles being accelerated by the shock front of a remnant. Interestingly, a large fraction of SNRs interacting with molecular clouds belong to the unique class of SNRs called mixed-morphology (MM). These remnants are characterised by their shell-like radio morphology which is contrasted with their centrally peaked thermal X-ray emission. Their plasmas are usually isothermal in nature, and a large number show evidence of enhanced abundances. Furthermore, a number of MM SNR show evidence for overionised plasma in the form of radiation recombination continuum or excess emission near the  $K\alpha$  lines of He-like elements. In addition to their unique X-ray properties, nearly one third of the total GeV  $\gamma$ -ray emitting SNR population are classified as MM.

In this paper, we analyse the X-ray and  $\gamma$ -ray emission of MM SNR MSH 11–61A. This remnant has ear like protrusions towards the northwest and east, and CO observations show that the remnant is interacting in a complex environment that seems to have a plane parallel density gradient and a large molecular cloud located to the west. Using a 111 ks archival *Suzaku* observation of the remnant, we perform a spatially resolved analysis of the X-ray emission of the remnant. We find that the majority of the X-ray emission arises from a recombining plasma, while the emission from the two ear like protrusions towards the east arise from an ionising plasma. Both plasmas have enhanced abundances indicating that a majority of the X-ray emission stems from shocked ejecta, while the recombining plasma arises from the adiabatic cooling of a plasma that had an initial temperature of at least 5 keV.

In addition to our X-ray analysis, we also analyse the  $\gamma$ -ray emission coincident with the remnant. MSH 11–61A is found in a complex region of the  $\gamma$ -ray sky, with  $\gamma$ -ray bright MSH 11–62 found  $\sim 1$  degree from the remnant, pulsar PSR J1105–6107 found  $\sim 0.4$  degrees from this position and a number of other *Fermi*-LAT sources immediately surrounding the remnant. We filter the pulsar contribution and remove the surrounding  $\gamma$ -ray sources and find significant ( $5\sigma$ )  $\gamma$ -ray emission in the direction of the remnant. Similar to our analysis in Chapter 3 of Kes 79, we perform broadband modelling of the non-thermal emission of MSH 11–61A. We consider both leptonic and hadronic cases and find that the emission most likely arises from the decay of a neutral pion.

In Section 2 of our paper found overleaf, we describe our analysis of the *Fermi*-LAT data, while in Section 3 we describe our analysis of the archival *Suzaku* observation. In Section 4 and 5 respectively, we attempt to determine the origin of the thermal X-ray emission and the nature of the observed  $\gamma$ -rays. Figure 1a shows how busy the  $\gamma$ -ray sky is surrounding the remnant, while Figure 1b highlights

$\gamma$ -ray emission arising from MSH 11–61A and the position of molecular cloud. Figure 4 shows the centrally bright X-ray emission as detected by *Suzaku*, while Figure 6 we have plotted the broadband non-thermal emission of MSH 11–61A and our best fit model.

## 4.2 Declaration for thesis chapter 4

### Declaration by candidate

In the case of the paper(s) contained in Chapter 4, the nature and extent of my contribution to the work was the following:

<b>Paper</b>	<b>Nature of contribution</b>	<b>Extent of contribution (%)</b>
III	Performed data reduction for both the X-ray and $\gamma$ -ray data; analysed and interpreted results; wrote paper.	95%

The following co-authors contributed to the work. If co-authors are students at Monash University, the extent of their contribution in percentage terms is stated:

<b>Name</b>	<b>Nature of contribution</b>	<b>Extent of contribution (%)</b>
Patrick Slane	Provided supervisory advice; provided guidance on modelling the X-ray background and interpreting the X-ray results; provided comments on the draft of the paper.	
Daniel Castro	Developed the code which models the $\gamma$ -ray emission arising from pion-decay, inverse Compton scattering, non-thermal bremsstrahlung and synchrotron; provided comments on the draft of paper.	
Adam Foster	Provided helpful discussion related to the atomic database used for the X-ray modelling and in regards to the physics of recombining plasmas; provided comments on the draft of paper.	
Randall K. Smith	Provided helpful discussion related to understanding of the physics behind recombining plasmas; provided comments on the draft of the paper.	

The undersigned hereby certify that the above declaration correctly reflects the nature and extent of the candidate's and co-authors' contributions to this work.

**Signatures:**

Katie Auchetl:



Date: 15th June 2015

Patrick Slane:



Date: 15th June 2015

Csaba Balázs:



Date: 15th June 2015

Jasmina Lazendic-Galloway:



Date: 15th June 2015

### 4.3 Published material: Paper III

Begins overleaf.

## MULTI-WAVELENGTH ANALYSIS OF THE GALACTIC SUPERNOVA REMNANT MSH 11–61A

KATIE AUCHETTL<sup>1,2</sup>, PATRICK SLANE<sup>1</sup>, DANIEL CASTRO<sup>3</sup>, ADAM R. FOSTER<sup>1</sup>, RANDALL K. SMITH<sup>1</sup>

ACCEPTED TO APJ: July 28, 2015

### ABSTRACT

Due to its centrally bright X-ray morphology and limb brightened radio profile, MSH 11–61A (G290.1-0.8) is classified as a mixed morphology supernova remnant (SNR). HI and CO observations determined that the SNR is interacting with molecular clouds found toward the north and southwest regions of the remnant. In this paper we report on the detection of  $\gamma$ -ray emission coincident with MSH 11–61A, using 70 months of data from the Large Area Telescope on board the *Fermi Gamma-ray Space Telescope*. To investigate the origin of this emission, we perform broadband modelling of its non-thermal emission considering both leptonic and hadronic cases and concluding that the  $\gamma$ -ray emission is most likely hadronic in nature. Additionally we present our analysis of a 111 ks archival *Suzaku* observation of this remnant. Our investigation shows that the X-ray emission from MSH 11–61A arises from shock-heated ejecta with the bulk of the X-ray emission arising from a recombining plasma, while the emission towards the east arises from an ionising plasma.

**Keywords:** ISM: individual (MSH 11–61A, G290.1-0.8) — cosmic rays — X-rays: ISM — gamma rays: ISM — supernovae: general — ISM: supernova remnants

### 1. INTRODUCTION

Since the launch of the Large Area Telescope (LAT) on-board the *Fermi Gamma-ray Space Telescope*, its improved sensitivity and resolution in the MeV-GeV energy range has lead to a number of supernova remnants (SNRs) being detected in GeV  $\gamma$ -rays. The shock-front of an SNR is expected to be able to accelerate cosmic rays (CRs) efficiently, producing non-thermal X-ray and  $\gamma$ -ray emission. As  $\gamma$ -rays can arise from leptonic processes such as inverse Compton (IC) scattering and non-thermal bremsstrahlung from high-energy electrons, or from hadronic emission arising from the decay of a neutral pion (produced in a proton-proton interaction) into two photons, a means of distinguishing between these two mechanisms is crucial for our understanding of the origin of this observed emission. Thermal and non-thermal emission from SNRs have provided increasing support in favour of CRs being accelerated at the shock front of the remnant (e.g. Tycho: Warren et al. 2005; RX J1713.7-3946: Uchiyama et al. 2007; W44, MSH 17-39 and G337.7-0.1: Castro et al. 2013). SNRs known to be interacting with dense molecular clouds (MCs) are ideal, indirect laboratories that one can use to detect and analyse  $\gamma$ -rays arising from accelerated protons. The interaction of the SNR's shockwave with dense molecular material is often inferred from the detection of one or more OH (1720 MHz) masers, but enhancement of excitation line ratios such as  $J = 2 \rightarrow 1/J = 1 \rightarrow 0$ , broadenings and asymmetries in molecular line features or morphological alignment of molecular features with SNR features can also allow one to determine SNR/MC interaction (see Slane et al. 2015 and references therein).

Some of the first SNRs detected by the *Fermi-LAT* (e.g. W44: Abdo et al. 2010b, Ackermann et al. 2013; IC443: Ackermann et al. 2013); 3C391: Castro & Slane 2010; and W49B: Abdo et al. 2010a) are part of a unique class called

Mixed-Morphology (MM) SNRs. Some of these SNRs are known to be interacting with MCs. These SNRs are characterised by their centrally peaked X-ray morphology which is thermal in nature, while their radio profiles are limb-brightened (Rho & Petre 1998). The evolutionary sequence leading to these unusual X-ray properties are not well understood and the morphology and characteristics of these SNRs are difficult to explain using standard SNR evolution models. There are two main models that are invoked in the literature to explain their characteristics. One possible model (White & Long 1991) assumes that in the vicinity of the supernova explosion there are many small, dense, cold cloudlets. These cloudlets are small enough that they do not affect the passage of the shock, and are sufficiently dense that they are neither blown apart nor swept up. Once the shock has passed, the cloudlets slowly evaporate, filling the interior of the SNR with a relatively dense gas that emits in X-rays. Another possible scenario is that thermal conduction results in the transport of heat and material to the center of the remnant, increasing the central density of the remnant, and smoothing the temperature gradient behind the shock (Cox et al. 1999).

The ionisation state of a thermal plasma in an SNR can be characterised by its ionisation temperature ( $T_Z$ ) which describes the extent to which the ions are stripped of their electrons and its electron temperature ( $T_e$ ) which describes the kinetic energy of the electrons. The thermal plasmas of SNRs have been thought to be either underionised, where  $T_Z < T_e$  or in collisional ionisation equilibrium  $T_Z = T_e$ . Recent observations by the *Suzaku* satellite have confirmed earlier suggestions based on *ASCA* data (Kawasaki et al. 2005), that the thermal plasma in some MM SNRs is overionised (recombining) (e.g. 3C391: Sato et al. 2014; Ergin et al. 2014). Recombining plasmas have ionisation temperatures that are higher than the electron temperatures and require rapid cooling of electrons either by thermal conduction (Kawasaki et al. 2002), adiabatic expansion via rarefaction and recombination (Itoh & Masai 1989) or the interaction with dense cavity walls or molecular clouds (Dwarkadas 2005).

MSH 11–61A (G290.1-0.8) is a Galactic MM SNR that is known to be interacting with MCs. It was first discovered

<sup>1</sup> Harvard-Smithsonian Center for Astrophysics, 60 Garden Street, Cambridge, MA 02138, USA

<sup>2</sup> School of Physics and Astronomy, Monash University, Melbourne, Victoria 3800, Australia

<sup>3</sup> MIT-Kavli Center for Astrophysics and Space Research, 77 Massachusetts Avenue, Cambridge, MA 02139, USA

by Mills et al. (1961) using the Sydney 3.5m cross-type radio telescope. It was first identified as an SNR by Kesteven (1968) and later classified as a shell-type SNR with a complex internal structure and ear-like protrusions towards the northwest and southeast using the Molongo Observatory Synthesis Telescope (MOST) at multiple different wavelengths (Kesteven & Caswell 1987; Milne et al. 1989; Whiteoak & Green 1996). It has an angular size of  $19' \times 11'$  and a radio-continuum spectral index of  $\alpha = -0.33 \pm 0.07$  (Reynoso et al. 2006). Radio continuum observations using the Australia Telescope Compact Array (ATCA) by Reynoso et al. (2006) showed filamentary emission with little shell structure, while the northern and southern edges of the remnant show evidence that the shock front could be interacting with a plane parallel density gradient. Using NANTEN CO images of MSH 11–61A, Filipovic et al. (2005) determine that the SNR is associated with a MC towards the south-west and northern rim of the remnant. HI observations using the Southern Galactic Plane Survey find that the molecular cloud is found at a local standard of rest velocity of  $\sim 13 \text{ km s}^{-1}$  (McClure-Griffiths et al. 2005).

MSH 11–61A was first detected in X-rays by Seward (1990) using a 10.9 ks Einstein Observatory observation. The 0.3 - 4.5 keV Imaging Proportional Counter (IPC) image of the remnant showed that the X-ray emission is peaked towards the center of the remnant. Using a 40 ks Advanced Satellite for Cosmology and Astrophysics (ASCA) GIS observation, Slane et al. (2002) were able to determine that the central X-ray emission is thermal in nature, classifying the remnant as a MM SNR. They modelled the X-ray emission using the cloudy ISM model by White & Long (1991) and derived an intercloud medium density of  $\sim 0.05 - 0.40 \text{ cm}^{-3}$  and an age of 10 - 20 kyr. Using *XMM-Newton*, García et al. (2012) analysed five regions along the axes of the remnant using an absorbed plane parallel non-equilibrium ionisation (VP-SHOCK) model and found that the physical conditions across the remnant are not homogeneous, with variation in ionisation state, temperature and elemental abundances. Kamitsukasa et al. (2015) analysed *Suzaku* data and found that in the center and in the northwest of the remnant the plasma is recombining, while everywhere else it is ionising.

The distance to MSH 11–61A has been measured by a number of different methods. HI measurements taken by the 64-m Parkes telescope (Dickel 1973; Goss et al. 1972) gives a lower limit of  $\sim 3.5$  kpc to the remnant.  $H\alpha$  measurements by Rosado et al. (1996) using a Fabry-Perot interferometer implied a distance of 6.9 kpc assuming a  $V_{LSR}$  of  $+12 \text{ km s}^{-1}$  for the SNR. Using CO measurements, Reynoso et al. (2006) derived a distance of 7 - 8 kpc assuming the Brand & Blitz (1993) rotation curve. Reynoso et al. (2006) derived a distance of  $7 \pm 1$  kpc using HI absorption measurements from ATCA, combined with data from the Southern Galactic Plane Survey, while Slane et al. (2002) estimated a distance of 8 - 11 kpc by modelling the thermal X-ray emission of the remnant as detected by ASCA. We use 7 kpc throughout this paper.

There are three pulsars close to the position of MSH 11–61A. Kaspi et al. (1997) discovered the young (spin-down age,  $\tau = 63$  kyr), energetic pulsar PSR J1105-6107 (J1105) which is located approximately  $25'$  away from the remnant. It has a spin-down luminosity of  $2.5 \times 10^{36} \text{ erg s}^{-1}$  and overlaps the position of the *EGRET*  $\gamma$ -ray source 3EG J1103-6106. It was also detected via periodicity searches in GeV  $\gamma$ -rays by the *Fermi-LAT* satellite (Abdo et al. 2013). It has a dispersion measure of  $271 \text{ cm}^{-3} \text{ pc}$  which implies a dis-

tance of  $\sim 7$  kpc using the standard Galactic electron density model (Cordes & Lazio 2002). Kaspi et al. (1997) considered the scenario that this pulsar is associated with the remnant and determined from proper motion measurements that it would need to be travelling with a transverse velocity of  $\sim 650 \text{ km s}^{-1}$  to have reached its current position, assuming a distance of 7 kpc to the pulsar and  $\tau = 63$  kyr. This is much larger than the average pulsar transverse velocity but much less than what has been suggested for other pulsar-SNR associations (e.g., Caraveo 1993), leading the authors to conclude that association is possible. Using the ASCA X-ray characteristics of MSH 11–61A, Slane et al. (2002) concluded that MSH 11–61A and J1105 are not associated under the assumption that the SNR evolved via thermal conduction or a cloudy ISM. These two models imply a transverse velocity of  $\sim 4.5 \times 10^3 \text{ km s}^{-1}$  and  $\sim 5.3 \times 10^3 \text{ km s}^{-1}$  respectively, which is much larger than the mean velocity ( $\sim 310 \text{ km s}^{-1}$ ) of young pulsars (Hobbs et al. 2005). The two other pulsars, PSR J1103-6025 (Kramer et al. 2003) and PSR J1104-6103 (Kaspi et al. 1996) are not associated with the remnant as they have characteristic ages much larger than 1 Myr, which is far greater than the expected lifetime of an SNR. Also nearby is the extended INTEGRAL source IGR J11014-6103, whose neutron star PSR J1101-6101 (Halpern et al. 2014) is travelling at a velocity exceeding 1000 km/s, which Pavan et al. (2014) associate with MSH 11–61A.

Using 70 months of *Fermi-LAT* data, we analyse the GeV  $\gamma$ -ray emission coincident with MSH 11–61A and investigate the nature of this emission using broadband modelling. In addition, we analyse archival *Suzaku* data and report on the spatial and spectral properties of the X-ray emission of this remnant. In Section 2 we describe how the *Fermi-LAT* data are analysed and present the results of this analysis. In Section 3 we present our spatial and spectral analysis of the *Suzaku* observation of MSH 11–61A, while in Section 4 and 5 we discuss the implications of our results.

## 2. OBSERVATIONS AND ANALYSIS OF MSH 11–61A

We analysed  $\sim 70$  months of reprocessed data collected by the *Fermi-LAT* from 4th August 2008 to 16th June 2014. We selected data within a radius of  $20^\circ$  centered on MSH 11–61A. We used the “P7REP\_SOURCE\_V15” instrument response function (IRF) which is based on the same in-flight event analysis and selection criteria that was used to generate the previous “PASS7\_V6” IRFs (details described in Ackermann et al. 2012). Due to the improved reconstruction of the calorimeter position as well as a 1% per year correction for the degradation of the light yield of the calorimeter, the new IRFs significantly improve the point spread function (PSF) of the LAT for energy  $> 5 \text{ GeV}^4$ . The systematic uncertainties in the effective area of the *Fermi-LAT* using “P7REP\_SOURCE\_V15” are 10% below 100 MeV, decreasing logarithmically in energy to 5% between 0.316 - 10 GeV and increasing logarithmically to 15% at 1 TeV<sup>5</sup>. We selected events with a zenith angle less than  $100^\circ$  and that were detected when the rocking angle of the LAT was greater than  $52^\circ$  to decrease the effects of terrestrial albedo  $\gamma$ -rays. We analysed the  $\gamma$ -ray data in the direction of MSH 11–61A us-

<sup>4</sup> More details found: [http://www.slac.stanford.edu/exp/glast/groups/canda/lat\\_Performance.htm](http://www.slac.stanford.edu/exp/glast/groups/canda/lat_Performance.htm)

<sup>5</sup> [http://fermi.gsfc.nasa.gov/ssc/data/analysis/LAT\\_caveats.html](http://fermi.gsfc.nasa.gov/ssc/data/analysis/LAT_caveats.html)

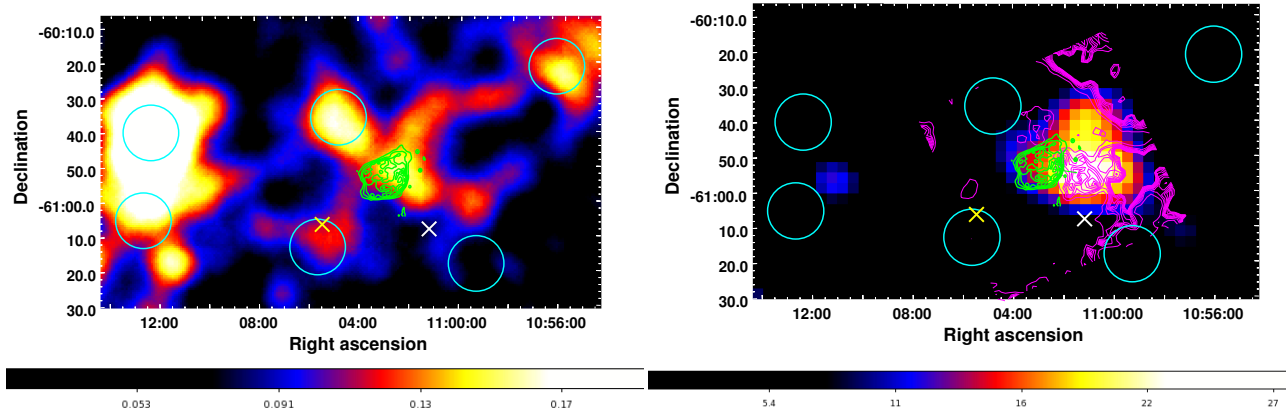


**Figure 1.** *Left:*  $2.5^\circ \times 1.5^\circ$  *Fermi-LAT* count map of the 2 - 200 GeV  $\gamma$ -ray emission surrounding MSH 11-61A (units: counts degree $^{-2}$ ). The pixel binning is  $0.01^\circ$  and the maps are smoothed with a Gaussian of width  $0.2^\circ$ . The brightest emission seen to the east of MSH 11-61A corresponds to the  $\gamma$ -ray bright SNR MSH 11-62. The yellow X corresponds to the radio position of PSR J1105-6107, while the white X corresponds to the position of ICG J11014-6103 (the lighthouse nebula). One can see that MSH 11-61A is located in a complicated region of the  $\gamma$ -ray emitting sky. 843 MHz MOST radio continuum contours are overlaid in green. *Right:*  $2.5^\circ \times 1.5^\circ$  TS map of MSH 11-61A. The magenta contours corresponds to the HI emission of the molecular cloud associated with the remnant as detected by the Southern Galactic Plane Survey (McClure-Griffiths et al. 2005). The HI emission contours range from 66 Kelvin at the edge of the molecular cloud interacting with MSH 11-61A to 100 Kelvin at the center of the molecular cloud over seven linearly spaced contour levels.

ing the Fermi Science Tools v9r33p0<sup>6</sup>

Due to the low count rates of  $\gamma$ -rays and the large PSF of the *Fermi-LAT*, the standard maximum likelihood fitting technique, *gtlike*, was used to analyse the  $\gamma$ -ray emission of the remnant. Given a specific emission model, *gtlike* determines the best-fit parameters of this model by maximising the joint probability of obtaining the observed data given an input model. *gtlike* accounts for background  $\gamma$ -ray emission by using diffuse Galactic and isotropic emission models described by the mapcube file `gll_iem_v05_rev1.fits` and the isotropic spectral template `iso_source_v05_rev1.txt`<sup>7</sup>. Gamma-ray emission from sources found in the Fermi-LAT second source catalogue are fixed to their position listed in the catalogue and their background contribution is calculated. The Galactic diffuse emission arises from the interaction of CRs with the interstellar medium and their subsequent decay into  $\gamma$ -rays, while the isotropic component arises from diffuse extragalactic  $\gamma$ -rays and residual charged particle emission.

To improve the angular resolution of the data while analysing the spatial properties of the  $\gamma$ -ray emission of MSH 11-61A, we selected  $\gamma$ -ray data converted in the *front* section of the *Fermi-LAT* with an energy range of 2 - 200 GeV. The improvement in spatial resolution in this energy range arises from the fact that the  $1-\sigma$  containment radius angle for *front*-selected photon events is  $< 0.3^\circ$ , while for lower energies it is much larger. To determine the detection significance, position and possible extent of the  $\gamma$ -ray emission coincident with MSH 11-61A we produced test statistic (TS) maps using *gttsmap* with an image resolution of  $0.05^\circ$ . The TS is defined as  $2\log(L_{ps}/L_{null})$ , where  $L_{ps}$  is the likelihood of a point source being found at a given position on a spatial grid and  $L_{null}$  is the likelihood of the model without the additional source.

<sup>6</sup> <http://fermi.gsfc.nasa.gov/ssc/data/analysis/software/>

<sup>7</sup> The most up to date Galactic and isotropic emission models can be found <http://fermi.gsfc.nasa.gov/ssc/data/access/lat/BackgroundModels.html>

To determine the spectral energy distribution (SED) of the  $\gamma$ -ray emission coincident with MSH 11-61A we use events converted in the *front* section of the LAT that have an energy of 0.2 - 204.8 GeV. This energy range is chosen to avoid the large uncertainties in the Galactic background model that arise below 0.2 GeV and to reduce the influence of the rapidly changing effective area of the LAT at low energies. We model the flux in each of 8 logarithmically spaced energy bins and estimate the best-fit parameters of the data using *gtlike*. We also include in the likelihood fit, background sources from the 24-month *Fermi-LAT* second source catalogue (Nolan et al. 2012) that are found within  $20^\circ$  region centered on MSH 11-61A. All evident background sources were identified in the *Fermi-LAT* second source catalogue and the associated parameters from the catalogue were used. We left the normalization of the Galactic diffuse emission, isotropic component and the background point sources within 5 degrees of MSH 11-61A free. For all other background point sources with a distance greater than 5 degrees from MSH 11-61A their normalisations were frozen to that listed in the 2nd Fermi-LAT catalogue. In addition to the statistical uncertainties that were obtained from the likelihood analysis, systematic uncertainties associated with the Galactic diffuse emission were also calculated by artificially altering the normalisation of this background by  $\pm 6\%$  from the best-fit value at each energy bin as outlined in Castro & Slane (2010).

In Figure 1 left panel, we have generated a  $2.5^\circ \times 1.5^\circ$  count map centered on MSH 11-61A that is smoothed by a Gaussian with a width similar to the PSF for the events selected. MSH 11-61A is located in a very complicated region of the sky. There are many *Fermi-LAT* sources close to the remnant, with  $\gamma$ -ray bright SNR MSH 11-62 (2FGL J1112.1-6040 and 2FGL J1112.5-6105) located  $\sim 1.2^\circ$ , and PSR J1105-6107 (2FGL J1105.6-6114) located  $\sim 0.36^\circ$ , from the remnant. There are four other *Fermi-LAT* sources in the immediate vicinity of MSH 11-61A (2FGL J1104.7-6036, 2FGL J1105.6-6114, 2FGL J1059.3-6118c and 2FGL J1056.2-6021), but none of these are coincident with the MOST radio contours of the SNR. We define a source re-

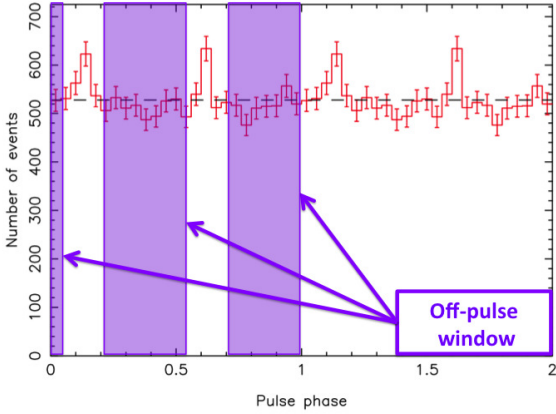


**Figure 2.** The pulse-phase diagram of PSR J1105-6107 obtained using events in an energy range of 0.1 - 300 GeV coming from a  $0.5^\circ$  radius around the position of the pulsar. The off-pulse window used for this analysis is defined between 0.00-0.05, 0.22-0.55 and 0.70-1.00 of the pulse phase. Here two cycles are shown.

gion at the position of MSH 11-61A to estimate the flux from the SNR. Due to the close proximity of PSR J1105-6107 (J1105) and the low resolution of the *Fermi-LAT* PSF ( $\sim 1^\circ$  for front events at 68% containment at  $\sim 0.6$  GeV), we can't rule out that this pulsar isn't contributing significantly to the observed  $\gamma$ -ray emission seen in Figure 1. Thus to analyse the spatial and spectral characteristics of the  $\gamma$ -ray emission of MSH 11-61A, we have to remove the pulsar contribution. As MSH 11-62 is located  $> 1^\circ$  away from MSH 11-61A, it is unlikely that it is contributing significantly to the observed  $\gamma$ -ray emission.

### 2.1. Removing the $\gamma$ -ray contribution of PSR J1105-6107

To avoid contamination from the pulsed emission of PSR J1105-6107 (J1105), we must perform our analysis in the off-pulse window of the pulsar light curve. The *Fermi-LAT* collaboration made available with its second *Fermi-LAT* catalogue of  $\gamma$ -ray pulsars (Yu et al. 2013) the ephemerides of 117  $\gamma$ -ray emitting pulsars that had been detected using three years of *Fermi-LAT* data. Due to the continuous observations of the *Fermi-LAT*, Yu et al. (2013) were able to directly determine regular times of arrival (TOAs) to produce a precise pulsar ephemeris. We use the available ephemeris for J1105 which is valid from MJD 54200 (April 2007) to MJD 56397 (April 2013). As we are interested in analysing over  $\sim 70$  months of *Fermi-LAT*, we need to check the validity of using the available J1105 ephemeris over the whole  $\sim 70$  months. Using the Parkes telescope, Yu et al. (2013) analysed J1105 searching for timing irregularities over a period of  $\sim 16$  years from August 1994 to September 2010 (MJD 49589 - MJD 55461). J1105 experienced a glitch at MJD 50417 (November 1996), MJD 51598 (February 2000), MJD 54711 (September 2008) and MJD 55288 (April 2010). The *Fermi-LAT* ephemeris of J1105 covers the glitches experienced by the pulsar since the beginning of the *Fermi-LAT* mission. As of writing, there have been no other reports in the literature that J1105 has undergone glitches since April 2010. We also tested whether the pulsar is noisy in  $\gamma$ -rays, as this can also indicate irregularities in the pulsar rotation that have not been incorporated in the ephemeris. We produced a pulse phase vs. events plot during the period of validity of the ephemeris (MJD 54200 to MJD 56397) and for the period between the end time of

the ephemeris and the end date of our data (MJD 56397 to MJD 56824) to see if the pulse peaks that we observe in Figure 2 disappear due to noise of the pulsar. We find that during both time periods we obtain the same pulse phase profile. As no glitches have been detected as of writing and the pulsar has not been noisy beyond MJD 56397, we assume that this ephemeris is valid for our whole data set.

The  $\gamma$ -ray photons were phase-folded using this ephemeris and the pulse phases were assigned to the *Fermi-LAT* data using the *Fermi-LAT* TEMPO2 plugin provided by the *Fermi-LAT* collaboration<sup>8</sup>. This plugin calculates the rotational phase of the pulsar for each photon arrival time in the *Fermi-LAT* data using the barycentric dates of each event. Using *ftselect*, we remove the pulse and use only the  $\gamma$ -ray photons in the off-pulse window (defined by the 0.00-0.05, 0.22-0.55 and 0.70-1.00 pulse phase intervals) to perform our spectral and morphological analysis. In Figure 2 we have plotted the pulse-phase diagram of J1105 obtained in the 0.10-300 GeV energy range using  $0.5^\circ$  radius around the position of J1105.

### 2.2. TS Map

In Figure 1 right panel we present a TS map of MSH 11-61A using the off-pulse  $\gamma$ -ray data. This was calculated using *gttssmap* over an energy of 0.2 - 2.0 GeV and using *front* events only. In addition to the diffuse Galactic background components, we include in the background model the *Fermi-LAT* sources associated with MSH 11-62 (2FGL J1112.1-6040 and 2FGL J1112.5-6105) and the four sources in the immediate vicinity of the remnant (2FGL J1104.7-6036, 2FGL J1105.6-6114, 2FGL J1059.3-6118c and J1056.2-6021). The TS map suggests that there is significant  $\gamma$ -ray emission coincident with MSH 11-61A and the MC associated with the remnant, as highlighted by the magenta contours. The peak of the  $\gamma$ -ray emission is found at a best fit position of  $(\alpha_{J2000}, \delta_{J2000}) = (11^h 01^m 29^s, -60^\circ 55' 29'')$ , placing it outside the SNR boundary, but consistent with being located along or inside the western limb given the angular resolution of the *Fermi-LAT*. The emission is detected with a significance of  $\sim 5\sigma$ , with the  $\gamma$ -ray emission at the center of the remnant producing a significance of  $\sim 4\sigma$ . One can see in Figure 1 right panel that the contribution of MSH 11-62 and the other *Fermi-LAT* sources surrounding the remnant have been modelled out, while the contribution from the pulsar (J1105) has been gated out successfully.

### 2.3. $\gamma$ -ray spectrum

The  $\gamma$ -ray spectrum of MSH 11-61A is shown in Figure 3, with the statistical errors plotted in black and systematic errors plotted in red. For energies above 6.40 GeV, only flux upper limits have been determined and are plotted as blue triangles. Additionally, the best fit power law and exponential cut-off power law models are plotted as the green dotted line and purple dot-dashed line respectively. The  $\gamma$ -ray spectrum can be fit using a simple power law with a spectral index of  $2.75^{+0.07}_{-0.06}$ , giving a reduced  $\chi^2 \sim 1$ . An exponential cut-off power law with  $E_{cut} = 4.20^{+1.91}_{-0.66}$  GeV and spectral index of  $2.49^{+0.17}_{-0.19}$  can fit the spectrum equally well giving a reduced  $\chi^2 \sim 0.8$  for the fit. For an energy range of 0.1-100 GeV, the integrated flux is  $(4.2^{+0.34}_{-0.98}) \times 10^{-11}$  erg cm $^{-2}$ s $^{-1}$ , assuming the

<sup>8</sup> [http://fermi.gsfc.nasa.gov/ssc/data/analysis/user/Fermi\\_plugin\\_doc.pdf](http://fermi.gsfc.nasa.gov/ssc/data/analysis/user/Fermi_plugin_doc.pdf)

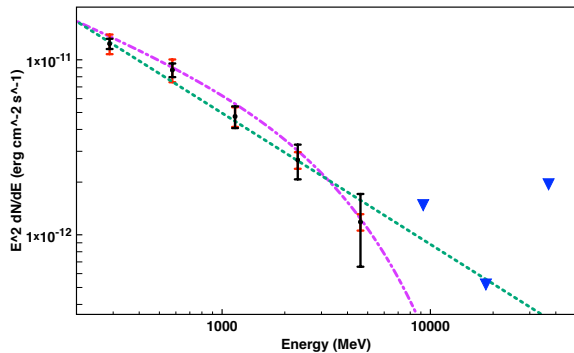


**Figure 3.** The *Fermi*-LAT  $\gamma$ -ray spectrum of MSH 11–61A. Statistical errors are shown as black error bars, systematic errors are plotted as red error bars, while the upper limits are plotted as blue triangles. The simple power law model with  $\Gamma = 2.75^{+0.07}_{-0.06}$  and exponential cut-off power law model with  $\Gamma = 2.49^{+0.17}_{-0.19}$  and  $E_{cut} = 4.20^{+1.91}_{-0.66}$  GeV are shown as the green dotted and magenta dot-dashed line respectively.

power law fit. Using a distance of 7 kpc, the luminosity of this  $\gamma$ -ray source in this energy range is  $(2.5^{+0.17}_{-0.63}) \times 10^{35}$  erg s $^{-1}$ .

### 3. SUZAKU OBSERVATIONS OF MSH 11–61A

MSH 11–61A was observed with *Suzaku* using X-ray imaging spectrometers (XIS) (Koyama et al. 2007) on 2011 July 25th for  $\sim 111$ ks (ObsID 506061010). For this observation only XIS0<sup>9</sup>, XIS1 and XIS3 observations are available as XIS2 has not been functional since November 2006<sup>10</sup>. Recently, Kamitsukasa et al. (2015) presented their analysis of this *Suzaku* observation. They found recombining plasma in the center and in the northwest of the remnant which has enhanced abundances and a temperature of  $\sim 0.5$  keV, while everywhere else the X-ray emission arises from an ionising ISM component with a temperature of  $\sim 0.6$  keV. In section 5.2.1, we estimate the density of the  $\gamma$ -ray emitting material based on our *Fermi*-LAT spectrum (Figure 3). To test whether this inferred density agrees with other observations, we have re-analysed the *Suzaku* data in order to estimate the density of the surrounding environment.

For our analysis we used the standard tools of *HEASOFT* version 6.16. We reprocessed the unfiltered public data using *aepipeline* (version 1.1.0) and use the current calibration database (CALDB) available as of 2014 July 1st (version 20140701). Following the standard screening criteria<sup>11</sup>, we filtered hot and flickering pixels, time intervals corresponding to *Suzaku* passing the South Atlantic Anomaly and night-earth and day-earth elevation angles less than  $5^\circ$  and  $20^\circ$ , respectively. We utilised events that had a grade of 0, 2, 3, 4 and 6 only. The total exposure of our observation is 111 ks for each of the XIS detectors. We extracted the spectra and images of the remnant from the  $5 \times 5$  and  $3 \times 3$  editing mode event files using XSELECT version 2.4. For the spectral analysis we generated the redistribution matrix file (RMF) and ancillary response files (ARF) using *XISRMPGEN* and *XISARFGEN*

<sup>9</sup> It is also important to note that a fraction of XIS0 has not been functional since 2009 June 23rd due to the damage caused by a micro meteorite. For more information see: <http://www.astro.isas.jaxa.jp/suzaku/doc/suzakumemo/suzakumemo-2010-01.pdf>.

<sup>10</sup> <http://www.astro.isas.jaxa.jp/suzaku/doc/suzakumemo/suzakumemo-2007-08.pdf>

<sup>11</sup> <http://heasarc.nasa.gov/docs/suzaku/processing/criteriaxis.html>

**Table 1**  
Best fit parameters for our background model.

Component	Parameter	Value
<i>Cosmic X-ray background</i>	$N_H (\times 10^{22} \text{ cm}^{-2})$	$1.47^{+1.07}_{-0.83}$
	$\Gamma$	1.40 (frozen)
<i>Galactic ridge emission</i>	$N_H (\times 10^{22} \text{ cm}^{-2})$	$0.61^{+0.08}_{-0.06}$
	kT (keV)	$0.22 \pm 0.02$
	Abundances	0.20 (frozen)
<i>Galactic halo</i>	$N_H (\times 10^{22} \text{ cm}^{-2})$	$1.64^{+0.13}_{-0.10}$
	kT (keV)	$0.58 \pm 0.02$
	Ne	$2.71^{+0.60}_{-0.40}$
	Mg	$2.31^{+0.23}_{-0.18}$
	Si	$3.48^{+0.34}_{-0.32}$
	Reduced $\chi^2$ (dof)	1.80 (1602)

Note: All uncertainties correspond to  $1\sigma$  errors.

respectively. To analyse the spectral data we used the X-ray spectral fitting package (XSPEC) version 12.8.2q with AtomDB 3.0.1<sup>12</sup> (Smith et al. 2001; Foster et al. 2012).

#### 3.1. Spectral analysis of the individual annulus and rectangular regions

We extracted spectra from a central circular region defined by region 1 in Figure 4 (right panel) and 6 annular regions of width  $0.82'$  to cover the central X-ray emission of the remnant (regions 2 - 7 in Figure 4, right panel). The radial size of these regions was chosen to be the same size as the angular resolution of *Suzaku* ( $\sim 0.8'$ ). These regions were chosen to fully enclose the bright central X-ray emission of the remnant, which is quite symmetric in nature. We also extracted spectra from three rectangular regions (regions 8 - 10 in Figure 4, right panel) that are not covered by the annulus regions, to enclose protrusions in the northwest, southeast, and east. Annular regions were chosen in order to characterise radial variations in the brightness, temperature, ionisation state and elemental abundances of the remnant, all of which are important for understanding the nature of the mixed morphology. Our choice of regions differs from those chosen by Kamitsukasa et al. (2015), who also analysed the *Suzaku* observation of MSH 11–61A. They extracted spectra from five regions that do not enclose the full X-ray emission from the remnant – a central region that corresponds to our regions 1, 2, and 3; a northwest region that encompasses our region 8 and a northwestern portion of region 7; and NE, SE, and SW regions that cover sectors of our annular regions and also encompass our region 9 in the east. All spectra were grouped by 20 counts using the FTOOLS command *grppha* and all available XIS detectors were used.

To estimate the background, we extract data from the full field of view of the XIS of our observation, excluding the calibration regions and the emission from the remnant. The background spectrum consists of two major components, the non X-ray background and the astrophysical background which is made up of the cosmic X-ray background, the Galactic ridge X-ray emission and the Galactic halo. We use *xisnxbgen* (Tawa et al. 2008) to generate a model for the NXB which we then subtract from our background spectrum. Similarly, we subtract a model for the NXB from our spectra obtained from the regions shown in Figure 4 right panel. Similar to Kamitsukasa et al. (2015), we model this NXB subtracted spectrum. We fix the cosmic X-ray background power law component to

<sup>12</sup> AtomDB 3.0.1 can be downloaded here: <http://www.atomdb.org/download.php>

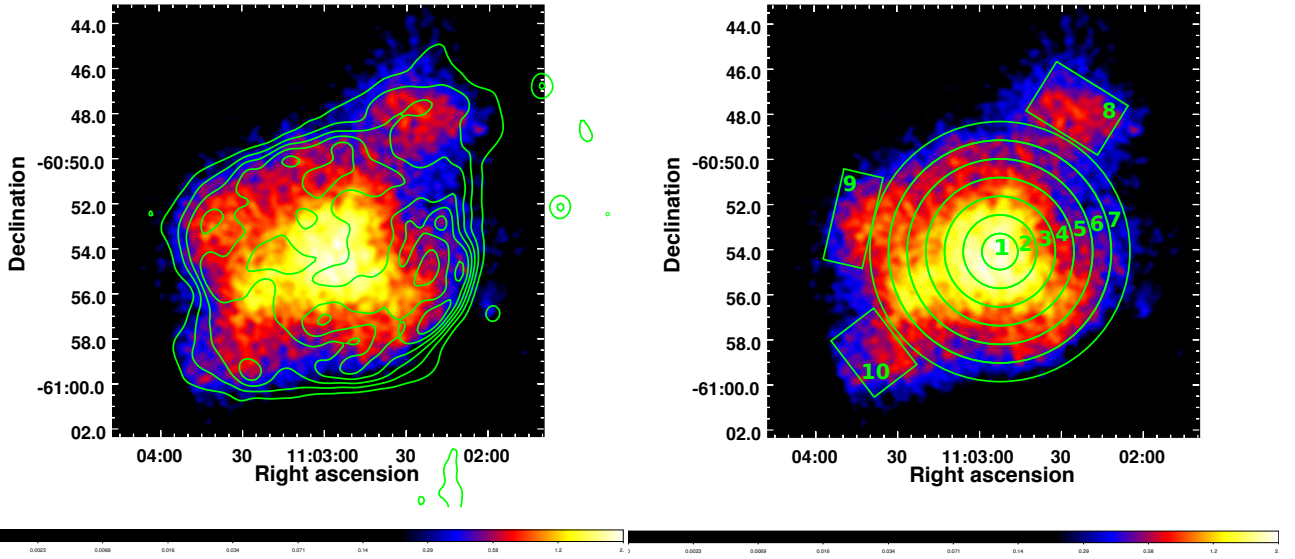


**Figure 4.** *Suzaku* XIS0 image of MSH 11–61A in the 0.5–7.0 KeV energy band. The image has been smoothed with a Gaussian function of width  $0.1'$  and has a logarithmic scaling applied to it. *Left* : The green contours correspond to the 843 MHz MOST radio continuum emission used in Figure 1. *Right* : Overlaid in green are the regions we use for spectral extraction, described in Section 3.1.

**Table 2**  
Spectral fits for all 10 individual regions.

Region	$N_H$ ( $10^{22}$ cm $^{-2}$ )	$kT$ (keV)	$kT_{init}$ (keV)	Ne	Mg	Si	S	Fe	$\tau$ ( $10^{12}$ s cm $^{-3}$ )	Reduced $\chi^2$
1	$1.76^{+0.12}_{-0.15}$	$0.43^{+0.03}_{-0.02}$	5	–	$3.23^{+0.52}_{-0.46}$	$6.32^{+1.07}_{-0.92}$	$1.92^{+0.24}_{-0.19}$	–	$1.59^{+0.19}_{-0.14}$	0.79
2	$1.20^{+0.12}_{-0.11}$	$0.42^{+0.02}_{-0.02}$	5	$0.23^{+0.12}_{-0.09}$	$1.82^{+0.26}_{-0.20}$	$4.96^{+0.38}_{-0.34}$	$2.51^{+0.38}_{-0.34}$	$0.11^{+0.08}_{-0.06}$	$1.29^{+0.08}_{-0.06}$	0.94
3	$1.32^{+0.14}_{-0.13}$	$0.40^{+0.03}_{-0.02}$	5	$0.35^{+0.17}_{-0.12}$	$2.04^{+0.33}_{-0.26}$	$4.65^{+0.30}_{-0.42}$	$2.62^{+0.43}_{-0.36}$	$0.14^{+0.10}_{-0.08}$	$1.26^{+0.06}_{-0.06}$	1.02
4	$1.81^{+0.24}_{-0.09}$	$0.34^{+0.02}_{-0.02}$	5	–	$2.93^{+0.33}_{-0.28}$	$5.69^{+0.73}_{-0.51}$	$3.72^{+0.41}_{-0.71}$	–	$1.34^{+0.04}_{-0.07}$	1.08
5	$1.87^{+0.10}_{-0.17}$	$0.27^{+0.06}_{-0.01}$	5	–	$2.49^{+0.33}_{-0.28}$	$5.21^{+0.74}_{-0.75}$	$3.34^{+1.52}_{-1.14}$	–	$1.28^{+0.09}_{-0.11}$	1.06
6	$1.66^{+0.04}_{-0.08}$	$0.30^{+0.03}_{-0.02}$	5	–	$2.67^{+0.51}_{-0.20}$	$3.69^{+0.67}_{-0.41}$	$2.12^{+0.46}_{-0.44}$	–	$1.00^{+0.09}_{-0.08}$	1.10
7	$1.67^{+0.21}_{-0.16}$	$0.36^{+0.05}_{-0.03}$	5	–	$4.11^{+1.07}_{-0.77}$	$7.05^{+1.92}_{-1.30}$	$4.27^{+1.42}_{-1.11}$	–	$1.09^{+0.08}_{-0.07}$	1.14
8	$2.27^{+0.23}_{-0.21}$	$0.42^{+0.04}_{-0.04}$	5	–	$2.59^{+0.58}_{-0.46}$	$4.87^{+1.11}_{-0.86}$	$2.91^{+0.83}_{-0.66}$	–	$0.90^{+0.05}_{-0.06}$	0.92
9	$2.00^{+0.45}_{-0.30}$	$0.80^{+0.22}_{-0.27}$	0.0808	–	$3.63^{+2.77}_{-1.02}$	$6.91^{+5.72}_{-3.96}$	$3.06^{+5.20}_{-1.43}$	–	$0.22^{+0.22}_{-0.11}$	0.84
10	$2.46^{+0.38}_{-0.37}$	$0.73^{+0.24}_{-0.14}$	0.0808	–	$4.69^{+1.62}_{-1.03}$	$6.67^{+2.96}_{-1.43}$	$2.86^{+1.17}_{-0.90}$	–	$0.19^{+0.19}_{-0.11}$	0.94

Note: All uncertainties correspond to the 90% confidence level.

that of Kushino et al. (2002), and use a single apc model with a temperature and surface brightness ( $\sim 1.0 \times 10^{-12}$  erg cm $^{-2}$  s $^{-1}$  deg $^{-2}$  for 0.5–2.0 keV) similar to that obtained by Henley & Shelton (2013) to define our Galactic halo component. We use a single low temperature apc model with subsolar abundances frozen to that of Kaneda et al. (1997) to define the Galactic ridge emission. We also use the Wilms et al. abundance table (Wilms et al. 2000). Our best-fit parameters for our background and their uncertainties are given in Table 1.

To model the X-ray emission from the remnant we used a non-equilibrium ionisation (NEI) collisional plasma model, VVRNEI, which is characterised by a final ( $kT$ ) and initial electron temperature ( $kT_{init}$ ), elemental abundances and a single ionisation timescale ( $\tau = n_e t$ ). This allows one to model a plasma that is ionising up to collisional equilibrium from a very low initial temperature  $kT_{init}$ , mimicking the standard NEI/VNEI model that is commonly used in the literature. Additionally, the RNEI/VVRNEI model can reproduce a recombining (overionised) plasma where one assumes that the plasma starts in collisional equilibrium with an initial temper-

ature  $kT_{init}$  that suddenly drops to its final temperature  $kT$ . For our analysis, the column density, ionisation timescale, normalisation, and final temperature were left as free parameters. Due to the strong emission lines from Mg, Si, and S the abundances of these elements were also left free. Additionally we also let Ne and Fe be free parameters for regions 2–3, as we found that varying these significantly improved the fit. All other elemental abundances were frozen to the solar values reported by Wilms et al. (2000). The foreground absorbing column density  $N_H$  was modelled using TBABS (Wilms et al. 2000). Figure 7 shows an example of the X-ray spectrum of MSH 11–61A as extracted from region 3. The spectra derived for each region shown in Figure 4 right panel all have similar features to the spectrum shown in Figure 7.

We found that for regions 1–8 the fit favoured an initial temperature larger than the final temperature, while regions 9 and 10 favoured an initial temperature smaller than the final temperature. When left free, these initial temperatures would hit the upper (or lower) limits of this parameter and the associated abundances we obtained for our fits were un-

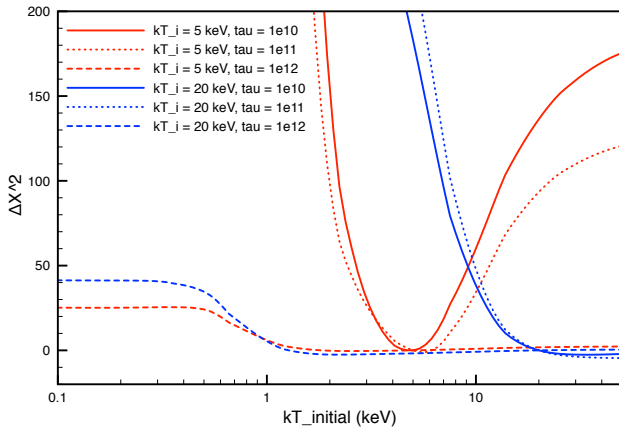


**Figure 5.** The sensitivity of our fits to changes in  $kT_{init}$  based on  $\Delta\chi^2$ . Here the red plots correspond to  $kT_{init} = 5$  keV, and the blue corresponds to  $kT_{init} = 20$  keV. The solid, dotted and dot-dashed lines correspond to  $\tau = 10^{10}$  s  $\text{cm}^{-3}$ ,  $10^{11}$  s  $\text{cm}^{-3}$  and  $10^{12}$  s  $\text{cm}^{-3}$  respectively. We assume  $kT = 0.5$  keV and  $n_H = 10^{22}$   $\text{cm}^{-2}$  for all spectra. From this plot we derive an upper limit for  $kT_{init}$  of 2 - 5 keV corresponding to a shock velocity of 1300 - 2100 km/s, for which we then use in our fits.

realistically high (abundances of [Mg], [Si] > 10 relative to Wilms et al. 2000). The ionisation timescale for all regions was  $\tau \sim 10^{12}$  s  $\text{cm}^{-3}$ .

To investigate the sensitivity of our fits to values of  $kT_{init}$ , we simulated spectra with similar counting statistics to those from our regions of investigation, using  $kT = 0.5$  keV,  $N_H = 10^{22}$   $\text{cm}^{-2}$ , and  $kT_{init} = 5$  keV or 20 keV. We considered cases for  $\log \tau = 10, 11, \text{ and } 12$ . We fit each spectrum to a TBABS\*VVRNEI model and then investigated the effect of freezing  $kT_{init}$  values over a range from 0.1 to 100 keV. The results are illustrated in Figure 5 where we plot  $\Delta\chi^2$  vs.  $kT_{init}$  for spectra with actual  $kT_{init}$  values of 5 keV (red) and 20 keV (blue). Here the solid, dotted, and dashed lines correspond, respectively, to  $\log \tau = 10, 11, \text{ and } 12$ . For low ionisation timescales the resulting fits are quite sensitive to the  $kT_{init}$  value, while for timescales similar to that found in MSH 11–61A ( $\tau \approx 10^{12}$  s  $\text{cm}^{-3}$ ), the fits are insensitive to  $kT_{init}$  (i.e. the  $\Delta\chi^2$  vs.  $kT_{init}$  plot plateaus) for temperatures greater than 2–5 keV. This is because above  $\sim 2$ –5 keV, it is only the emission from Fe and Ni that is significantly impacted by higher  $kT_{init}$  values, because all other abundant ions are fully stripped at these temperatures. Our observations do not have enough counts around the Fe and Ni lines to provide sensitivity to such an effect (though longer observations, particularly with higher resolution, would provide such sensitivity; see below).

Based on where  $\Delta\chi^2$  vs.  $kT_{init}$  plot plateaus for  $\tau \approx 10^{12}$  s  $\text{cm}^{-3}$ , we fix value of  $kT_{init}$  at 5 keV for all regions other than 9 and 10. For the latter regions, whose fits indicate  $kT_{init} < kT$ , we fix the initial temperature at the minimum available value for the VVRNEI model (80.8 eV). In Table 2, we list the best fit parameters for each of our spectra. All uncertainties correspond to the 90% confidence level.

A recombining plasma that has an initial temperature of 2 - 5 keV implies that the shock must have had a velocity of  $\sim 1300$  - 2100  $\text{km s}^{-1}$ , assuming electron-ion equilibrium. This high initial velocity suggests that the recombining plasma could be the result of the SNR shock front initially expand-

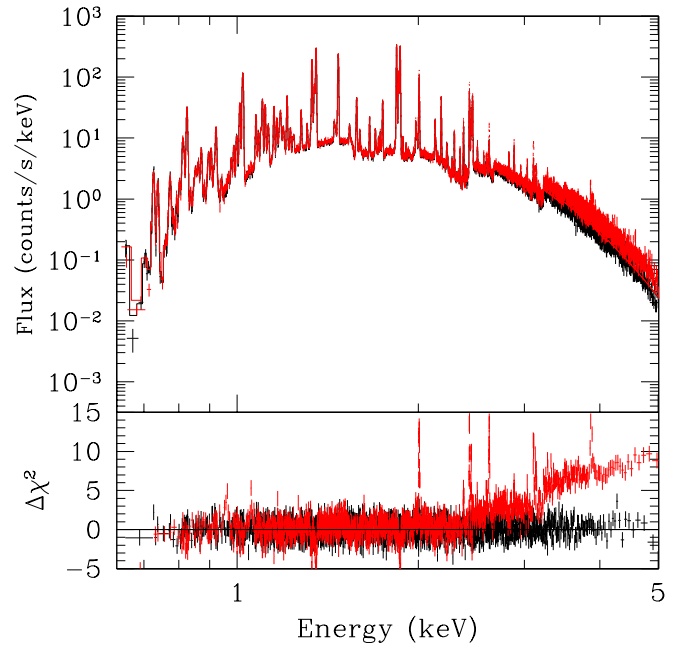


**Figure 6.** A 20 ks background subtracted spectrum simulated for *ASTRO-H* for a recombining plasma that has an initial temperature of 2 keV (black) and one that has an initial temperature of 50 keV (red). The model was based on that obtained for region 8 but with the initial temperature set to 2 keV and 50 keV. With this observation one can easily differentiate between a recombining plasma that has two different initial temperatures.

ing into a dense CSM, reaching a high ionisation state corresponding to the high initial expansion velocity (and, thus, shock temperature). Such a scenario might result from expansion into an  $r^{-2}$  density profile characteristic of a stellar wind, with subsequent expansion into the lower density regions resulting in rapid cooling, leaving an overionised plasma (Itoh & Masai 1989; Moriya 2012).

Even though our current data are unable to differentiate between a plasma that has an initial temperature of 2 - 5 keV or one that has initial temperature greater than this, with the launch of *ASTRO-H* we will be able to differentiate between these two cases. In Figure 6 we have plotted a simulated background-subtracted spectrum that we would obtain in a 20 ks observation using the calorimeter on *ASTRO-H* for a plasma that has an initial temperature of 2 keV and one that has an initial temperature of 50 keV, assuming our fit parameters for region 8. The background spectrum for *ASTRO-H* was obtained from SIMX simulations<sup>13</sup>. Here the black spectrum corresponds to a plasma that has an initial temperature of 2 keV (or an initial velocity of  $\sim 1300$   $\text{km s}^{-1}$ ), while the red spectrum corresponds to a plasma that has an initial temperature of 50 keV (or an initial velocity of  $\sim 7000$  km/s, typical of the high initial expansion speed of an SNR). One can see that with a 20 ks *ASTRO-H* observation, we could easily differentiate between two plasmas that have different initial temperatures.

Our spectra from MSH 11–61A are best described by a recombining plasma model with the exception of emission from regions 9 and 10, in the eastern and southeastern outskirts, where an ionising plasma is observed. Our results for the central regions (1 - 3) agree well with those of Kamitsukasa et al. (2015), who also find a recombining plasma for their south-

<sup>13</sup> <https://hea-www.harvard.edu/simx/>

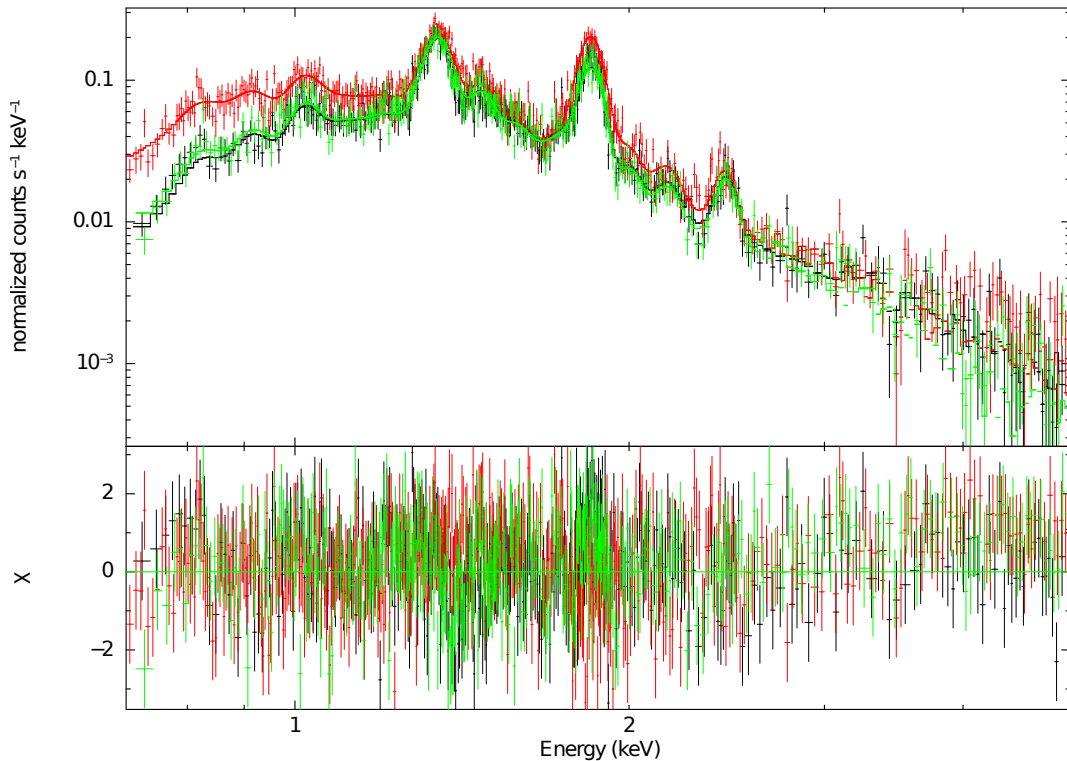


**Figure 7.** The *Suzaku* XIS0, XIS1 and XIS3 spectrum extracted from region 3 in Figure 4. These spectra were fitted simultaneously using our background model described in Table 1 and an absorbed VVRNEI model as described by the parameters listed in Table 2. The spectra are overlaid with the best fit model with their  $\chi^2$  residuals. The spectra derived for each region shown in Figure 4 right panel all have similar features as the spectrum shown here.

western region, in agreement with our results. In contrast, for their southeastern and northeastern regions, Kamitsukasa et al. (2015) obtain best fits for an ionising plasma. Given that these regions combine emission from the eastern and southeastern protrusions (our regions 9 and 10), for which we also observe an ionising plasma, with emission from the outer symmetric portion of the SNR, where we observe a recombining plasma, the combination of two components may explain the partial discrepancy. Conversely, Kamitsukasa et al. (2015) report an ionising plasma for their southwestern region, which covers regions for which we obtain a recombining plasma. This may result from our annular regions averaging over multiple components.

All regions have an ionisation timescale of  $\sim 1.0 \times 10^{12}$   $\text{cm}^{-3}$  s, indicating that the X-ray emitting plasma across the whole remnant is close to ionisation equilibrium (Smith & Hughes 2010). The temperature of the recombining components ranges from 0.27 keV to 0.43 keV near the bright central X-ray emission. Interestingly, the regions that are best described by an ionising plasma have the highest temperatures out of all the regions that we analysed, with temperatures of 0.80 keV and 0.73 keV respectively. On average, our derived temperatures are lower than that derived by Kamitsukasa et al. (2015), García et al. (2012) in their *XMM-Newton* analysis, and Slane et al. (2002) in their *ASCA* analysis.

We find in all regions strong emission lines coming from Mg, Si and S and all regions require super-solar abundances of these elements. The enhancement of elemental abundances is observed in many MM SNRs and indicates that some of the X-ray emission we are observing arises from ejecta that have been dispersed throughout the remnant and been mixed with

the swept up shocked material. Similar to Kamitsukasa et al. (2015), and García et al. (2012) we also find an underabundance of Ne and Fe in regions 2 - 3. Unlike, Kamitsukasa et al. (2015) we do not find evidence for overabundance of Ar or the underabundance of O suggested by García et al. (2012). When we freed these parameters we found that they do not significantly improve our fit, thus we kept them at solar. Our estimated abundances are slightly higher than that derived by Kamitsukasa et al. (2015), García et al. (2012) and Slane et al. (2002). This discrepancy arises from the fact that in our analysis we use the abundance table by Wilms et al. (2000) and the newly updated ATOMDB 3.0.1, while Kamitsukasa et al. (2015) and García et al. (2012) use the table derived by Anders & Grevesse (1989) and ATOMDB 3.0 and ATOMDB 2.0.2 respectively.

Our derived column density towards MSH 11–61A ranges between  $(1.20^{+0.12}_{-0.11} - 2.46^{+0.38}_{-0.37}) \times 10^{22}$   $\text{cm}^{-2}$ . The column density is highest in regions 8 - 10 which directly interacts with the surrounding environment. Our estimates for  $N_H$  are higher than the column density derived by Slane et al. (2002), García et al. (2012) and Kamitsukasa et al. (2015). This discrepancy arises from the fact that we use a different abundance table and a different absorption model.

### 3.2. Deriving the density of the X-ray emitting gas

The density of the X-ray emitting gas was calculated from the normalisation of the VVRNEI models using  $n_e = 1.2n_H$ . We estimate the volume for each region by taking an area equivalent to the extracted SNR regions shown in Figure 4 right panel and projecting this area through a filled sphere. The estimated density  $n \approx 1.1n_H$  (assuming ISM abundances) is listed for each region in Table 3.

**Table 3**

Number density of the X-ray emitting material estimated from the best fits of the 10 different regions shown in Figure 4.

Region	$n$ ( $d_7^{-0.5} f^{-0.5} \text{ cm}^{-3}$ )
1	$0.66^{+0.28}_{-0.23}$
2	$0.71^{+0.24}_{-0.22}$
3	$0.85^{+0.31}_{-0.30}$
4	$1.28^{+1.17}_{-0.43}$
5	$2.43^{+0.96}_{-1.37}$
6	$2.68^{+1.01}_{-1.20}$
7	$2.41^{+1.28}_{-1.15}$
8	$5.87^{+2.82}_{-2.32}$
9	$1.77^{+1.32}_{-0.93}$
10	$2.23^{+1.41}_{-1.17}$

The inferred density ranges from  $n = (0.66^{+0.28}_{-0.23} - 5.87^{+2.82}_{-2.32}) d_7^{-0.5} f^{-0.5} \text{ cm}^{-3}$  and is highest in region 8 which is coincident with the location of the dense molecular cloud found towards the west. The density is lowest towards the center of the remnant where the brightest X-ray emission is located, while the eastern part of the remnant has a density that is intermediate of the central regions of MSH 11–61A. Our density estimates for the bulk of the remnant are consistent with the densities derived by Slane et al. (2002) who attempted to reproduce the observed temperature and brightness profiles of the remnant using the cloudy ISM model by White & Long (1991) and a hydrodynamical model that traces the evolution of the remnant, while incorporating the effects of thermal conduction.

#### 4. THE ORIGIN OF THE THERMAL X-RAY EMISSION

The total X-ray emitting mass in MSH 11–61A is given by  $M_X = 1.4n_H m_H fV$ , where  $m_H$  is the mass of the hydrogen atom,  $V$  is the volume from which the emission is observed, and  $f$  is the filling factor. Using the estimated volumes and derived densities for regions 1–7, we sum the masses to obtain  $M_X \approx 480 d_7^{5/2} f^{1/2} M_\odot$ . This is comparable to the swept up mass derived by Slane et al. (2002).

The enhancement of Mg, Si and S abundances throughout the remnant suggests that the observed X-ray emission arises in part from supernova ejecta. Assuming that all ejecta have been shocked, we can estimate the mass of the ejecta components based upon the measured abundances:  $M_i = [(a_i - 1)/1.4](n_i/n_H)(m_i/m_H)M_X$  where  $M_i$  is the ejecta mass of species  $i$ ,  $a_i$  is its abundance relative to ISM abundances, as listed in Table 2,  $m_i$  is the atomic mass, and  $n_i/n_H$  is its ISM abundance relative to hydrogen. We find that, using the average of the measured abundances, the total ejecta masses of Mg, Si, and S are, respectively,  $0.37d_7^{5/2} f^{1/2} M_\odot$ ,  $0.80d_7^{5/2} f^{1/2} M_\odot$ , and  $0.26d_7^{5/2} f^{1/2} M_\odot$ . However, we note that the abundances for Ne and Fe are both lower than ISM values, meaning that we have no evidence for ejecta components for these species, and suggesting caution in interpreting all of the abundances. Taken at face value, however, the Mg, Si, and S ejecta mass estimates are consistent with a progenitor mass  $> 25M_\odot$  (Thielemann et al. 1996).

Recombining plasma can arise from two main scenarios: thermal conduction which is the rapid cooling of electrons due to the interaction of the hot ejecta with the cold, dense surrounding environment (Cox et al. 1999); or adiabatic expansion which can occur when the SNR shockwave expands through a dense circumstellar medium into a low density ISM

(Itoh & Masai 1989).

For thermal conduction to be the more likely scenario, the recombining plasma is expected to be coincident with the location of the molecular cloud, there should be a temperature decrease towards the molecular cloud and one would expect the thermal conduction timescale  $t_{cond}$  to be less than or comparable to the age of the remnant. We find recombining plasma in regions that are directly interacting with the molecular cloud (Regions 7 and 8), and we do see a slight temperature decrease towards the molecular cloud based on the annulus regions. The thermal conduction timescale is given by (Spitzer 1962; Zhou et al. 2014)  $t_{cond} \sim kn_e l_T^2 / \kappa \sim 56(n_e/1\text{cm}^{-3})(l_T/10\text{pc})^2(kT/0.6\text{keV})^{-5/2}(\ln\Lambda/32)\text{kyr}$ , where  $n_e$  is the electron density and is calculated from our best-fits listed in Table 2,  $l_T$  is the scale length of the temperature gradient,  $k$  is Boltzmann’s constant,  $\kappa$  is the thermal conductivity for a hydrogen plasma and  $\ln \Lambda$  is the Coulomb logarithm. Assuming a distance of 7 kpc to the remnant and a radius of  $\sim 5.77'$ , we calculate the length of the temperature gradient to be  $\sim 3.6 \times 10^{19} \text{ cm}$ . Using the temperature and density of region 7 (see Table 7 and Table 3 respectively), the thermal conduction timescale is estimated to be  $\sim 334 \text{ kyr}$ . This is  $\sim 16$  times greater than the age of the remnant ( $\sim 10 - 20 \text{ kyr}$ ), making it unlikely that the overionised plasma arises via thermal conduction.

Another possibility is that the recombining plasma arises from adiabatic cooling. To calculate  $t_{recomb}$ , we use the best fit ionisation timescale for region 1 - 8 listed in Table 2 and divide these by the electron density of each region. We obtain a recombining timescale between  $\sim (2 - 125) d_7^{-0.5} f^{-0.5} \text{ kyr}$ , which is comparable to the age of MSH 11–61A, making this scenario the most likely. This is consistent with the results reported by Kamitsukasa et al. (2015) and the velocity implied by our upper limit for  $kT_{init}$ .

#### 5. THE NATURE OF $\gamma$ -RAY EMISSION

##### 5.1. Pulsar contribution and the Integral source ICG J11014-6103

Pulsars that are detected within the *Fermi-LAT* energy band (see the second *Fermi-LAT* Pulsar catalogue by Abdo et al. 2013), have spectra that is well characterised by a power law with an exponential cut-off of 1 - 5 GeV. As the  $\gamma$ -ray spectrum of MSH 11–61A can be described using an exponential cut-off of  $E_{cut} \sim 4.2\text{GeV}$ , we still need to consider the scenario that the  $\gamma$ -ray emission we observe arises from a nearby pulsar other than J1105-6107.

Using the Australian Telescope National Facility (ATNF) Pulsar Catalogue (Manchester et al. 2005), there are 9 pulsars including J1105-6107 within  $5^\circ$ , whose spin down power is sufficient to produce the  $\gamma$ -ray flux of MSH 11–61A. All of these pulsars, except for J1105-6107, are  $>1^\circ$  from the centroid of the  $\gamma$ -ray emission making it unlikely that any of these pulsars are contributing significantly to the observed emission of MSH 11–61A. As we removed the contribution of J1105-6107 from the  $\gamma$ -ray data as described in Section 2.1, we can also rule out its contribution.

Recently, Pavan et al. (2014) investigated the nature of the X-ray and radio emission of the INTEGRAL source ICG J11014-6103, which they call the lighthouse nebula. In X-rays this nebula exhibits a prominent jet-like feature that is perpendicular to an elongated cometary tail, and a point source. The source of this X-ray structure is a neutron star travelling supersonically and we have plotted its position as

the white  $X$  shown in Figure 1. This neutron star has a spin down power of  $\dot{E} \sim 10^{37}$  erg s $^{-1}$ . As the  $\gamma$ -ray luminosity of MSH 11–61A is  $2.5 \times 10^{35}$  erg s $^{-1}$ , the PSR of ICG J11014-6103 would require an efficiency of  $L_\gamma/\dot{E} \sim 2.5\%$  to produce the observed  $\gamma$ -rays, which is plausible. In an attempt to disentangle the likely source of the  $\gamma$ -ray emission, we have plotted as the magenta contours in Figure 1 right panel, the HI contours of the molecular cloud associated with MSH 11–61A. If one assumes that the pulsar of ICG J11014-6103 can produce significant  $\gamma$ -ray emission, we would expect the detection significance peak to be skewed towards the position of ICG J11014-6103 instead of in the direction of the remnant and MC as is observed. Thus even though we cannot rule out that ICG J11014-6103 is contributing to the  $\gamma$ -ray emission in Figure 3, the association of the molecular cloud and the detection significance in this region suggests that the emission most likely arises from the interaction of the SNR with the molecular cloud, rather than ICG J11014-6103.

### 5.2. Modelling the broadband emission of MSH 11–61A

To investigate the nature of the broadband emission from MSH 11–61A we use a model that calculates the non-thermal emission produced by a distribution of electrons and protons. The  $\pi^0$  decay model is based on the proton-proton interaction model by Kamae et al. (2006), with a scaling factor of 1.85 for helium and heavy nuclei as suggested by Mori (2009). The leptonic emission models are based on those presented by Baring et al. (1999) and Bykov et al. (2000) for the synchrotron/IC and non-thermal bremsstrahlung emission mechanisms. We assume a spectral distribution of our accelerated particles to be:

$$\frac{dN_i}{dp} = a_i p^{-\alpha_i} \exp\left(-\frac{p}{p_{0i}}\right), \quad (1)$$

where  $i$  is the particle species,  $a_i$  is the normalisation of the particle distribution,  $\alpha_i$  is the particle distribution index which is equal to  $(1-\Gamma)/2$ , where  $\Gamma$  is the photon index and  $p_{0i}$  is the exponential particle momentum cut-off. This distribution is transformed from momentum space to energy space such that the exponential cut-off is defined by an energy input,  $E_{0i}$ . The sum of the integrals of each spectral distribution is set to equal the total energy in accelerated particles within the SNR shell,  $E_{CR} = \epsilon E_{SNR}$ , where  $\epsilon$  is the efficiency of the SNR in depositing energy into cosmic rays.

#### 5.2.1. Hadronic origin of the observed $\gamma$ -rays

In Figure 8, we have plotted the model fits to the broadband emission of MSH 11–61A. The radio spectrum is a combination of multiple observations by Milne et al. (1989), Whiteoak & Green (1996), and Filipovic et al. (2005). The X-ray upper limit was derived by fitting a power law with a photon index similar to that of RX J1713.7-3946 (Uchiyama et al. 2003), Kepler and RCW 86 (Bamba et al. 2005) ( $\Gamma = 2.3$ ), to our models of the *Suzaku* data. The upper limit corresponds to the flux in which the additional non-thermal component begins to affect our reduced  $\chi^2$ . The solid magenta line corresponds to the  $\pi^0$ -decay model that adequately reproduces the observed  $\gamma$ -ray spectrum of MSH 11–61A. We have also plotted as the purple dot-dashed line the synchrotron model that sufficiently reproduces the radio spectrum, assuming an electron-proton ratio ( $K_{ep}$ ) of 0.01, while the IC model falls below the plotted axis. For completeness we have also plotted the non-thermal

bremsstrahlung contribution as the orange dashed line. Table 4 lists the parameters which reproduce the  $\pi^0$ -decay, synchrotron emission, IC and non-thermal bremsstrahlung models plotted in Figure 8.

A  $\pi^0$ -decay model arising from a proton distribution with a power law index of  $\alpha_p = 4.34$  and a cut-off energy of  $E_0^p \sim 6.05$  GeV, adequately described the  $\gamma$ -ray spectrum of MSH 11–61A. The cut-off energy of the proton spectrum derived in this model is much smaller than the TeV cut-off one would expect for protons (Reynolds 2008). This could indicate that due to the high density of the surrounding environment, efficient CR acceleration is suppressed allowing accelerated particles to escape the emission volume (Malkov et al. 2011, 2012).

As non-thermal X-ray emission has not been observed from MSH 11–61A, we are unable to constrain the cut off energy of the electron population. Thus to model the radio emission of MSH 11–61A we assume the electron distribution has the same cut-off energy as the proton distribution. We are able to reproduce the radio spectrum using an electron distribution that has a power law index of  $\alpha_e=3.15$  and a magnetic field of  $28\mu\text{G}$ . The magnetic field implied by the synchrotron modelling is larger than the magnetic field of the ISM ( $\sim 3-5\mu\text{G}$ ). This enhancement could arise from magnetic field amplification due to the compression of the surrounding medium by the SNR shock-wave.

In the  $\pi^0$ -decay model, the calculated  $\gamma$ -ray flux is proportional to the ambient density of the surrounding ambient medium and the total proton energy. Assuming a conservative upper limit of 40% of the total supernova explosion energy goes into accelerating CRs, we can estimate the density of the  $\gamma$ -ray emitting material. For our  $\pi^0$ -decay model of MSH 11–61A we obtain an ambient density of  $9.15 \text{ cm}^{-3}$ . Similar to many other SNRs that exhibit hadronic emission (e.g. W41, MSH 17-39, G337.7-0.1: Castro et al. (2013); Kes 79: Auchettl et al. (2014)), this density is much larger than the ambient density estimate derived from our X-ray analysis (see Table 3). This discrepancy could arise from the SNR shock-wave interacting with dense clumps of material that are cold enough such that do not radiate significantly in X-rays (Castro & Slane 2010; Inoue et al. 2012). If these clumps have a high filling factor, then the densities that we derive in our X-ray analysis would underestimate the mean local density. Our inferred ambient densities as well as the association of MSH 11–61A with a molecular cloud towards the west of the remnant supports the conclusion that MSH 11–61A is interacting with dense material that does not radiate in X-rays.

An alternative scenario is that the enhanced  $\gamma$ -ray emission arises from highly energetic particles escaping the acceleration region and are interacting with dense gas upstream of the shock (e.g. Aharonian & Atoyan (1996), Gabici et al. (2008), Lee et al. (2008) and Fujita et al. (2009)). However, a majority of these particles come from the high-energy portion of the  $\gamma$ -ray spectrum and the observation of “low” energy  $\gamma$ -rays may lead to inconsistencies with this scenario.

#### 5.2.2. Leptonic emission of the observed $\gamma$ -rays

For inverse Compton scattering to be the dominant mechanism producing the  $\gamma$ -rays of MSH 11–61A, we would require greater than the entire kinetic explosion energy just in electrons, assuming that the electron to proton ratio is similar to that measured at Earth ( $K_{ep} \sim 0.01$ ) and that this emission arises from a non-thermal population of electrons being accel-

**Table 4**  
Model parameters and density estimates for the pion decay and leptonic model for MSH 11-61A.

Object	Distance (kpc)	$\alpha_{proton}$	$\alpha_{elec}$	$E_0^{proton}$ (GeV)	$E_0^{elec}$ (GeV)	Magnetic field ( $\mu G$ )	Ambient density $n_0$ ( $cm^{-3}$ )	X-ray density $n$ ( $cm^{-3}$ )
MSH 11-61A	7.00	4.39	3.15	6.05	6.05	28	9.20	see Table 3

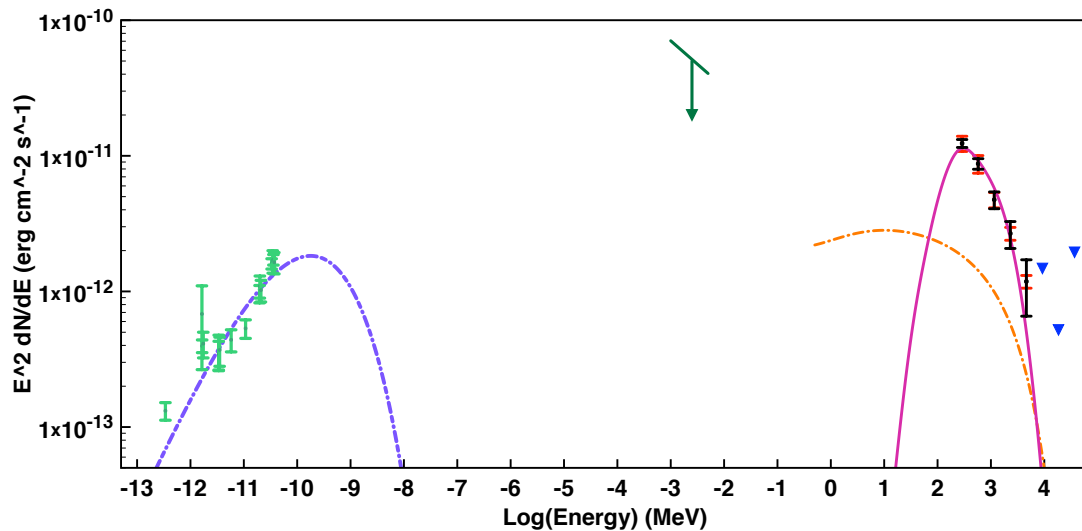


**Figure 8.** Broadband fits to the non-thermal radio emission (green data points), non-thermal X-ray upper limit derived from the *Suzaku* data (dark green limit) and the *Fermi*-LAT  $\gamma$ -ray emission (as described in Figure 3) of MSH 11-61A. The pion decay, non-thermal bremsstrahlung and synchrotron models defined by the parameters in Table 4 are shown as the solid magenta line, dashed orange line and dot-dashed purple line, respectively. The corresponding IC model falls below the plotted axis.

erated by the shock-front. This makes it difficult to conclude that IC scattering is the dominant mechanism producing the observed  $\gamma$ -rays.

For non-thermal bremsstrahlung to dominate the GeV emission we require a  $K_{ep} > 0.2$ , assuming the maximum density derived from our X-ray analysis (see Table 3). Local measurements imply  $K_{ep} \sim 0.01$  (Gaisser et al. 1998), while  $\gamma$ -ray modelling of other SNRs imply  $K_{ep} < 0.01$  (e.g. Ellison et al. 2010), making it unlikely that non-thermal bremsstrahlung emission is the dominant emission mechanism.

## 6. CONCLUSION

70 months of *Fermi*-LAT data reveal significant ( $\sim 5\sigma$ )  $\gamma$ -ray emission from SNR MSH 11-61A. This emission is consistent with being located along or inside the western limb of the remnant given the angular resolution of the *Fermi*-LAT and is adjacent to regions that show a strong recombining plasma component. By modelling the broadband spectrum, we find that the emission is best described by a hadronic model, while a leptonic scenario is energetically unfavourable. This is consistent with CO and HI observations that indicate the SNR is interacting with a molecular cloud towards the north and southwest. Similar to previous studies, the inferred density from our pion decay model is much higher than that implied by the thermal X-ray emission. *Suzaku* data reveal that the bulk of the X-ray emission of MSH 11-61A arises from a single recombining plasma with enhanced abundances of Mg, Si and S with some regions also requiring an underabundance of Ne and Fe, while the emission towards the east of the remnant arises from an ionising plasma with Mg, Si and S. The origin of the recombining plasma is most like

adiabatic cooling. We find that the results from our central regions (1 - 3) and our regions 9 - 10, agree well with those that Kamatsukasa et al. (2015) obtained for their corresponding regions. The enhancement of Mg, Si and S suggests that some of the observed emission arises from shocked ejecta and that the progenitor of MSH 11-61A had a mass  $> 25M_{\odot}$ .

## REFERENCES

- Abdo, A. A., Ackermann, M., Ajello, M., et al. 2010a, *ApJ*, 722, 1303  
 Abdo, A. A., Ackermann, M., Ajello, M., et al. 2010b, *Science*, 327, 1103  
 Abdo, A. A., Ajello, M., Allafort, A., et al. 2013, *ApJS*, 208, 17  
 Ackermann, M., Ajello, M., Albert, A., et al. 2012, *ApJS*, 203, 4  
 Ackermann, M., Ajello, M., Allafort, A., et al. 2013, *Science*, 339, 807  
 Aharonian, F. A., & Atoyan, A. M. 1996, *A&A*, 309, 917  
 Anders, E., & Grevesse, N. 1989, *GeCoA*, 53, 197  
 Auchettl, K., Slane, P., & Castro, D. 2014, *ApJ*, 783, 32  
 Bamba, A., Yamazaki, R., Yoshida, T., et al. 2005, *ApJ*, 621, 793  
 Baring, M. G., Ellison, D. C., Reynolds, S. P., et al. 1999, *ApJ*, 513, 311  
 Brand, J., & Blitz, L. 1993, *A&A*, 275, 67  
 Bykov, A. M., Chevalier, R. A., Ellison, D. C., et al. 2000, *ApJ*, 538, 203  
 Caraveo, P. A. 1993, *ApJ*, 415, L111  
 Castro, D., & Slane, P. 2010, *ApJ*, 717, 372  
 Castro, D., Slane, P., Carlton, A., et al. 2013, *ApJ*, 774, 36  
 Cordes, J. M., & Lazio, T. J. W. 2002, *astro-ph/0207156*  
 Cox, D. P., Shelton, R. L., Maciejewski, W., et al. 1999, *ApJ*, 524, 179  
 Dickel, J. R. 1973, *ApL*, 15, 61  
 Dwarkadas, V. V. 2005, *ApJ*, 630, 892  
 Ellison, D. C., Patnaude, D. J., Slane, P., et al. 2010, *ApJ*, 712, 287  
 Ergin, T., Sezer, A., Saha, L., et al. 2014, *ApJ*, 790, 65  
 Filipovic, M. D., Payne, J. L., & Jones, P. A. 2005, *SerAJ*, 170, 47  
 Foster, A. R., Ji, L., Smith, R. K., et al. 2012, *ApJ*, 756, 128  
 Fujita, Y., Ohira, Y., Tanaka, S. J., et al. 2009, *ApJ*, 707, L179  
 Gabici, S., Casanova, S., & Aharonian, F. A. 2008, *AIP Conf. Proc.*, 1085, 265  
 Gaisser, T. K., Protheroe, R. J., & Stanev, T. 1998, *ApJ*, 492, 219

- García, F., Combi, J. A., Albacete-Colombo, J. F., et al. 2012, *A&A*, 546, A91
- Goss, W. M., Radhakrishnan, V., Brooks, J. W., et al. 1972, *ApJS*, 24, 123
- Halpern, J. P., Tomsick, J. A., Gotthelf, E. V., et al. 2014, *ApJ*, 795, L27
- Henley, D. B., & Shelton, R. L. 2013, *ApJ*, 773, 92
- Hobbs, G., Lorimer, D. R., Lyne, A. G., et al. 2005, *MNRAS*, 360, 974
- Inoue, T., Yamazaki, R., Inutsuka, S., et al. 2012, *ApJ*, 744, 71
- Itoh, H., & Masai, K. 1989, *MNRAS*, 236, 885
- Kamae, T., Karlsson, N., Mizuno, T., et al. 2006, *ApJ*, 647, 692
- Kamitsukasa, F., Koyama, K., Uchida, H., et al. 2015, *PASJ*, 67, 16
- Kaneda, H., Makishima, K., Yamauchi, S., et al. 1997, *ApJ*, 491, 638
- Kaspi, V. M., Bailes, M., Manchester, R. N., et al. 1997, *ApJ*, 485, 820
- Kaspi, V. M., Manchester, R. N., Johnston, S., et al. 1996, *AJ*, 111, 2028
- Kawasaki, M., Ozaki, M., Nagase, F., et al. 2005, *ApJ*, 631, 935
- Kawasaki, M. T., Ozaki, M., Nagase, F., et al. 2002, *ApJ*, 572, 897
- Kesteven, M. J., & Caswell, J. L. 1987, *A&A*, 183, 118
- Kesteven, M. J. L. 1968, *AuJPh*, 21, 369
- Koyama, K., Tsunemi, H., Dotani, T., et al. 2007, *PASJ*, 59, 23
- Kramer, M., Bell, J. F., Manchester, R. N., et al. 2003, *MNRAS*, 342, 1299
- Kushino, A., Ishisaki, Y., Morita, U., et al. 2002, *PASJ*, 54, 327
- Lee, S.-H., Kamae, T., & Ellison, D. C. 2008, *ApJ*, 686, 325
- Malkov, M. A., Diamond, P. H., & Sagdeev, R. Z. 2011, *NatCo*, 2, 194  
—, 2012, *PhPl*, 19, 082901
- Manchester, R. N., Hobbs, G. B., Teoh, A., et al. 2005, *AJ*, 129, 1993
- McClure-Griffiths, N. M., Dickey, J. M., Gaensler, B. M., et al. 2005, *ApJS*, 158, 178
- Mills, B. Y., Slee, O. B., & Hill, E. R. 1961, *AuJPh*, 14, 497
- Milne, D. K., Caswell, J. L., Kesteven, M. J., et al. 1989, *PASAu*, 8, 187
- Mori, M. 2009, *APH*, 31, 341
- Moriya, T. J. 2012, *ApJ*, 750, L13
- Nolan, P. L., Abdo, A. A., Ackermann, M., et al. 2012, *ApJS*, 199, 31
- Pavan, L., Bordas, P., Pühlhofer, G., et al. 2014, *A&A*, 562, A122
- Reynolds, S. P. 2008, *ARA&A*, 46, 89
- Reynoso, E. M., Johnston, S., Green, A. J., et al. 2006, *MNRAS*, 369, 416
- Rho, J., & Petre, R. 1998, *ApJ*, 503, L167
- Rosado, M., Ambrocio-Cruz, P., Le Coarer, E., et al. 1996, *A&A*, 315, 243
- Sato, T., Koyama, K., Takahashi, T., et al. 2014, *PASJ*, 66, 124
- Seward, F. D. 1990, *ApJS*, 73, 781
- Slane, P., Bykov, A., Ellison, D. C., et al. 2015, *Space Sci. Rev.*, 188, 187
- Slane, P., Smith, R. K., Hughes, J. P., et al. 2002, *ApJ*, 564, 284
- Smith, R. K., Brickhouse, N. S., Liedahl, D. A., et al. 2001, *ApJ*, 556, L91
- Smith, R. K., & Hughes, J. P. 2010, *ApJ*, 718, 583
- Spitzer, L. 1962, *Physics of Fully Ionized Gases*, (2nd ed.; New York: Interscience)
- Tawa, N., Hayashida, K., Nagai, M., et al. 2008, *PASJ*, 60, 11
- Thielemann, F.-K., Nomoto, K., & Hashimoto, M.-A. 1996, *ApJ*, 460, 408
- Uchiyama, Y., Aharonian, F. A., & Takahashi, T. 2003, *A&A*, 400, 567
- Uchiyama, Y., Aharonian, F. A., Tanaka, T., et al. 2007, *Nature*, 449, 576
- Warren, J. S., Hughes, J. P., Badenes, C., et al. 2005, *ApJ*, 634, 376
- White, R. L., & Long, K. S. 1991, *ApJ*, 373, 543
- Whiteoak, J. B. Z., & Green, A. J. 1996, *A&AS*, 118, 329
- Wilms, J., Allen, A., & McCray, R. 2000, *ApJ*, 542, 914
- Yu, M., Manchester, R. N., Hobbs, G., et al. 2013, *MNRAS*, 429, 688
- Zhou, P., Safi-Harb, S., Chen, Y., et al. 2014, *ApJ*, 791, 87

---

# X-ray analysis of the proper motion and pulsar wind nebula for PSR J1741-2054

---

*X-ray analysis of the proper motion and pulsar wind nebula for PSR J1741-2054*

Katie Auchettl, Patrick Slane, Roger W. Romani, Bettina Posselt, George G. Pavlov, Oleg Kargaltsev, C-Y Ng, Tea Temim, Martin. C. Weisskopf, Andrei Bykov, Douglas A. Swartz

Published in ApJ, 804 (2015), 68

DOI: 10.1088/0004-637X/802/1/68

e-Print: [arXiv:1501.03225](https://arxiv.org/abs/1501.03225) [astro-ph]

---

## 5.1 Introductory remarks

The core-collapse of a star with a mass of  $8M_{\odot}$  or greater will produce a highly compact and very dense neutron star. These neutron stars are rapidly rotating due to conservation of angular momentum and this rapid rotation produces a highly relativistic and magnetised wind of particles that interacts with the surrounding environment producing a pulsar wind nebula (PWN). These relativistic particles will predominantly interact with surrounding magnetic fields producing synchrotron radiation which is observable in radio and X-ray wavelengths. The morphology of the PWN is dependent on the properties of the pulsar such as its space velocity and direction of motion. Pulsars with high space velocities will have a bow shock morphology due to the pulsar wind being confined by ram pressure. In addition, pulsars and their PWN that are found within 1 kpc of Earth are thought to be one of the main contributors to the electron positron anomaly discussed in Chapter 1.

[Romani et al. \(2010\)](#) discovered a very long, non-radiative  $H\alpha$  bow shock nebula surrounding one of the closest, middle aged pulsars known, PSR J1741-2054. Using a short *Chandra* observation they found within this bow shock nebula a long X-ray trail, as well as some evidence for small scale structure immediately surrounding the pulsar. PSR J1741-2054 has also been considered one of four pulsars that could be solely responsible for the observed cosmic-ray anomaly discussed in Chapter 1 ([Di Mauro et al., 2014](#); [Feng & Zhang, 2015](#)). Unfortunately, the X-ray observation that discovered the X-ray PWN of PSR J1741-2054 was too short to perform a detailed analysis of the X-ray emission from the pulsar and its nebula. Thus in this paper, we use  $\sim 300$  ks to constrain the proper motion of the pulsar; look for small scale structure immediately surrounding the pulsar point source; characterise the emission from the pulsar and the X-ray trail; determine its space velocity and direction of motion in attempt to shed light on its birth site. We find that the pulsar has a proper motion of  $\mu = 109 \pm 10$  mas yr $^{-1}$  in a direction consistent with the symmetry axis of the  $H\alpha$  nebula and aligned with the extended X-ray emission of the PWN. We find no compelling evidence of the pulsar being correlated with nearby OB association making it difficult to determine the birth site of this pulsar. We find that the X-ray emission from the pulsar is best described by an absorbed powerlaw plus blackbody, while the emission from PWN and its extended trail show no sign of synchrotron cooling. We also find no conclusive evidence of small scale structure immediately surrounding the pulsar which we could attribute to a torus-like feature.

In Section 3 of the paper found overleaf, we describe our method for finding the proper motion of the pulsar. In Section 4 we describe the image deconvolution techniques that we used in an attempt to search for small scale structure. In Section 5 we described our spectral analysis of the pulsar and PWN and in Section 6 we discuss our results. Figure 1 shows the extended X-ray emission from PSR

J1741-2054, while Figure 2 highlights the proper motion of the pulsar. In Figure 5 we have plotted the past trajectory of the pulsar, assuming the properties derived in our analysis and finally Figure 6 shows the X-ray PWN confined by  $H\alpha$  bow shock nebula.

## 5.2 Declaration for thesis chapter 5

### Declaration by candidate

In the case of the paper(s) contained in Chapter 5, the nature and extent of my contribution to the work was the following:

<b>Paper</b>	<b>Nature of contribution</b>	<b>Extent of contribution (%)</b>
IV	Performed data reduction and analysis of the X-ray data, as well as interpretation of X-ray results; wrote paper.	85%

The following co-authors contributed to the work. If co-authors are students at Monash University, the extent of their contribution in percentage terms is stated:

<b>Name</b>	<b>Nature of contribution</b>	<b>Extent of contribution (%)</b>
Patrick Slane	Provided supervisory advice; provided guidance on X-ray analysis and interpretation of results; provided comments on the draft of the paper; contributed to paper write up; Co-I on original <i>Chandra</i> proposal.	
Roger Romani	Principle investigator of original <i>Chandra</i> proposal; provided guidance on X-ray analysis and interpretation of results; produced Figure 5 and 6 in paper; provided comments on the draft of the paper.	
Bettina Posselt	Provided helpful comments regards to modelling the PSF with MARX and to interpreting the feature surrounding the pulsar; provided comments on the draft of the paper.	

George Pavlov	Provided helpful comments related to interpreting the feature surrounding the pulsar; provided comments on the draft of the paper; Co-I on original <i>Chandra</i> proposal.	
Oleg Kargaltsev	Provided comments on the draft of the paper; Co-I on original <i>Chandra</i> proposal.	
C-Y. Ng	Provided comments on the draft of the paper; Co-I on original <i>Chandra</i> proposal.	
Tea Temim	Provided comments on the draft of the paper; Co-I on original <i>Chandra</i> proposal.	
Martin Weisskopf	Provided comments on the draft of the paper; Co-I on original <i>Chandra</i> proposal.	
Andrei Bykov	Provided helpful comments in regards to the minimum energy/magnetic field calculation; provided comments on the draft of the paper; Co-I on original <i>Chandra</i> proposal.	
Douglas Swartz	Provided comments on the draft of the paper.	

The undersigned hereby certify that the above declaration correctly reflects the nature and extent of the candidate's and co-authors' contributions to this work.

**Signatures:**

Katie Auchettl:

Date: 15th June 2015

Patrick Slane:

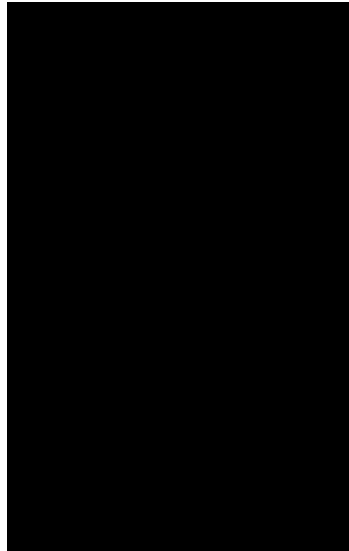
Date: 15th June 2015

Csaba Balázs:

Date: 15th June 2015

Jasmina Lazendic-Galloway:

Date: 15th June 2015



## 5.3 Published material: Paper IV

Begins overleaf.

## X-RAY ANALYSIS OF THE PROPER MOTION AND PULSAR WIND NEBULA FOR PSR J1741-2054

KATIE AUCHETTL<sup>1,2</sup>, PATRICK SLANE<sup>1</sup>, ROGER W. ROMANI<sup>3</sup>, BETTINA POSSELT<sup>4</sup>, GEORGE G. PAVLOV<sup>4</sup>, OLEG KARGALTSEV<sup>5</sup>,  
C-Y. NG<sup>6</sup>, TEA TEMIM<sup>7,8</sup>, MARTIN. C. WEISSKOPF<sup>9</sup>, ANDREI BYKOV<sup>10</sup>, AND DOUGLAS A. SWARTZ<sup>9</sup>

<sup>1</sup>Harvard-Smithsonian Center for Astrophysics, 60 Garden Street, Cambridge, MA 02138, USA

<sup>2</sup>School of Physics & Astronomy, Monash University, Melbourne, Victoria 3800, Australia

<sup>3</sup>Department of Physics, Stanford University, Stanford, CA 94305, USA

<sup>4</sup>Department of Astronomy & Astrophysics, Pennsylvania State University, 525 Davey Lab, University Park, PA 16802, USA

<sup>5</sup>Department of Physics, The George Washington University, 725 21st St, NW, Washington, DC 20052, USA

<sup>6</sup>Department of Physics, The University of Hong Kong, Pokfulam Road, Hong Kong, China

<sup>7</sup>Observational Cosmology Lab, Code 665, NASA Goddard Space Flight Center, Greenbelt, MD 20771, USA

<sup>8</sup>CRESST, University of Maryland-College Park, College Park, MD 20742, USA

<sup>9</sup>NASA/Marshall Space Flight Center, ZP12, 320 Sparkman Drive, Huntsville, AL 35805, USA

<sup>10</sup>A.F. Ioffe Physical-Technical Institute, St. Petersburg 194021, also St.Petersburg State Politechnical University, Russia

Received 2014 December 22; accepted 2015 February 20; published 2015 March 24

### ABSTRACT

We obtained six observations of PSR J1741-2054 using the *Chandra* ACIS-S detector totaling  $\sim 300$  ks. By registering this new epoch of observations to an archival observation taken 3.2 yr earlier using X-ray point sources in the field of view, we have measured the pulsar proper motion at  $\mu = 109 \pm 10$  mas yr<sup>-1</sup> in a direction consistent with the symmetry axis of the observed H $\alpha$  nebula. We investigated the inferred past trajectory of the pulsar but find no compelling association with OB associations in which the progenitor may have originated. We confirm previous measurements of the pulsar spectrum as an absorbed power law with photon index  $\Gamma = 2.68 \pm 0.04$ , plus a blackbody with an emission radius of  $(4.5^{+3.2}_{-2.5})d_{0.38}$  km, for a DM-estimated distance of  $0.38d_{0.38}$  kpc and a temperature of  $61.7 \pm 3.0$  eV. Emission from the compact nebula is well described by an absorbed power law model with a photon index of  $\Gamma = 1.67 \pm 0.06$ , while the diffuse emission seen as a trail extending northeast of the pulsar shows no evidence of synchrotron cooling. We also applied image deconvolution techniques to search for small-scale structures in the immediate vicinity of the pulsar, but found no conclusive evidence for such structures.

*Key words:* pulsars: individual (PSR J1741-2054) – X-rays: general

### 1. INTRODUCTION

PSR J1741-2054 (J1741) is one of the closest middle-aged ( $\tau_c = 390$  kyr) pulsars known. It has a period of  $P = 413$  ms and was first discovered in  $\gamma$ -rays using the Large Area Telescope (LAT) on the *Fermi Gamma-ray Space Telescope* by a blind search for periodic  $\gamma$ -ray pulsations from Fermi-LAT point sources (Abdo 2009). It was subsequently detected in archival Parkes radio data and observed using the Green Bank Telescope (Camilo et al. 2009). The pulsar has a spin-down energy loss rate of  $\dot{E} = 9.5 \times 10^{33}$  erg s<sup>-1</sup> which is moderately low compared to those of other  $\gamma$ -ray pulsars. The pulsar has a very small dispersion measure (DM) =  $4.7$  pc cm<sup>-3</sup> and a magnetic field of  $2.7 \times 10^{12}$  G. Using the NE2001 Galactic electron density model, the low DM implies a distance of  $0.38$  kpc (Cordes & Lazio 2002). At this distance, its measured radio flux at  $1400$  MHz ( $S \sim 160$   $\mu$ Jy) makes it one of the least luminous radio pulsars known. Its  $\gamma$ -ray pulsations lag behind its radio pulsations by  $\delta = 0.29$  P, implying that our line of sight tangentially cuts the  $\gamma$ -ray cone, while nearly missing the radio beam (Camilo et al. 2009). This makes J1741 a transitional object between a classical radio/ $\gamma$ -ray loud pulsar such as Vela and the radio-quiet Geminga-type pulsars. Interestingly, Romani et al. (2010) detected a  $20''$  long, non-radiative H $\alpha$  bow shock nebula around the pulsar. Modeling of the bow shock suggested that the pulsar is traveling with a velocity of  $\sim 150$  km s<sup>-1</sup>, while the observation of negative radial velocities from both sides of the nebula imply that the velocity is directed out of the plane of the sky at an angle of  $15^\circ \pm 10^\circ$ .

Using a short *Chandra* ACIS-S observation (observation ID (ObsID): 11251), Romani et al. (2010) detected an X-ray pulsar wind nebula (PWN) within this H $\alpha$  nebula and a long ( $>2$  arcmin) X-ray trail at an angle of  $45^\circ \pm 5^\circ$  east from north. Romani et al. (2010) also suggested that there are asymmetries in the small scale structure surrounding the pulsar, which they associate with a compact  $2''5$  equatorial toroidal structure. Marelli et al. (2014) and Karpova et al. (2014) performed a spectral analysis of the pulsar emission using *XMM-Newton* and *Chandra* and determined that a two-component (blackbody plus power-law) model is required to obtain satisfactory spectral fits.

In this paper, we use  $\sim 300$  ks of *Chandra* data of J1741 that were obtained as part of the Cycle 14 *Chandra* Visionary Project “A Legacy Study of the Relativistic Shocks of PWNe,” plus a  $\sim 49$  ks archival observation, to constrain the pulsar motion, and the geometry of the PWN outflow. We discuss our approach to image registration and proper motion measurement in Section 3, followed by a discussion in Section 4 of our image deconvolution efforts to search for small-scale structure around the pulsar. In Section 5 we discuss the results of our spectral fits for the pulsar emission and that of the extended PWN, and compare these with previous results. In Section 6 we discuss the implications of the proper motion measurements, including comparisons with the observed H $\alpha$  nebula surrounding J1741, and discuss the lack of evidence of for synchrotron cooling in the PWN trail. Our conclusions are summarized in Section 7.

**Table 1**  
*Chandra* Observations of PSR J1741-2054

Observation ID	Exposure Time (ks)	Observation Date
<i>Archival</i>	...	...
11251	48.78	2010-05-21
<i>New observations</i>	...	...
14695	57.15	2013-02-06
14696	54.30	2013-02-19
15542	28.29	2013-04-01
15638	29.36	2013-04-02
15543	57.22	2013-05-15
15544	55.73	2013-07-09

## 2. X-RAY DATA ANALYSIS

We obtained 282 ks of new *Chandra* ACIS-S exposure time of J1741. Table 1 lists the parameters for each of the six new observations that we obtained, including the archival observation. To reduce pileup, the CCDs were operated in half-frame VFaint mode so that events were read out every 1.7 s. The pulsar was placed near the optimum focus on the backside illuminated S3 chip. In addition to our six observations, there is a 48.8 ks archival observation (ObsID: 11251), which was taken on 2010 May 21. Each new observation has a roll angle similar to the roll angle of the 2010 epoch ( $\sim 90^\circ$ ), except for ObsID: 15544. This observation has a roll angle of  $\sim 260^\circ$  as the nominal roll angle of *Chandra* is rotated by  $180^\circ$  during the time of the year this observation was completed. The data were analysed with *CIAO* 4.6.2 after all observations were reprocessed using the CALDB 4.5.9. No flaring occurred in any of the observations so the full exposure times were used.

Using all seven observations we produced a merged, exposure-corrected image of J1741 by reprojecting the new observations to a common tangent plane based on the WCS information of ObsID: 11251 (*CIAO* task: *reproject\_obs*) and combined all reprojected observations into an exposure corrected image using the *CIAO* task *flux\_obs*. The merged ACIS-S image of the extended emission around the pulsar, smoothed with a  $3''$  Gaussian, is shown in Figure 1. The pulsar point source lies at the apex of the diffuse X-ray emission, while a diffuse, faint X-ray trail extending  $\sim 1.9'$  is seen toward the northeast of the pulsar.

## 3. REGISTRATION AND THE PROPER MOTION

To constrain the proper motion of the pulsar, we registered each of the new *Chandra* images to the archival image using field point sources that were identified using the *CIAO* tool *wavdetect*. We selected sources with a detection significance of  $> 3\sigma$  that were found on the S3 chip in both the 2010 observation and the corresponding new observation. These sources are highlighted in white and the pulsar is labeled as *P* in Figure 1.

Careful consideration and modeling of the point-spread function (PSF) must be undertaken to reduce the effect of changes in the PSF shape on the count distribution of our point-sources. To improve the astrometric accuracy and reduce this effect, we simulate a PSF for each point source position, in each observation, and use it to fit for the position of the source.

To simulate a PSF of a point source, we use the software suite *SAOTrace*<sup>11</sup> which is designed to simulate the propagation of photons from astronomical objects through the optics of the *Chandra* X-ray satellite. We use the aspect solution file of each observation and provided spectral information for the ray trace by extracting the spectrum of each stellar source using the *CIAO* task *specextract*. We model the spectra using an absorbed Mekal model in *SHERPA*. To improve the accuracy of the PSF modeling, we increase the normalization of this spectrum by a factor of 100 before passing it into *SAOTrace*. A model of a point source at its position is obtained by passing the raytrace from *SAOTrace* into the program MARX.<sup>12</sup> Each PSF model is corrected for the science instrument module (SIM) offset from nominal location and filtered using the Good Time Interval data from the original event file.

To determine the position of the sources we use the maximum likelihood “figure of merit” (FoM) technique developed by van Etten et al. (2012). We generate a 39 pixel by 39 pixel image of the modeled PSF, binned to 1/9 ACIS pixel resolution. This is then compared to 0.3–5.0 keV source images of the same size but binned to native ACIS pixel resolution. PSF models and source images are produced for all observations and for each registration source. The PSF is shifted along the *x* and *y* axes of the 1/9 pixel grid and rebinned to native ACIS pixels. We then compute the FoM at each offset in pixel coordinates, giving us a map of the likelihood of the observed counts with respect to the *x* and *y* position. To determine the best-fit position of the source, we fit a two-dimensional Gaussian to the FoM surface, with the minimum of this surface providing the best fit position of the source. The standard deviations along *x* and *y* are estimated by calculating the square root of the eigenvalues of the covariance matrix.

Prior to registration we checked each source for any optical counterparts using VizieR.<sup>13</sup> Sources 6, 8, 9, 10 and 13 all have optical counterparts within  $2''$  of the PSF-fit position. Source 8 and 13 have estimated proper motions of  $(\mu_{R.A.}, \mu_{Decl.}) = (22, -62)$  mas yr<sup>-1</sup> and  $(20, -22)$  mas yr<sup>-1</sup>, respectively (errors  $\delta\mu_{R.A.} \sim 7$  mas yr<sup>-1</sup>,  $\delta\mu_{Decl.} \sim 15$  mas yr<sup>-1</sup>). We corrected for these nominal proper motions, but also confirmed that our final astrometric solution was insignificantly changed if we excluded these two stars from the analysis.

Using the FoM positions of our registration sources and their uncertainties as a reference grid to perform the relative astrometry, we determined the best translation transformation needed to register the images from the two epochs using the *CIAO* command *wcs\_match*. For each observation we adopt the *Chandra*-determined roll angle. In Table 2 we list the best-fit frame shifts and their uncertainties. The uncertainties in these shifts were calculated by adding in quadrature the errors in the differences between each source before and after shift. Adding a rotation to the transformation did not produce a statistically significant improvement on the best-fit translation.

To calculate the position of the pulsar after registration, we first calculate the position of the pulsar in the unregistered frames. We simulate a PSF at the position of the pulsar in each observation using the method described for the registration sources. To define the energy dependence of the PSF, we extract a spectrum of the pulsar and fit it with an absorbed

<sup>11</sup> <http://cxooptics.cfa.harvard.edu/SAOTrace/Index.html>

<sup>12</sup> <http://space.mit.edu/CXC/MARX/>

<sup>13</sup> <http://vizier.u-strasbg.fr/viz-bin/VizieR>

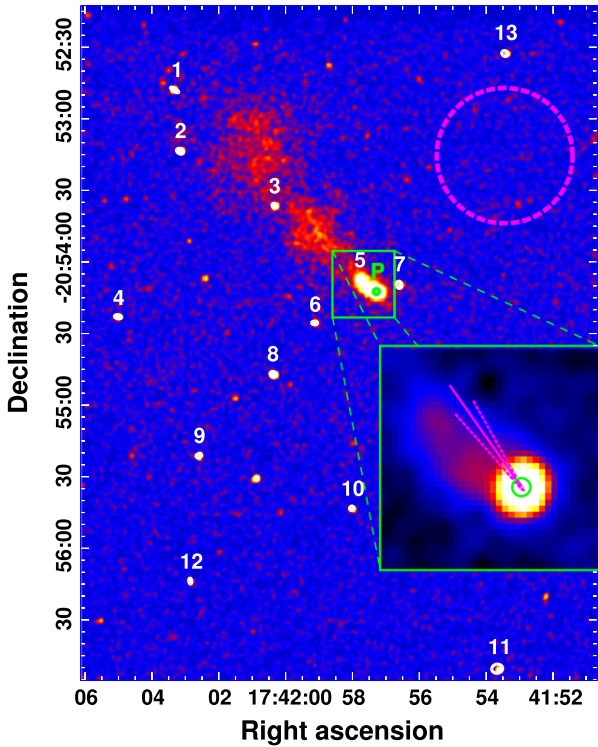


**Figure 1.** Merged *Chandra* exposure-corrected 0.3–5.0 keV ACIS-S image of the extended emission around J1741-2051. This was produced using *reproject\_obs* and *flux\_obs* and incorporates all available *Chandra* observations. The image is smoothed using a Gaussian of width  $3''$  and plotted on the logarithmic scale. The reference sources numbered 1 through 13 were used for relative astrometry, while the pulsar is labeled as *P*. Other sources seen in the image are not suitable for astrometry because, being variable, they were not significantly detected in both the archival observation and one of the new epoch observations. We included a cutout region around the pulsar to show the point source. The magenta lines show our derived proper motion (solid) and its uncertainty (dashed), traced back from the pulsar position. The background region used for spectral analysis is shown as the magenta dashed circle.

**Table 2**  
Frame Shifts and Their Uncertainties Used for Registration

ObsID	R.A. (arcsec)	Decl. (arcsec)
14695	$-0.02 \pm 0.02$	$0.48 \pm 0.02$
14696	$-0.01 \pm 0.02$	$0.25 \pm 0.02$
15542	$0.02 \pm 0.04$	$0.43 \pm 0.04$
15638	$-0.06 \pm 0.03$	$0.36 \pm 0.03$
15543	$0.23 \pm 0.02$	$0.29 \pm 0.03$
15544	$-0.11 \pm 0.03$	$-0.29 \pm 0.03$

power law plus blackbody model (see Section 5). For each observation, we generate a 6 pixel by 6 pixel image of the PSF model of the pulsar that is binned to 1/4 ACIS pixel resolution. Using an image of the 0.3–5.0 keV pulsar events of the same size and binning, we fit for the position of the pulsar in *SHERPA*. In this fit, we used a delta function (the pulsar) plus a two-dimensional Gaussian (the circumpulsar PWN), both convolved with the PSF. The resulting pulsar fit position for each frame was then registered by applying the best-fit transformations (Table 2).

To quantify the proper motion of the pulsar, we plot in Figure 2 the offset in the position of the pulsar between the

archival observation and the new observations against the number of years since the archival observation. The uncertainties in the offset are calculated by adding in quadrature the uncertainties in the fit positions of the pulsar, the uncertainty in the frame shifts and the systematic uncertainty associated with choosing a particular tangent plane when creating an image in sky coordinates. We fit the offset using a linear function that corresponds to the positional shift of the pulsar between the archival observation and the new observations and this is seen as the dashed line in Figure 2.

We obtain a proper motion of  $\mu_{R.A.} \cos(\delta) = -63 \pm 12$  mas yr $^{-1}$  and  $\mu_{Decl.} = 89 \pm 9$  mas yr $^{-1}$ . This corresponds to a total proper motion of  $109 \pm 10$  mas yr $^{-1}$ . Assuming a distance of 0.38 kpc to the pulsar, this translates to a transverse velocity of  $(196 \pm 18)d_{0.38} \text{ km s}^{-1}$ . The position angle of the proper motion is  $215^\circ \pm 6^\circ$  east of north. The proper motion axis points in the opposite direction of the extended X-ray trail as expected (see Figure 1).

#### 4. X-RAY IMAGING

Using the archival *Chandra* observation of J1741 (ObsID: 11251), Romani et al. (2010) performed a PSF subtraction of the pulsar point source to look for any small-scale structure surrounding the pulsar. They discovered that the region around the pulsar appears to be slightly extended and they associate this feature with the equatorial torus of the PWN. Using the same data as analyzed here, Karpova et al. (2014) searched for evidence of such structure by performing fits to a two-dimensional Gaussian convolved with PSF models generated for each observation. They found no evidence for any small-scale extended features other than for a small emission feature associated with a known mirror artifact.<sup>14</sup> We have carried out a similar investigation using image deconvolution techniques. We simulate a PSF of the pulsar in each observation using MARX following re-reduction of our *Chandra* observations with CALDB 4.4.7 to match the calibration data used for MARX. We define the energy dependence of the PSF as described in Section 3 and use the dither pattern of the observation with an aspect blur of 0.07, which corresponds to the uncertainty in the telescope pointing.<sup>15</sup> We also correct for SIM offset. Using this PSF we deconvolve a 0.3–5.0 keV pulsar image using the Lucy–Richardson deconvolution algorithm (Lucy 1974) implemented using the *CIAO* task *arestore*. All images were binned to quarter-ACIS pixel. We ran *arestore* multiple times using a number of different iterations between 10 and 200 to determine convergence of new features. No new structures appeared after 50 iterations.

The deconvolved image from one observation is shown in Figure 3. The emission is well described by a point source, with the exception of the artifact feature (identified in cyan). We thus see no conclusive evidence of other small-scale structure in the immediate region surrounding the pulsar, consistent with the results reported by Karpova et al. (2014).

<sup>14</sup> [http://cxc.harvard.edu/ciao/caveats/psf\\_artifact.html](http://cxc.harvard.edu/ciao/caveats/psf_artifact.html)

<sup>15</sup> <http://space.mit.edu/CXC/marx/news.html>

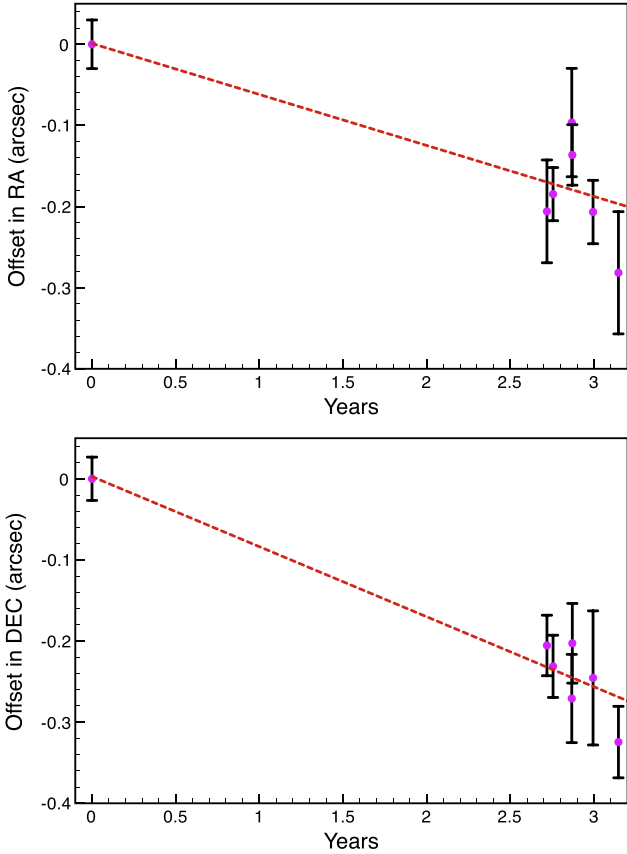


**Figure 2.** Offset in the position of the pulsar in R.A. (top) and decl. (bottom) in the new observations from the position of the pulsar in the archival observation plotted against the time since the first observation of PSR J1741 with *Chandra* (years). The dashed line corresponds to the line of best fit in which the slope corresponds to the proper motion of the pulsar.

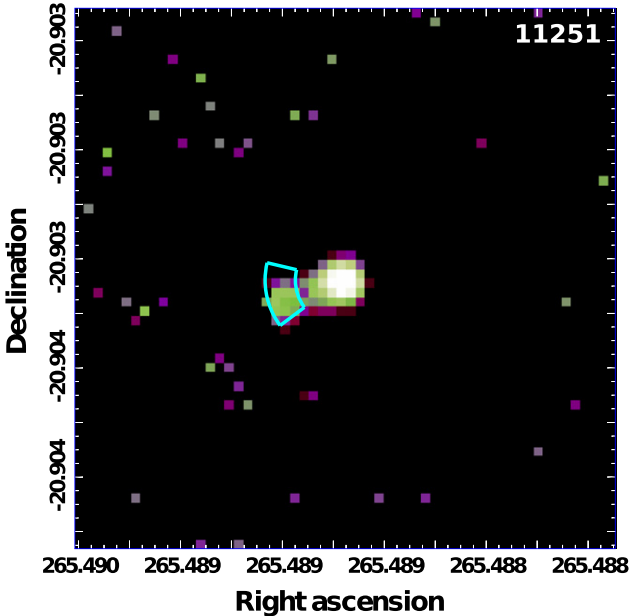


**Figure 3.** Deconvolved image of J1741-2054 from ObsID 11251 obtained using *arestore* after 50 iterations. The cyan region corresponds to the PSF asymmetry seen in *Chandra* data when pushing to sub-ACIS-pixel resolution. The image has been logarithmically stretched and the color enhanced to highlight the observed features.

## 5. SPECTRAL ANALYSIS OF THE X-RAY EMISSION OF THE PULSAR AND ITS TRAIL

### 5.1. Pulsar

As noted above, modeling of the *Chandra* PSF for use in determining an accurate pulsar position requires knowledge of the source spectrum. *XMM-Newton* observations establish a two-component spectrum for the pulsar, with a blackbody accompanied by a power law (Marelli et al. 2014). Similar results were derived by Karpova et al. (2014) using the same *Chandra* data reported here. We have re-analyzed these data by extracting events from a  $0''.70$  radius region centered on the pulsar, shown as the green circle in Figure 4(a). The size of this region was chosen to minimise the contamination from the PWN, and subsequent modeling results have been corrected for the finite encircled energy fraction. All spectra were grouped with a minimum of 20 counts per bin, and a background spectrum was obtained using a source-free circular region with a radius of  $30''$ , as shown by the magenta circle in Figure 1. Using the *CIAO pileup\_map*, we determined that approximately 5% of the pulsar events suffer from pileup. We thus included a pileup model in our spectral fits, where the frame time is 1.7 s and the PSF fraction is allowed to vary. All other parameters in the pileup model were frozen at default values.

To constrain the column density, we fit spectra from the compact nebula to the northeast of the pulsar (see Section 5.2) using an absorbed power law (more details in Section 5.2). We obtained  $N_H = (1.20^{+0.08}_{-0.07}) \times 10^{21} \text{ cm}^{-2}$ , in good agreement with the above studies, and adopt this value in all our models of the pulsar spectrum. We use the Wilms et al. abundance table throughout our analysis (Wilms et al. 2000). Modeling the spectrum with a power-law plus blackbody model, we obtained a photon index of  $\Gamma = 2.68 \pm 0.04$  and a blackbody spectrum with a temperature of  $kT_{\text{eff}} = 61.7 \pm 3.0 \text{ eV}$ , in excellent agreement with the results reported by Marelli et al. 2014 and Karpova et al. (2014). Omitting the pile-up correction yields similar values. We use the best-fit values above for PSF modeling of the pulsar.

We also ran fits using magnetized neutron star atmosphere models (*nsa* and *nsmax* in *SHERPA*) for the thermal component. These gave somewhat different temperatures and emitting areas, but did not significantly improve the quality of the fit. For example a magnetic carbon atmosphere model (*nsmax* model 12006, Mori & Ho (2007)) gave a temperature of  $kT_{\text{eff}} = 86.0 \pm 9.0 \text{ eV}$  and emission radius of  $R_{\text{emis}} = (4.90^{+3.0}_{-2.3})d_{0.38} \text{ km}$ . The power law component was only slightly affected with  $\Gamma = 2.63 \pm 0.03$ .

### 5.2. PWN and its Extended X-ray Trail

To analyse the spectrum of the compact nebula described above, we extracted spectra from each observation using the cyan rectangular region in Figure 4(a) and combined these using *specextract*. We used the same background spectrum as for the pulsar spectrum. The compact nebula contains a total of  $\sim 900$  counts and we binned the combined spectrum with a minimum of 20 counts per spectral bin. The PWN spectrum is consistent with an absorbed power law with an index of  $\Gamma = 1.60 \pm 0.20$ .

To determine whether there is any spectral variation in the PWN and its extended trail, we extract spectra from the five regions defined in Figure 4(b). These regions correspond to roughly the same spectral regions reported by Marelli et al.

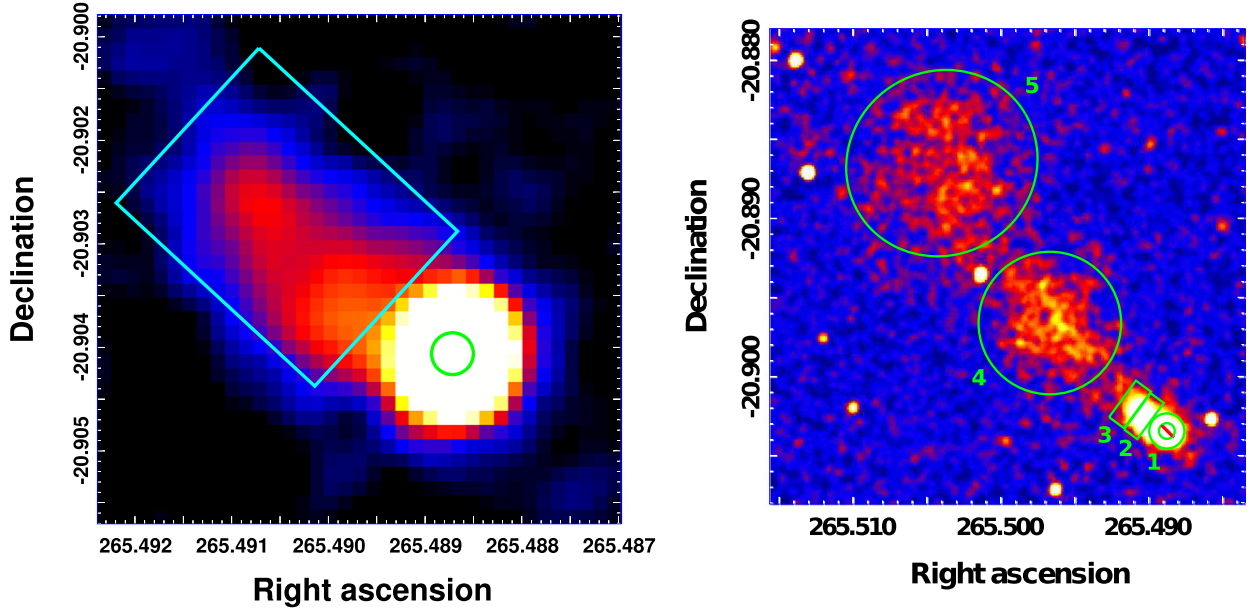


**Figure 4.** Logarithmically scaled, merged *Chandra* exposure-corrected 0.3–5.0 keV ACIS-S image of the pulsar and its extended emission. Left: the green circular region defines the  $0''70$  region used to extract the spectrum of the pulsar from all available observations. The cyan rectangular region defines the region used to extract the spectrum of the pulsar’s compact nebula from all observations. Right: the green regions define the apertures used to look for spectral variability in the extended emission of the pulsar. The pulsar was excluded from the spectral extraction of region 1.

**Table 3**

Spectral Fit Values of the Extended Emission of the Pulsar Defined by the Cyan Colored Region in Figure 4(a) and the Green Regions Defined in Figure 4(b)

Region	$N_H(\times 10^{21}) \text{ cm}^{-2a}$	$\Gamma$	Absorbed Flux $10^{-14} \text{ erg cm}^{-2} \text{ s}^{-1}$	Unabsorbed Flux $10^{-14} \text{ erg cm}^{-2} \text{ s}^{-1}$	$\chi^2/\text{dof}$
Compact PWN	$1.20^{+0.08}_{-0.07}$	$1.60 \pm 0.20$	$2.86^{+0.17}_{-0.20}$	$3.15^{+0.09}_{-0.07}$	0.90
1	...	$1.97^{+0.18}_{-0.17}$	$1.56^{+0.13}_{-0.12}$	$1.81 \pm 0.33$	0.99
2	...	$1.50^{+0.16}_{-0.15}$	$1.54^{+0.15}_{-0.10}$	$1.67 \pm 0.16$	0.84
3	...	$1.57^{+0.20}_{-0.19}$	$0.81^{+0.08}_{-0.11}$	$1.10 \pm 0.11$	0.80
4	...	$1.63^{+0.12}_{-0.11}$	$4.35^{+0.28}_{-0.15}$	$4.81^{+0.04}_{-0.14}$	0.99
5	...	$1.70^{+0.10}_{-0.11}$	$5.40^{+0.29}_{-0.36}$	$6.03^{+0.06}_{-0.16}$	1.16

**Note.** All uncertainties are one  $\sigma$ .

<sup>a</sup> Fixed at value from joint compact nebula.

(2014), except that we investigate smaller regions in the compact nebula near the pulsar. In the outer portions of the nebula, the count rate is too low to obtain good spectra in smaller regions. We model each region individually using an absorbed power law, where we fix column density to the value derived earlier from fits to the inner nebula region but let photon index and the normalization vary. We have listed in Table 3 the absorbed flux, unabsorbed flux and the reduced  $\chi^2$  for each region, as well as the best-fit parameters from fitting the trail spectra. There is no evidence of systematic variation in the photon index of the compact nebula and trail (regions 1–5). The photon index of region 1 is slightly higher than that of the other four regions, but is consistent within uncertainties with all regions except for region 2. This slight variation between region 1 and 2 could suggest that region 1 is affected by leakage of the softer emission from the point source. Modeling the photon index as a function of distance from the pulsar using a linear regression fit with a constant function in *SHERPA*, we obtain  $\Gamma = 1.67 \pm 0.06$  for the trail. The global PWN index derived from the *SHERPA* fit and the values we obtained in Table 3 are consistent with Karpova et al. (2014) and Marelli

et al. (2014), who derived  $\Gamma = 1.74 \pm 0.07$  and  $\Gamma = 1.78 \pm 0.15$  respectively for the PWN.

## 6. DISCUSSION

Using *Chandra* observations of PSR J1741-2054 that span a  $\sim 3.2$  yr period, relative astrometry measurements have identified a proper motion of  $\mu = 109 \pm 10 \text{ mas yr}^{-1}$ . This corresponds to a modest velocity of  $(196 \pm 18)d_{0.38} \text{ km s}^{-1}$ , which agrees well with the velocity derived by Romani et al. (2010) using  $\text{H}\alpha$  spectroscopy. The larger distance of Karpova et al. (2014) gives a transverse velocity of  $\sim 400 \text{ km s}^{-1}$ , inconsistent with that obtained from optical spectroscopy. The direction of the proper motion is  $205^\circ \pm 6^\circ$  east of north, opposite the elongated X-ray trail. Ng & Romani (2004); Johnston et al. (2005) and Ng & Romani (2007) found that the direction of proper motion of a pulsar is, generally, approximately parallel to its rotation axis.

In Figure 5 we plot the pulsar track (red) in Galactic coordinates (note the expanded  $b$  scale). This has the pulsar skimming above the plane. It does not intersect the plane itself unless one extrapolates an unreasonable  $\sim 2 \times 10^6$  yr;

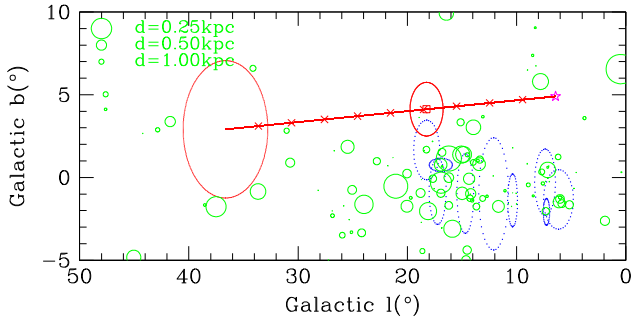


**Figure 5.** The past trajectory (red) of PSR J1741-2051 in Galactic coordinates. Positions are marked every  $10^5$  yr, with uncertainty ellipses at  $\tau_c = 3.91 \times 10^5$  yr and at  $10^6$  yr. For comparison we show the locations and sizes of OB associations from the Mel'Nik & Efremov (1995) catalog (blue dotted ellipses) and the *Hipparcos* sample of OB stars (green circles). A substantial concentration of OB stars at  $\sim 0.3$ – $0.6$  kpc lies near the pulsar track at  $\sim \tau_c$  and a more distant ( $d = 1.45$  kpc) OB association overlaps with the track uncertainty at this age.

however, the track starts within the  $\sim 50$  pc OB star scale height for  $t \sim \tau_c$  and distances  $d < 1$  kpc. For comparison we plot the positions of the *Hipparcos* catalog OB stars (green), with circle size proportional to the parallax. This set is quite complete, with useful parallaxes, to  $\sim 500$  pc, and increasingly incomplete at larger distances. At large distance the cataloged OB associations (Mel'Nik & Efremov 1995) provide plausible pulsar birthsites, and their cataloged extent is plotted by the blue dotted ellipses. Intriguingly, one association overlaps the pulsar track, but this is at a likely unreasonable catalog distance of 1.45 kpc. We conclude that, with the pulsar motion passing along the Galactic plane, there will be many superposed massive star locations, and no definitive birthsite can be identified. However, there are certainly many plausibly associated massive stars consistent with our preferred  $d \sim 0.4$  kpc, especially considering that some pulsar progenitors may be OB runaways with significant offset during their pre-explosion lifetime.

Neither our deconvolved nor our PSF-subtracted images indicate conclusive evidence of small-scale structure surrounding the pulsar that might be associated with a torus or jet-like feature. The equatorial torus structure that Romani et al. (2010) associate with a diagonal excess seen  $\sim 0.75$  from the core of the pulsar image seems to have arisen from the mirror asymmetry. Karpova et al. (2014) perform a similar analysis and come to the same conclusion. However, it is interesting to compare the nebula head and proper motion with the  $H\alpha$  structure described in Romani et al. (2010). In Figure 6 we see that the pulsar lies very close to the bow shock limb (accuracy limited by our relative X-ray/optical astrometry). Interestingly, our measured proper motion is consistent with, although nominally slightly south of, the  $H\alpha$  nebula's symmetry axis. However the X-ray PWN trail fills only the southern half of the apparent  $H\alpha$  cavity, punching out through a gap at the back end of the  $H\alpha$  emission and continuing to the arcmin-scale trail beyond. The origin of this asymmetry is unclear, but a clue may be seen in the X-ray contours, whose ridge line lies at PA  $\approx 70^\circ$ , i.e., misaligned with the proper motion by  $\approx 35^\circ$ . This suggests a second symmetry axis in the PWN, possibly due to a pulsar jet or other outflow concentration. This directs the shocked PWN plasma to the southeast, preferentially filling this half of the  $H\alpha$  cavity. A more complete discussion of the PWN geometry, including the 3D  $H\alpha$  kinematics, is in preparation.

The X-ray spectrum of the pulsar requires a combination of non-thermal and thermal model components. The emission is dominated by the non-thermal component ( $\sim 75\%$  of unabsorbed flux), indicating that the majority of the X-ray emission is magnetospheric in nature. The emitting radius implied by the blackbody model for J1741 corresponds to  $(4.5^{+3.2}_{-2.5})d_{0.38}$  km. This is substantially smaller than any viable neutron star radius (Lattimer & Prakash 2007), suggesting that this thermal emission arises from hot spots on the surface, plausibly near the magnetic poles (Ho & Heinke 2009). In fact, Marelli et al. (2014) do detect a pulsed thermal component for PSR J1741, also supporting such a surface temperature inhomogeneity.

The X-ray emission from the compact nebula and the trail is consistent with an absorbed power law. There is no discernible evidence of spectral variation with distance from the pulsar and the spectrum of the entire tail can be described by  $\Gamma = 1.67 \pm 0.06$ . We compute the minimum (equipartition) energy by approximating the X-ray emission from the PWN (region 2, 3, 4 and 5 in Figure 4(b)) as a cylinder with length  $l \sim 108$  arcsec ( $0.20d_{0.38}$  pc) and width  $w \sim 18$  arcsec ( $0.03d_{0.38}$  pc), comprising a volume of  $V \sim 5.0 \times 10^{51} \phi d_{0.38}^3$  cm<sup>3</sup>, where  $\phi$  is filling factor. The minimum energy in relativistic particles and magnetic field required to produce a synchrotron source of a given luminosity (Pacholczyk 1970) yield  $E_{\min} \sim C(1 + \kappa)^{4/7} V^{3/7} L_{\text{syn}}^{4/7}$ , where  $\kappa$  is the ion to electron energy ratio,  $L_{\text{syn}}$  is the synchrotron luminosity and  $C$  is a function dependent on energy, electron charge, speed of light and the mass of the electron in Gaussian cgs units (see Pacholczyk 1970). In the following, we considering only the leptonic case, where  $\kappa = 0$ . The total luminosity of the PWN is  $L(0.5\text{--}10.0 \text{ keV}) = 2.36 \times 10^{30} \text{ erg s}^{-1}$ , giving  $E_{\min} \sim 5.50 \times 10^{40} \phi^{3/7} d_{0.38}^{17/7} \text{ erg}$ . The associated minimum-energy magnetic field is  $B_{\min} \sim (D(1 + \kappa)L_{\text{syn}})^{2/7} V^{-2/7}$ , where  $D$  is a function similar to  $C$ . This magnetic field is  $\sim 15 \phi^{-2/7} d_{0.38}^{-2/7} \mu\text{G}$ , leading to a lifetime of the X-ray emitting leptons of  $\tau_{\text{syn}} \sim 6.4 \times 10^4 B_{\mu\text{G}}^{3/2} E_{\text{keV}}^{-1/2} \text{ yr}$  or  $\sim 1100$  yr at an observed photon energy of 1 keV. This is comparable to the (length/proper motion) =  $108''/109 \sim 10^3$  yr required for the pulsar to traverse the bright trail with our observed proper motion. Thus it is not surprising that there is no dramatic spectral steepening along the trail. If the PWN electrons flow at even faster speeds within the trail, this conclusion is even stronger.

## 7. CONCLUSION

Using  $\sim 300$  ks of *Chandra* ACIS-S observations of PSR J1741-2054, we were able to determine the proper motion of the pulsar with a detection significance  $> 3\sigma$ . The direction of the proper motion is aligned with the extended PWN emission, and corresponds well with a symmetry axis of the associated  $H\alpha$  nebula. The diffuse X-ray emission immediately behind the pulsar is concentrated in the southeastern portion of the  $H\alpha$  nebula, possibly suggesting another flow axis from a jet or torus in the pulsar system. The trajectory of the pulsar, extrapolated over the characteristic age, does not provide a compelling correlation with known OB associations at the distance of the pulsar, although there are many massive stars consistent with this distance that could potentially have had a common origin.

The pulsar spectrum is well described by an absorbed power law accompanied by a blackbody with an emission radius of

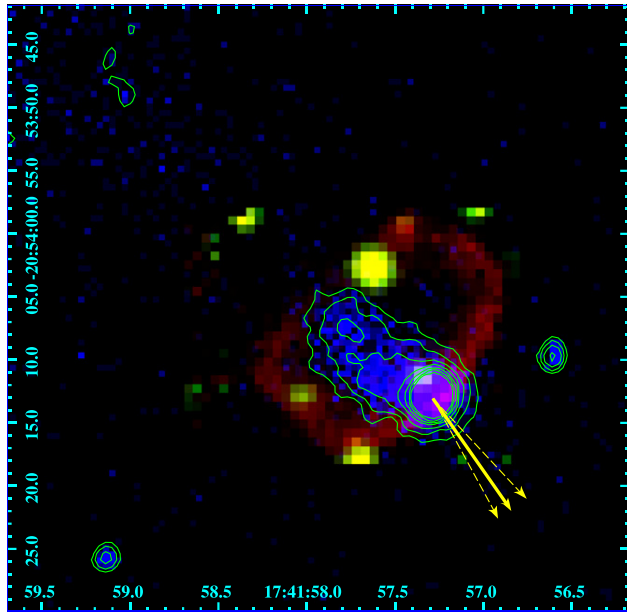


**Figure 6.** The head of the PSR J1741-2051 nebula. The red channel shows  $H\alpha$  emission at  $6562\text{--}6564\text{ \AA}$  while the green channel shows the average of the continuum  $6551\text{--}6561, 6565\text{--}6575\text{ \AA}$  with data abstracted from an AAT SPIRAL IFU observation. The blue channel shows the  $0.3\text{--}7\text{ keV}$  X-ray photons from our combined new observation. Green contours help one to read the X-ray structure, while the yellow arrows show our measured proper motion, with the arrow heads marking the position in 100 yr.

$(4.5^{+3.2}_{-2.5})d_{0.38}\text{ km}$  and a temperature of  $kT_{\text{eff}} = 61.7 \pm 3.0\text{ eV}$ , as found in earlier works. The thermal component, a hot region on the neutron star surface, is augmented by a magnetospheric

or unresolved PWN power law component. The PWN plus its extended trail can be well described using an absorbed power law and there is no evidence of variation in the photon index with distance from the pulsar. The integrated luminosity of the PWN over the  $0.5\text{--}10\text{ keV}$  is  $2.36 \times 10^{30}\text{ erg s}^{-1}$ . This represents  $0.02\%$  of the pulsar spin down power, which is not atypical. We find no conclusive evidence of small-scale structure surrounding the pulsar that we can associate with a torus or jet-like structure.

## REFERENCES

- Abdo, A. A. e. a. 2009, *Sci*, **325**, 840  
 Camilo, F., Ray, P. S., Ransom, S. M., et al. 2009, *ApJ*, **705**, 1  
 Cordes, J. M., & Lazio, T. J. W. 2002, arXiv:astro-ph/0207156  
 Ho, W. C. G., & Heinke, C. O. 2009, *Natur*, **462**, 71  
 Johnston, S., Hobbs, G., Vigeland, S., et al. 2005, *MNRAS*, **364**, 1397  
 Karpova, A., Danilenko, A., Shibanov, Y., Shternin, P., & Zyuzin, D. 2014, *ApJ*, **789**, 97  
 Lattimer, J. M., & Prakash, M. 2007, *PhR*, **442**, 109  
 Lucy, L. B. 1974, *AJ*, **79**, 745  
 Marelli, M., Belfiore, A., Saz Parkinson, P., et al. 2014, *ApJ*, **790**, 51  
 Mel'Nik, A. M., & Efremov, Y. N. 1995, *AstL*, **21**, 10  
 Mori, K., & Ho, W. C. G. 2007, *MNRAS*, **377**, 905  
 Ng, C.-Y., & Romani, R. W. 2004, *ApJ*, **601**, 479  
 Ng, C.-Y., & Romani, R. W. 2007, *ApJ*, **660**, 1357  
 Pacholczyk, A. G. 1970, *Radio Astrophysics. Nonthermal Processes in Galactic and Extragalactic Sources*, ed. G. Burbidge, & M. Burbidge (San Francisco, CA: Freeman)  
 Romani, R. W., Shaw, M. S., Camilo, F., Cotter, G., & Sivakoff, G. R. 2010, *ApJ*, **724**, 908  
 van Etten, A., Romani, R. W., & Ng, C.-Y. 2012, *ApJ*, **755**, 151  
 Wilms, J., Allen, A., & McCray, R. 2000, *ApJ*, **542**, 914

---

## Conclusions and Future Work

When a star goes supernova,  $\sim 1\%$  of its explosion energy is converted into kinetic energy that forms an expanding shock-wave. The interaction of this shock-wave with surrounding material produces what we know as a supernova remnant (SNR). If the original progenitor has a mass  $\geq 8M_{\odot}$ , this can lead to the formation of a very dense, very compact and rapidly rotating stellar object called a pulsar. The rapid rotation produces a pulsar wind which interacts with the surrounding environment producing a pulsar wind nebula (PWN). These objects produce both thermal and non-thermal emission over the entire electromagnetic spectrum, which provides us with information about their evolution and dynamics; details about the original progenitor star and its explosion mechanism; the impact that these objects have on their surroundings; the effect that the original progenitor had on shaping the surrounding environment; the nucleosynthesis yield of the original progenitor; and the chemical composition of the surrounding environment. In addition, SNRs and pulsars also provide a unique window into studying the physics associated with accelerating particles. Galactic cosmic rays with energies less than  $10^{15}$  eV are thought to arise from SNRs accelerating particles at their shock-fronts, while pulsars and their nebulae that are found within 1 kpc of Earth are thought to contribute to the observed excess in electrons and positrons seen by numerous experiments such as *Fermi*-LAT (Abdo et al., 2009b; Ackermann et al., 2010) and *PAMELA* (Adriani et al., 2009b,a). The detection of non-thermal X-ray and  $\gamma$ -ray emission from these objects has established the presence of relativistic particles in some SNRs and PWNe. As a consequence, these objects are important probes for studying in detail the injection, propagation and interaction of cosmic rays with the interstellar medium, as well as providing answers to some of science's most fundamental questions such as "what is the origin of cosmic rays?".

Due to the intimate connection that SNRs, pulsars and PWNe have with cosmic rays, one of the main aims of this thesis is to better understand the energetics and acceleration of cosmic rays at the shock front of an SNR and at the termination shock of a pulsar wind; the radiative losses that these particles experience as they interact with the surrounding medium; and how these particles propagate through

the interstellar medium. We do this by analysing the  $\gamma$ -ray emission from SNRs Kes 79 and MSH 11–61A, which are known to be interacting with molecular clouds (Chapter 3 and 4). These remnants were chosen as SNRs interacting with molecular clouds are ideal, indirect laboratories that one can use to detect and analyse emission arising from  $\pi^0$  decay. We also analyse the non-thermal X-ray emission arising from a PSR J1741-2054 and its nebulae to characterise, as well as constrain, the energy and magnetic field required to produce the observed emission (Chapter 5). The studies highlighted above are focused on localised emission from these individual sources. This localised emission usually dominates over the non-thermal background making it easier for one to differentiate this emission from other sources of emission. But as these particles propagate and diffuse through the Galaxy, it becomes more difficult to be able to extract a unique signal from individual sources. As a consequence it becomes important to be able to determine the theoretical spectrum of cosmic rays assuming basic propagation parameters. By constraining the “background” cosmic ray spectrum, this allows one to better determine and characterise any “non-standard” contribution to the measured cosmic ray spectrum at Earth. Using the numerical Galactic cosmic ray propagation package GALPROP, which models the propagation of relativistic charged particles through the Galaxy, we determined this theoretical background with uncertainties and utilised it to try to shed light on the origin of the electron-positron anomaly (Chapter 1).

In addition to analysing the non-thermal emission from SNRs and pulsars, this thesis aimed to better understand the origin and characteristics of X-ray emission arising from Kes 79, MSH 11–61A and PSR J1741-2054. Using *XMM-Newton*, and *Suzaku* respectively, we probed the temperature, ionisation state, and elemental abundances of the shocked gas of Kes 79 and MSH 11–61A. This allowed us to determine their evolutionary properties and constrain the density of the X-ray emitting plasma which was compared with our inferred density from our  $\gamma$ -ray modelling. Using *Chandra*, we were able to extract the temperature, radius, and proper motion of PSR J1741-2054, better characterising the properties of this unique object.

Below I will summarise the major results of each chapter and then highlight ongoing and future research that may improve our understanding of the thermal and non-thermal emission of SNRs interacting with molecular clouds, as well as improving our understanding of the origin and properties of J1741-2054.

## 6.1 Summary

Using the *Fermi*-LAT satellite we were able to reveal and characterise GeV  $\gamma$ -ray emission in the direction of Kes 79 and MSH 11–61A. These remnants are known

to be interacting with molecular clouds based on the presence of strong molecular line emission from HI and CO observations. To investigate the origin of this emission, we performed broadband modelling of the non-thermal emission of each remnant and in both cases, the  $\gamma$ -ray emission is dominated by hadronic emission from a population of relativistic protons. Similar to previous studies of SNRs interacting with molecular clouds (e.g., [Castro et al. 2013b](#)), we find that the inferred density from our  $\gamma$ -ray analysis is high, consistent with the presence of dense molecular clouds. We compared this inferred density to the density of the X-ray emitting material derived from analysing the X-ray emission of each remnant. As found in previous studies we find a large discrepancy between these two density estimates, which indicates that the bulk of the  $\gamma$ -rays originate from material that is not producing X-rays. Higher resolution  $\gamma$ -ray observations of the remnant would be able to localise where the  $\gamma$ -ray emission arises from, while ALMA observations would be able to map the clumpiness of the preshock and postshock density. Detailed modelling of how SNR evolve into dense environments and how clumps are formed would also help shed light on this discrepancy, and thus help us better understand the location, distribution and characteristics of the observed  $\gamma$ -ray emission.

Apart from studying the  $\gamma$ -ray emission from Kes 79 and MSH 11–61A, we also analysed the thermal X-ray emission from these remnants. For Kes 79, its X-ray emitting plasma can be best described by a two temperature component plasma with enhanced abundances of Mg, Si, and S. This indicates that the observed emission arises, at least in part, from shocked ejecta. Assuming that the remnant is in a Sedov phase of evolution, we derived the amount of swept up mass, the explosion energy, age of the remnant, temperature and velocity of the forward shock.

For MSH 11–61A we found that the bulk of its X-ray emission can be described by a single recombining plasma with enhanced abundances of Mg, Si and S, and an underabundance of Ne and Fe. This makes MSH 11–61A one of the growing number of SNRs with a recombining plasma. Towards the east of the remnant, the emission is best described by an ionising plasma with enhanced Mg, Si and S. Our analysis suggests that the recombining plasma arises from adiabatic cooling, and that the progenitor of MSH 11–61A had a mass  $> 13M_{\odot}$ .

Over the last couple of decades, numerous experiments have hinted towards an excess of high energy cosmic ray electrons and positrons. This was confirmed using *PAMELA*, *AMS-02* and the *Fermi*-LAT satellites, which found that the electron positron sum could not be explained assuming diffusive propagation and that the positron fraction was increasing rather than decreasing as predicted by conventional propagation physics. These discrepancies lead to a large number of proposed explanations ranging from pulsars, SNRs, modification of the cosmic-ray propagation physics and dark matter annihilation/decay. However, the existence

and statistical significance of these deviations is dependent on our theoretical prediction of what constitutes the cosmic ray background. As the origin and physics of cosmic ray diffusion is not well understood, this leads to a large uncertainty in our theoretical model of cosmic ray propagation, making it difficult to estimate this background. To combat this, we subjected a number of different cosmic ray observations to a Bayesian likelihood analysis so that we were able to constrain the parameter space of our propagation model. This allowed us to extract with uncertainties, the cosmic ray background and determine the existence, size, shape and significance of the deviation that has led to the plethora of explanations in the literature. We then compared this extracted signal to different explanations in the literature (pulsars, supernova remnants and dark matter annihilation) and find that due to the large uncertainty, we are unable to draw any conclusion about the origin of this cosmic ray anomaly. With more higher resolution cosmic ray data, we would be able to reduce the uncertainty on both the background and anomalous signal making it easier to rule out or confirm the many different explanations for this observed excess.

Pulsars dissipate their rotational energy by generating relativistic winds, which in turn produce a population of high energy electrons and positrons, which we observe as synchrotron emitting nebulae. If the pulsar has a high space velocity given to it as a result of a “kick” by the original supernova explosion, the corresponding nebula will have a bow-shock morphology due to the pulsar wind being confined by ram pressure. PSR J1741-2054 is one of a small number of pulsars for which its X-ray emitting PWN (detected by [Romani et al. 2010](#)) is contained within a bright  $H\alpha$  bow shock nebula. This pulsar is one of the closest ( $\sim 0.38\text{kpc}$ ), middle-aged ( $\tau_c = 390\text{ kyr}$ ) pulsars known and was first discovered using the *Fermi*-LAT satellite. Using nearly 300 ks of *Chandra* data, we constrained the proper motion of the pulsar and find that it is travelling  $109\pm 10\text{ mas yr}^{-1}$  in a direction consistent with the symmetry axis of its bow shock nebula and the extended PWN emission. We find no correlation with known OB associations in which the progenitor may have originated, making it difficult to draw a conclusion of where it was born. We also characterised the emission of the pulsar and PWN and find that the diffuse emission in the extended X-ray trail shows no evidence of synchrotron cooling. We search for small scale structure in the immediate vicinity of the pulsar, but found no conclusive evidence for a torus or jet-like structure. Future work on this object aims to better understand the properties of the system. This includes using Hubble Space Telescope data to map the structure of the  $H\alpha$  bow shock nebula, so that we could better determine the flow geometry and characteristics of the pulsar wind. In addition these observations would allow one to produce a more accurate proper motion estimate as the proper motion derived from X-ray observation may have been affected by fluctuations (variation in brightness and number of counts) in the PWN emission. From this, we would

be able to derive the pulsar’s space velocity more accurately, produce an improved distance measurement and help constrain the birth site of this pulsar.

## 6.2 Future Work

A large fraction of SNRs known to be interacting with molecular clouds are members of the mixed morphology (MM) SNR subclass. [Rho & Petre \(1998\)](#), first characterised these MM SNRs using *ROSAT* X-ray data and determined that these remnants have a shell-like morphology in radio and have bright thermal X-rays in its centre. [Rho & Petre \(1998\)](#) determined that there were 19 MM SNRs, whose thermal X-rays are characterised by a uniform temperature and their emission arises from swept up interstellar medium (ISM). Since this original paper, there have been significant advancements in the resolution and sensitivity of X-ray satellites. As a consequence this has increased the number of known MM SNRs to 37 ([Zhang et al., 2015](#)), and revealed that these remnants are much more complicated than originally described.

A large number of these remnants now show evidence of enhanced abundances. The presence of enhanced abundances implies that the X-ray emission arises, at least in part, from shock-heated ejecta. In many of these systems the mass of the X-ray emitting material appears to be much higher than what one expects from the emission to arise primarily from ejecta, implying a contribution from interstellar or circumstellar material. [Rho & Petre \(1998\)](#) observed that the temperature of these remnants is uniform, however new high resolution data now shows that the temperature varies across these remnant. In addition, a large number of these remnants show evidence of overionisation, contrary to what is expected from standard SNR evolution models.

Apart from their unique X-ray characteristics, MM SNRs comprise a significant fraction of the  $\gamma$ -ray population, nearly half of all known MM SNRs are  $\gamma$ -ray sources, with at least a third of all GeV emitting SNRs classified as MM SNRs. A large number of MM SNRs are known to be interacting with molecular clouds which may contribute at least partially to why these remnants are so dominant in  $\gamma$ -rays. However, a complete understanding of the  $\gamma$ -ray emission arising from these objects is not known. Interestingly, nearly all SNRs with recombining plasmas are detected in  $\gamma$ -rays

The properties and conditions that lead to these characteristics are poorly understood and have not been investigated, or modelled in detail. With the large amount of high resolution archival X-ray data available for many known and candidate MM SNRs, in addition to the publicly available  $\gamma$ -ray data from the *Fermi Gamma-ray Space telescope*, we are now in a prime position to carry out the most detailed investigation of MM SNRs to date. This will allow us to

better understand the nature and characteristics of the central X-ray emission, as well as determine the  $\gamma$ -ray properties of these objects. Unlike the systematic analysis of [Rho & Petre \(1998\)](#), a large number of MM SNRs have been analysed individually by many different authors, with many different analysis recipes. This makes it difficult to assess the high energy emission properties of these objects as a class similar to that completed by [Rho & Petre \(1998\)](#). Using the available X-ray and  $\gamma$ -ray data we will systematically, and consistently, analyse the high energy emission from these objects in attempt to better understand the nature and characteristics of the observed emission, as well as determining the influence that the surrounding environment has on these properties.

The results from this analysis will be combined with detailed modelling using the *CR-hydro-NEI* code produced by [Lee et al. \(2012\)](#) to better understand the structure, formation and evolution of MM SNRs. Assuming different MM SNR models, we will be able to derive the conditions that lead to the observed X-ray and  $\gamma$ -ray properties of these remnants. We would also be able to investigate different environmental conditions, ejecta compositions of the original progenitor, and different cosmic-ray acceleration properties. The results from our X-ray and  $\gamma$ -ray analysis will constrain the parameter space of our models, as well as assert which model best describes the observed emission and evolutionary characteristics of these remnants.

In addition we will be able to establish what fraction of the total number of X-ray emitting Galactic SNRs ( $\sim 70$ ) are MM SNRs and if they are the dominant X-ray emitting SNR population. We will also be able to determine the number that show enhanced abundances and calculate the total mass of swept up material, as well as the total mass of ejecta. From this, we will be able to determine limits on the mass of the original progenitor, and take steps towards determining whether the phenomenon of MM SNR is a phase that all SNRs go through or whether properties are related to a characteristic of the original progenitor, or environment.

# Appendices



---

# Bayesian Inference and Model Selection

## A.1 Definitions of Probability

The application of Bayesian methods in astrophysics, particle physics, and cosmology has increased dramatically in the last few decades, due to the increasing volume and complexity of data sets and the computational power available to process them (Trota, 2008). The information available to us for scientific research is always an incomplete subset of a much larger amount of non accessible information. Due to this, our developed knowledge about natural phenomenon is unavoidably probabilistic. There are two main probability definitions in the literature that are used in statistical inference: Frequentist and Bayesian probability.

The classical (Frequentist) view defines probability to be: “in the limit of infinite equally probable repetitions of the event, the probability of the event occurring is the number of times an event occurs divided by the total number of trials” (Gregory, 2005; Trota, 2008). This definition of probability is unsatisfactory as it:

1. Assumes that repeated trials have the same probability of occurring.
2. It does not apply to unrepeatable outcomes.
3. This definition holds only for an infinite sequence of repetitions. In reality we only get a finite number of measurements when doing experiments.

Many of the limitations associated with the frequentist definition of probability can be avoided by recognising that the mathematical rules of probability represent sound principles of logic that can be used to make statistical inference about any hypothesis of interest. This stance on probability is called Bayesian inference (or Bayesian analysis) (Gregory, 2005; Trota, 2008).

In Bayesian inference, probability is defined as a measure of the degree of belief in a proposition. This definition has the advantage over the frequentist view point as:

1. It can be applied to any event regardless if it is repeated or a unique situation.
2. It provides us with a probability definition that can handle situations where we have access to only one data set.

3. Nuisance parameters (parameters which influence ones data but are of no interest to the study) are dealt with naturally through the process of integrating over the nuisance parameter(s)<sup>1</sup>. In the frequentist view, there is no simple way of dealing with nuisance parameters and neglecting them or setting them to a best fit value can lead to major errors in the parameter estimation.
4. Prior information about your hypothesis and/or data is easily incorporated into a Bayesian statistical analysis. This has an advantage as some parameters will represent a physical quantity such as the mass of a particle, where a prior experimental measurement restricts the possible value of this parameter. Frequentist analysis finds it difficult to incorporate prior knowledge which can lead to meaningless parameter estimates.

## A.2 Bayes' Theorem

The fundamental tool of Bayesian analysis is *Bayes' theorem*. Bayes' theorem is derived using the symmetric forms of the conditional probability product rule  $P(H_i(\Theta), D|I) = P(D, H_i(\Theta)|I)$ . Rewriting the product rules one obtains Bayes' theorem, which defines how the probability of our hypotheses should change when one incorporates new experimental data  $D$  (Trotta, 2008):

$$P(H_i(\Theta)|D, I) = \frac{P(D|H_i(\Theta), I)P(H_i(\Theta)|I)}{P(D|I)}, \quad (\text{A.1})$$

Here  $H_i(\Theta)$  are our hypotheses which are a function of the parameters ( $\Theta$ ). These hypotheses define what we want to assess in light of a continuous data set  $D$ . All terms in Bayes' theorem are conditional on some prior information  $I$ , which contains all the preceding information about our hypotheses. This allows us to calculate the posterior probability,  $P(H_i(\Theta)|D, I)$ , which represents our state of belief about our hypotheses in light of the data  $D$ . The posterior is proportional to the likelihood function  $P(D|H_i(\Theta), I)$  multiplied by the prior probability of the hypothesis  $P(H_i(\Theta)|I)$ . The likelihood function encodes the changes in the plausibility of our hypotheses when we take experimental data into account. While the prior,  $P(H_i(\Theta)|I)$ , represents the state of knowledge about our hypothesis before including the experimental data. The term  $P(D|I)$  is called the Bayesian evidence (or marginalised likelihood), and represents the probability of the hypothesis in terms of the experimental data alone.

If we assume that we have a mutually exclusive set of hypotheses (i.e. a set of hypotheses for which one hypothesis is true while all others are false) then the Bayesian evidence can be calculated by marginalising (integrating or summing

---

<sup>1</sup>This method is called marginalisation.

depending if its a continuous or discrete set of data) over the set of hypotheses (Trotta, 2008; Gregory, 2005).

$$P(D|I) = \sum_i P(D, H_i(\Theta)) = \sum_i P(D|H_i(\Theta), I) \times P(H_i(\Theta)|I) \quad (\text{A.2})$$

As  $P(D|I)$  does not depend on the hypothesis  $H_i(\Theta)$ , it acts as a normalisation factor in Bayes' theorem. But it has the added advantage of being the central quantity for model comparison.

### A.2.1 Prior $P(H_i(\Theta)|I)$

The prior  $P(H_i(\Theta)|I)$  choice is an important feature of Bayesian inference. The presence of a prior highlights the main principle of Bayesian analysis, that there can be no inference without assumptions (Trotta, 2008). It allows you to formulate your assumptions and knowledge about the problem in question before one includes the data. Frequentist analysts regard the use of a prior as problematic and subjective as the theory does not specify how a prior should be selected. But the use of a prior provides an uncertainty for the unknown quantity in question i.e. the parameters in your hypothesis.

It is natural for different researchers to choose different priors due to their past research experience and methods. But as long as the prior is non zero in regions where the likelihood is large, then repeated applications of Bayes' theorem will lead to a posterior probability that converges to a common shape and conclusion. In model comparison analysis, the prior is important as it determines the penalty given to a more complex model with multiple free parameters.

### A.2.2 Nuisance Parameters

It is quite common that the hypothesis space for a particular hypothesis is dependent on the values of the model parameters  $\Theta$ . These parameters can usually be split into two sets,  $\Theta = \{\varpi, \xi\}$  where  $\varpi$  are the parameters that we are interested in and  $\xi$  that are the nuisance parameters. Nuisance parameters are parameters which influence ones data but are of no interest to the study. As we do not care about the values of the nuisance parameters, they are dealt with easily in Bayesian analysis by integrating over all their possible values.

$$P(\varpi|D, H_i) = \int P(\varpi, \xi|D, H_i) d^{N_\xi} \xi \quad (\text{A.3})$$

where  $N_\xi$  is the number of  $\xi$  parameters that we are integrating over. By marginalising we can determine what the data and prior information can tell us about the parameters we are interested in, independent of the nuisance parameters. The resulting  $P(\varpi|D, H_i)$  is called the marginalised posterior probability of  $\varpi$ .

### A.2.3 Calculation of the likelihood and the Bayesian evidence

The hardest part of Bayesian analysis is calculating the Bayesian evidence function  $P(D|I)$ , as it is usually multi-dimensional integrals over large parameter spaces.

The likelihood function,  $P(D|H_i(\Theta), I)$ , is calculated from a  $\chi^2$  analysis of the available experimental data  $D = d_i \pm \sigma_{i;exp}$  and the theoretical predictions  $T = t_i \pm \sigma_{i;the}$  of the model assumed in  $H_i$ . The combined theoretical and experimental uncertainties is defined by  $\sigma_i^2 = \sigma_{i;exp}^2 + \sigma_{i;the}^2$  where the theoretical uncertainty is  $\sigma_{i;the}^2$  and the experimental uncertainty is  $\sigma_{i;exp}^2$ . The most difficult part of this calculation is to calculate the theoretical predictions  $T$ . The likelihood function for any piece of data  $d_i$  is

$$P(d_i|H_i(\Theta), I) = \frac{1}{\sqrt{2\pi}\sigma_i} \exp\left(-\frac{1}{2}\chi_i^2(d_i, \Theta; H)\right) \quad (\text{A.4})$$

where  $\chi^2$  is defined as:

$$\chi_i^2(d_i, \Theta; H) = \frac{(d_i - t_i(\Theta; H))^2}{\sigma_i} \quad (\text{A.5})$$

If the experimental data used is statistically independent (i.e. the results of one experiment must not influence one's expectation of the results of another experiment), then the likelihood functions for each measurable can be factorised into:

$$P(D|\Theta, H) = P(d_1, d_2, \dots, d_n|\Theta, H) = \prod_i P(d_i|\Theta, H) \quad (\text{A.6})$$

The Bayesian evidence for a given hypothesis  $H$  is calculated by multiplying Equation A.6 by  $P(\Theta|H)$  and integrating this expression over the full parameter space  $d^N\Theta$ :

$$P(D|H) = \int P(D|\Theta, H)P(\Theta|H)d^N\Theta. \quad (\text{A.7})$$

### A.2.4 Model/Hypothesis testing using the evidence function.

Typically, there will be more than one competing hypothesis available to explain a set of data. Bayesian model comparison uses Bayes' theorem to calculate the relative probability of each hypothesis in light of the data and prior information. The best hypothesis is one that optimises the balance between prediction and quality of fit. Bayesian model comparison has an inbuilt principle of simplicity when optimising the balance between prediction and quality of fit. This is known as Occam's razor (Gregory, 2005; Trotta, 2008).

A hypothesis with the larger number of parameters represents a more complex hypothesis. Bayesian model comparison offers a formal method of evaluating whether the extra complexity of a model is required by the data. If the data does not justify the additional complexity, Bayes' theorem will penalise the more complex model by assigning it the smaller probability.

Table A.1: This is a summary of the Jeffreys' scale. The Jeffrey's scale is an empirical scale for evaluating the strength of evidence when comparing two models [Trotta \(2008\)](#).

$ \ln B_{01} $	Odds	Probability	Strength of evidence
$< 1.0$	$\lesssim 3 : 1$	$< 0.750$	Inconclusive
1.0	$\sim 3 : 1$	0.750	Weak evidence
2.5	$\sim 12 : 1$	0.923	Moderate evidence
5.0	$\sim 150 : 1$	0.993	Strong evidence

An advantage that Bayesian model selection has over frequentist chi-square tests to determine goodness of fit, is that instead of rejecting all hypotheses if the chi-square value is too high, it insists that it is pointless to reject a theory unless there is an another hypothesis which can describe the data better. Bayesian model selection requires one to specify explicitly two or more alternative hypotheses, where we assume that one of the hypothesis is true. If we divide the posterior probability ( $P(H_i(\Theta)|D, I)$ ) of each hypothesis, we get the ratio of the probabilities of the two models.

$$O_{ij} = \frac{P(D|H_i(\Theta), I)P(H_i(\Theta)|I)}{P(D|H_j(\Theta), I)P(H_j(\Theta)|I)} \quad (\text{A.8})$$

$$O_{ij} \equiv B_{ij} \times \frac{P(H_i(\Theta)|I)}{P(H_j(\Theta)|I)} \quad (\text{A.9})$$

where  $B_{ij}$  is the Bayes' factor and  $\frac{P(H_i(\Theta)|I)}{P(H_j(\Theta)|I)}$  is the posterior odds.

The Bayes' factor  $B_{ij}$  is the ratio of the two hypothesis evidence and it gives a numerical value to our degree of belief in the two competing hypotheses. To determine the strength of the evidence in favour of one model over the other, the Bayes' factors are compared to an empirically calibrated scale called the Jeffrey's scale which is shown in [Table A.1 \(Jeffreys, 1967\)](#). This gives you a numerical value for the odds in favour of a particular hypothesis, the probability of a hypothesis being favoured over the other and the corresponding strength of the evidence for one of the hypotheses.



---

## Solving the cosmic ray transport equation

There are numerous different techniques which can be employed to solve the transport equation, and they all lead to very similar fluxes at Earth (Bertone, 2010). Under simplifying assumptions (i.e. assuming no reacceleration in your diffusion model (Baltz & Edsjö, 1999)), Equation 1.42 can be solved analytically by utilizing Green functions. The Green function defines the probability of a particular cosmic ray species of energy  $E_{source}$  at the source, produced at a location in the galaxy to be detected at earth  $E_{earth}$ , with  $E_{earth} < E_{source}$ . The Green function is then integrated over the diffusion volume and the corresponding energy range that one is analysing (Bertone, 2010). This method is usually used for propagating positrons (e.g.,: Delahaye et al. 2009b).

A two dimensional fully analytical model of the transport equation can be obtained using the Bessel expansion method (Bertone, 2010). This method assumes that cosmic ray species diffuse into a diffusive halo which mimics the cylindrical shape and approximate interstellar medium composition of the Milky Way. At the edges of this diffusive halo, this method assumes that the cosmic ray flux vanishes; hence diffusive re-acceleration and energy losses are confined to the diffusive halo. A disadvantage of this method is that one requires a numerical solution to determine the diffusion of the cosmic rays in energy space.

Most realistic cases of cosmic ray propagation requires one to include the influence of various aspects of the astrophysical environment and the spectra of the cosmic rays. As a consequence, an analytical solution of Equation 1.42 is not always available. Hence a numerical solution is a required. A completely numerical solution has been developed by Strong and Moskalenko in the publicly available code called GALPROP (Moskalenko et al., 2011).

### B.1 GALPROP

GALPROP is a mix of FORTRAN and C++ code which numerically solves the transport equation (Equation 1.42) on a two dimensional spatial grid, where the Galaxy is assumed to have cylindrical symmetry. It also has the capability of fully

solving the transport equation in three dimensions. As observations of galaxies other than our local galaxy suggest that cosmic rays are diffusing in a cylindrical slab (Delahaye et al., 2009a), we use the two dimensional spatial grid version of GALPROP.

The coordinates of the Galaxy are  $(R, z, p)$  where  $R$  is the galactocentric radius,  $z$  is the distance from galactic plane and  $p$  is the total particle momentum. The user has the ability to define all aspects of the propagation model, the spatial grid, the propagation processes, and the distribution, spectral shape and isotropic composition of the sources (Strong et al., 2007). This is defined in the input file which GALPROP reads. Usually the propagation region is bounded by a radius of  $R_h = 0 - 20$  kpc and a total height  $2Z_h$ , where  $Z_h = 1 - 20$  kpc.

One of the benefits of GALPROP is that it uses astrophysical input to provide a realistic ISM that the cosmic rays are propagated through. In its calculation, GALPROP incorporates astrophysical input such as the distribution of molecular, ionised and atomic hydrogen, and the interstellar radiation field, as well as the distribution of cosmic ray sources. These are important to incorporate as they significantly affect the production of secondary cosmic rays species and the type and magnitude of energy losses experienced by these species.

The ISM has three different hydrogen components (HI, HII, H<sub>2</sub>) which have markedly different galactic distributions (Figure B.1). The molecular H<sub>2</sub> gas distribution is mostly concentrated in the plane of the galaxy, while atomic hydrogen HI has a much broader distribution. Ionised hydrogen HII is broader than atomic hydrogen but its percentage by mass is much smaller than the total gas. The interstellar hydrogen gas distribution in GALPROP uses HI and CO surveys to trace the atomic and molecular hydrogen gas in the ISM, introducing the effect of Galactic structure on the propagation of cosmic rays. It assumes that the distribution of hydrogen gas is cylindrically symmetric and is related to the emissivity per gas atom in the Galaxy (Strong & Mattox, 1996). The HI gas number density (atom cm<sup>-3</sup>) is defined by:

$$n_{\text{HI}}(R, z) = \frac{Y(R)}{n_{\text{GB}}} \begin{cases} \sum_{i=1,2} A_i \exp\left(-\frac{\ln(2)z^2}{z_i^2}\right) + A_3 e^{-\frac{|z|}{z_3}}, & R \leq 8 \text{ kpc} \\ \text{interpolated,} & 8 < R < 10 \text{ kpc} \\ n_{\text{DL}} \exp\left(-z^2 \frac{e^{-0.22R}}{z_4^2}\right), & R \geq 10 \text{ kpc} \end{cases} \quad (\text{B.1})$$

where  $Y(R)$  is the relative number density distribution of HI in our Galaxy (Moskalenko et al., 2002). This is taken from the table of Gordon & Burton (1976). The  $Y(R)$  used in GALPROP is renormalised so that it agrees with the total integral perpendicular to the plane determined by Dickey & Lockman (1990). This is done so that  $Y(R)$  becomes a continuous function over the whole radius range.

The Galactic disk densities for  $4 < R < 8$  kpc are  $n_{\text{GB}} = 0.33 \text{ cm}^{-3}$  and

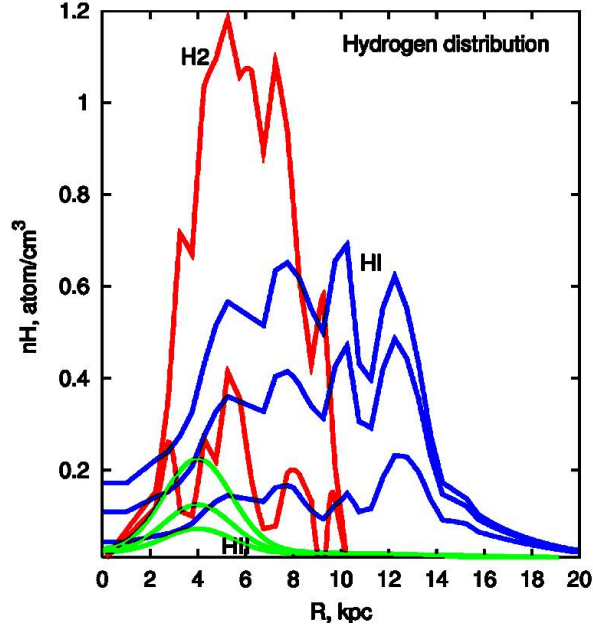


Figure B.1: The gas distribution is important for the production of secondary cosmic rays and the energy losses that they experience. As a consequence, it is important to incorporate their density distribution as a function of radius in any cosmic ray propagation model. The interstellar hydrogen gas distribution can be well described by three different components as shown in this figure. Here molecular hydrogen ( $H_2$ ) is shown in red and is mostly concentrated mostly in the plane. The three red curves correspond to different altitudes above the plane (explicitly 0, 0.1 and 0.2 kpc above the Galactic plane). In blue is the distribution of atomic hydrogen ( $H\text{I}$ ) at different altitudes, while in green is the distribution of ionised hydrogen ( $H\text{II}$ ) at different altitudes. In GALPROP,  $H\text{I}$ ,  $H_2$  and  $H\text{II}$  are described by Equations B.1, B.2 and B.3 respectively (Strong & Moskalenko, 1998).

$n_{DL}=0.57 \text{ cm}^{-3}$ , and are taken from Gordon & Burton (1976) and Dickey & Lockman (1990) respectively. For  $R < 8 \text{ kpc}$ , this is calculated from the approximation of the column density given by Dickey & Lockman (1990). For  $R > 10 \text{ kpc}$ ,  $Y(R)$  is obtained from the approximation of the  $H\text{I}$  density given by Cox et al. (1986). The parameter values in Equation B.1 are  $A_1 = 0.395$ ,  $A_2 = 0.107$ ,  $A_3 = 0.064$ ,  $z_1 = 0.106$ ,  $Z_2 = 0.265$ ,  $Z_3 = 0.403$ ,  $Z_4 = 0.0523$ . The  $H_2$  number density ( $\text{mol cm}^{-3}$ ) is calculated by (Moskalenko et al., 2002):

$$n_{H_2}(R, z) = 3.24 \times 10^{-22} \mathcal{X} \epsilon_0(R) \exp - \ln 2 \frac{(z - z_0)^2}{z_h^2} \quad (\text{B.2})$$

where  $\epsilon_0(R)$  ( $\text{K km s}^{-1} \text{ kpc}^{-1}$ ) is the CO volume emissivity,  $z_0(R)$  and  $z_h(R)$  are the height scale and width of the molecular hydrogen gas distribution which is defined in the table of Bronfman et al. (1988).  $\mathcal{X} \equiv n_{H_2}/\epsilon_{CO} = 1.9 \times 10^{20} \text{ mol cm}^{-2} \text{ K}^{-1} \text{ km}^{-1} \text{ s}$  is a conversion factor (Strong & Mattox, 1996) that is

used to relate the molecular hydrogen ( $\text{H}_2$ ) column density to the integrated CO temperature (Strong & Mattox, 1996). The ionised component HII (atom  $\text{cm}^{-3}$ ) is calculated using the two component model of Cordes et al. (1991),

$$n_{\text{HII}}(R, z) = \sum_{i=1,2} n_i e^{-|z|/h_i - (R-R_i)^2/a_i^2}, \quad (\text{B.3})$$

where  $n_1 = 0.025$ ,  $n_2 = 0.200$ ,  $h_1 = 1$  kpc,  $h_2 = 0.15$  kpc,  $R_1 = 0$ ,  $R_2 = 4$  kpc,  $a_1 = 20$  kpc,  $a_2 = 2$  kpc. The first term in the expansion of  $n_{\text{HII}}(R, z)$  represents the warm ionised hydrogen gas distribution. The second term in the expansion represents the distribution of the HII regions and is assumed to be concentrated at  $R = 4$  kpc (Strong & Moskalenko, 1998).

The interstellar radiation field (ISRF) is used to calculate the spectrum of  $\gamma$ -rays that arise from energy losses experienced by CRs. The ISRF calculation used in GALPROP is based on a theoretical model developed by Moskalenko et al. (2006) and Porter & Strong (2005).

After propagation, the distribution of the cosmic ray sources is chosen to reproduce the cosmic ray distribution determined by Strong & Mattox (1996) who analysed EGRET gamma ray data. The cosmic ray source distribution has the form:

$$q(R, z) = q_0 \left( \frac{R}{R_\odot} \right)^\eta \exp \left( -\zeta \frac{R - R_\odot}{R_\odot} - \frac{|z|}{0.2 \text{ kpc}} \right) \quad (\text{B.4})$$

where  $q_0$  is a normalisation constant,  $\eta$  and  $\zeta$  are input parameters. The terms with R-dependence is identical to the distribution of SNRs derived by Case & Bhattacharya (1996) for 194 known remnants at that time (Green, 1996). The source distribution of all primary cosmic ray is assumed to be the same.

GALPROP solves the transport equation numerically for  $Z \geq 1$  nuclei, as well as for electrons and positrons. The calculation is started using the heaviest primary element defined by the user (such as Nickel-64), and the propagated solution is then used to compute the source term for the secondary products of this element. This process is continued until protons, secondary electrons, positrons and anti-protons are produced and a steady state solution is obtained (Strong et al., 2007). The spectrum of  $\gamma$ -rays and synchrotron emission is realistically calculated in conjunction with interstellar gas distributions derived from HI and CO surveys, ISRF and magnetic field models derived from detailed theoretical calculations (Strong et al., 2007; Bertone, 2010).

The numerical solution of the transport equation is based on a Crank-Nicolson implicit second-order scheme (Strong et al., 2007). It is called an implicit scheme because it finds a solution by solving an equation involving the current state of the system and a later state of the system. The spatial boundary conditions assumes free particle escape. The transport equation (Equation 1.42 in one dimension),

being a differential equation can be written in the finite difference form:

$$\frac{\partial \psi_i}{\partial t} = \frac{\psi_{\Delta t}^{t+\Delta t} - \psi^{t+\Delta t}}{\Delta t} = \frac{\alpha_1 \psi_{i-1}^{t+\Delta t} - \alpha_2 \psi_i^{t+\Delta t} + \alpha_3 \psi_{i+1}^{t+\Delta t}}{2\Delta t} + \frac{\alpha_1 \psi_{i-1}^t - \alpha_2 \psi_i^t + \alpha_3 \psi_{i+1}^t}{2\Delta t} + q_i \quad (\text{B.5})$$

This is the Crank-Nicolson method, where each solution to the derivative is updated using the scheme:

$$\psi_i^{t+\Delta t} = \psi_i^t + \frac{\alpha_1}{2} \psi_{i-1}^{t+\Delta t} - \frac{\alpha_2}{2} \psi_i^{t+\Delta t} + \frac{\alpha_3}{2} \psi_{i+1}^{t+\Delta t} + \frac{\alpha_1}{2} \psi_{i-1}^t - \frac{\alpha_2}{2} \psi_i^t + \frac{\alpha_3}{2} \psi_{i+1}^t + q_i \Delta t, \quad (\text{B.6})$$

where  $\alpha$  is the step size and  $\Delta t$  is the time step. This method uses a combination of implicit and explicit terms, forming the time average solution to the differentials. This method is unconditionally stable for all  $\alpha$  and  $\Delta t$ , but it is accurate in time up to second order.

The above Crank-Nicolson method is one dimensional, but to realistically describe cosmic ray propagation in our galaxy, one requires it to be generalised to two or three spatial and one momentum dimensions. Expanding to include these extra dimensions involves solving a large set of matrix equations which are not tri-diagonal<sup>1</sup>. As a consequence we cannot solve these equations directly. To solve this multidimensional derivative, the Alternating Direction Implicit (ADI) method is used. This method splits the finite difference equations of the transport equation into two or more equations (where the number is dependent on the number of dimensions that you have). These are solved by applying the implicit updating scheme (Equation B.6 generalised to multi-dimensions) of each dimension operator in each dimension in turn, whilst keeping the other coordinates fixed. The coefficients for the finite differencing scheme in two spatial dimensions and one momentum dimension corresponding to the Crank-Nicolson method used by GALPROP are listed in Table B.1

For the two dimensional solution of GALPROP, the three spatial boundary conditions imposed at each iteration is:

$$\psi(R, z_h, p) = \psi(R, -z_h, p) = \psi(R_h, z, p) = 0. \quad (\text{B.7})$$

No boundary conditions are imposed for the momentum dimension. The grid intervals are typically  $\Delta R = 1$  kpc,  $\Delta Z = 0.1$  kpc. A standard run of GALPROP will usually start with an initial time step of  $10^9$  years and will finish on the timestep of  $10^4$  years for nucleons and finish on the timestep of  $10^2$  years for electrons, performing  $\sim 60$  iterations per timestep.

<sup>1</sup>A tri-diagonal matrix has non-zero elements in the main diagonal, and the first diagonal above and below the main diagonal, e.g.

$$M = \begin{pmatrix} a & b & 0 & 0 \\ c & d & e & 0 \\ 0 & f & g & h \\ 0 & i & j & k \end{pmatrix}$$

Table B.1: Coefficients for the Crank-Nicolson method. Here “a” represents  $P_j^i \equiv p_i - p_j$ 

Process	Coordinate	$\alpha_1/\Delta t$	$\alpha_2/\Delta t$	$\alpha_3/\Delta t$
Diffusion	$R$	$D_{xx} \frac{2R_i - \Delta R}{2R_i(\Delta R)^2}$	$D_{xx} \frac{2R_i}{R_i(\Delta R)^2}$	$D_{xx} \frac{2R_i + \Delta R}{2R_i(\Delta R)^2}$
	$z$	$D_{xx}/(\Delta z)^2$	$2D_{xx}/(\Delta z)^2$	$D_{xx}/(\Delta z)^2$
Convection	$z > 0$ ( $V > 0$ )	$V_{i-1}/\Delta z$	$V_i/\Delta z$	0
	$z < 0$ ( $V < 0$ )	0	$-V_i/\Delta z$	$-V_{i+1}/\Delta z$
	$p(dV/dz > 0)$	0	$-\frac{1}{2}p_i \frac{dV}{dz}/P_{i-1}^i$	$-\frac{1}{3}p_{i+1} \frac{dV}{dz}/P_i^{i+1}$
Diffusive reacceleration <sup>a</sup>	$p$	$\frac{2D_{pp,i-1}}{P_{i-1}^{i+1}} \left( \frac{1}{P_{i-1}^i} + \frac{2}{P_{i-1}^i} \right)$	$\frac{2}{P_{i-1}^{i+1}} \left( \frac{D_{pp,i+1}}{P_i^{i+1}} + \frac{D_{pp,i-1}}{P_{i-1}^i} \right)$	$\frac{2D_{pp,i+1}}{P_{i-1}^{i+1}} \left( \frac{1}{P_i^{i+1}} + \frac{2}{P_{i+1}^i} \right)$
Energy loss <sup>a</sup>	$p$	0	$\dot{p}_i/P_i^{i+1}$	$\dot{p}_{i+1}/P_i^{i+1}$
Fragmentation	$R, z, p$	0	$1/3\tau_f$	0
Radioactive decay	$R, z, p$	0	$1/3\tau_r$	0

The main assumptions and limitations of GALPROP (Strong et al., 2007; Fan et al., 2010) are:

1. It can only calculate energies below  $10^{15}$  eV.
2. It cannot calculate the trajectory of the cosmic ray.
3. Assumes uniform source abundance.
4. Can only calculate the cosmic rays which occur on scales  $> 10$  pc.
5. No clumpy ISM can be included.
6. All cosmic rays are assumed to be formed in one single type of astrophysical source such as a SNR.
7. Propagation of cosmic rays are isotropic.
8. Distribution of cosmic ray sources are continuous.

---

## Bibliography

- Abdo, A. A., Ackermann, M., Ajello, M., et al. 2009a, *ApJL*, 706, L1
- . 2009b, *Physical Review Letters*, 102, 181101
- . 2010a, *ApJ*, 722, 1303
- . 2010b, *Science*, 327, 1103
- . 2010c, *ApJ*, 712, 459
- . 2011, *ApJ*, 734, 28
- Acciari, V. A., Aliu, E., Arlen, T., et al. 2009, *ApJL*, 698, L133
- . 2011, *ApJL*, 730, L20
- Ackermann, M., Ajello, M., Atwood, W. B., et al. 2010, *Physical Review D*, 82, 092004
- Ackermann, M., Ajello, M., Allafort, A., et al. 2013a, *Science*, 339, 807
- . 2013b, *Science*, 339, 807
- Ackermann, M., Ajello, M., Albert, A., et al. 2014, *PhRvL*, 112, 151103
- Adriani, O., Barbarino, G. C., Bazilevskaya, G. A., et al. 2009a, *Nature*, 458, 607
- . 2009b, *Physical Review Letters*, 102, 051101
- . 2011, *Science*, 332, 69
- Aguilar, M., Alberti, G., Alpat, B., et al. 2013, *Physical Review Letters*, 110, 141102
- Aharonian, F. 2004, *Very High Energy Cosmic Gamma Radiation: A Crucial Window on the Extreme Universe* (World Scientific)

- Aharonian, F., Akhperjanian, A. G., Bazer-Bachi, A. R., et al. 2008a, *A&A*, 481, 401
- Aharonian, F., Akhperjanian, A. G., Barres de Almeida, U., et al. 2008b, *Physical Review Letters*, 101, 261104
- Aharonian, F., Akhperjanian, A. G., de Almeida, U. B., et al. 2009a, *ApJ*, 692, 1500
- Aharonian, F., Akhperjanian, A. G., Anton, G., et al. 2009b, *A&A*, 508, 561
- Aharonian, F. A., & Atoyan, A. M. 1996, *A&A*, 309, 917
- . 2000, *A&A*, 362, 937
- Ahn, H. S., Allison, P., Bagliesi, M. G., et al. 2010, *ApJL*, 714, L89
- Alcaraz, J., Alpat, B., Ambrosi, G., et al. 2000a, *Physics Letters B*, 490, 27
- . 2000b, *Physics Letters B*, 484, 10
- Aleksić, J., Alvarez, E. A., Antonelli, L. A., et al. 2012, *A&A*, 541, A13
- AMS-01 Collaboration, Aguilar, M., Alcaraz, J., et al. 2007, *Physics Letters B*, 646, 145
- Araya, M. 2013, *MNRAS*, 434, 2202
- Arons, J. 1981, *ApJ*, 248, 1099
- Asakimori, K., Burnett, T. H., Cherry, M. L., et al. 1998, *ApJ*, 502, 278
- Aschenbach, B. 1993, *Advances in Space Research*, 13, 45
- . 1998, *Nature*, 396, 141
- Axford, W. I., Leer, E., & Skadron, G. 1977, *International Cosmic Ray Conference*, 11, 132
- Baade, W., & Zwicky, F. 1934, *Proceedings of the National Academy of Science*, 20, 254
- Baltz, E. A., & Edsjö, J. 1999, *Physical Review D*, 59, 023511
- Barwick, S. W., Beatty, J. J., Bhattacharyya, A., et al. 1997, *ApJL*, 482, L191
- Beatty, J. J., Bhattacharyya, A., Bower, C., et al. 2004, *Physical Review Letters*, 93, 241102
- Bell, A. R. 1978a, *MNRAS*, 182, 147

- . 1978b, *MNRAS*, 182, 443
- Bertone, G. 2010, *Particle dark matter: observations, models and searches* (Cambridge University Press)
- Bethe, H., & Heitler, W. 1934, *Royal Society of London Proceedings Series A*, 146, 83
- Biermann, P. L., Becker, J. K., Dreyer, J., et al. 2010, *ApJ*, 725, 184
- Blandford, R. D., & Ostriker, J. P. 1978, *ApJL*, 221, L29
- Blasi, P. 2009, *Physical Review Letters*, 103, 051104
- Blasi, P., & Amato, E. 2011, in *High-Energy Emission from Pulsars and their Systems*, ed. D. F. Torres & N. Rea, 624
- Blondin, J. M., Wright, E. B., Borkowski, K. J., & Reynolds, S. P. 1998, *ApJ*, 500, 342
- Blumenthal, G. R., & Gould, R. J. 1970, *Reviews of Modern Physics*, 42, 237
- Bocchino, F., Miceli, M., & Troja, E. 2009, *A&A*, 498, 139
- Boezio, M. 2014, *Brazilian Journal of Physics*, 44, 441
- Boezio, M., Carlson, P., Francke, T., et al. 1999, *ApJ*, 518, 457
- . 2000, *ApJ*, 532, 653
- Boezio, M., Bonvicini, V., Schiavon, P., et al. 2003, *APh*, 19, 583
- Bogovalov, S. V., Chechetkin, V. M., Koldoba, A. V., & Ustyugova, G. V. 2005, *MNRAS*, 358, 705
- Brogan, C. L., Frail, D. A., Goss, W. M., & Troland, T. H. 2000, *ApJ*, 537, 875
- Brogan, C. L., Goss, W. M., Hunter, T. R., et al. 2013, *ApJ*, 771, 91
- Bronfman, L., Cohen, R. S., Alvarez, H., May, J., & Thaddeus, P. 1988, *ApJ*, 324, 248
- Brun, F., de Naurois, M., Hofmann, W., et al. 2011, *ArXiv e-prints*, arXiv:1104.5003
- Case, G., & Bhattacharya, D. 1996, *A&AS*, 120, C437
- Cassam-Chenaï, G., Hughes, J. P., Reynoso, E. M., Badenes, C., & Moffett, D. 2008, *ApJ*, 680, 1180

- Castro, D., & Slane, P. 2010, *ApJ*, 717, 372
- Castro, D., Slane, P., Carlton, A., & Figueroa-Feliciano, E. 2013a, *ApJ*, 774, 36
- . 2013b, *ApJ*, 774, 36
- Chang, J., Adams, J. H., Ahn, H. S., et al. 2008, *Nature*, 456, 362
- Chevalier, R. A. 1974, *ApJ*, 188, 501
- . 2005, *ApJ*, 619, 839
- Cioffi, D. F., McKee, C. F., & Bertschinger, E. 1988, *ApJ*, 334, 252
- Claussen, M. J., Frail, D. A., Goss, W. M., & Gaume, R. A. 1997, *ApJ*, 489, 143
- Consolandi, C., & AMS-02 Collaboration. 2014, *ArXiv e-prints*, arXiv:1402.0467
- Coppi, P. S., & Blandford, R. D. 1990, *MNRAS*, 245, 453
- Cordes, J. M., Weisberg, J. M., Frail, D. A., Spangler, S. R., & Ryan, M. 1991, *Nature*, 354, 121
- Cox, D. P., Shelton, R. L., Maciejewski, W., et al. 1999, *ApJ*, 524, 179
- Cox, P., Kruegel, E., & Mezger, P. G. 1986, *A&A*, 155, 380
- Cui, W., & Cox, D. P. 1992, *ApJ*, 401, 206
- Delahaye, T., Brun, P., Donato, F., et al. 2009a, *ArXiv e-prints*, arXiv:0905.2144
- Delahaye, T., Lineros, R., Donato, F., et al. 2009b, *A&A*, 501, 821
- Dermer, C. D. 1986, *A&A*, 157, 223
- Di Mauro, M., Donato, F., Fornengo, N., Lineros, R., & Vittino, A. 2014, *JCAP*, 4, 6
- Dickey, J. M., & Lockman, F. J. 1990, *ARA&A*, 28, 215
- Diehl, E., Ellithorpe, D., Müller, D., & Swordy, S. P. 2003, *APh*, 18, 487
- Dwarkadas, V. V. 2005, *ApJ*, 630, 892
- Dyer, K. K., Reynolds, S. P., & Borkowski, K. J. 2004, *ApJ*, 600, 752
- Erlykin, A. D., & Wolfendale, A. W. 2012, *APh*, 35, 449
- Fan, Y.-Z., Zhang, B., & Chang, J. 2010, *International Journal of Modern Physics D*, 19, 2011

- Feng, J., & Zhang, H.-H. 2015, ArXiv e-prints, arXiv:1504.03312
- Fermi, E. 1949, *Physical Review*, 75, 1169
- Filippenko, A. V. 1997, *ARA&A*, 35, 309
- Frail, D. A. 2011, *MmSAI*, 82, 703
- Frail, D. A., Goss, W. M., Reynoso, E. M., et al. 1996, *AJ*, 111, 1651
- Frail, D. A., Goss, W. M., & Slysh, V. I. 1994, *ApJL*, 424, L111
- Frail, D. A., & Mitchell, G. F. 1998, *ApJ*, 508, 690
- Fujita, Y., Kohri, K., Yamazaki, R., & Ioka, K. 2009, *Physical Review D*, 80, 063003
- Gaensler, B. M., & Slane, P. O. 2006, *ARA&A*, 44, 17
- Gaensler, B. M., van der Swaluw, E., Camilo, F., et al. 2004, *ApJ*, 616, 383
- Gaisser, T. K., Protheroe, R. J., & Stanev, T. 1998, *ApJ*, 492, 219
- Garnavich, P. M., Jha, S., Challis, P., et al. 1998, *ApJ*, 509, 74
- Gendeleev, L., Profumo, S., & Dormody, M. 2010, *JCAP*, 2, 16
- Ghavamian, P., Hughes, J. P., & Williams, T. B. 2005, *ApJ*, 635, 365
- Ginzburg, V. L., & Syrovatskii, S. I. 1964, *The Origin of Cosmic Rays*
- Golden, R. L., Stochaj, S. J., Stephens, S. A., et al. 1996, *ApJL*, 457, L103
- Gordon, M. A., & Burton, W. B. 1976, *ApJ*, 208, 346
- Gotthelf, E. V. 2004, in *IAU Symposium*, Vol. 218, *Young Neutron Stars and Their Environments*, ed. F. Camilo & B. M. Gaensler, 225
- Grasso, D., Profumo, S., Strong, A. W., et al. 2009, *Astroparticle Physics*, 32, 140
- Green, D. A. 1996, *VizieR Online Data Catalog*, 7187, 0
- . 2014, *Bulletin of the Astronomical Society of India*, 42, 47
- Gregory, P. 2005, *Bayesian logical data analysis for the physical sciences: a comparative approach with Mathematica support* (Cambridge University Press)
- Gronenschild, E. H. B. M., & Mewe, R. 1982, *A&AS*, 48, 305
- Haino, S., Sanuki, T., Abe, K., et al. 2004, *PhLB*, 594, 35

- Hanabata, Y., Katagiri, H., Hewitt, J. W., et al. 2014, *ApJ*, 786, 145
- Harding, A. K., & Muslimov, A. G. 1998, *ApJ*, 508, 328
- . 2001, *ApJ*, 556, 987
- . 2002, *ApJ*, 568, 862
- Hareyama, M., & RUNJOB Collaboration. 2006, *Journal of Physics Conference Series*, 31, 159
- Harrus, I., Smith, R., Slane, P., & Hughes, J. 2006, in *ESA Special Publication*, Vol. 604, *The X-ray Universe 2005*, ed. A. Wilson, 369
- Heger, A., Fryer, C. L., Woosley, S. E., Langer, N., & Hartmann, D. H. 2003, *ApJ*, 591, 288
- Hess, V. 1912, *Physikalische Zeitschrift*, 13, 1084
- Hester, J. J. 2008, *ARA&A*, 46, 127
- Hillas, A. M., ed. 1972, *Cosmic rays. Selected Readings in Physics*.
- Hillebrandt, W., & Niemeyer, J. C. 2000, *ARA&A*, 38, 191
- Hinton, J. A., & Hofmann, W. 2009, *ARA&A*, 47, 523
- Hollenbach, D., & McKee, C. F. 1989, *ApJ*, 342, 306
- Hooper, D., Blasi, P., & Dario Serpico, P. 2009, *JCAP*, 1, 25
- Hughes, J. P., & Helfand, D. J. 1985, *ApJ*, 291, 544
- Hugoniot, M. 1889, *Journal de lâ€™École Polytechnique*, 57, 1
- Hwang, U., Decourchelle, A., Holt, S. S., & Petre, R. 2002, *ApJ*, 581, 1101
- Itoh, H. 1977, *PASJ*, 29, 813
- . 1984, *ApJ*, 285, 601
- Itoh, H., & Masai, K. 1989, *MNRAS*, 236, 885
- Ivanenko, I. P., Shestoporov, V. Y., Chikova, L. O., et al. 1993, *International Cosmic Ray Conference*, 2, 17
- Jeffreys, H. 1967, *Theory of probability*, *International series of monographs on physics* (Clarendon Press)
- Jones, D. O., Rodney, S. A., Riess, A. G., et al. 2013, *ApJ*, 768, 166

- Kaastra, J. S., & Jansen, F. A. 1993, *A&AS*, 97, 873
- Kaastra, J. S., Paerels, F. B. S., Durret, F., Schindler, S., & Richter, P. 2008, *SSRv*, 134, 155
- Kachelrieß, M., & Ostapchenko, S. 2012, *PRD*, 86, 043004
- Kargaltsev, O., & Pavlov, G. G. 2008, in *American Institute of Physics Conference Series*, Vol. 983, 40 Years of Pulsars: Millisecond Pulsars, Magnetars and More, ed. C. Bassa, Z. Wang, A. Cumming, & V. M. Kaspi, 171–185
- Kawasaki, M., Ozaki, M., Nagase, F., Inoue, H., & Petre, R. 2005, *ApJ*, 631, 935
- Kawasaki, M. T., Ozaki, M., Nagase, F., et al. 2002, *ApJ*, 572, 897
- Kennel, C. F., & Coroniti, F. V. 1984, *ApJ*, 283, 710
- Keohane, J. W., Reach, W. T., Rho, J., & Jarrett, T. H. 2007, *ApJ*, 654, 938
- Komissarov, S. S., & Lyubarsky, Y. E. 2004, *MNRAS*, 349, 779
- Koyama, K., Kinugasa, K., Matsuzaki, K., et al. 1997, *PASJ*, 49, L7
- Koyama, K., Petre, R., Gotthelf, E. V., et al. 1995, *Nature*, 378, 255
- Krymskii, G. F. 1977, *Soviet Physics Doklady*, 22, 327
- Lacey, C. K., Lazio, T. J. W., Kassim, N. E., et al. 2001, *ApJ*, 559, 954
- Lagage, P. O., & Cesarsky, C. J. 1983, *A&A*, 125, 249
- Lai, D. 2004, in *Cosmic explosions in three dimensions*, ed. P. Höflich, P. Kumar, & J. C. Wheeler, 276
- Lattimer, J. M., & Prakash, M. 2007, *PhR*, 442, 109
- Lazendic, J. S., & Slane, P. O. 2006, *ApJ*, 647, 350
- Lee, S.-H., Ellison, D. C., & Nagataki, S. 2012, *ApJ*, 750, 156
- Lockett, P., Gauthier, E., & Elitzur, M. 1999, *ApJ*, 511, 235
- Longair, M. 2011, *High Energy Astrophysics* (Cambridge University Press)
- Lopez, L. A., Pearson, S., Ramirez-Ruiz, E., et al. 2013a, *ApJ*, 777, 145
- Lopez, L. A., Ramirez-Ruiz, E., Castro, D., & Pearson, S. 2013b, *ApJ*, 764, 50
- Lukasiak, A., Ferrando, P., McDonald, F. B., & Webber, W. R. 1994, *ApJ*, 423, 426

- Macquorn Rankine, W. J. 1870, Royal Society of London Philosophical Transactions Series I, 160, 277
- Malkov, M. A., & O’C Drury, L. 2001, Reports on Progress in Physics, 64, 429
- Malyshev, D., Cholis, I., & Gelfand, J. 2009, Physical Review D, 80, 063005
- Manchester, R. N., Hobbs, G. B., Teoh, A., & Hobbs, M. 2005, AJ, 129, 1993
- Manchester, R. N., & Taylor, J. H. 1977, Pulsars
- Masai, K. 1984, Ap&SS, 98, 367
- McKee, C. F. 1974, ApJ, 188, 335
- McKee, C. F., & Ostriker, J. P. 1977, ApJ, 218, 148
- Menn, W., Hof, M., Reimer, O., et al. 2000, ApJ, 533, 281
- Mertsch, P., & Sarkar, S. 2011, in Cosmic Rays for Particle and Astroparticle Physics, ed. S. Giani, C. Leroy, & P. G. Rancoita, 535–543
- Miceli, M., Bocchino, F., Decourchelle, A., Ballet, J., & Reale, F. 2010, A&A, 514, L2
- Minkowski, R. 1941, PASP, 53, 224
- Morlino, G., & Caprioli, D. 2012, A&A, 538, A81
- Moskalenko, I. V., Porter, T. A., & Strong, A. W. 2006, ApJL, 640, L155
- Moskalenko, I. V., & Strong, A. W. 1998, ApJ, 493, 694
- Moskalenko, I. V., Strong, A. W., Ormes, J. F., & Potgieter, M. S. 2002, ApJ, 565, 280
- Moskalenko, I. V., Strong, A. W., Porter, T. A., et al. 2011, The GALPROP code for cosmic-ray transport and diffuse emission production, <http://galprop.stanford.edu/>, last checked: 01.03.2015
- Muraishi, H., Tanimori, T., Yanagita, S., et al. 2000, A&A, 354, L57
- Neronov, A., Semikoz, D. V., & Taylor, A. M. 2012, Physical Review Letters, 108, 051105
- Nguyen Luong, Q., Motte, F., Hennemann, M., et al. 2011, A&A, 535, A76
- Nguyen-Lu’o’ng, Q., Motte, F., Carlhoff, P., et al. 2013, ApJ, 775, 88
- Nomoto, K. 1982, ApJ, 253, 798

- Olive, K. A., & Particle Data Group. 2014, *Chinese Physics C*, 38, 090001
- Özel, F. 2013, *Reports on Progress in Physics*, 76, 016901
- Pacholczyk, A. G. 1970, *Radio astrophysics. Nonthermal processes in galactic and extragalactic sources*
- Pacini, F., & Salvati, M. 1973, *ApJ*, 186, 249
- Pannuti, T. G., Rho, J., Borkowski, K. J., & Cameron, P. B. 2010, *AJ*, 140, 1787
- Panov, A. D. 2013, *Journal of Physics Conference Series*, 409, 012004
- Park, S., Hughes, J. P., Slane, P. O., et al. 2007, *ApJL*, 670, L121
- Patnaude, D. J., Ellison, D. C., & Slane, P. 2009, *ApJ*, 696, 1956
- Pavlov, G. G., & Zavlin, V. E. 2003, in *Texas in Tuscany. XXI Symposium on Relativistic Astrophysics*, ed. R. Bandiera, R. Maiolino, & F. Mannucci, 319–328
- Perlmutter, S., Aldering, G., della Valle, M., et al. 1998, *Nature*, 391, 51
- Pihlström, Y. M., Sjouwerman, L. O., Frail, D. A., et al. 2014, *AJ*, 147, 73
- Podsiadlowski, P., Joss, P. C., & Hsu, J. J. L. 1992, *ApJ*, 391, 246
- Porter, T. A., & Strong, A. W. 2005, *International Cosmic Ray Conference*, 4, 77
- Profumo, S. 2012, *Central European Journal of Physics*, 10, 1
- Raymond, J. C. 1979, *ApJS*, 39, 1
- Raymond, J. C., & Smith, B. W. 1977, *ApJS*, 35, 419
- Reynolds, S. P. 1998, *ApJ*, 493, 375
- . 2008, *ARA&A*, 46, 89
- Rho, J., & Petre, R. 1998, *ApJL*, 503, L167
- Riess, A. G., Strolger, L.-G., Casertano, S., et al. 2007, *ApJ*, 659, 98
- Romani, R. W., Shaw, M. S., Camilo, F., Cotter, G., & Sivakoff, G. R. 2010, *ApJ*, 724, 908
- Ruderman, M. A., & Sutherland, P. G. 1975, *ApJ*, 196, 51
- Ryan, M. J., Ormes, J. F., & Balasubrahmanyam, V. K. 1972, *Physical Review Letters*, 28, 985
- Rybicki, G. B., & Lightman, A. P. 1979, *Radiative processes in astrophysics*

- Sawada, M., & Koyama, K. 2012, PASJ, 64, 81
- Schaab, C., Sedrakian, A., Weber, F., & Weigel, M. K. 1999, A&A, 346, 465
- Schlickeiser, R. 2002, Cosmic Ray Astrophysics
- Sedov, L. I. 1959, Similarity and Dimensional Methods in Mechanics
- Seta, M., Hasegawa, T., Dame, T. M., et al. 1998, ApJ, 505, 286
- Shaviv, N. J., Nakar, E., & Piran, T. 2009, Physical Review Letters, 103, 111302
- Shelton, R. L., Cox, D. P., Maciejewski, W., et al. 1999, ApJ, 524, 192
- Shelton, R. L., Kuntz, K. D., & Petre, R. 2004, ApJ, 611, 906
- Shklovskii, I. 1953, Doklady Akademii Nauk SSSR, 91, 475
- Shklovskii, I. S. 1962, AZh, 39, 591
- Slane, P., Bykov, A., Ellison, D. C., Dubner, G., & Castro, D. 2014, SSRv, arXiv:1406.4364
- Slane, P., Gaensler, B. M., Dame, T. M., et al. 1999, ApJ, 525, 357
- Slane, P., Smith, R. K., Hughes, J. P., & Petre, R. 2002, ApJ, 564, 284
- Smith, R. K., & Hughes, J. P. 2010, ApJ, 718, 583
- Spitzer, L. 1965, Physics of fully ionized gases
- Stage, M. D., Allen, G. E., Houck, J. C., & Davis, J. E. 2006, Nature Physics, 2, 614
- Stanev, T. 2010, High Energy Cosmic Rays, doi:10.1007/978-3-540-85148-6
- Strong, A. W., & Mattox, J. R. 1996, A&A, 308, L21
- Strong, A. W., & Moskalenko, I. V. 1998, ApJ, 509, 212
- Strong, A. W., Moskalenko, I. V., & Ptuskin, V. S. 2007, Annual Review of Nuclear and Particle Science, 57, 285
- Suzuki, N., Rubin, D., Lidman, C., et al. 2012, ApJ, 746, 85
- Taylor, G. 1950, Royal Society of London Proceedings Series A, 201, 159
- Temim, T., Slane, P., Gaensler, B. M., Hughes, J. P., & Van Der Swaluw, E. 2009, ApJ, 691, 895
- Thielemann, F.-K., Nomoto, K., & Hashimoto, M.-A. 1996, ApJ, 460, 408

- Thompson, A., Vaughan, D., for X-ray optics, C., & advanced light source. 2009, X-ray Data Booklet (Lawrence Berkeley Laboratory)
- Thoudam, S., & Hörandel, J. R. 2012, MNRAS, 421, 1209
- . 2013, MNRAS, 435, 2532
- Tomassetti, N. 2012, ApJL, 752, L13
- Trotta, R. 2008, Contemporary Physics, 49, 71
- Truelove, J. K., & McKee, C. F. 1999, ApJS, 120, 299
- Tucker, W. H., & Gould, R. J. 1966, ApJ, 144, 244
- Uchiyama, Y., Aharonian, F. A., Tanaka, T., Takahashi, T., & Maeda, Y. 2007, Nature, 449, 576
- Uchiyama, Y., Funk, S., Katagiri, H., et al. 2012, ApJL, 749, L35
- van der Swaluw, E., Achterberg, A., Gallant, Y. A., Downes, T. P., & Keppens, R. 2003, A&A, 397, 913
- van der Swaluw, E., Achterberg, A., Gallant, Y. A., & Tóth, G. 2001, A&A, 380, 309
- van der Swaluw, E., Downes, T. P., & Keegan, R. 2004, A&A, 420, 937
- Velázquez, P. F., Martinell, J. J., Raga, A. C., & Giacani, E. B. 2004, ApJ, 601, 885
- Vink, J. 2012, A&ARv, 20, 49
- Vink, J., Kaastra, J. S., & Bleeker, J. A. M. 1996, A&A, 307, L41
- Vladimirov, A. E., Jóhannesson, G., Moskalenko, I. V., & Porter, T. A. 2012, ApJ, 752, 68
- Wardle, M. 1999, ApJL, 525, L101
- Warren, J. S., Hughes, J. P., Badenes, C., et al. 2005, ApJ, 634, 376
- Wefel, J. P., adams, J. H., Ahn, H. S., et al. 2008, International Cosmic Ray Conference, 2, 31
- Weisskopf, M. C., Hester, J. J., Tennant, A. F., et al. 2000, ApJL, 536, L81
- White, R. L., & Long, K. S. 1991, ApJ, 373, 543
- Winkler, P. F., & Long, K. S. 1997, ApJ, 491, 829

- Woltjer, L. 1972, *ARA&A*, 10, 129
- Woosley, S., & Janka, T. 2005, *Nature Physics*, 1, 147
- Woosley, S. E., & Weaver, T. A. 1995, *ApJS*, 101, 181
- Yamaguchi, H., Ozawa, M., Koyama, K., et al. 2009, *ApJL*, 705, L6
- Yoon, Y. S., Ahn, H. S., Allison, P. S., et al. 2011, *ApJ*, 728, 122
- Yuan, Q., Huang, X., Liu, S., & Zhang, B. 2014, *ApJL*, 785, L22
- Yuan, Q., Zhang, B., & Bi, X.-J. 2011, *PhRvD*, 84, 043002
- Yüksel, H., Kistler, M. D., & Stanev, T. 2009, *Physical Review Letters*, 103, 051101
- Zatsepin, V. I., & Sokolskaya, N. V. 2006, *A&A*, 458, 1
- Zeldovich, Y. B., & Raizer, Y. P. 1966, *Elements of gasdynamics and the classical theory of shock waves*
- Zhang, G.-Y., Chen, Y., Su, Y., et al. 2015, *ApJ*, 799, 103